

Titre: Applications of doppler optical coherence tomography
Title:

Auteur: Zhiqiang Xu
Author:

Date: 2008

Type: Mémoire ou thèse / Dissertation or Thesis

Référence: Xu, Z. (2008). Applications of doppler optical coherence tomography [Ph.D. thesis, École Polytechnique de Montréal]. PolyPublie.
Citation: <https://publications.polymtl.ca/8172/>

 **Document en libre accès dans PolyPublie**
Open Access document in PolyPublie

URL de PolyPublie: <https://publications.polymtl.ca/8172/>
PolyPublie URL:

Directeurs de recherche: Romain Maciejko, & Olivier T. Guenat
Advisors:

Programme: Unspecified
Program:

UNIVERSITÉ DE MONTRÉAL

APPLICATIONS OF DOPPLER
OPTICAL COHERENCE TOMOGRAPHY

ZHIQIANG XU
DÉPARTEMENT DE GÉNIE PHYSIQUE
ÉCOLE POLYTECHNIQUE DE MONTRÉAL

THÈSE PRÉSENTÉE EN VUE DE L'OBTENTION
DU DIPLÔME DE PHILOSOPHIAE DOCTOR (Ph.D.)
(GÉNIE PHYSIQUE)

AOÛT 2008



Library and
Archives Canada

Published Heritage
Branch

395 Wellington Street
Ottawa ON K1A 0N4
Canada

Bibliothèque et
Archives Canada

Direction du
Patrimoine de l'édition

395, rue Wellington
Ottawa ON K1A 0N4
Canada

Your file *Votre référence*
ISBN: 978-0-494-46121-1
Our file *Notre référence*
ISBN: 978-0-494-46121-1

NOTICE:

The author has granted a non-exclusive license allowing Library and Archives Canada to reproduce, publish, archive, preserve, conserve, communicate to the public by telecommunication or on the Internet, loan, distribute and sell theses worldwide, for commercial or non-commercial purposes, in microform, paper, electronic and/or any other formats.

The author retains copyright ownership and moral rights in this thesis. Neither the thesis nor substantial extracts from it may be printed or otherwise reproduced without the author's permission.

AVIS:

L'auteur a accordé une licence non exclusive permettant à la Bibliothèque et Archives Canada de reproduire, publier, archiver, sauvegarder, conserver, transmettre au public par télécommunication ou par l'Internet, prêter, distribuer et vendre des thèses partout dans le monde, à des fins commerciales ou autres, sur support microforme, papier, électronique et/ou autres formats.

L'auteur conserve la propriété du droit d'auteur et des droits moraux qui protègent cette thèse. Ni la thèse ni des extraits substantiels de celle-ci ne doivent être imprimés ou autrement reproduits sans son autorisation.

In compliance with the Canadian Privacy Act some supporting forms may have been removed from this thesis.

Conformément à la loi canadienne sur la protection de la vie privée, quelques formulaires secondaires ont été enlevés de cette thèse.

While these forms may be included in the document page count, their removal does not represent any loss of content from the thesis.

Bien que ces formulaires aient inclus dans la pagination, il n'y aura aucun contenu manquant.


Canada

UNIVERSITÉ DE MONTRÉAL

ÉCOLE POLYTECHNIQUE DE MONTRÉAL

Cette thèse intitulée:

APPLICATIONS OF DOPPLER
OPTICAL COHERENCE TOMOGRAPHY

présentée par: XU Zhiqiang

en vue de l'obtention du diplôme de: Philosophiae Doctor

a été dûment accepté par le jury d'examen constitué de:

M. FRANCOEUR Sébastien, Ph.D., président

M. MACIEJKO Romain, Ph.D., membre et directeur de recherche

M. GUENAT Olivier, Ph.D., membre

M. KADEM Lyes, Ph.D., membre

To my parents

ACKNOWLEDGEMENTS

My Ph.D. project is a continuation of the research initiated during my Master's degree work in the Optoelectronic Laboratory at École Polytechnique. Professor Romain Maciejko has been my supervisor since early 2001. In the past eight years, I have to say that I have received much help from him and I wouldn't have been able to accomplish the work presented in this dissertation without his generous support and guidance. Prof. Maciejko led me step-by-step through the whole training process which covers many of the most important aspects of scientific research. He always encouraged me to propose new ideas and to develop them with appropriate experiments. His help also includes his broad vision and insights which can dig out the most valuable wealth from experimental results in order to produce high quality papers. Here, I would like to express my most sincere appreciation to him.

I am also grateful to Dr. Lionel Carrion for his friendly assistance in many aspects. He has always been available when I needed help, whether academic or otherwise. We had many fruitful discussions on OCT and Doppler OCT implementations, control of light sources, sample fabrication as well as offline data processing. Dr. Carrion has always been patient and willing to spend hours discussing problems and finding out the solutions with me. Over the years, he has given me much precious advice. Without him, I would not have been able to obtain the many good results for the projects covered in this thesis.

For the design and construction of the experimental systems, I would like to give my thank to Mr. Francis Boismenu for providing insightful suggestions and technical assistance. He has made several instrumental components for my setups in the past few years including lens holders, an adjustable sample stage, a probe station and a frequency counter setup. His

precisely made components ensured the fine alignment of our experimental setups. Thanks, Francis, and hopefully there will be nobody else who rushes to you in a hurry and hands you the design drawing and asks for the finished component for within half an hour later.

I also wish to give my thanks to Prof. Lyes Kadem and his PhD student, Othman Ahmed Smadi, from Department of Mechanical Engineering, Concordia University. With them, I worked as a visiting student in Prof. Kadem's laboratory on the theoretical model for the bifurcation using Gambit and Fluent. It was Prof. Kadem who gave me a course on blood flow dynamics and showed me the importance of determining the wall shear stress distribution within blood vessels. His advice was very helpful in an objective of comparing Doppler OCT with the theoretical models of blood flow and fluid dynamics. These applications have added value to my research project greatly. I am also very grateful for his kind offer of being on my thesis committee.

I am grateful to have collaborated with Prof. Olivier Guenat and his group. This has allowed us to apply Doppler OCT techniques to microfluidics, (lab-on-a-chip). I worked with Caroline Miville-Godin to prepare the PDMM microfluidics sample and developed the proper way to connect the inlet/outlet tubes without leakage. I enjoyed spending time in the clean room working with Dr. Philippe Vasseur. From him, I learned how to seal our microfluidics sample with RIE.

I am very grateful to the members of my thesis committee, Prof. André Garon, Prof. Sébastien Francoeur, Prof. Lyes Kadem, Prof. Olivier T. Guenat and Prof. Romain Maciejko, for their time and effort.

I would like to thank my friends, Yougui Liao, Changqing Zhang, Dequan Yang, Ning Guo,

Ji Li, Li Li, Yulin Zhang, Hui Lin, Xiaopei Li, and many others. I enjoyed chatting during lunch time when we gathered in the first floor cafeteria.

Finally, I would like to say thanks to my parents, my wife and my sons for their constant support and love. Without their love and support, I would not have gotten this far.

RÉSUMÉ

Durant la dernière décennie, la Tomographie par Optique Cohérente (TOC) a constitué une avancée majeure dans le domaine de l'imagerie biomédicale. Cette technique permet d'imager en détail, à distance et de façon quasi non destructive la morphologie de tissus biologiques transparents ou opaques avec une résolution en profondeur de l'échelle du micron. Dans la première partie de ce mémoire, nous décrivons le développement et les performances des systèmes TOC réalisés au laboratoire. Chaque système est basé sur un interféromètre de Michelson «à l'air libre» ou fibré et utilise une gamme spectrale spécifique. La seconde partie du mémoire traite de la TOC Doppler, un important complément de la TOC. Cette technique permet l'évaluation simultanée de l'information structurale et de la distribution des vitesses de flux en un point défini à l'intérieur de l'échantillon. Les travaux réalisés récemment dans notre laboratoire ont pour but de mesurer des flux de façon plus précise et dans une plage dynamique élargie ainsi que d'appliquer cette technique dans des domaines de recherche variés tels que la microfluidique ou encore l'hémodynamique.

Une étude à différentes longueurs d'onde des propriétés optiques de tissus biologiques (telles que l'absorption ou la diffusion) a été réalisée dans notre laboratoire. Le premier système TOC est constitué d'un laser Titane:Saphir émettant des impulsions de longueur d'onde centrale 810 nm et de 10 fs de durée, associé à un interféromètre «à l'air libre». Les deux autres systèmes utilisent des sources infrarouges émettant à des longueurs d'onde centrales de 1310 nm et 1560 nm, respectivement, et sont utilisées avec des interféromètres fibrés. Une étude comparative utilisant ces trois sources a été réalisée sur divers tissus biologiques in vitro. Une méthode graphique appliquée aux images obtenues a illustré comment les propriétés optiques peuvent affecter la qualité des images en termes de profondeur de pénétration et d'intensité de rétrodiffusion. Nous en avons conclu l'avantage

de travailler avec une longueur d'onde d'émission de 810 nm pour une bonne amplitude de rétrodiffusion et un bon contraste, alors que des sources émettant à 1560 nm donnent une bonne profondeur de pénétration. La source émettant à 1310 nm représente un bon compromis entre les deux cas de figure. Finalement, le choix d'une source est déterminant non seulement pour la résolution axiale, mais aussi pour la profondeur et le contraste des images TOC.

En complément de cette technique, la TOC Doppler est un domaine de recherche de plus en plus populaire et prometteur, notamment pour les applications dans la recherche cardiovasculaire et en microfluidique. Nous avons consacré une partie de nos efforts à la recherche de méthodes précises et efficaces pour le traitement des données expérimentales. Ainsi, nous avons appliqué une distribution spectro-temporelle de type pseudo-Wigner au traitement de données de la TOC Doppler et nous avons comparé sa performance avec celles de plusieurs méthodes couramment utilisées telles que la Transformée de Fourier à court terme, la méthode résolue en phase basée sur la transformée de Hilbert, ou encore la méthode d'autocorrélation. Nous en avons conclu que la distribution de type pseudo-Wigner est dans l'ensemble plus précise que les autres méthodes couramment utilisées pour l'analyse par TOC Doppler des distributions de vitesses dans le plan de l'image, surtout dans le cas des hautes vitesses.

Nous avons également mis en relief les avantages de la TOC dans le domaine temporel par rapport à la TOC dans le domaine spectral dans le cas de certaines applications où une mesure précise des vitesses est essentielle. Etant donné que le signal d'interférence TOC mesuré localement peut être approximé par une onde mono-périodique, nous avons développé pour le traitement des données un nouveau modèle simple et peu fastidieux basé sur la détermination des points pour lesquels le signal TOC croise l'axe des abscisses,

autrement dit l'axe d'amplitude nulle. Dans le cas d'un écoulement laminaire, la mesure des écarts entre deux points successifs nous permet de déterminer la fréquence Doppler. Cette méthode a été comparée aux approches couramment utilisées en TOC Doppler. Les résultats montrent que dans le cas d'un écoulement laminaire, la méthode des « points de croisement nuls » donne les résultats les plus précis, en particulier pour les hautes vitesses, et permet de réduire de façon substantielle les temps de calcul. De plus, cette méthode permet d'atteindre potentiellement une plage dynamique des vitesses de 70 dB. Cette caractéristique s'avère être un avantage majeur en métrologie dans le cas où l'on voudrait mesurer des vitesses dans un intervalle s'étalant sur plusieurs ordres de grandeur.

Nous avons utilisé cette méthode pour la mesure d'écoulements réels dans des dispositifs. Notamment, les résultats préliminaires obtenus sur des distributions de vitesses dans un circuit microfluidique et dans un fantôme représentant une sténose artérielle sont présentés dans ce mémoire. Nous décrivons également une méthode pour obtenir une distribution vectorielle des vitesses dans le plan de l'image obtenue de la sténose en superposant les distributions scalaires des vitesses obtenues par la TOC Doppler à différents angles d'incidence de la lumière. Cette évaluation quantitative des profils de flux sanguin dans des vaisseaux et des artères peut apporter des informations très importantes pour l'étude de certaines maladies cardiovasculaires telles que l'athérosclérose.

Ces travaux ont mené aux publications suivantes :

1. **Z. Xu**, L. Carrion, and R. Maciejko, "A zero-crossing detection method applied to Doppler OCT," *Opt. Express*, vol. 16, pp. 4394-4412, 2008.
2. **Z. Xu**, L. Carrion, and R. Maciejko, "An assessment of the Wigner distribution method in Doppler OCT," *Opt. Express*, vol. 15, pp. 14738-14749, 2007.
3. Carrion, L., Lestrade, M., **Xu, Z.**, Touma, G., Maciejko R., and Bertrand, M., "Comparative study of optical sources in the near infrared for optical coherence tomography applications," *Journal of Biomedical Optics*, vol. 12, no. 1, pp. 140171-140178, 2007.

4. R. Maciejko, L. Carrion, M. Lestrade, **Z. Xu**, and R. Kashyap, "Optical sources for OCT," *Photons*, vol. 3 no. 1, pp. 28-30, 2005.
5. Lionel Carrion, Michel Lestrade, **Zhiqiang Xu**, Gaby Touma, and Romain Maciejko, "Comparison of optical coherence tomography profiles for three different wavelengths in the near infrared," *Proc. SPIE* 5969, 596922, 2005.
6. Lionel Carrion, **Zhiqiang Xu**, Michel Lestrade, and Romain Maciejko, "Utilisation de nouvelles sources lumineuses pour la tomographie en optique cohérente," *ACFAS, Optique Guidée et Photonique VIII*, pp. 119-121, 2004.
7. **Zhiqiang Xu**, Lionel Carrion, and Romain Maciejko, "Marked advantage of the Wigner distribution method in Doppler OCT," *CIPI Poster*, Ottawa, 2007.
8. **Zhiqiang Xu**, Lionel Carrion, and Romain Maciejko, "Marked advantage of the Wigner distribution method in Doppler OCT," *The Third Graduate Student Physics Conference (CAM2007)*, Montreal, 2007.
9. **Zhiqiang Xu**, Michel Lestrade, and Romain Maciejko, "Experiments on optical coherence tomography," *Femtotech*, Montreal, May 2003.

ABSTRACT

A major development in biomedical imaging in the last decade has been optical coherence tomography (OCT). This technique enables microscale resolution, depth resolved imaging of the detailed morphology of transparent and nontransparent biological tissue in a noncontact and quasi-noninvasive way. In the first part of this dissertation, we will describe the development and the performance of our home-made OCT systems working with different wavelength regions based on free-space and optical fiber Michelson interferometers. The second part will focus on Doppler OCT (DOCT), an important extension of OCT, which enables the simultaneous evaluation of the structural information and of the fluid flow distribution at a localized position beneath the sample surface. Much effort has been spent during the past few years in our laboratory aimed at providing more accurate velocity measurements with an extended dynamic range. We also applied our technique in different research areas such as microfluidics and hemodynamics.

Investigations on the optical properties of the biological tissues (such as absorption and scattering) corresponding to different center wavelengths, have been performed in our laboratory. We used a 10 femtosecond Ti:sapphire laser centered at about 810 nm associated with a free-space Michelson interferometer. The infrared sources were centered at about 1310 and 1560 nm with all-fiber interferometers. Comparative studies using three different sources for several *in vitro* biological tissues based on a graphical method illustrated how the optical properties affect the quality of the OCT images in terms of the penetration depth and backscattering intensity. We have shown the advantage of working with 810-nm emission wavelength for good backscattering amplitude and contrast, while sources emitting at 1570 nm give good penetration depth. The 1330-nm sources provide a good compromise between the two. Therefore, the choice of the source will ultimately determine the longitudinal

resolution and the imaging depth for OCT imaging.

Doppler OCT is becoming an increasingly popular field of investigation within optical coherence tomography with potentially important applications in cardiovascular and microfluidic research. We have spent some of the effort on searching for accurate and efficient methods for processing the experimental data. We applied the pseudo Wigner time-frequency distribution method to the data processing of Doppler OCT and compared its performance to that of the short-time Fourier transform method, the Hilbert-based phase-resolved method and the autocorrelation method. We concluded that the pseudo Wigner-distribution signal processing method is overall more precise than other often-used methods in Doppler OCT for the analysis of cross-sectional velocity distributions, especially in the high velocity regime.

We also discovered the advantage of using the time-domain instead of the frequency domain for Doppler OCT for some applications where precise Doppler-speed metrology is essential. Based on the fact that the obtained local OCT interference signal is almost a single periodic waveform, we have developed a novel, simple and less time-consuming processing method based on the zero-crossing points in an OCT signal for the measurement of the Doppler frequency in a laminar flow. This method was compared to other processing approaches currently used in Doppler OCT. The results show that in the case of laminar flow, the zero-crossing method gives the more precise results, especially in the higher velocity regime with a substantial economy in processing time and an increase in dynamic range which can reach 70 dB. This feature becomes a major advantage in metrology if one wants to measure velocities over several orders of magnitude.

We have applied this technique to some real flow models and the preliminary results on flow velocity distributions obtained in the case of a microfluidic circuit and in that of a phantom of a blood vessel stenosis and bifurcation will be described in this thesis. We also proposed the method to successfully obtain the 2D velocity vector map in the phantom models by overlapping the Doppler OCT scalar velocity distributions of different incident angles. This quantitative knowledge of blood velocity profiles in the vessels can provide very important information in studying some cardiovascular diseases such as atherosclerosis.

This research has led to the following publications:

1. **Z. Xu**, L. Carrion, and R. Maciejko, "A zero-crossing detection method applied to Doppler OCT," *Opt. Opt. Express*, vol. 16, pp. 4394-4412, 2008.
2. **Z. Xu**, L. Carrion, and R. Maciejko, "An assessment of the Wigner distribution method in Doppler OCT," *Opt. Express*, vol. 15, pp. 14738-14749, 2007.
3. Carrion, L., Lestrade, M., **Xu, Z.**, Touma, G., Maciejko R., and Bertrand, M., "Comparative study of optical sources in the near infrared for optical coherence tomography applications," *Journal of Biomedical Optics*, v 12, no. 1, pp. 140171-140178, 2007.
4. R. Maciejko, L. Carrion, M. Lestrade, **Z. Xu**, and R. Kashyap, "Optical sources for OCT," *Photons*, vol. 3 no. 1, pp. 28-30, 2005.
5. Lionel Carrion, Michel Lestrade, **Zhiqiang Xu**, Gaby Touma, and Romain Maciejko, "Comparison of optical coherence tomography profiles for three different wavelengths in the near infrared," *Proc. SPIE 5969*, 596922, 2005.
6. Lionel Carrion, **Zhiqiang Xu**, Michel Lestrade, and Romain Maciejko, "Utilisation de nouvelles sources lumineuses pour la tomographie en optique cohérente," *ACFAS, Optique Guidée et Photonique VIII*, pp. 119-121, 2004.
7. **Zhiqiang Xu**, Lionel Carrion, and Romain Maciejko, "Marked advantage of the Wigner distribution method in Doppler OCT," *CIPI Poster*, Ottawa, 2007.
8. **Zhiqiang Xu**, Lionel Carrion, and Romain Maciejko, "Marked advantage of the Wigner distribution method in Doppler OCT," *The Third Graduate Student Physics Conference (CAM2007)*, Montreal, 2007.
9. **Zhiqiang Xu**, Michel Lestrade, and Romain Maciejko, "Experiments on optical coherence tomography," *Femtotech*, Montreal, May 2003.

CONDENSÉ EN FRANÇAIS

Le but de mon travail de graduation est de développer des systèmes d'imagerie optique basés sur la Tomographie par Cohérence Optique (TOC) et de les utiliser pour étudier les microstructures de tissus biologiques et pour caractériser les écoulements liquides dans des dispositifs et des fantômes. A notre échelle, nous avons contribué aux avancées réalisées dans divers domaines reliés à la TOC: l'amélioration de méthodes théoriques pour le traitement des fréquences Doppler mesurées à partir de l'interférogramme donné par le système TOC, le développement de l'instrumentation à la fois pour la TOC structurelle et la TOC Doppler, la mise en évidence de la façon dont les propriétés optiques des échantillons affectent la qualité des images, et l'application de cette technique optique à l'étude de la distribution des vitesses d'écoulement dans des dispositifs de microfluidique et dans des fantômes de systèmes cardiovasculaires comme les sténoses et les jonctions artérielles. Dans ce mémoire, nous décrirons ces développements réalisés au cours des dernières années. Nous présenterons également les avantages des systèmes de TOC temporels par rapport aux systèmes TOC spectraux en termes de précision et de plage dynamique des vitesses mesurées.

Le second chapitre présente les principes et les développements de la TOC (utilisée pour l'imagerie de tissus biologiques) ainsi que de la TOC Doppler (utilisée pour la détermination des vitesses d'écoulement). Un système TOC « free-space » utilisant un laser Titane:Saphir pulsé a été réalisé et optimisé en termes de polarisation, de dispersion des vitesses de groupe, de profil spectral, et de détection balancée du signal d'enveloppe. Un autre système tout fibré a été réalisé et utilisé avec deux types de sources large bande émettant dans le proche infrarouge autour de longueurs d'onde centrales de 1.3 μm et 1.5 μm , respectivement. Un programme d'acquisition des données et de gestion des balayages axial et transverse pour la

réalisation d'images en 2 D a été réalisé. Ce logiciel permet de modifier plusieurs paramètres et fonctions, notamment la vitesse et les pas de balayage, ou encore les régions dans lesquelles les balayages axial et transverse sont effectués. La distance entre deux balayages axiaux consécutifs est choisie en fonction de la résolution transverse du système expérimental qui est égale au diamètre du point focal du faisceau se propageant dans l'échantillon. L'enveloppe du signal a été obtenue de façon analogique à l'aide d'un filtre passe bas. De cette façon, le taux d'échantillonnage du convertisseur analogique/numérique peut être réduite de 100 kHz à 592 Hz. Le temps d'acquisition des données est également réduit d'un ordre de grandeur par rapport au temps mis pour l'acquisition du signal complet. Une méthode de déconvolution a également été développée dans un programme afin d'éliminer l'effet dû aux lobes secondaires dans les signaux de TOC, ce qui a pour effet de donner un meilleur contraste sans détériorer la résolution des images obtenues.

Une fois réalisés, les systèmes TOC ont été utilisés pour l'étude des relations entre les propriétés optiques des échantillons et la qualité des images en termes de contraste et de profondeur de pénétration. A l'aide d'une méthode graphique appliquée à l'évolution de la puissance lumineuse rétrodiffusée au fur et à mesure de sa propagation dans l'échantillon, nous avons réalisé des études comparatives sur différents tissus biologiques *in vitro* en utilisant trois sources différentes émettant à des longueurs d'onde centrales de 810 nm, 1.3 μm , et 1.5 μm . Étant donné que le coefficient de diffusion est plus élevé pour les faibles longueurs d'onde et qu'à l'inverse l'absorption de l'eau est plus élevée à 1.5 μm , nous avons démontré que les sources émettant autour de la longueur d'onde centrale de 1.3 μm se révèlent être un bon compromis pour l'obtention d'images de qualité présentant une bonne profondeur de pénétration.

Le troisième chapitre décrit l'utilisation d'une distribution de type pseudo-Wigner pour

le calcul des fréquences Doppler contenues dans l'interférogramme de TOC mesuré. Nous avons montré que cette méthode donne des fréquences Doppler en un temps donné plus précises par rapport aux méthodes plus couramment utilisées dans la TOC Doppler. Dans le cas classique d'un écoulement laminaire dans un tube capillaire rectiligne, les résultats donnés par la méthode de type pseudo-Wigner sont comparés avec d'autres résultats donnés par la méthode Transformée de Fourier à court terme, la méthode résolue en phase basée sur la transformée de Hilbert, ou encore la méthode d'autocorrélation. En ce qui concerne la précision, l'erreur globale moyennée sur un balayage axial par rapport au profil théorique d'un écoulement laminaire est de 22.08 % pour la méthode d'autocorrélation, 10.32 % pour la Transformée de Fourier à court terme, 2.97 % pour la méthode de Hilbert et 1.56 % pour la méthode de type pseudo-Wigner, respectivement. Nous pouvons donc en conclure que la méthode de type pseudo-Wigner est dans l'ensemble plus précise que les méthodes utilisées jusqu'alors.

Dans le chapitre 4, nous décrivons le développement pour le traitement des données un nouveau modèle simple et peu fastidieux basé sur la détermination des points pour lesquels le signal TOC croise l'axe des abscisses, autrement dit l'axe d'amplitude nulle. Nous avons démontré que cette méthode de détection du passage à zéro est capable de déterminer la fréquence instantanée d'un signal TOC sur un intervalle de temps plus court que certaines méthodes utilisées en TOC Doppler (Transformée de Fourier à court terme, pseudo-Wigner, Hilbert), ce qui en fait une méthode plus résolue. De même, cette méthode utilise des opérations arithmétiques simples et ne nécessite aucune évaluation d'intégrales, ce qui réduit le temps de calcul pour le traitement des images. L'élaboration de cette méthode constitue le premier résultat important de cette thèse pour le développement de la TOC Doppler. Nous avons émis l'hypothèse que l'application de la méthode de détection de passage à zéro au signal TOC temporel donne les meilleures mesures de vitesses en termes de précision et de

plage dynamique. Plusieurs résultats confirment cette hypothèse. En premier lieu, nous avons comparé à partir des publications récentes les caractéristiques des systèmes TOC temporels avec celles des systèmes spectraux, notamment leur sensibilité, la vitesse maximale mesurée, et le taux de répétition des balayages axiaux. Il ressort de cette étude que les systèmes TOC temporels peuvent couvrir une plage de vitesses s'étendant de $7 \mu\text{m/s}$ à 0.56 m/s à un taux de répétition du balayage axial de 8 kHz , ce qui correspond au domaine de l'imagerie en temps réel. Jusqu'ici, les systèmes TOC spectraux couvrent une gamme dynamique des vitesses moins large (entre 45 et 50 dB), mais ils peuvent fonctionner avec des taux de répétition axiaux plus élevés. Nous démontrons au Chapitre 4 que les systèmes TOC temporels peuvent couvrir une plage des vitesses allant de $1 \mu\text{m/s}$ jusqu'à 10 ou 20 m/s, ce qui donne une gamme dynamique de 60 dB et plus. Dans le cas de vitesses de balayage axial faibles, nous avons calculé des gammes dynamiques supérieures à 80 dB. La principale raison pour laquelle les systèmes spectraux donnent une estimation moins précise de la vitesse provient du fait que l'interférogramme est obtenu en appliquant la transformée de Fourier inverse au signal mesuré. Ainsi, l'information sur la vitesse est obtenue de façon indirecte en prenant la partie imaginaire de l'interférogramme (ce qui donne l'information sur la phase de chaque balayage axial), puis en calculant pour chaque point axial la différence de phase entre deux balayages successifs. Pour que cette mesure soit valide, le déplacement transverse entre deux balayages axiaux consécutifs doit être faible par rapport au diamètre du faisceau. Ceci implique un suréchantillonnage du signal et donc une acquisition d'image plus longue et fastidieuse. Le principal avantage du système TOC temporel est qu'il permet d'accéder directement à l'interférogramme. Ainsi, la phase locale est mesurée directement à partir du signal temporel, ce qui évite d'éventuelles ambiguïtés ou encore des informations incomplètes.

Par la suite, nous avons comparé la méthode de passage à zéro avec deux autres

méthodes (méthodes Hilbert et pseudo-Wigner) dans le cas classique d'un flux laminaire dans un tube rectiligne. Après avoir déterminé les fréquences instantanées pour les trois différentes méthodes, nous avons calculé leur distribution statistique locale et nous n'avons conservé que les mesures proches du maximum de la distribution. Ainsi, les fréquences associées au bruit du signal sont éliminées à l'aide de cette méthode, ce qui équivaut à un filtre passe bande adaptatif. Les données filtrées sont ensuite ajustées par une courbe parabolique typique d'un flux laminaire. En comparant les paramètres ajustés par les trois méthodes avec les paramètres déduits des mesures expérimentales, la méthode de passage à zéro offre la meilleure précision sur tout le profil du tube à l'exception des régions très proches des parois. La méthode basée sur la distribution pseudo-Wigner donne également de bons résultats. Elle est moins précise dans la région des vitesses maximales mais elle donne des résultats sensiblement meilleurs dans les régions caractérisées par des vitesses faibles. Finalement, la méthode basée sur la transformée de Hilbert se révèle être la moins fiable. La raison pour laquelle la méthode de passage à zéro donne les meilleurs résultats provient du fait que cette méthode est essentiellement locale et donne la fréquence instantanée en un temps donné sans avoir recours à une intégration sur une fenêtre temporelle ou au calcul de transformées mathématiques complexes. De plus, nous avons également montré que le temps de calcul lié à la méthode de passage à zéro est réduit d'un ordre de grandeur par rapport aux autres méthodes citées plus haut.

La TOC Doppler devient un champ d'application de plus en plus populaire au sein de la TOC, notamment dans le domaine de la recherche cardiovasculaire et dans la microfluidique. Dans le Chapitre 5 de cette dissertation, nous avons appliqué notre approche présentée plus haut à la mesure de distributions de vitesses dans différentes géométries appropriées à la microfluidique ou encore à l'hémodynamique cardiovasculaire, notamment des géométries de sténoses et de branchements artériels. Nous avons obtenu des images haute résolution de

flux vectoriels qui nous permettent d'envisager la description dynamique du flux et la mesure de la contrainte de cisaillement aux parois (CCP), deux facteurs déterminants pour l'évaluation et la compréhension de la formation des plaques athérosclérotiques.

Les limites des méthodes et des systèmes de mesure de profils de vitesses proviennent pour la plupart d'une résolution spatiale et d'une précision des mesures de vitesses limitées. Ainsi, une évaluation des caractéristiques reliées aux flux sanguins ne peut être réalisée avec une grande précision. Par exemple, le flux sanguin dans des régions proches des parois artérielles n'a jamais pu être estimé correctement, pas même par les systèmes les plus performants tels que l'imagerie par résonance magnétique à contraste de phase. Nous avons appliqué avec succès notre système de TOC Doppler dans le domaine de la microfluidique ainsi que dans le domaine de l'hémodynamique cardiovasculaire. Nous avons notamment mesuré les distributions vectorielles dans le plan d'images obtenues de fantômes modélisant diverses régions artérielles (sténose, bifurcation artérielle). Ces résultats préliminaires représentent un point de départ important pour une meilleure compréhension de la dynamique fluide impliquée dans certaines maladies cardiovasculaires. Afin de valider les résultats obtenus, nous les avons comparés avec les profils de vitesses modélisés à l'aide du logiciel de CFD: FLUENT. Les résultats donnés par la simulation illustrent les profils de vitesse dans le cas d'un écoulement constant alors que nos résultats expérimentaux donnent des mesures instantanées.

La TOC Doppler bénéficie d'une très bonne résolution spatiale ($\sim 10 \mu\text{m}$). C'est pourquoi cette méthode peut être utilisée pour mesurer les distributions de vitesses fluidiques dans des microcanaux aussi fins que des tubes capillaires. Le comportement des fluides dans les microcanaux peuvent être très différents de leur comportement à l'échelle macroscopique à cause de plusieurs paramètres, notamment les tensions de surface ou encore les pertes

d'énergie. A cause de ces différences, les comportements fluidiques dans un microcanal peuvent être très difficiles à décrire par la théorie. Ainsi, il est important d'obtenir une description expérimentale précise de la distribution des vitesses dans les circuits microfluidiques. Une mesure expérimentale des vitesses fluidiques dans des microcanaux rectilignes de 100 μm d'épaisseur montre que le profil des vitesses a une variation parabolique. L'écoulement reste donc laminaire dans ces microcanaux malgré leurs très petites dimensions. Les méthodes déjà utilisées dans ce domaine, comme par exemple la méthode d'ultrasons Doppler ou encore la vélocimétrie laser Doppler, se caractérisent par une résolution limitée et donnent des résultats peu précis. La TOC Doppler est actuellement la seule méthode capable de décrire avec une résolution suffisante les vitesses fluidiques dans des microcanaux.

Notre système de TOC Doppler a été utilisé sur un système microfluidique afin de détecter d'éventuels défauts structurels. Les profils de vitesses sur huit microcanaux de dimensions identiques à l'intérieur de ce système ont été obtenus. Ces profils révèlent des défauts structurels sur certains de ces microcanaux. Ces défauts peuvent être très importants dans la mesure où ils peuvent grandement modifier les profils de vitesse. Pour chacun de ces microcanaux, on s'attend à un écoulement laminaire présentant un profil de vitesse parabolique. Cependant, les distributions de vitesses mesurées se révèlent être beaucoup plus complexes. De plus, les vitesses des écoulements diffèrent d'un microcanal à un autre. Par conséquent, la mesure directe des profils de vitesses à l'intérieur des systèmes de microfluidique donne des informations très importantes et très utiles à la fois pour l'inspection structurelle des dispositifs et pour le contrôle des vitesses d'écoulements à l'intérieur de ces systèmes. La capacité de résoudre des profils de vitesses à l'échelle micrométrique avec la TOC Doppler dépend de la longueur de cohérence de la source, qui est de 10 μm dans notre cas.

La Tomographie par Cohérence Optique (TOC) Doppler permet la détermination de profils de vitesses enfouis sous la surface de tissus biologiques transparents et opaques. En particulier, la TOC Doppler peut donner des informations précises sur le gradient de vitesses dans les régions proches des parois. Ces avantages donnent à la TOC Doppler une position dominante pour devenir la meilleure technique de mesure des profils de vitesses fluidiques et acquérir ainsi un intérêt clinique pour la mesure des contraintes de cisaillement aux parois (CCP). Une discussion détaillée à propos des applications de cette méthode à la mesure expérimentale de la vitesse de cisaillement aux parois est incluse dans le manuscrit.

Étant donné que la TOC Doppler n'est sensible qu'à la projection de la vitesse sur l'axe optique, nous avons proposé une procédure nous permettant d'avoir accès aux champs vectoriels des vitesses en 2D à l'intérieur des fantômes. Ainsi, l'information sur le gradient des vitesses est obtenue de façon très précise et nous permet de calculer les vitesses de cisaillement en tous points sur les parois. Par la suite, la CCP est obtenue en multipliant la vitesse de cisaillement par la viscosité dynamique du fluide. La méthode que nous proposons pour la détermination des profils vectoriels de vitesses est basée sur l'acquisition de profils Doppler à deux angles d'inclinaison différents. Pour plus de facilité, la première acquisition se fait à incidence normale par rapport à la surface externe de l'échantillon. La seconde acquisition se fait à un angle de 9 ou 10° par rapport à l'incidence normale. Par rapport aux autres méthodes utilisées pour les profils vectoriels, comme par exemple la méthode d'élargissement spectral ou encore la détection à deux angles simultanée, notre méthode donne des mesures plus précises et peut être appliquée à des échantillons plus larges. Cette méthode graphique a été appliquée pour la détection vectorielle des vitesses sur deux modèles couramment utilisés dans le domaine de l'hémodynamique cardiovasculaire : les sténoses et les bifurcations.

Les fantômes étudiés dans notre cas ont des dimensions de l'ordre de 10 mm. Par conséquent, la source optique émettant à 1500 nm ne peut détecter le profil des vitesses sur toute la profondeur des fantômes si l'on utilise la solution de suspension intralipide couramment utilisée dans les applications de TOC Doppler. Ceci est dû à la forte absorption de l'eau dans le domaine spectral du proche infrarouge, ce qui a pour effet de limiter la profondeur de pénétration de notre source optique à quelques millimètres seulement. C'est pourquoi la solution utilisée dans notre cas se compose d'une suspension de particules d'oxyde de titane jouant le rôle de diffuseurs (diamètre d'environ $1\mu\text{m}$) dans de l'huile de soya. La profondeur de pénétration de la lumière à l'intérieur de ce fluide est supérieure à 14 mm en raison de sa faible absorption dans le proche infrarouge. La viscosité de l'huile de soya a été mesurée à 0.04970 Pa.s.

Les premières mesures sur le fantôme de bifurcation ont été effectuées sur le tube principal avant la bifurcation avec un angle d'inclinaison de 9° par rapport à la normale au tube. La longueur du balayage axial est de 3.6 mm avec un taux d'échantillonnage de 100 kHz. Le profil des vitesses sur le diamètre du tube a été obtenu. La vitesse maximale au centre du tube est de 31.14 mm/s. Ce profil de vitesses a une forme parabolique, ce qui indique un régime laminaire et unidirectionnel dans cette région de l'échantillon. La fréquence mesurée au bord des parois, où la vitesse est supposée nulle, s'apparente à la fréquence porteuse du signal et est égale à 1.724 kHz. La vitesse d'écoulement moyennée sur toute la section du tube est égale à la moitié de la vitesse maximale (15.57 mm/s). Nous avons utilisé cette valeur pour effectuer les simulations avec le logiciel FLUENT.

Les simulations obtenues avec FLUENT montrent que dans la majeure partie du fantôme, l'écoulement se fait parallèlement aux parois du tube car les composantes des vitesses dans la direction perpendiculaire aux parois est nulle. Néanmoins, certaines régions

à l'intérieur du fantôme, notamment les régions proches de l'embranchement du tube principal et des bifurcations, montrent clairement un régime non laminaire. Plusieurs vortex sont mis à jour dans ces régions caractérisées par des vitesses non nulles dans les directions normales aux parois.

En se basant sur la méthode décrite plus haut, nous avons effectué des acquisitions de TOC Doppler de distributions de vitesses 2D à des angles de 0° et 9° par rapport à la normale à la paroi du tube. Comme il a été prévu par la théorie, le liquide s'écoule le long du tube dans la majeure partie de l'échantillon et les composantes des vitesses normales à la paroi sont quasi-nulles. Les zones de hautes turbulences sont repérées à chaque fois que les composantes de vitesses mesurées à incidence normale deviennent élevées. Ces zones sont importantes car elles indiquent la présence de vortex et de perturbations dans l'écoulement. En combinant les deux projections obtenues à des inclinaisons différentes, nous avons obtenu, pour la première fois à notre connaissance, une représentation de la distribution vectorielle de vitesses dans une branche d'une bifurcation fantôme avec une bonne précision. A partir des projections des vitesses dans la direction parallèle aux parois, nous pouvons déduire la CCP le long de la paroi. Une autre contribution majeure de cette thèse réside dans la mesure de la distribution des CCP pour la première fois avec une haute résolution. Cette distribution contient des informations très utiles pouvant améliorer le diagnostic et la compréhension de certaines maladies cardiovasculaires. Ces résultats constituent un progrès important en comparaison aux autres méthodes de détection des CCP. En effet, ces méthodes sont basées sur l'hypothèse que le flux est laminaire et utilisent la vitesse maximale pour déterminer les CCP. Ces méthodes sont fiables dans les régions où le flux est laminaire, mais ne peuvent s'appliquer aux zones de turbulence.

Nous avons réalisé les mêmes expériences sur un autre type de fantôme modélisant un

cas très étudié en hémodynamique cardiovasculaire: la sténose. Ce modèle est couramment utilisé pour étudier les caractéristiques des écoulements sanguins lorsque les vaisseaux subissent un rétrécissement de leur diamètre. Notre objectif est de proposer et de démontrer les performances de la TOC Doppler pour étudier les profils des vitesses d'un écoulement laminaire dans un fantôme de sténose à la fois avec une profondeur de pénétration très élevée (~12 mm) et avec une très bonne précision. Globalement, la distribution 2D de vitesses obtenue montre clairement un régime laminaire sur tout le diamètre de la sténose. Ce résultat est attribué au fait que les vitesses d'écoulement sont très faibles et sont associées à un nombre de Reynolds peu élevé, ce qui indique que l'écoulement est stable. De plus, si on compare avec les résultats obtenus sur la bifurcation, la sténose ne révèle pas de régions instables où les vitesses se situent en dehors de la plage de mesures du système TOC Doppler. Ces résultats s'expliquent aussi par le fait que le diamètre de la sténose évolue de façon très progressive et ne présente aucun changement abrupt. Dans la région proche de l'étranglement de la sténose, nous pouvons clairement identifier un écoulement laminaire avec des vitesses accrues. Cependant, les régions où le diamètre varie plus rapidement présentent des vortex proches des parois. Ces régions jouent un rôle important dans la formation de la plaque athérosclérotique dans la mesure où elles sont propices aux dépôts des molécules de gras sur les parois artérielles.

En conclusion, nous avons conçu et implémenté des systèmes TOC et TOC Doppler basés sur des interféromètres free-space et fibrés. Des images TOC structurelles de tissus biologiques ont été obtenues avec une haute résolution dans le visible, le proche infrarouge et l'infrarouge. Une méthode de détection de passage à zéro a été proposée et appliquée aux signaux TOC temporels pour la TOC Doppler et s'avère être jusqu'alors la méthode la plus performante en termes de précision et de plage dynamique. Nous avons aussi proposé une méthode expérimentale afin d'obtenir la distribution vectorielle des vitesses et d'avoir ainsi

accès à des informations plus complètes par rapport aux distributions des vitesses projetées. Plusieurs applications de cette méthode ont été réalisées avec succès sur divers modèles d'écoulements.

TABLE OF CONTENTS

DEDICATION	iv
ACKNOWLEDGEMENTS.....	v
RÉSUMÉ.....	viii
ABSTRACT.....	xii
CONDENSÉ EN FRANÇAIS.....	xv
TABLE OF CONTENTS	xxvii
TABLE OF FIGURES	xxxii
LIST OF APPENDICES.....	xxxix
CHAPTER 1 Introduction	1
1.1 The principle of Optical Coherence Tomography	1
1.2 Applications of Optical Coherence Tomography	4
1.3 The principle of Doppler Optical Coherence Tomography.....	5
1.4 Comparison of time-domain OCT versus frequency-domain OCT	8
1.5 Optical properties of tissues	11
1.6 Conclusion.....	16
CHAPTER 2. Experimental setup	18
2.1 Overview	18
2.2 Free-space system based on Ti:sapphire pulsed laser.....	18
2.3 Fibre-optic based system using near-infrared sources	24
2.4 Evaluating the envelope detector	29

2.5 OCT microscope assembly	31
2.6 Data acquisition parameters and interface	33
2.7 Doppler setup in general.....	34
2.8 Experimental results	37
i). OCT images with the 810 nm Ti:sapphire laser	37
ii). OCT images with the 1310 nm MPB source.....	39
iii). OCT images with the 1570 nm SLD source	42
iv). Comparison of OCT images with three different sources.....	45
v). Measurements of attenuation and backscattering.....	47
CHAPTER 3 An assessment of the Wigner distribution method in Doppler OCT	54
3.1 Introduction	54
3.2 Description of the commonly used methods in Doppler OCT	55
3.3 Description of the proposed Wigner distribution method	59
3.4 Experimental setup.....	61
3.5 Results and discussion.....	62
CHAPTER 4 A zero-crossing detection method applied to Doppler OCT	80
4.1 Introduction.....	80
4.2. Principles.....	83
4.3. Experimental setup.....	88
4.4. Results and discussion	88
4.4.1 Comparison with the Wigner method.....	88
4.4.2 Other methods.....	93

4.4.3 Methodology and results.....	94
4.4.4 Susceptibility to noise.....	97
4.5 Conclusion	102
CHAPTER 5 Application of the time-domain Doppler OCT system	104
5.1 Introduction.....	104
5.2. Principle	106
5.2.1 Wall shear stress.....	106
5.2.2 Vector velocity field.....	107
5.3. Experimental setup.....	110
5.3.1 Doppler OCT setup	110
5.3.2 Experimental details.....	111
5.4. Results and discussion	113
5.4.1 Simulation results by Fluent.....	113
5.4.2 Experimental results	122
5.4.3 Discussion.....	135
5.5 Conclusion	137
5.6 Flow in the phantom of a stenosis using Doppler OCT [80]	138
5.6.1 Experimental sample and setup.....	139
5.6.2 Experimental results and discussion	141
5.6.3 Vector velocity map	144
5.7 Applications in microfluidics and in a rectangular channel.....	148
CHARPTEr 6 Conclusion.....	157

6.1 Summary	157
6.2 Unsolved issues	159
6.3 Future prospects	160
REFERENCES.....	162
APPENDICES	169

TABLE OF FIGURES

Fig. 1.1 A schematic diagram of a free-space Michelson interferometer	2
Fig. 1.2 The Fourier transform (F.T.) relationship between the spectral density of a continuous spectrum source and the interference trace	4
Fig. 1.3 Schematic of the DOCT probe. (a) Sample arm. (b) Interferogram.	7
Fig. 1.4 Tissue properties. (i) absorption coefficient: A-water, B- whole blood, C-aorta, E-skin (cross-hatched area); (ii) reduced scattering coefficient: D- human tissue (in brown).....	13
Fig. 1.5 Diagram of the sample holder used for attenuation and backscattering measurements	14
Fig. 2.1 Absorption spectrum of main chromophores in tissue (oxy-hemoglobin, HbO ₂ ; deoxy-hemoglobin, Hb; and water, H ₂ O). μ_a : Absorption coefficient.	19
Fig. 2.2 Simplified schematic diagram of the Ti:Sapphire laser cavity. OC: output coupler. CM: chirped mirror. P: prism.	21
Fig. 2.3 The measured spectrum of the Ti:sapphire laser under pulsed conditions.	22
Fig. 2.4 Free-space interferometer OCT setup operated with a Ti:Sapphire laser.....	23
Fig. 2.5 Interference trace produce by the Ti:sapphire laser with a mirror as the sample ...	24
Fig. 2.6 Spectra of the sources. (a): original MPB source (solid) and filtered (dashed) MPB source. (b): Source at 1.5 μm	26
Fig. 2.7 Profiles of OCT signals obtained with (a) the original and (b) the filtered MPB source.....	27
Fig. 2.8 Fiber-optic OCT setup operated with near infrared sources.	28
Fig. 2.9 Acquisition time and penetration depth are strongly affected as the sampling rate changes. Solid line: penetration depth. Dashed line: time for completing an A-scan of 1 mm length. Dotted line: consuming time for completing an A-scan	

of 10 mm length.....	30
Fig. 2.10 Effect of the envelope detection of a single interferogram obtained with the MPB source. Solid line: envelope detection at 592 Hz sampling rate. Blue line: raw signal at 5.3 kHz.	31
Fig. 2.11 Effect of the envelope detection of a single interferogram by the JDSU source. Solid line: envelope detection at 592 Hz sampling rate. Blue line: raw signal at 5.3 kHz.....	31
Fig. 2.12 Probe station of the fiber-optic based OCT setup.	32
Fig. 2.13. Experimental setup for the Doppler frequency-shift measurements. FC: fiber coupler, PC: polarization controller, MO: microscope objective	36
Fig. 2.14 Sample arm of the Doppler OCT setup shows the positions of the sample holder and the microscope objective.	36
Fig. 2.15 OCT image of a chicken heart ventricle wall with Ti:sapphire laser.....	38
Fig. 2.16 OCT image of a onion peel with Ti:sapphire laser.	38
Fig. 2.17 OCT image of a fish scale.	39
Fig. 2.18 OCT images of a chicken heart obtained with the MPB source. (a): original full spectrum mode which has a higher resolution but with the sidelobe effect. (b): filtered mode which has lower resolution but without the sidelobes on the image.	41
Fig. 2.19 Effects of deconvolution on the OCT images of chicken heart (a): original full spectrum mode. (b): filtered mode.	42
Fig. 2.20 OCT image of chicken heart with 1570 nm infrared source.....	43
Fig. 2.21 OCT image of sheep cerebellum with 1570 nm infrared source. (a): original image. (b): after deconvolution.	44
Fig. 2.22 OCT image of sheep brain sample with 1570 nm infrared source. (a): original image. (b): after devonvolution.	45

Fig. 2.23 OCT image of sheep brain sample without structure. (a): original image. (b): after devolution.	45
Fig. 2.24 OCT images of a chicken heart ventricle wall (top row) and mouse earlobe (bottom row). From left to right, 810 nm Ti:Sapphire laser, 1330 nm broadband source, and 1570 nm SLD.....	47
Fig. 2.25 Measured aperture function for the sources used in the experiment. Points are measured data while solid curves are fits with a Gaussian function.....	48
Fig. 2.26 Comparison of OCT profiles for a single in-depth scan (a) and for a spatially and temporally averaged in-depth scan (b). The peak in the middle of the scan is an artifact.	49
Fig. 2.27. Comparison of attenuation and backscattering coefficients of several samples measured by OCT with 810, 1330 and 1570 nm sources.	51
Fig. 2.28. Comparison of ratio of backscattered power over incident power as a function of depth for several samples at 810, 1330 and 1570 nm sources.....	52
Fig. 3.1. Sample arm of the experimental setup for the Doppler frequency-shift measurements.	62
Fig. 3.2 OCT cross-sectional image of the tube. The white line indicates the A-scan that is studied afterwards in this thesis.....	63
Fig. 3.3 (a) The original interferogram signal along the center of the tube and (b) the normalized data.....	64
Fig. 3.4 Small segment of the detected signal at a 100 kHz sampling rate. The boxed region represents the STFT window size.	65
Fig. 3.5 STFT time-frequency distribution of the sample signal.....	66
Fig. 3.6 Time-frequency distribution of the sample signal obtained with the Wigner distribution.....	67
Fig. 3.7 Comparison of the frequency spectra calculated with two time-frequency methods.	

.....	68
Fig. 3.8 Spectra calculated at each sampling point of the signal using the Wigner	69
Fig. 3.9 Block diagram of the algorithm used in the comparison.	71
Fig. 3.10 Two-dimensional frequency distribution of the signal using the STFT method. The black dots indicate the maximum frequency values of the spectra at each measured point while the yellow trace corresponds to the filtered frequency distribution.....	73
Fig. 3.11. Two-dimensional frequency distribution of the signal using the Wigner method. The black dots indicate the maximum frequency values of the spectra at each measured point while the yellow trace corresponds to the filtered frequency distribution.....	74
Fig. 3.12. Two-dimensional frequency distribution of the signal using the Hilbert method. The black dots indicate the raw frequencies at each measured point. The yellow trace corresponds to the filtered frequency distribution.....	75
Fig. 3.13. Two-dimensional frequency distribution of the signal by the autocorrelation method. The black dots indicate the raw frequencies and the yellow trace shows the resulting frequency distribution after noise rejection.....	76
Fig. 3.14 Computed flow profiles using a quadratic fit.....	77
Fig. 4.1 A sample signal used to calculate the zero-crossing points (red cross) and the defined time durations.	85
Fig. 4.2 Effective sampling parameter of map velocity and precision of calculated frequency as a function of Doppler frequency F	87
Fig. 4.3. (a). The original interferogram signal along the center of the tube and (b) the normalized data.....	89
Fig. 4.4. Color-coded 3D time-frequency distribution of the signal along the center of the tube using the Wigner method.	90

- Fig. 4.5. Small segment of the detected signal at a 100 kHz sampling rate. The stars indicate the zero-crossing points..... 91
- Fig. 4.6 Comparison of Wigner and zero-crossing time-frequency distributions of the sample signal of Fig. 4.5. The points correspond to the Wigner method using the maximum values of the local spectra. The stars come from the zero-crossing method. 91
- Fig. 4.7 Two-dimensional frequency distribution of the signal by the zero-crossing method. The black dots indicate the obtained frequencies and the yellow trace shows the resulting frequency distribution after noise rejection..... 93
- Fig. 4.8. Computed flow profiles using a quadratic fit..... 94
- Fig. 4.9 Comparison of the deviations of the three methods from the theoretical results... 95
- Fig. 4.10 OCT image of the tube profile. The superimposed contour plots correspond to the frequencies calculated using experimental values and the Pseudo-Wigner method (black solid curves). The white curves indicate the calculated frequencies using the zero-crossing method. The white curve near the center of the tube is the contour at 9 kHz given only by zero-cross method..... 96
- Fig. 4.11 3D velocity distribution of the cross section of the tube calculated from experimental values using the zero-crossing method. 96
- Fig. 4.12 (a). OCT raw signal sample (black curve) and normalized signal sample (blue curve) used for frequency calculation. (b). Local frequencies calculated with different methods..... 99
- Fig. 4.13 Normalized frequency distributions obtained with the three methods with fluid at rest (red) and with fluid in motion (blue)..... 100
- Fig. 4.14. FM SNR $f_{\max}/\Delta f$ at the center of the capillary tube calculated by the three methods (a) without and (b) with flow motion inside the tube..... 101
- Fig. 4.15 FM SNR $f_{\max}/\Delta f$ at the edge of the capillary tube calculated by the three methods (a)

without and (b) with flow motion inside the tube.....	101
Fig. 4.16 The frequency spread Δf at the edge of the capillary tube (a) and in the middle of the tube (b) as a function of the source power. Black line has a slope of -0.5 . Dark brown dotted line represents the linear fit of the zero-crossing method results and has a slope of -0.29	102
Fig. 5.2 Graphic method for obtaining the velocity vector by means of two measured velocity components with a known angle.....	108
Fig. 5.3 The velocity and its projections.....	109
Fig. 5.4. Configuration of the bifurcation sample.....	111
Fig. 5.5. Experimental setup for measurement of the Doppler frequency-shift for the bifurcation sample.	112
Fig. 5.6. Measured viscosities of the vegetable oil and the soya oil.....	113
Fig. 5.7 Main panel of Gambit.....	114
Fig. 5.8. Interface window of Gambit to create cylindrical objects.	114
Fig. 5.9. The finished bifurcation phantom before meshing.	115
Fig. 5.10. Defining the two points where the three tubes were jointed together.....	115
Fig. 5.11. The windows for creating face and splitting the volume.	116
Fig. 5.12. The window for creating boundary layers.....	117
Fig. 5.13. The finished boundary layer meshing of the tubes.	118
Fig. 5.14. The window for meshing a real volume.....	118
Fig. 5.15. The meshed bifurcation model (surface plot).....	119
Fig. 5.16. The boundary layers on one end face of the bifurcation model.....	119
Fig. 5.17. Vector velocity within the phantom	121
Fig. 5.18. Velocity distribution within the phantom.....	121
Fig. 5.19 The interferogram of the inlet tube.....	122
Fig. 5.20 The Doppler frequency shifts of the interferogram calculated with the	

zero-crossing method. Black points: raw frequency signal. Yellow points: Maximum likelihood values. Red points: Frequencies at each pixel.....	124
Fig. 5.21 The Doppler frequency shifts of one scan based on the zero-crossing method. The green line indicates the frequency of the non moving objects.....	127
Fig. 5.22 The 2D Doppler frequency shifts in the right branch tube at 9 ° Doppler angle	128
Fig. 5.23 The Doppler frequency shifts of one A-scan in the red area of Fig. 5.23 based on the zero-crossing method. The black line indicates that the frequency increases linearly in the beginning.....	129
Fig. 5.24 The 2D Doppler frequency shifts in the right branch tube at 0 ° Doppler angles	130
Fig. 5.25 The rotated 2D Doppler frequency shift distribution for the 9 ° Doppler angle (left) which spatial dimensions match the Doppler frequency shift distribution for the 0 ° Doppler angle (right).....	131
Fig. 5.26 The vector velocity distribution within the lower branch tube.	132
Fig. 5.27 The WSS values (a) obtained with the measured y-axis velocity values (b). The WSS calculated based on Eq. 5.1 (solid curve), average of the WSS (dashed line), calculated WSS based on the measured velocity at 1 mm from the border (dotted line), and based on Eq. 5.2 (dash-dot line).	134
Fig. 5.28 The WSS calculated along the tube. The measured average WSS (dashed curve), calculated WSS based on the measured velocity at 1 mm from the border (dotted curve), and based on Eq. 5.2 (dash-dot curve).....	135
Fig. 5.29 The velocity change with time at a specified position within the phantom. (a) Stationary velocity. (b) Unstable velocity.....	136
Fig. 5.30 The velocity curves at two positions within the phantom with nine measurements. Blue: velocity at the vertex (red mark in Fig. 5.4). Red: other region. At the origin, the large frequency fluctuations correspond to low SNR.....	137
Fig. 5.31 A typical arterial stenosis [81].....	138

Fig. 5.32 The picture of the Plexiglas stenosis phantom used for the experiments.	140
Fig. 5.33 The cross-sectional OCT image of the stenosis sample with scattering particles.	141
Fig. 5.34 The raw data of the cross-sectional velocity distribution of the stenosis.....	142
Fig. 5.35 The color coded 2D velocity distribution of the stenosis phantom.....	143
Fig. 5.36 3D representation of the 2D velocity distribution of the stenosis phantom.....	144
Fig. 5.37 Schematic representation of light propagation inside the stenosis.....	145
Fig. 5.38 Flow profile inside the tube 4 mm before the beginning of the stenosis. The redcurve is a parabolic fit.	146
Fig. 5.39 Flow profiles and 2D vectorial flow maps inside a stenosis phantom at mean flow rates of 70 $\mu\text{l/s}$ (a, b, c) and 30 $\mu\text{l/s}$ (d, e, f). From left to right, Doppler frequency map at 0° incidence angle, Doppler frequency map at 10° incidence angle, and 2D flow map superposed on structural OCT image.....	148
Fig. 5.40 Cross-sectional image of the microchannel.....	150
Fig. 5.41 2D and 3D Velocity distribution within the microchannel.	151
Fig. 5.42 Overlap of the structural image with the velocity distribution map.....	152
Fig. 5.43 Example of microfluidic circuit developed at Ecole Polytechnique (O. Guenat).	153
Fig. 5.44 Structure of the microchannels in the microfluidic sample (O. Guenat).	153
Fig. 5.45 2D visualizations of fluid dynamics of the microchannel sample. (a) microchannel indicated as dotted line in Fig. 5.45 (b)) microchannel indicated as dashed line in Fig. 5.45.....	154
Fig. 5.46 2D local velocity distributions at different cross-sections in steady flow in a Y junction circuit.	156

LIST OF APPENDICES

APPENDIX A Data processing with the STFT method.....	169
APPENDIX B Data processing with the Wigner method.....	171
APPENDIX C Data processing with the Hilbert method.....	173
APPENDIX D Data processing with the autocorrelation method.....	175
APPENDIX E Data processing with the zero-crossing method.....	177

CHAPTER 1

Introduction

In this chapter, we provide a theoretical background of Optical Coherence Tomography (OCT), including structural OCT as well as Doppler OCT, an important extension of OCT that is applied to detect the flow velocity distribution noninvasively beneath the sample surface. From a comparison between time domain (TD) OCT and frequency domain (FD) OCT, we argue that time domain OCT has some advantages in Doppler OCT since a more precise frequency or velocity determination can be achieved from the recorded signal with a much higher dynamic range. Moreover, the scattering and absorption responses of several biological samples at different wavelengths are also discussed.

1.1 The principle of Optical Coherence Tomography

Optical coherence tomography (OCT) is a relatively new imaging technique [1]. It achieves micrometer-scale resolution in providing cross-sectional tomographic images of the internal microstructure of materials and biological tissues by measuring the echo time delay and intensity of the backscattered or backreflected light from the sample. This method is somewhat similar to B-mode ultrasound tomography that is widely used in clinical applications. It allows the investigation of soft biological tissues transparent to X-rays with a much higher resolution (in the sub-10 μm range). Because OCT can acquire images that approach the resolution of histology, several potential applications have been investigated in a wide range of medical and biological applications [2-5].

The principle of OCT is based on the interference of beams from a partially coherent light source in a Michelson (or other) interferometer as shown in Fig. 1.1. An optical beam backreflected or backscattered from within a biological tissue at a given depth will contain time-of-flight information, which can be used to determine the longitudinal locations of

reflective boundaries and backscattering sites in the sample. The OCT experimental system consists of four main components namely a broadband source, an interferometer with a scanning arm, a data acquisition system and an image processing unit.

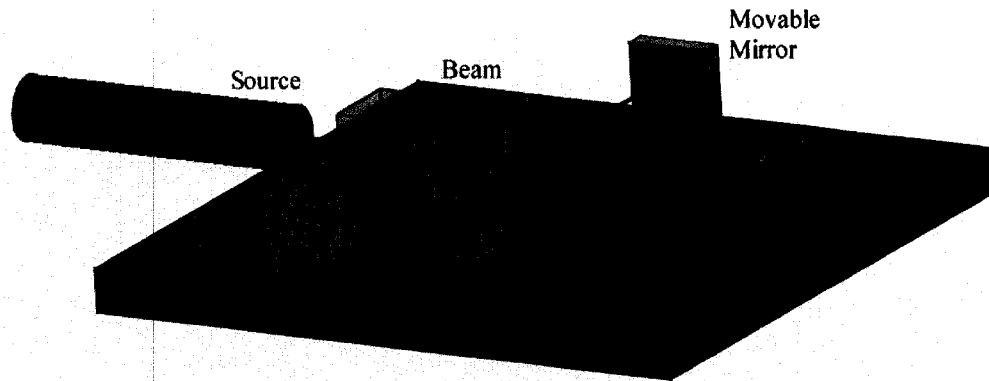


Figure 1.1 A schematic diagram of a free-space Michelson interferometer

The incident broadband light source is directed onto a beamsplitter that splits this broadband light beam into a reference beam E_R and a sample beam E_S . The reference beam E_R is reflected by a movable mirror in order to provide the reference position information. The sample beam illuminates the biological specimen that needs to be imaged. The reflected sample and reference beams interfere at the beamsplitter. Therefore, the output of the interferometer is the sum of the electromagnetic fields of these two reflected beams. In the case of low-coherence light, the interference signal between the reference and the sample beams can be observed only when the optical path lengths of the reference and sample arms are matched to within the coherence length of the source L_c . In this situation, the longitudinal scan is achieved by translating the reference mirror along the optical axis of the reference arm of the system until the path-delay matched position is reached. By measuring the field autocorrelation of the light, the echo time delay and the magnitude of the reflected light can be determined. The former consists of the position information of the internal structure of the tissue sample, and the latter gives us their reflecting intensity. This information provides an

axial image of the sample within the sample beam. The OCT system performs a series of longitudinal scans at different lateral locations in order to create a two-dimensional map of the reflection sites in the sample.

If the lengths of the reference arm and the sample arm are L_R and L_S , respectively, the optical path difference is then:

$$\Delta = L_R - L_S, \quad (1-1)$$

The detected interference intensity at this path difference becomes:

$$I(\Delta) \approx 2I_0 \int_0^{\infty} S(\nu) \cos(2\pi\Delta\nu) d\nu \quad (1-2)$$

where $S(\nu)$ is the spectral density of the source.

We see that there is a Fourier transform relationship between the spectral density of a continuous spectrum light source and the interference intensity distribution produced by the source. If the spectral density of a light source is the Gaussian distribution function,

$$S(\nu) \propto e^{-4 \ln 2 \left(\frac{\nu - \nu_0}{\Delta\nu}\right)^2}, \quad (1-3)$$

where $\Delta\nu$ is the full-width at half maximum (FWHM) bandwidth of the source as illustrated in Fig 1.2 (a), the interference intensity can be written as:

$$\begin{aligned} I(\Delta) &\approx 2I_0 \int_0^{\infty} S(\nu) \cos(2\pi\Delta\nu) d\nu \\ &\propto e^{-4 \ln 2 \left(\frac{\Delta}{L_c}\right)^2} \cos(2\pi\Delta\nu) \end{aligned} \quad (1-4)$$

where

$$L_c = \frac{2 \ln 2}{\pi} \left(\frac{\lambda_0^2}{\Delta\lambda}\right) = 0.44 \times \frac{\lambda_0^2}{\Delta\lambda} \quad (1-5)$$

is the coherence length of the source.

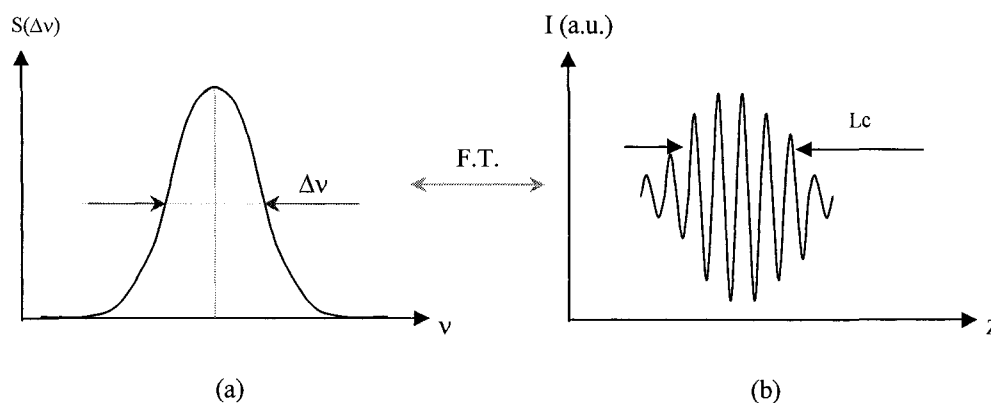


Figure 1.2 The Fourier transform (F.T.) relationship between the spectral density of a continuous spectrum source and the interference trace

Here, λ_0 is the center wavelength of the source and $\Delta\lambda$ is the FWHM bandwidth of the source. Fig 1.2 (b) shows that the interference fringes can be observed only when the optical path length difference is less than the coherence length of the source L_c . The broader the spectral density of the light source, the narrower the interference intensity pattern.

Unlike the conventional microscopy imaging systems whose axial resolution of the image depends on the beam-focusing conditions, the axial resolution of OCT is only determined by the coherence length of the light source L_c . Therefore, the coherence length of a light source becomes one of the most important parameters for estimating the OCT system ability to perform high-resolution imaging. For instance, an axial resolution of $1 \mu\text{m}$ has been obtained by means of an ultra-short pulse Ti: Sapphire laser which generates a pulse duration of 5 fs and which has a bandwidth of over 300 nm [6]. Other sources, although less powerful, have achieved a similar resolution [7].

1.2 Applications of Optical Coherence Tomography

Advances in using near-infrared light have helped the development of OCT imaging in strongly scattering tissues. Although the penetration of light in highly scattering tissues is limited to a few millimeters, which is lower than that of ultrasound, magnetic resonance

imaging, or x-ray computed tomography, the resolution, (around $10 \mu\text{m}$), is substantially higher than in these modalities such that OCT can reveal important features of tissue morphology. The clinical and pre-clinical applications of OCT are currently focusing on the following issues. Thanks to the transparency of ocular structures, ophthalmology remains the main field of OCT application. OCT was initially demonstrated for retinal imaging and recently, about eight retinal layers have been discriminated based on ultrahigh resolution OCT [8, 9]. Moreover, the retinal thickness measurements have been proven to be highly reliable and reproducible [10, 11]. The application of OCT has also spread in many new clinical areas, especially the endoscopic imaging of highly scattering tissues, in a number of medical and surgical specialties, such as gastroenterology, dermatology, cardiology and oncology.

Today, optical in vivo biopsy is one of the most challenging fields for OCT. The high resolution, sufficient penetration depth, and potential for functional imaging found in OCT makes it a serious option for optical biopsy, which can be used to assess tissue and cell functions. These advantages have helped the OCT technology to grow rapidly and represent a unique opportunity for the transfer of biomedical optics to the patient bedside.

1.3 The principle of Doppler Optical Coherence Tomography

The Doppler effect is based on the principle that the frequency of a wave acquires a certain shift due to relative motion between the source and the observer. This effect has been used to detect and measure the velocity of moving objects of different sizes for many years. Recently, Doppler OCT (DOCT) has appeared as a new extension to OCT which combines the measurement of the Doppler frequency shifts contained in the backscattered signal to obtain high-resolution tomographic images of static and moving constituents simultaneously in highly scattering biological tissues [4, 12, 13]. In addition to structural OCT which generates images based on location and amplitude variations of the OCT cross-correlation

trace, Doppler OCT also yields precious information on the frequency content of the detected fringe intensity coming from the interference between the reference and target arms. These interference fringes can be observed only when the optical path lengths between the light backscattered from the sample and that from the reference arm are matched within the coherence length of the broad bandwidth light source. This technique is analogous to Doppler ultrasound except that light reflections are detected instead of sound. The blood flow distribution at a localized position up to 1 mm beneath the tissue surface has been measured using Doppler OCT [12, 14]. Blood flow within the heart of an animal has also been reported [15, 16].

The interferometric fringe frequency detected in OCT arises from the net sum of Doppler shifts generated by the moving reference mirror (f_r) and moving scatterers in the sample (f_s). The interferometric detector current $i_d(t)$ is given by:

$$i_d(t) = A(t) \cos[2\pi(f_r - f_s)t + \varphi(t)], \quad (1-6)$$

where $A(t)$ is the amplitude of the reflection, and $\varphi(t)$ is a phase term dependent on the axial position of the scatterer.

The flow velocity induced by the Doppler frequency shift Δf_D , which is the difference between the carrier frequency f_C of the OCT signal (i.e. the frequency of the OCT signal when the scatterer is at rest) and the measured frequency f_{OCT} of the interference fringe intensity trace results from the motion of the scatterers within the sample:

$$\begin{aligned} \Delta f_D &= f_{OCT} - f_C = f_{OCT} - \frac{2 \cdot v_{scan}}{\lambda_0} \\ &= \frac{1}{2\pi} (\vec{k}_s - \vec{k}_I) \cdot \vec{v} \end{aligned} \quad (1-7)$$

where v_{scan} is the speed of the in-depth scanning reference arm, λ_0 is the center wavelength of the source, \vec{k}_s and \vec{k}_I are the wave vectors of the incoming and scattered light, respectively, \vec{v} is the velocity of the moving particle as shown in Fig. 1.3. Given the angle θ between the

probe beam and the direction of motion of the scatterer, the change in frequency is related to the velocity by Eq. (1-8):

$$v = \frac{\lambda_0 \Delta f_D}{2n_{\text{sample}} \cos(\theta)} \quad (1-8)$$

where n_{sample} is the local refractive index of the sample.

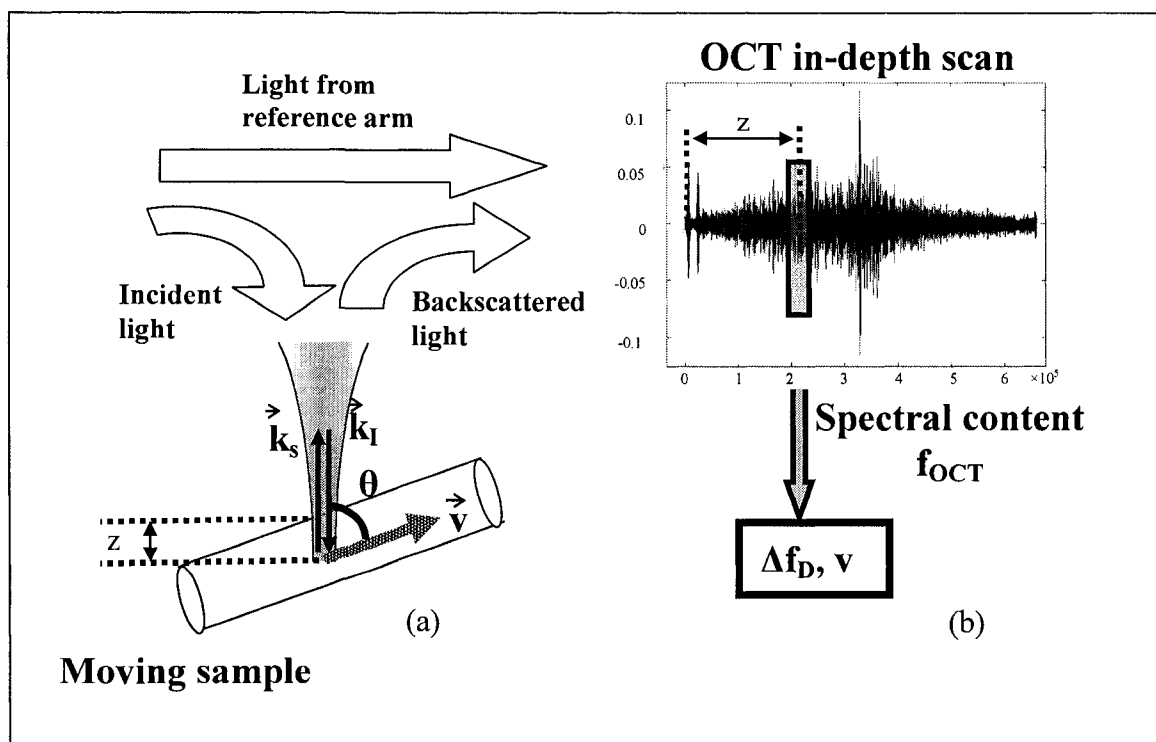


Fig. 1.3 Schematic of the DOCT probe. (a) Sample arm. (b) Interferogram.

Normally, the Doppler shift at each scan position can be determined by computing the time-dependent power spectrum of the received interference fringe intensity (also called the interferogram) using the fast Fourier Transform (FFT). Each local Fourier transform provides the spectral information for a particular time segment at position z , also called the FFT window (see Fig. 1.3 b). The window is then shifted to the next time segment in order to generate another local spectrum. The spectral centroid method is often used for each FFT window to obtain the first moment of the power spectrum of each time segment. The final

flow velocity image is produced by displaying these first moments at each pixel. In this method, the size of the FFT window strongly affects the spatial resolution of the flow image reconstruction.

1.4 Comparison of time-domain OCT versus frequency-domain OCT

There are two types of OCT implementations: The first one refers to time-domain (TD) OCT which yields the interferogram by sweeping the reference mirror; the other one is known as Fourier domain or frequency-domain (FD) OCT, in which the axial scan of the reference mirror is replaced by a spectral decomposition of the signal output from the interferometer. The auto correlation trace can be calculated by applying an inverse Fourier-transform (FT) to this signal. The information of the full depth scan can be acquired within a single exposure which can improve imaging speed dramatically. It is now common knowledge that FDOCT has a sensitivity and a signal-to-noise ratio better than TDOCT. However, in the case of Doppler OCT, the most important parameters one ought to consider, are the accuracy (precision) in speed determination and the Doppler velocity dynamic range (lowest and highest speed) that can be detected. With these ideas in mind, we have made a survey on the performance of TD and FD OCT systems with respect to speed sensitivity, maximum speed, and A-scan rate from current literature. Table 1.1 illustrates some of the results of this survey. From this table, it is quite clear that TDOCT systems for Doppler analysis, can cover the velocity span from $7 \mu\text{m/s}$ to 0.56 m/s (leading to a velocity dynamic range of the order of 45-50 dB) at an A-scan rate of 8 kHz, which is quite sufficient for real time imaging [17]. So far, the Fourier domain systems do not seem to have reached the same velocity dynamic range but they do operate at higher A-scan rates. We also found that the achieved speed sensitivity for time-domain systems was of the order of $7 \mu\text{m/s}$ [17] whereas for spectral systems, it was more in the range of $50 \mu\text{m/s}$ [18] but no doubt, the situation evolves constantly. Similarly, for the maximum measurable speed, we found 560 mm/s for

TDOCT [17] and 191 mm/s for FDOCT [19]. In terms of A-scan rates, Doppler FDOCT systems achieve 25 kHz [20] and Doppler TDOCT systems, 8 kHz [17]. The claim of better SNR performance for frequency-domain systems over time-domain systems is based on the consideration of the AM (amplitude modulation) noise for the reconstruction of the structural OCT image. In the case of Doppler OCT, frequency modulation (FM) noise should be considered. Phase noise has been analyzed in terms of Gaussian noise in a relatively straightforward manner. In the case of Doppler OCT, the SNR performance for frequency-domain systems compared to time-domain systems is still a subject of debate.

Table 1.1 The performance of some TD and FD OCT systems concerning the velocity span

System	Speed sensitivity (mm/s)	Max speed (mm/s)	A-scan rate (Hz)
TDOCT (Short-time-Fourier trans.) [Yaz. Opt Expr 1, 424 (1997)]	0.46	3.45	8
TDOCT with STFT [Chen et al, Opt Lett 22, 1119 (1997)]	0.1	2	0.5
TDOCT with STFT [Izatt et al, Opt Lett 22, 1439 (1997)]	0.56	4.5	5
TDOCT with STFT [Bonesi et al, Laser Phys Lett4, 304 (2007)]	0.44	+/- 65	4
TDOCT with STFT [Wang et al, Meas Sci Tech 15, 725 (2004)]	0.16	30	6
TDOCT with Hilbert [Chen et al, IEEE J Sel Top Q El 5, 1134 (1999)]	0.01	0.1 (aliased)	80
TDOCT with phase locked loop detector [Zvyagin et al, Opt Lett 25, 1645 (2000)]	0.25	20	40
TDOCT with hardware autocorrelation		246	8,000

[Rollins et al, J Biomed Opt 7, 123 (2002)]			
TDOCT with phase resolved method [Wang et al., Appl Phys Lett 85, 1855 (2004)]	0.01	+/- 1	500
TDOCT with digital autocorrelation [Westphal et al., Opt Lett 27, 34 (2002)]	0.4	2.9 (aliased) 8.4 (unaliased)	3,840
TDOCT with Kasai estimator [Yang et al., Opt Expr 11, 794 (2003)]	+/- 0.017	+/-2 (aliased)	
TDOCT with 2D Kasai estimator [Morofke et al., Opt Lett 32, 253 (2007)]	0.007	+/- 560 (aliased)	8,000
TDOCT with phase resolved Hilbert method [Schaefer et al., IEEE Trans Biomed Eng 51, 186 (2004)]		350 (aliased) 1400 (unaliased)	8
FDOCT (Phase resolved) [Leitgeb et al, Opt Lett 29, 171 (2004)]	0.05	5	10,000
FDOCT (Phase resolved) [Leitgeb et al, Proc SPIE 5316, 141 (2004) et Opt Expr 11, 3116 (2003)]	0.2	5	25,000
FDOCT (Phase resolved) [Vakoc et al, Opt Expr 13, 5483 (2005)]		+/- 20 (aliased) 191 (unaliased)	15,600
FDOCT (Phase resolved) [Bachmann et al, Opt Expr 15, 408 (2007)]	0.55	+/- 9.7 (aliased)	23,200

In FDOCT, the frequency shift is obtained indirectly, either by using phase resolved methods from the inverse Fourier Transform of the spectral signal and by taking the

imaginary part of the temporal signal which gives the phase information for each A-scan (Hilbert transform) [19, 20] or by calculating the phase difference between two successive A-scans [18]. This method suffers from an aliasing phenomenon caused by 2π ambiguities in the relation between the flow and the phase that limits the maximum determinable Doppler shift. This maximum velocity corresponds to a phase change of 2π within a time between two successive A-scans. For typical FDOCT systems, the axial scanning rate is around 20 kHz, which brings typical maximum aliased speed values of several tens of mm.s⁻¹. Velocities higher than this range need to be obtained with phase unwrapping methods [19], but their use appears to be limited either to simple or laminar flow profiles. Again, at the end, one is not sure how accurate the instantaneous phase determination is. The TDOCT advantage for Doppler velocity determination is foremost that of simplicity since it gives us direct access to the interferogram. The phase can be “read-out directly” or locally from the time signal, avoiding the potential ambiguities and possible loss of phase information or “blurring” when using less direct spectral methods such as phase-unwrapping or successive A-scans.

In conclusion, we have decided to consider time-domain OCT as the preferred approach for the Doppler frequency determination provided that this technique can provide more accurate values and a wider dynamic range for the measured velocity.

1.5 Optical properties of tissues

The optical properties of a sample under investigation such as absorption and scattering coefficients play an important role in OCT penetration depth and contrast. This spectral dependency of the studied sample tissue needs to be addressed if one wants to obtain OCT images with the best resolution possible over a penetration depth as large as possible. Fig. 1.4 depicts the absorption and scattering coefficients of human tissue in the wavelength from 0.2 μm to 2 μm . It is clearly shown that water is a main constituent and has a major effect on the

absorption spectrum in most tissues. There exists a window between 600 nm and 900 nm where the absorption effect is the lowest leading to a longer penetration depth within the tissue. The scattering coefficients are inversely proportional to the wavelength which is much stronger in the low absorption window area and becomes very weak at around 1.5 μm where the absorption coefficients are very strong. The reduced scattering coefficient is plotted as curve D on Fig. 1.4. The penetration depth of the OCT image is determined by the whole attenuation effect which includes both the absorption and scattering of the light beam.

The often-used formula for calculating the transmitted optical power as light propagates through a medium is Beer's law in which the penetration depth is defined as the inverse of the attenuation coefficient of the medium α_t :

$$P_T(z) = P_0 \exp(-\alpha_t z) \quad (1-9)$$

where P_0 and $P_T(z)$ are the incident light optical power and the transmitted power after propagation through a medium thickness of z , respectively. To theoretically determine the total attenuation and the backscattering coefficients of a light beam for a given distance through a medium is quite complicated since many parameters of the tissue such as the index of refraction, the polarization state and the density are not homogeneously distributed. Experimental methods are therefore preferred [17].

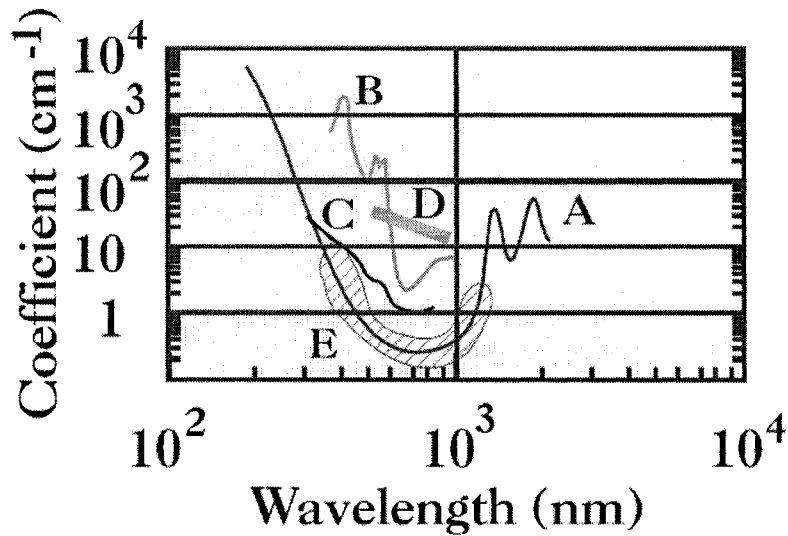


Fig. 1.4 Tissue properties. (i) absorption coefficient: A-water, B- whole blood, C-aorta, E- skin (cross-hatched area); (ii) reduced scattering coefficient: D- human tissue (in brown) [7].

The experimental setup for obtaining attenuation and backscattering coefficients by means of a graphical method is shown in Fig. 1.5. A sample holder made by a thin (130 μm) glass coverslip is used to hold the sample tissue. The glass plate touches the sample from the top. The principal assumption made is that the incoming wave, after being transmitted by the glass-sample interface, undergoes an attenuation over the optical length z' . The backscattered part at that depth travels in the opposite direction and propagates the same optical length with same attenuation. The reflection R_{GS} and transmission coefficients T_{GS} of the glass-sample interface are given by:

$$R_{GS} = \left(\frac{n_G - n_S}{n_G + n_S} \right)^2, \quad T_{GS} = \frac{4n_G n_S}{(n_G + n_S)^2} \quad (1-10)$$

where n_G and n_S are the index of refraction of glass and the tissue respectively.

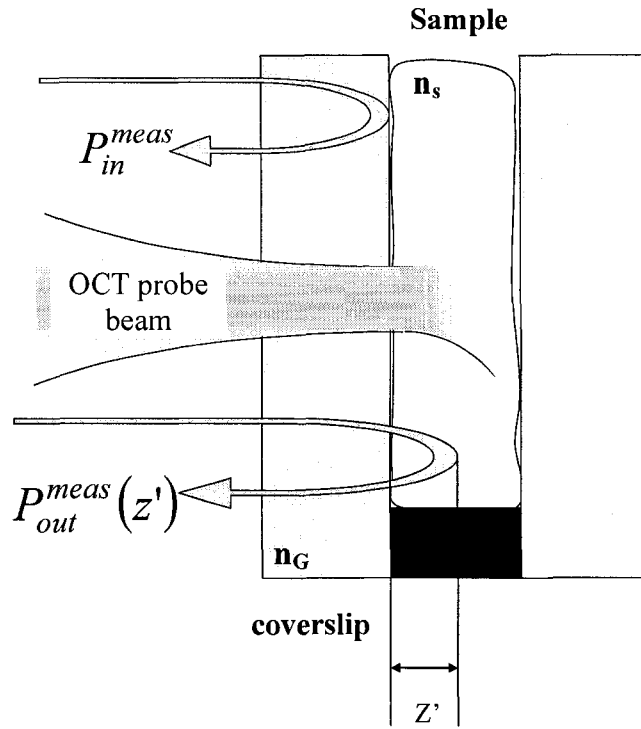


Fig. 1.5 Diagram of the sample holder used for attenuation and backscattering measurements

The power of the incident beam P_{in} can be derived from the amplitude of the backreflection from the glass-sample interface which is measured as P_{in}^{meas} . The transmission coefficient of the glass-air interface is T_{GA} . We have the relationship:

$$T_{GA} \cdot R_{GS} \cdot P_{in} = P_{in}^{meas} \quad (1-11)$$

The light power after crossing the glass-sample interface becomes:

$$P_{in} \cdot T_{GS} = P_{in}^{meas} \cdot T_{GS} / (R_{GS} \cdot T_{GA}) \quad (1-12)$$

By applying Beer's law here, the light power becomes $P_{in}^{meas} \cdot \exp(-\alpha_t z') \cdot T_{GS} / (R_{GS} \cdot T_{GA})$ after it propagates through a medium thickness of z , referring to an optical path of $z' = n_s \cdot z$. Let's suppose that the beam is backscattered by the discontinuities located at this position z with a backscattering coefficient of α_b , and that the scattered beam propagates in

the opposite direction through the same medium thickness z . After it reaches and passes through the glass-sample interface, this backscattered beam is detected by the photodetector. The measured power can be presented as:

$$P_{in}^{meas} \cdot \exp(-2 \cdot \alpha_t z') \cdot T_{GS}^2 / R_{GS} \cdot \alpha_b. \quad (1-13)$$

If we consider the fact that OCT signal amplitude measured at one point of the depth scan arises not only from a scattering center at this point, but also from a contribution of all the scattering centers located at distances less than half the coherence length l_c from this point, we obtain the following formula [3]:

$$\frac{P_{out}^{meas}(z')}{A(z')} = \frac{P_{in}^{meas}}{A_{in}} \cdot \frac{l_c}{2} \cdot \alpha_b \cdot \exp(-2 \alpha_t z') \cdot \frac{T_{GS}^2}{R_{GS}} \quad (1-14)$$

where $A(z')$ and A_{in} are correction factors that arise from the aperture function of the interferometer at z' and at glass-sample interface, respectively. We rewrite Eq. 1-14 as:

$$\frac{2P_{out}^{meas}(z') \cdot A_{in} \cdot R_{GS}}{P_{in}^{meas} \cdot l_c \cdot A(z') \cdot T_{GS}^2} = \alpha_b \cdot \exp(-2 \alpha_t z') \quad (1-15)$$

Taking the logarithm on both sides and using $B(z')$ to indicate the left side of the equation, we obtain the final formula:

$$B(z') = \ln(\alpha_b) - 2 \cdot \alpha_t \cdot z' \quad (1-16)$$

where

$$B(z') = \ln\left(\frac{2P_{out}^{meas}(z') \cdot A_{in} \cdot R_{GS}}{P_{in}^{meas} \cdot l_c \cdot A(z') \cdot T_{GS}^2}\right) \quad (1-17)$$

From Eq. 1-16, it is possible to measure the attenuation and backscattering coefficients using a graphical method [21]. To apply this method, first, we need to obtain all the parameters from the data of each A-scan: P_{in}^{meas} and P_{out}^{meas} can be read directly from the received interference signal, R_{GS} and T_{GS} can be calculated from n_G and n_S . The measurement of n_S can be carried out by means of comparing the OCT-measured optical path of the sample chamber when it holds tissue sample and when it is empty. Once $B(z')$ is obtained experimentally, we rewrite $B(z')$ as a function of optical depth z' . The curve obtained should be a line whose slope and offset gives α_t and α_b , respectively.

1.6 Conclusion

In this chapter, the scope of this dissertation has been presented. OCT and Doppler OCT are seen as a novel biomedical imaging tool which can provide structural information and flow velocity measurements of a biological tissue. One of the main objectives of this research was to build a high accuracy multi-wavelength time-domain system for Doppler OCT experiments. A comparison of time-domain versus frequency-domain OCT has been provided keeping in mind the specific requirements of Doppler measurements. Absorption and backscattering coefficients were also discussed theoretically and a graphical method for measuring these coefficients has been given in detail. These preliminaries should help us gain a better understanding of how the optical properties of the sample affect the quality of the final OCT images. The results on structural OCT can be also applied to the functional OCT images such as velocity distribution plots.

This dissertation is structured as the follows. In chapter 2, the fabrications and developments of the OCT systems and Doppler OCT systems are described. Cross-sectional OCT images of tissues are displayed and investigated using three different wavelengths for obtaining the optical properties of the samples. In Chapter 3 and 4, we present our

contributions on the data processing algorithms for Doppler OCT. This dissertation focuses on the development of high accuracy and high dynamic range Doppler OCT which has the potential to non-invasively detect the velocity distribution beneath the surface of the samples. Chapter 5 illustrates some of our applications of Doppler OCT in microfluidics and cardiovascular phantoms. Significant improvements are shown over existing conventional tools. Finally, a conclusion is given which summarizes the dissertation and some possible future work is pointed out.

CHAPTER 2

Experimental setup

2.1 Overview

In this chapter, we will focus on the development of the experimental setups that have been built in the laboratory. The setups are implementations of experimental OCT systems based on both free-space Michelson interferometers and all-fiber interferometers. We will describe some improvements in the design and construction of the systems, such as the amplitude envelope detection for the shortening of the data acquisition time, a deconvolution method for the elimination of the side-lobes effect in order to enhance the image contrast, a probe station assembly and polarization control components that provide high quality OCT images for a short acquisition time and with an easy operation. The investigation of how the optical properties of a sample affect the performance of the cross-sectional OCT images by means of a graphical method will also be presented.

2.2 Free-space system based on Ti:sapphire pulsed laser

The properties of the light source have a great impact on the OCT image quality. Amongst them, the most important one is the wavelength bandwidth ($\Delta\lambda$) of the light source since it is the main factor that determines the longitudinal or axial resolution of the OCT system. To date, the state-of-the-art axial resolution of OCT has reached 1 μm using a Ti:Sapphire modelocking pulsed laser which generates a pulse of 5 fs duration with a bandwidth of over 300 nm [6]. Another important property of the light source is its central wavelength (λ_0) since it strongly affects the depth of each A-scan. Usually, the researchers prefer the near infrared range as a best choice for sources since the typical tissue constituents, such as water and blood, have a low light absorption in this spectral region, as shown in Fig. 2.1. Because of its central wavelength at about 800 nm, the ultra-short Ti:Sapphire mode-locked pulsed laser has been widely used as a source for experiments in OCT.

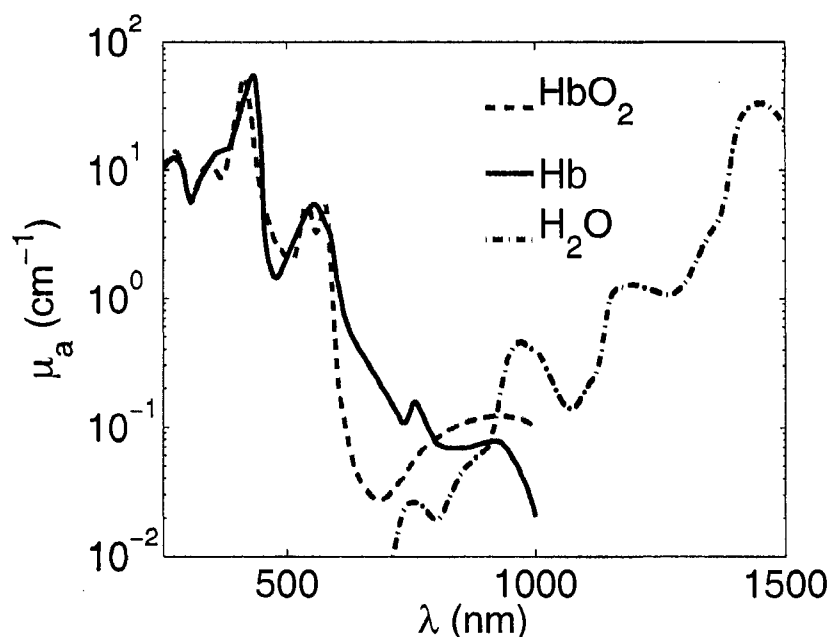


Fig. 2.1 Absorption spectrum of main chromophores in tissue (oxy-hemoglobin, HbO₂; deoxy-hemoglobin, Hb; and water, H₂O). μ_a : Absorption coefficient.

In our laboratory, a Ti:sapphire femtosecond pulsed laser made by R&D Ultrafast Lasers Ltd., is used for the experiments. This Kerr-lens mode-locking, ultrashort pulsed laser gives a maximum bandwidth of 100 nm at about 810-nm central wavelength. The corresponding coherence length is measured to be 3.5 μm . In general, the titanium-doped sapphire crystal is the most successful laser medium in ultrafast lasers because of its broad gain bandwidth (300 nm wavelength range centered around 810 nm) and excellent mechanical and thermal properties. Let us introduce a few words about mode locking. The Fabry-Perot cavity in which the Titanium-doped sapphire crystal is placed allows lasing over its longitudinal modes and suppresses all other frequencies by destructive interference. For example, considering a laser cavity formed by two plane mirrors separated by a distance of $L = 300$ mm, the allowed laser modes are those for which L is an exact multiple of half the wavelength of the light λ_i , such that $L = q \lambda_i / 2$, where q is an integer known as the mode order. Thousands of laser modes can, in principle, be supported within the laser cavity. Each

of these modes can oscillate independently, with no fixed relationship to each other. The laser operates in the continuous wave state. If a fixed phase relationship between the existing laser modes is induced, a train of laser pulses can be obtained by interference effects between these modes. In that case, the laser is said to operate in the mode-locked regime. These laser pulses can be of extremely brief duration. For instance, for the 300 nm wavelength range Ti:sapphire laser, the shortest Gaussian pulse that can be produced is of the order of 3 - 4 femtoseconds. In laser cavity, the total index of refraction can be written as:

$$n(\omega, t) = n_0 + n_2 I(\omega, t) \quad (2-1)$$

where I is the intensity of the propagating beam. The index n_2 is the nonlinear index of refraction and causes the Kerr-lens effect. The Gaussian TEM₀₀ modes propagate through the crystal and induce a graded-index lens due to the intensity distribution. This causes a self-focusing of the laser beam. Since the laser pulse has a much higher intensity than the CW beam, it is focused more strongly and closer to the center and is more collimated than the other lasing modes. Thus the pulse circulating in the cavity will receive a higher gain inducing the mode-locked operation [22-24].

The main condition to achieve a mode-locked effect is to tune the overall dispersion of the laser optical resonator at either zero dispersion or at a slightly negative dispersion. This is referred as the group velocity dispersion (GVD) compensation. In the laser cavity, there is a certain amount of frequency-dependent dispersion introduced mostly by the Ti:sapphire crystal. This positive dispersion has to be compensated in order to produce ultrashort laser pulses. This can be achieved by means of either Brewster prism pairs or chirped mirrors or both. Among these two methods, prism pairs can compensate the group delay dispersion (GDD), but for the higher order dispersion, compensation needs to be done with the aid of chirped mirrors. A detailed description of the GVD dispersion compensation within the Ti:sapphire femtosecond pulse laser cavity can be found in my Master's thesis [25] in which

the prism pair only are used. Another point under consideration is that chirped mirrors always induce a fixed negative dispersion whereas the prism pair can tune the value of the induced negative dispersion by translating the prisms into or out of the laser beam. Our laser employs both a prism pair and chirped mirrors that provide the advantage of a fine adjustment of the induced negative dispersion thus obtaining sub-10 femtosecond laser pulses. The simplified schematic of this Ti:sapphire laser oscillator is shown in Fig. 2.2.

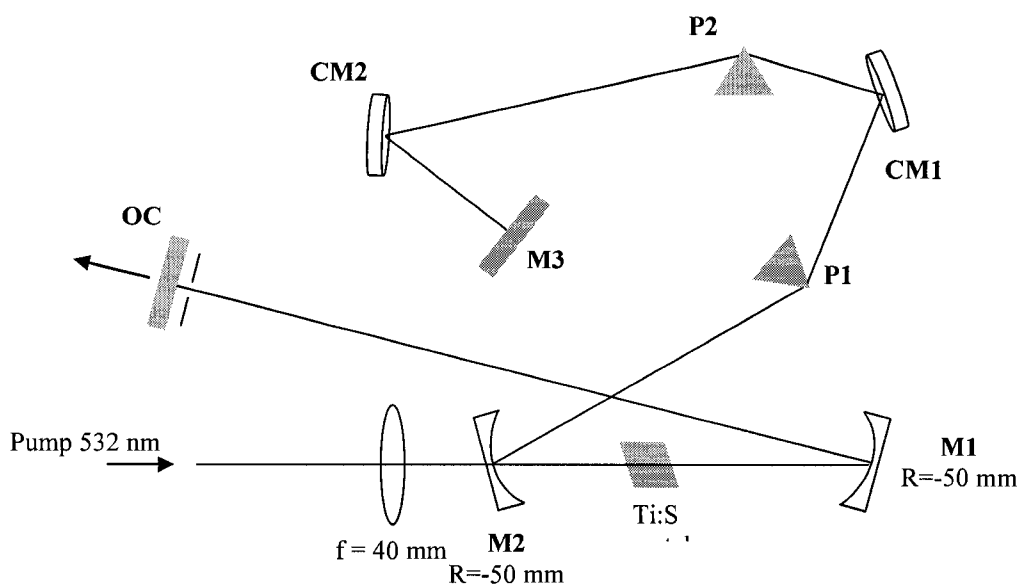


Fig. 2.2 Simplified schematic diagram of the Ti:Sapphire laser cavity. OC: output coupler. CM: chirped mirror. P: prism.

With the above configuration of the laser cavity, the mode-locked ultrashort pulse can be easily obtained when the prisms are slightly inserted into the laser beam. Under this condition, the chirped mirrors provide the main contribution to the dispersion compensation. A shaking mirror is used to fire up the mode-locking. The received laser pulses are stable and powerful, but the bandwidth is narrow (about 40 – 50 nm). Once mode-locking is established, we then translate the prisms into the laser beam little by little while keeping mode-locking on. During this procedure, one can observe that the spectrum becomes broader, the power

decreases and the laser becomes less stable. We can keep going until the bandwidth is close to 100 nm around 810 nm central wavelength, while checking that its stability is acceptable and the output power is higher than 100 mW. Fig. 2.3 shows the measured spectrum of the Ti:sapphire laser under pulsed condition acquired by a spectrum analyser. Then, the laser is ready for OCT experiments.

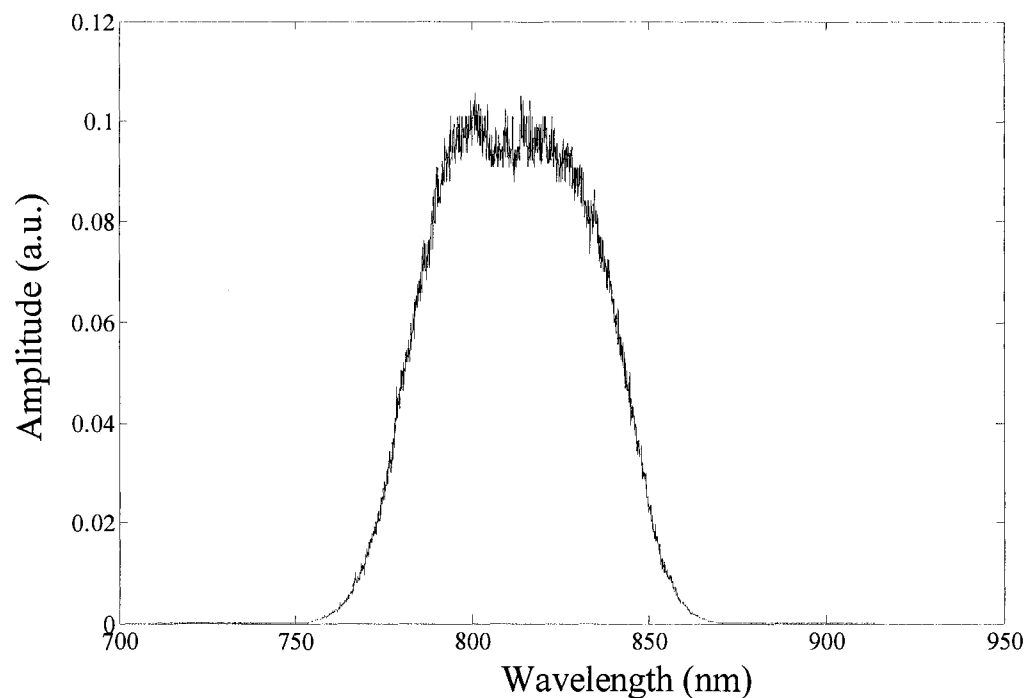


Fig. 2.3 The measured spectrum of the Ti:sapphire laser under pulsed conditions.

The schematics of the free-space (FS) OCT setup using the Ti:sapphire laser as the broad bandwidth source is depicted in Fig. 2.4. The laser output is collimated and directed into the system. The laser beam is divided by the power beamsplitter into two arms: the sample arm and the reference arm. Each arm has one near infrared, low-numerical aperture (0.25 N.A., 10 X magnification) microscope objective in order to get a wide depth of field. The sample and reference mirror scans are done by motorized stages moving at a typical speed of 1.3 mm/s. The output optical power is measured with a dual balanced detector so as

to remove relative intensity noise, thus improving the signal-to-noise ratio. We measured a typical noise reduction of more than 20 dBm compared to normal detection. A phase quadrature between the impinging waves on each detector is achieved in the FS interferometer by means of a polarizing cube coupled with a half-wave and a quarter-wave plate. The acquisition system consists of an envelope detector which suppresses the carrier frequency, a signal amplifier and a digital multimeter. A PC does the data acquisition and image processing is done with an in-house code developed in the laboratory.

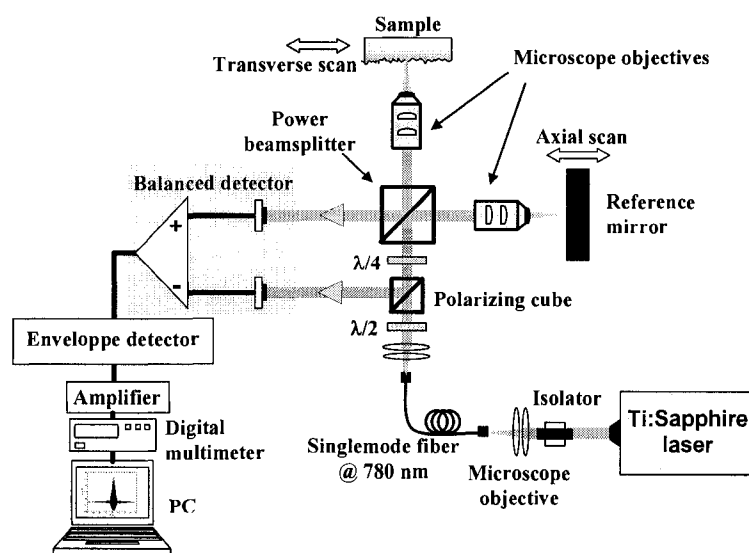


Fig. 2.4 Free-space interferometer OCT setup operated with a Ti:Sapphire laser.

This free-space OCT setup was tested and evaluated by putting a totally reflective mirror as a sample as shown in Fig. 2.4. The bandwidth is close to 100 nm at around 810 nm central wavelength. The recorded interference signal is illustrated in Fig. 2.5. The measured coherence signal is typically 3.5 μm which is the main parameter determining the axial resolution of the OCT image. We observe that the sidelobes are much suppressed in the interferogram. This is due to the spectrum shape of the laser that is close to Gaussian. This is an advantage of using the Ti:sapphire laser as a source for OCT since sidelobes can induce spurious effects on OCT profiles. This is very important since sidelobes induced by highly

reflective interfaces may mask signals coming from weakly reflective structures located in the same area.

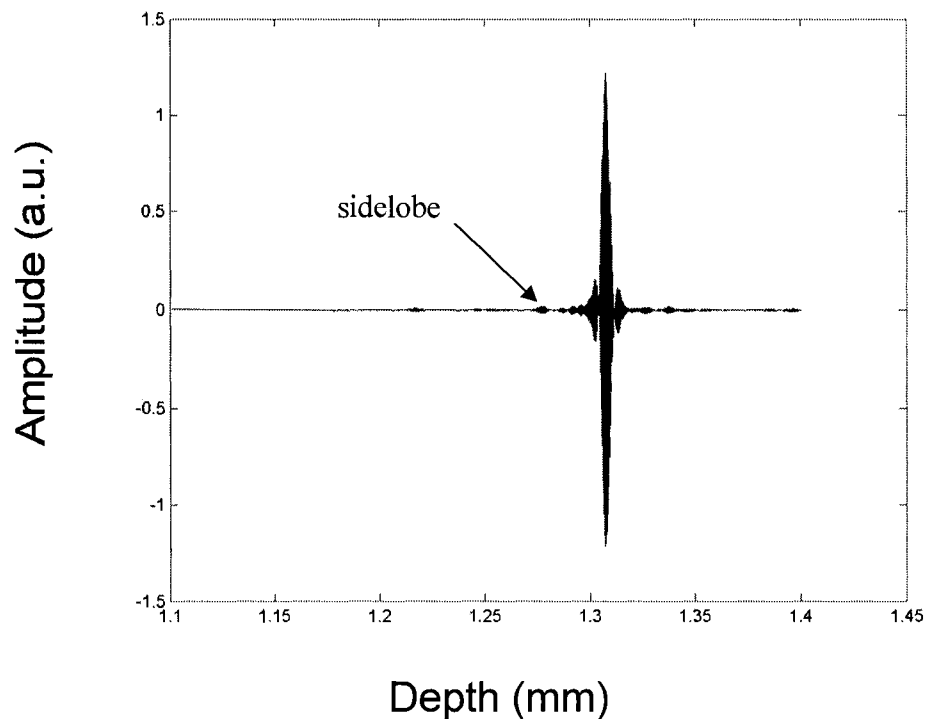


Fig. 2.5 Interference trace produce by the Ti:sapphire laser with a mirror as the sample

2.3 Fibre-optic based system using near-infrared sources

Two infrared broad bandwidth sources were also used in OCT experiments: a 1.3 μm central wavelength laser pumped high power continuous light source (BBS series from MPB communications, Inc., as shown in Fig. 2.6a) and a 1.5 μm central wavelength superluminescent diode (SLD) from JDS Uniphase, Inc, as shown in Fig. 2.6 (b). The latter has a 60 nm bandwidth light at 1570 nm central wavelength which amounts to a coherence length of 23 μm . The former uses nonlinearly transformed light from a high power laser to produce a broad bandwidth. For a better performance in OCT experiments, this source was used in two different modes. In the original mode, the emission spectrum had more than 100 nm bandwidth centered near 1330 nm with 1 W continuous power. This configuration leads

to a coherence length of 8 μm . In order to get a quasi-Gaussian spectrum, the source can also be operated with an internal filter that removes the two peaks in the spectrum (dashed line in Fig. 2.6a). In this case, the extinction of the sidelobes from the interference signals leads to a better quality of the OCT image. Thus, the bandwidth is narrowed to 60 nm and coherence length increases to 18 μm , but the sidelobes are almost totally removed from OCT interference signal, as shown in Fig. 2.7 (b).

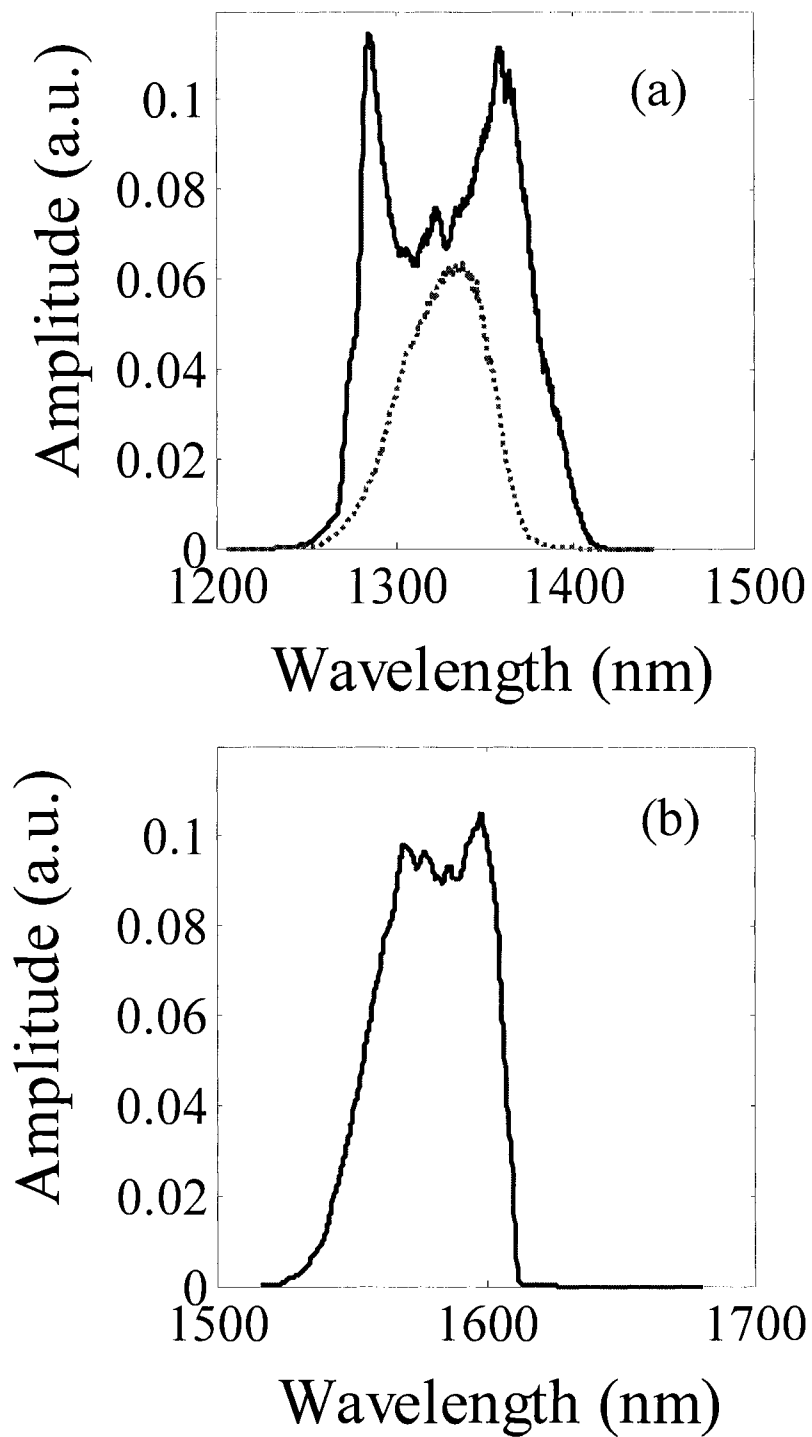


Fig. 2.6 Spectra of the sources. (a): original MPB source (solid) and filtered (dashed) MPB source. (b): Source at 1.5 μm .

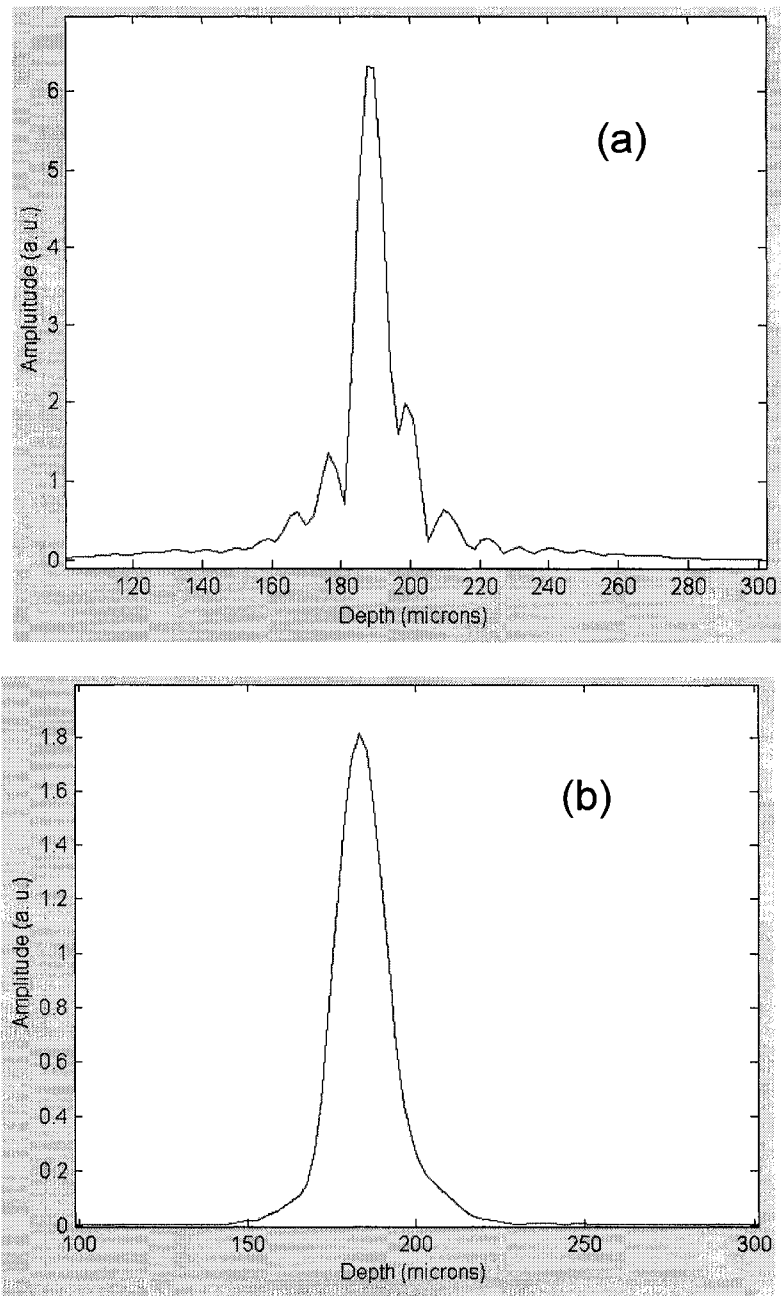


Fig. 2.7 Profiles of OCT signals obtained with (a) the original and (b) the filtered MPB source.

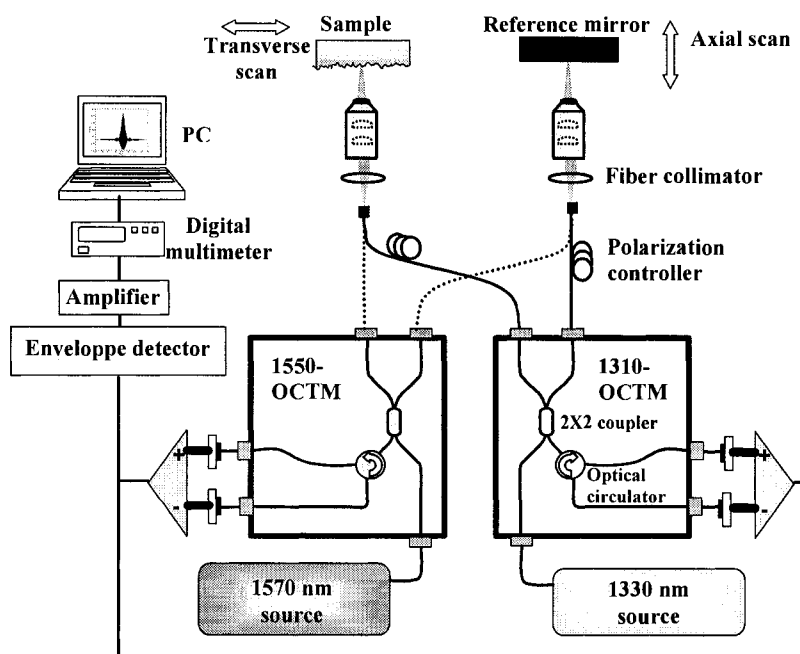


Fig. 2.8 Fiber-optic OCT setup operated with near infrared sources.

A diagram of the customized fiber-optic interferometers (1550-OCTM and 1310-OCTM) is depicted in Fig. 2.8. Light from the source is directed into the system by a standard connector. The beam is then divided by a 50/50 optical fiber coupler into two arms: the sample arm and the reference arm. In each one, the beam is collimated with variable focal length, broadband fiber collimators and then focused by near infrared, low-numerical aperture (0.25 N.A., 10 X magnification) microscope objectives in order to get a wide depth of field. As before, the sample and reference mirror scans are done by motorized stages moving at a typical speed of 1.3 mm/s. Again, the output optical power is measured with a dual balanced detector so as to remove relative intensity noise, thus improving signal-to-noise ratio. We measured also a typical noise reduction of more than 20 dBm compared to normal detection. A phase quadrature between impinging waves on each detector is obtained by means of a broadband fiber circulator. The same acquisition system is used. Since fibers are polarization sensitive, polarization controllers are used in the fiber interferometers to match the polarization states between the reference and sample arms. This

polarization state matching is performed by monitoring the signal interference trace on the screen of a digital oscilloscope.

2.4 Evaluating the envelope detector

In our setup, the A/D conversion is achieved by means of a digital multimeter with a maximum sampling rate of 100 kHz. Therefore, two limitations are introduced in the OCT acquisition. The first one is the total amount of data taken within one longitudinal scan: what can be transferred to the buffer limits the depth of each scan for a given sampling rate. The second one is the data downloading speed from the multimeter to the PC which can highly decrease the image acquisition time of an OCT run. The completion time and the axial depth of one A-scan as a function of the sampling rate are shown in Fig. 2.9. It is quite clear that the sampling rate plays a very important role which strongly affects the performance of the OCT image acquisition. Our goal is to obtain the interference signal with as little distortion as possible while consuming as little time as possible. A recorded signal consists of both the envelope and the carrier frequency. Normally, for producing an undistorted interference trace, a 50 kHz sampling rate is often selected. However, in our OCT setup the carrier frequency is not required for structural imaging. This refers to the first step of the image reconstruction. So, we got the idea that if the envelope of the signal could be obtained before being sent to the multimeter, we would not need to drive the A/D converter at a very high sampling rate to obtain the amplitude of the signal. In that way, a substantial amount of time could be saved. This function was achieved with a homemade hardware low-pass filter. An Analog Devices AD536A circuit was used for the RMS to DC conversion, and a two-pole Sallen-Key filter, as suggested by the Analog Device's guide, was also used in order to remove ripples from the signal.

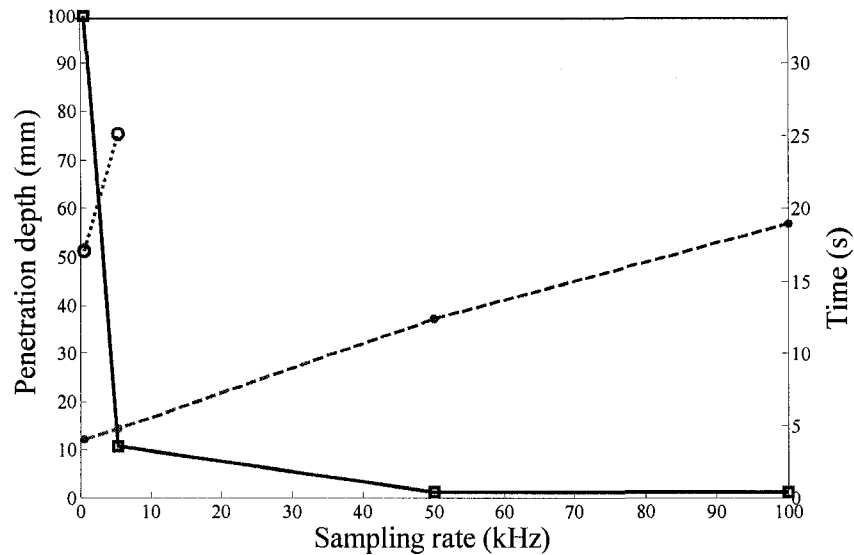


Fig. 2.9 Acquisition time and penetration depth are strongly affected as the sampling rate changes. Solid line: penetration depth. Dashed line: time for completing an A-scan of 1 mm length. Dotted line: consuming time for completing an A-scan of 10 mm length.

The effect of the envelope detection of a single interferogram is shown in Fig. 2.10 and Fig. 2.11. These results have shown good agreement between the actual interference signals and the single line envelope of the signals. The sampling rate for envelope detection is 10 times less than that for the raw signal detection. Furthermore, our recorded interferogram at 5.3 kHz sampling rate had some distortions due to a lack of sampling points. This problem has been overcome by the envelope detection since the signal under detection is easily acquired at a much lower sampling rate (592 Hz).

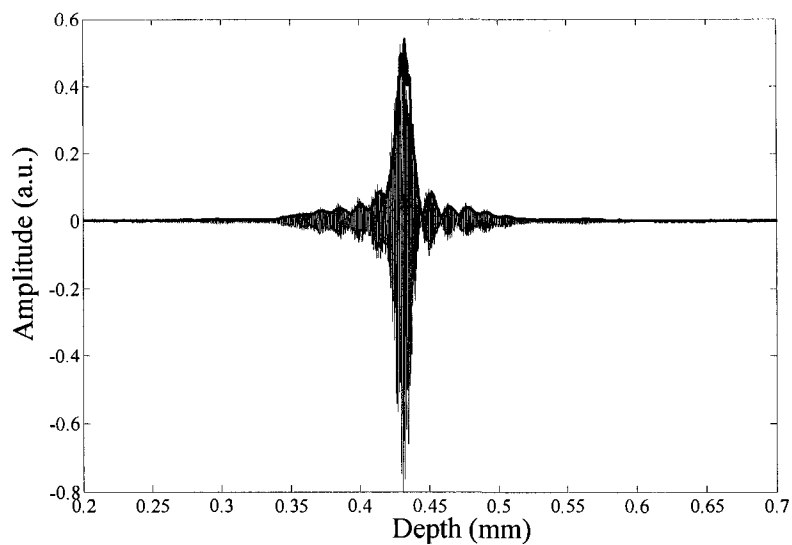


Fig. 2.10 Effect of the envelope detection of a single interferogram obtained with the MPB source. Solid line: envelope detection at 592 Hz sampling rate. Blue line: raw signal at 5.3 kHz.

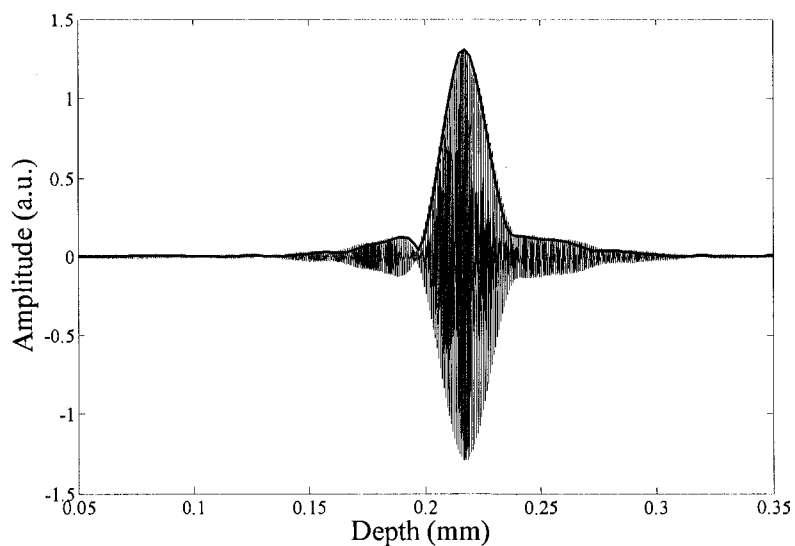


Fig. 2.11 Effect of the envelope detection of a single interferogram by the JDSU source. Solid line: envelope detection at 592 Hz sampling rate. Blue line: raw signal at 5.3 kHz.

2.5 OCT microscope assembly

There is a similarity between a microscope which is used to produce enlarged images of small objects and OCT which produces enlarged 2D or 3D cross-sectional images of small

objects. The main difference between them is that OCT detects the in-depth internal microstructure beneath the surface of the sample (A-scan) and proceeds with a series of longitudinal scans at different lateral locations (B-scan) in order to create a two-dimensional map of the sample. For better performance and easy operation, the design of the probe station of an OCT system can be similar to that of a simple microscope. This way, the sample stage is designed to be horizontal and maintains the sample with stability without the help of holders. It is then convenient for the positioning of the sample during the image acquisition. Moreover, a horizontal sample stage allows some special samples to be scanned more easily, such as a sample in a box filled with some liquid.

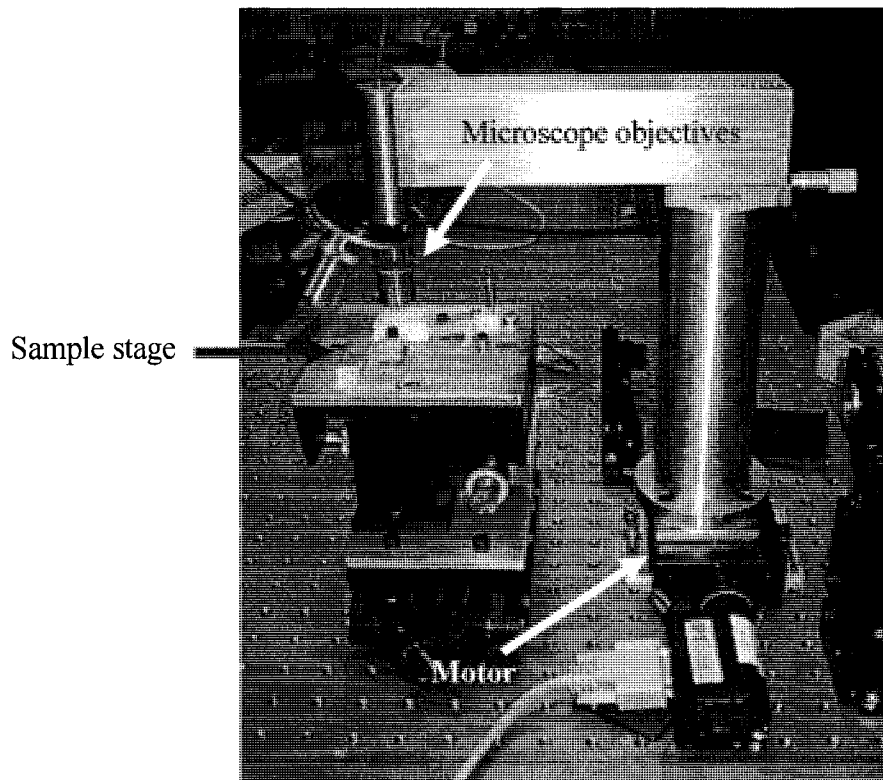


Fig. 2.12 Probe station of the fiber-optic based OCT setup.

Fig. 2.12 shows the specially made, probe station. The sample stage can be adjusted by a 3-axis stage with high precision. The probe head can be moved horizontally to position of the

imaging area with high precision. Microscope objectives with different numerical apertures, for example, 0.25 N.A. 0.40 N.A. 0.60 N.A., can be easily switched from one another. This is an important advantage of the setup since it allows the selection of the working conditions of either long penetration depth together with poorer lateral resolution (low N.A. objective) or short penetration depth together with good lateral resolution (high N.A. objective). This choice is dictated mostly by the size, attenuation coefficient and internal structure of the sample. The sample arm of the setup consists of an optical fibre connected with a near-infrared collimator and the microscope objective. Both of them have been mounted on the two ends of a copper tube and precisely aligned. This probe head can be moved up and down by a manual positioner and laterally by a PC controlled moving stage. This microscope assembly for the OCT experiments has been tested with many samples and found superior over the previously used horizontal probe station in which the sample had to be mounted vertically. When the sample is held vertically, a special sample holder has to be employed and proves inconvenient when switching samples. In that case, some samples need to be fixed on the sample holder with special glue, so that one needs to prepare the sample in advance since it takes time for the glue to dry. This was a major limitation of the system since some biological tissues need preservation to keep them fresh. Such samples had to be placed inside a special purpose small chamber filled with saline solution. Much care had to be paid to prevent the sample stage from leaks. With the new horizontal sample stage, the problems were solved by putting the sample inside a small plastic box filled with a saline solution.

2.6 Data acquisition parameters and interface

The electronic part is one of the major issues of an OCT setup. It is an assembly of various components including a PC, a digital multimeter, two computer-controlled linear positioners, an envelope detection circuit, a balanced detector with a built-in amplifier, and a

digital oscilloscope. Two proprietary programs were used to fulfill the data acquisition and the results display tasks. The former one has been improved several times compared to the version presented in my Master's thesis, and the latter is a new graphic user interface (GUI) program based on Matlab.

Because a digital multimeter is employed for the A/D conversion, the maximum sampling rate can reach 100 kHz. We have set 5 sampling rate options to choose from. Among them, 592 Hz is the one that is often chosen when working with the envelope detector because it provides both undistorted signals and short acquisition time. The A-scan depth can be set at will until the maximum range of the positioner, 100 mm, has been reached. The data is saved as a Matlab file which contains all the useful experimental information, including the date, the moving speed of the reference mirror, the sampling rate, the start and end positions of the two motor stages, and so on. Some of this information will be called by the data processing program and shown in the final OCT image.

The data processing program, the GUI, has two main features. The first one is that it has an enhanced contrast button that emphasizes the structure against the noise level. The second one is that this program can decrease the effects of the sidelobe-induced resolution degradation. This refers to the deconvolution function of the program. The ceiling and the threshold settings of the amplitude of the signal are adjustable. The effects of contrast and the brightness adjustments of the image can be monitored online until a satisfying image is produced as a final result.

2.7 Doppler setup in general

Recently [26], as an important development of OCT, Doppler OCT has attracted researchers interest and has become an active OCT research fields. In addition to the usual structural information which is extracted from the position and the amplitude of the OCT cross-correlation trace, Doppler OCT also yields precious information on the frequency

content of the detected fringe intensity coming from the interference between the reference and target arms. These interference fringes can be observed only when the optical path lengths between the light backscattered from the sample and that from the reference arm are matched to within the coherence length of the broad bandwidth light source. The flow velocity measurement is based on the principle that the Doppler frequency shift Δf_D in the interference fringe intensity modulation results from the motion of the scatterers within a sample [5]:

$$\Delta f_D = \frac{1}{2\pi} (\vec{k}_s - \vec{k}_i) \cdot \vec{v} . \quad (2-2)$$

where \vec{k}_s and \vec{k}_i are the wave vectors of the incoming and scattered light, respectively, and \vec{v} is the velocity of the moving scatterer.

We have performed flow measurements with the Doppler OCT system depicted in Fig. 2.13. This experimental setup is based on our fiber-optic Michelson interferometer OCT setup but the sample arm has been modified to satisfy the requirements of Doppler OCT. In the sample arm, a sample holder has been designed and built. It can be precisely adjusted along 5-axes in order to align the fluid sample, as shown in Fig. 2.14. The flow rate was set by a controller and a pump. The angle between the probing beam and the flow direction can also be precisely adjusted to chose the Doppler angle of the sample. The carrier frequency of the fringe signal was 1.94 kHz since the scan speed of the reference mirror was set at 1.5 mm/s with the source centered at 1545 nm. In principle, if the Reynolds number is much less than the critical number, the flow can be considered as laminar and the velocity profile in a circular tube is parabolic [27]:

$$V(r) = V_c \left[1 - \left(\frac{r}{d/2} \right)^2 \right] . \quad (2-3)$$

where $V(r)$ is the velocity at radial position r , V_c is the central peak velocity, and d is the inner diameter of the tube.

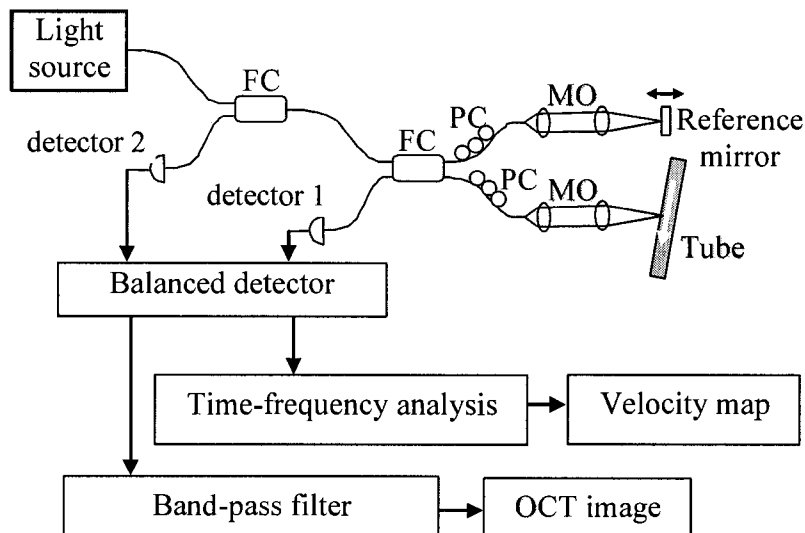


Fig. 2.13. Experimental setup for the Doppler frequency-shift measurements. FC: fiber coupler, PC: polarization controller, MO: microscope objective

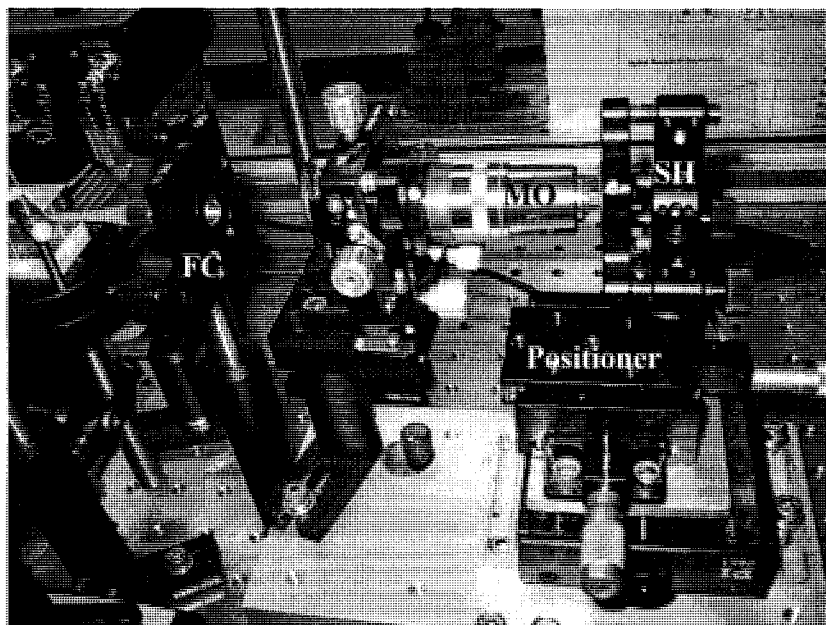


Fig. 2.14 Sample arm of the Doppler OCT setup shows the positions of the sample holder and the microscope objective. FC: fiber collimator. MO: microscope objective. SH: sample holder.

2.8 Experimental results

We have used our OCT setups to acquire high quality cross-sectional images of several samples with three different sources. The detailed structural information inside the body of the samples can be seen clearly. An investigation of the effects of the optical properties of the sources OCT images has been performed in order to discover which source can give the best OCT image in terms of penetration depth and the contrast.

i). OCT images with the 810 nm Ti: sapphire laser

In our lab, the best resolution OCT images were obtained with the Ti:sapphire laser as the source and with the free-space setup. The system uses broadband beam splitters. The resolution of the OCT image can be as high as $3.5 \mu\text{m}$, such that many details inside the sample are revealed. Moreover, since the spectrum of the laser is almost Gaussian, the sidelobe effect which may be strong for other infrared sources is very weak in this case. No deconvolution is necessary for the OCT images produced by the Ti:sapphire laser. Here we show some OCT images of biological tissues to assess image quality. Fig. 2.15 is an OCT image of a chicken heart sample. We can distinguish two different zones on the depth profile. Accurate details on the first layer which is believed to be the endocardium can be seen. Furthermore, we can also see some interfaces in the second zone which is almost homogeneous everywhere. On Fig. 2.16, the onion cell's structure of the first three layers can be clearly seen. In Fig. 2.17, we can observe that a fish scale consists of two different layers: the first one is more transparent and the other one has more scattering. The interface between these two layers is clearly seen on the image.

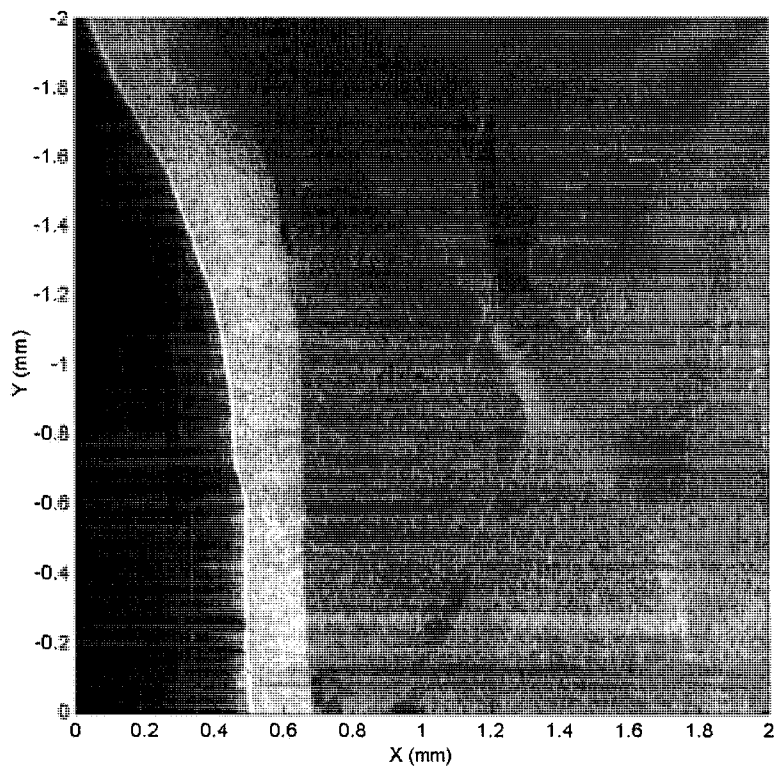


Fig. 2.15 OCT image of a chicken heart ventricle wall with Ti:sapphire laser.

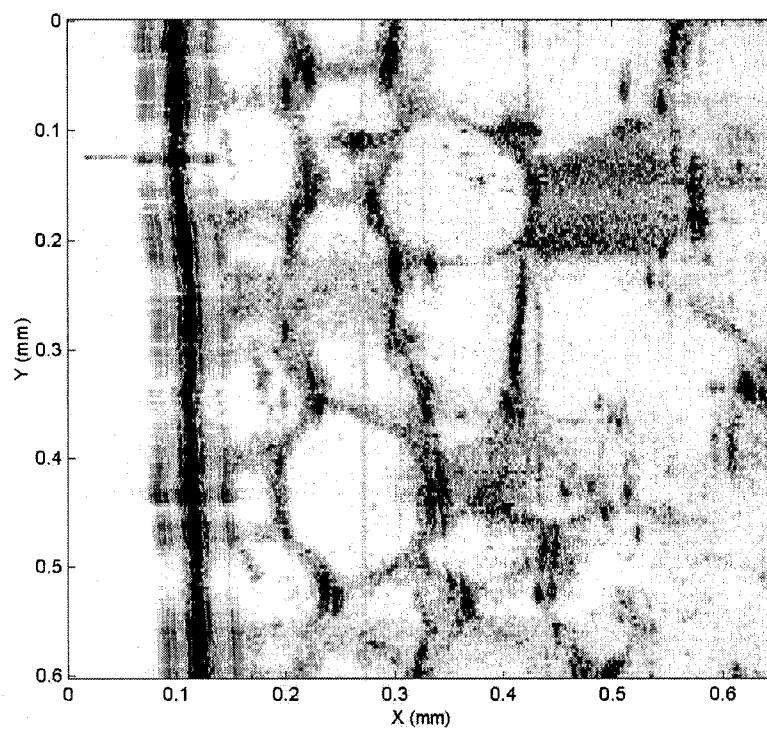


Fig. 2.16 OCT image of an onion peel with Ti:sapphire laser.

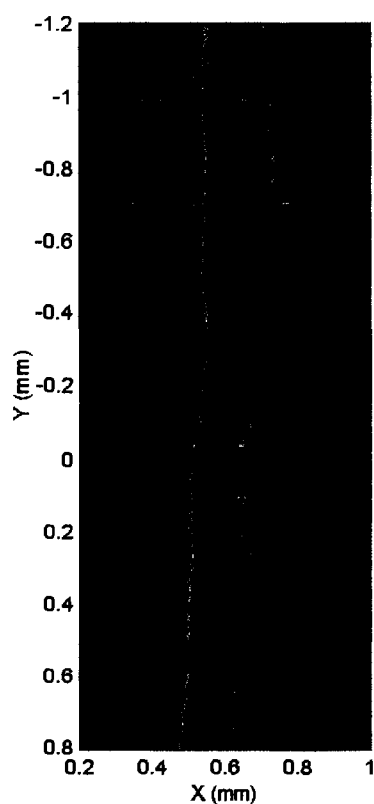


Fig. 2.17 OCT image of a fish scale.

ii). OCT images with the 1310 nm MPB source

The 1.3 μm central wavelength infrared broad-bandwidth source from MPB communications, Inc. has two different operating modes regarding the shape of the spectrum. As previously discussed in section 2.3, the original operation uses the full spectrum with more than 100 nm bandwidth centered near 1330 nm, at 1 W continuous power, leading to a coherence length of 8 μm . The filtered operation of the source removes the two peaks of the original spectrum leading to a quasi-Gaussian spectrum which can suppress the sidelobes in the interferogram. This way, a better resolution of the OCT image can be obtained at the cost of increasing the coherence length to 18 μm since the bandwidth is narrowed to 60 nm. But the sidelobes are almost totally removed from OCT signal. This approach relies on spectral filtering to remove the sidelobes removing. We also tried another

method for the sidelobes removal based on a software approach that uses deconvolution. Deconvolution is a software-based data processing procedure which is performed on the received experimental data after the OCT acquisition[28]. The principle of deconvolution works as follows. The impulse response of the OCT system is acquired using a hard reflection off a mirror as a sample. The equivalent filter response is then obtained by a Fourier transform. Later on, the signals are corrected by dividing out this system filter response.

Fig. 2.18 illustrates the effect of spectral filtering on the OCT image of a chicken heart tissue. In (a), we can see that the image has a better axial resolution compared to that of (b). However, image (a) really suffers from a strong sidelobe effect, especially at the surface of the sample where the back reflection is believed to be much stronger than that from inside of the tissue. By this treatment, OCT image can be improved by a better contrast without degrading the resolution of the image. We performed deconvolution on the two images of Fig. 2.18, and the results are shown in Fig. 2.19.

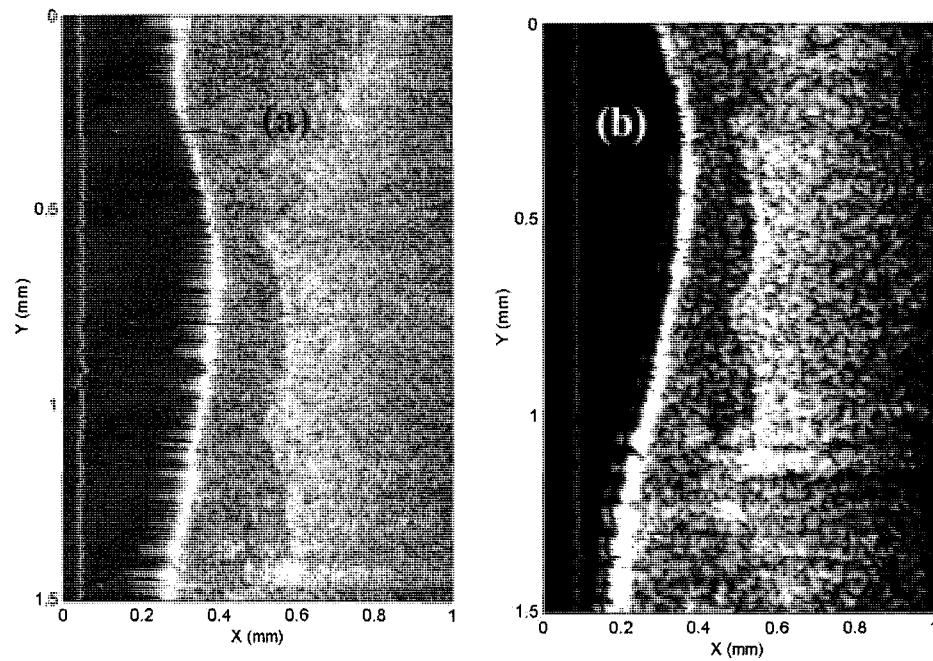


Fig. 2.18 OCT images of a chicken heart obtained with the MPB source. (a): original full spectrum mode which has a higher resolution but with the sidelobe effect. (b): filtered mode which has lower resolution but without the sidelobes on the image.

From 2.19 (a), we can see that, by applying the deconvolution treatment on the original full spectrum mode image, one obtains the best image with clear details and with all the sidelobes suppressed. Due to the decreased coherence length of the filtered mode, the final image after deconvolution has improved sharpness with the drawback of poorer resolution.

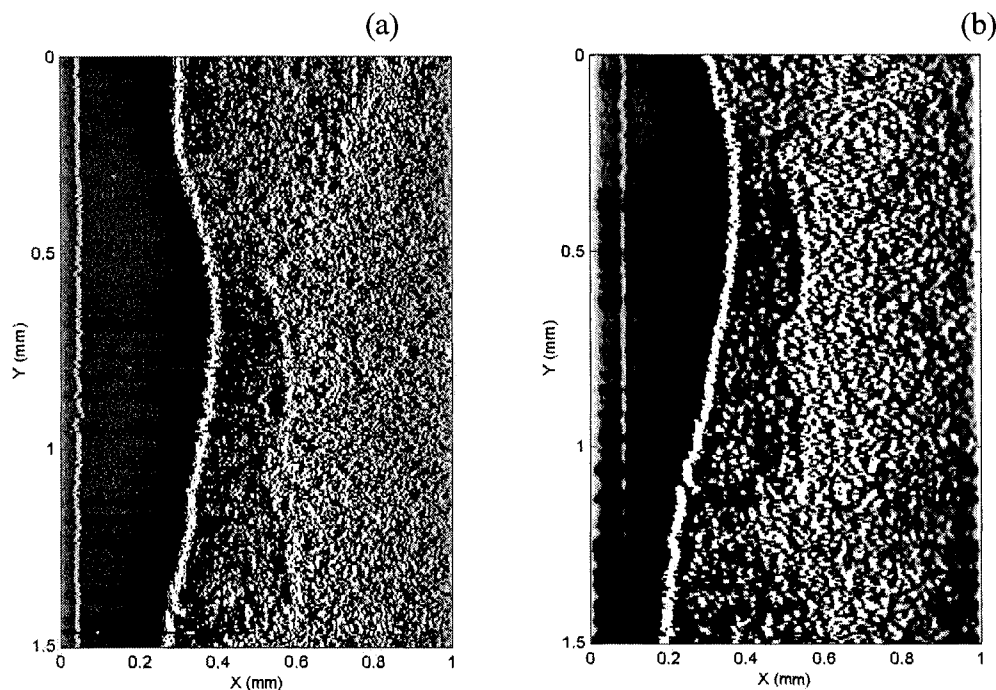


Fig. 2.19 Effects of deconvolution on the OCT images of chicken heart (a): original full spectrum mode. (b): filtered mode.

iii). OCT images with the 1570 nm SLD source

The third source that was used is a superluminescent diode (SLD) from JDS Uniphase, Inc. that has a 60 nm bandwidth at 1570 nm central wavelength. The coherence length of this source is 23 μm . Compared to the previous sources, this source has the potential of reaching deeper into the tissue because the scattering coefficient is inverse proportional to the wavelength. Therefore, less backscattering allows the light to propagate through the sample without a strong decrease in power. Loss comes predominantly from absorption. Furthermore, the light backscattered from the structures inside the sample propagate back with less loss. More details at larger depths can be seen if the absorption at this wavelength is small. Fig. 2.20 displays a high quality OCT image obtained with this infrared source even though it suffers from resolution loss due to a narrower spectral width, more absorption in this spectral region and less backscattering.

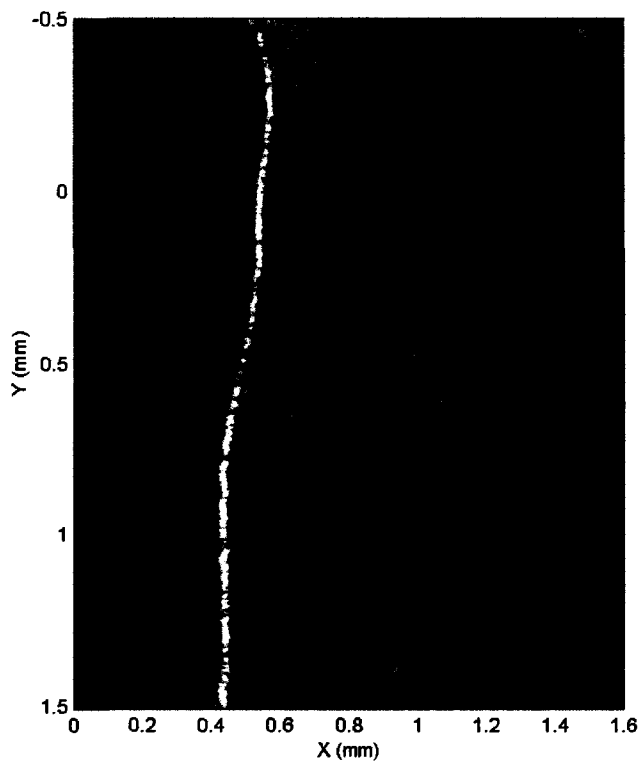


Fig. 2.20 OCT image of chicken heart with 1570 nm infrared source

Because this source is not filtered to reshape the spectrum to make it near Gaussian, the only way to remove the side lobes from the image is to apply the software deconvolution method. Fig. 2.21 shows an OCT image of a piece of sheep cerebellum: (a) the original image and (b) the image after software deconvolution. After the deconvolution, the image is greatly improved in terms of contrast and axial resolution. We can observe a small region (middle right side of the image) where the scattering coefficient is stronger compared with the rest region of the sample which looks pretty homogeneous.

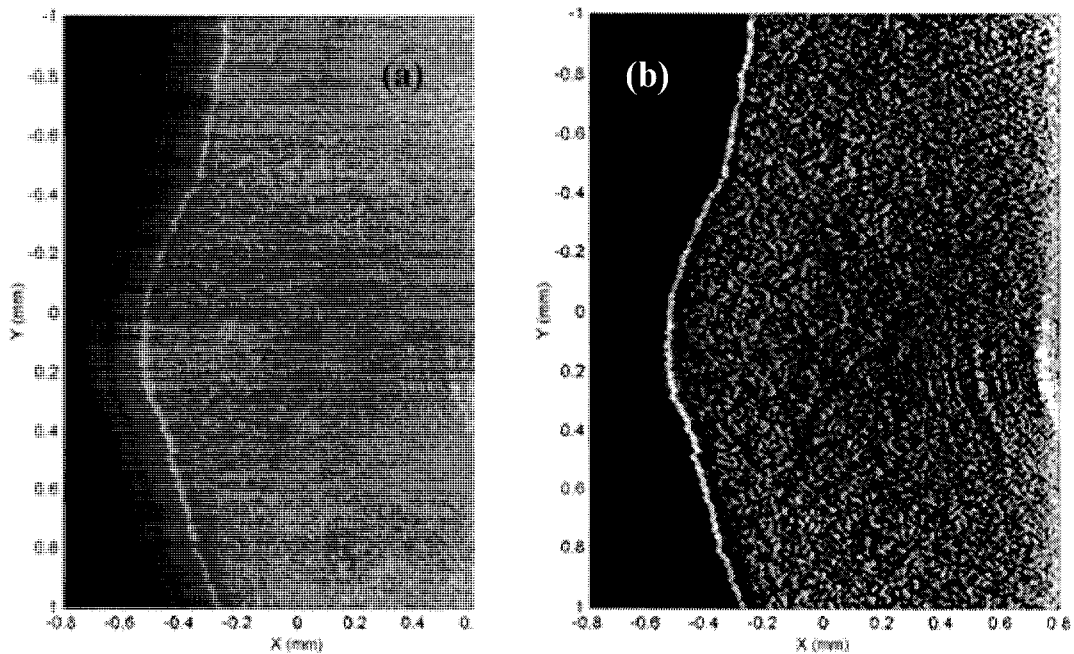


Fig. 2.21 OCT image of sheep cerebellum with 1570 nm infrared source. (a): original image. (b): after deconvolution.

Another sheep brain sample containing some clear structures was investigated with OCT and Fig. 2.22 shows the images. As in the previous figure, (a) is the original image and (b), the image after deconvolution. After deconvolution, the image is also much clearer and some structures which are dim in the original image become visible. The next sheep brain sample without specific structures shows that the material properties are totally homogenous. This is the most common material in the sample with good optical properties for OCT, namely less absorption and high scattering. Fig. 2.23 shows the results for this sample (a) without processing, and (b) after deconvolution.

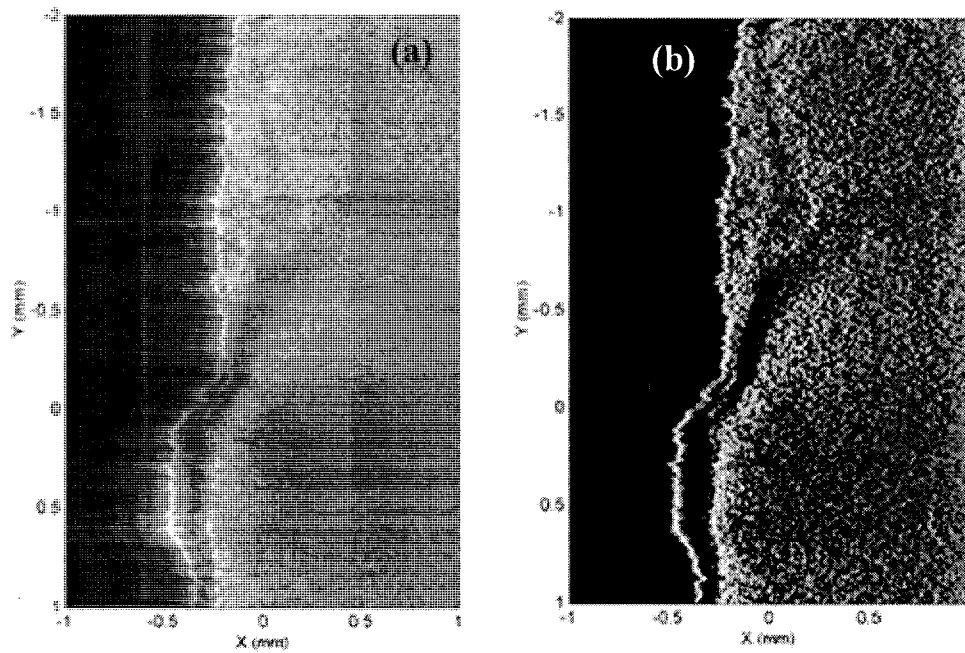


Fig. 2.22 OCT image of sheep brain sample with 1570 nm infrared source. (a): original image. (b): after deconvolution.

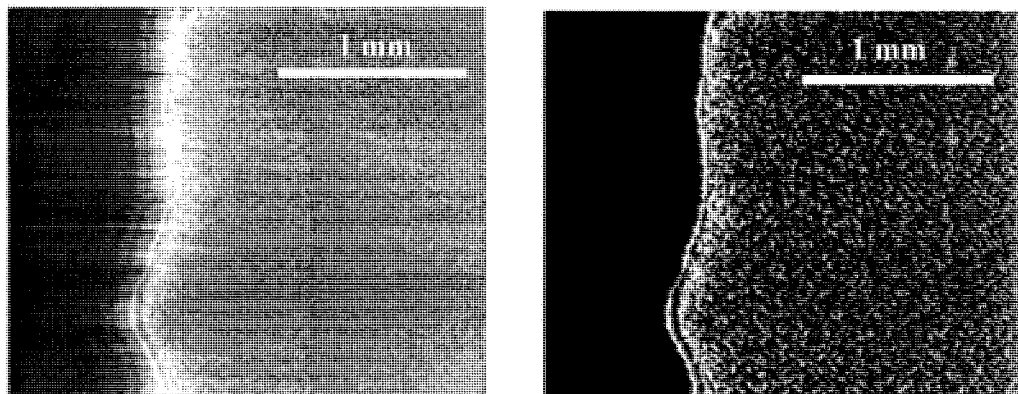


Fig. 2.23 OCT image of sheep brain sample without structure. (a): original image. (b): after deconvolution.

iv). Comparison of OCT images with three different sources

Given the importance of the source, we underlook a comparison. For the first time to our knowledge, images of the same in vitro samples were obtained with three different sources in

our laboratory. In order to limit the influence of the depth of field, we placed the samples in such a way that the focus was located in the middle of the A-scan. We also used the same optical power for each source, as well as the same ratio between the reference and the probe powers. On the top row of Fig. 2.24 we show images from a chicken heart ventricle wall. The bottom row shows a mouse earlobe profile. The images obtained at 1330 and 1570 nm have been treated by the deconvolution method in order to remove the sidelobes and thus improve image sharpness. For the image made with 810 nm Ti:sapphire laser, we present the original image since the deconvolution treatment does not provide any marked advantage.

From the chicken heart sample, we can distinguish two different regions in the depth profile. On the left, the image obtained with the Ti:Sapphire laser shows accurate details on the first layer (which is believed to be the endocardium) not only because the depth resolution is better than with the other sources, but also because the backscattering seems to be higher as well. Moreover, as expected from a semi-empirical law stating that scattering behaves as an inverse power of the wavelength [29], (backscattering decreases for higher wavelengths): we notice that the endocardium is less and less visible when wavelength increases. Despite the fact that absorption is supposed to be higher at 1330 and 1570 nm, the total loss is lower for higher wavelengths because the scattering contribution is more important. As a consequence, the penetration depth is higher for 1330 nm and 1570 nm, as seen on the images: the second layer on the heart images is emphasized at 1330 and 1570 nm, and the backscattered intensity is quite homogeneous over the whole mouse ear thickness for 1330 and 1570 nm, while it decreases with depth at 810 nm.

From the heart image, it is not obvious to claim that the penetration depth is higher at 1570 nm than at 1330 nm. However, as backscattering seems to be lower, we can conclude that absorption is higher at 1570 nm. From these images, we conclude that a source at 1330 nm gives the best results in terms of penetration depth and contrast.

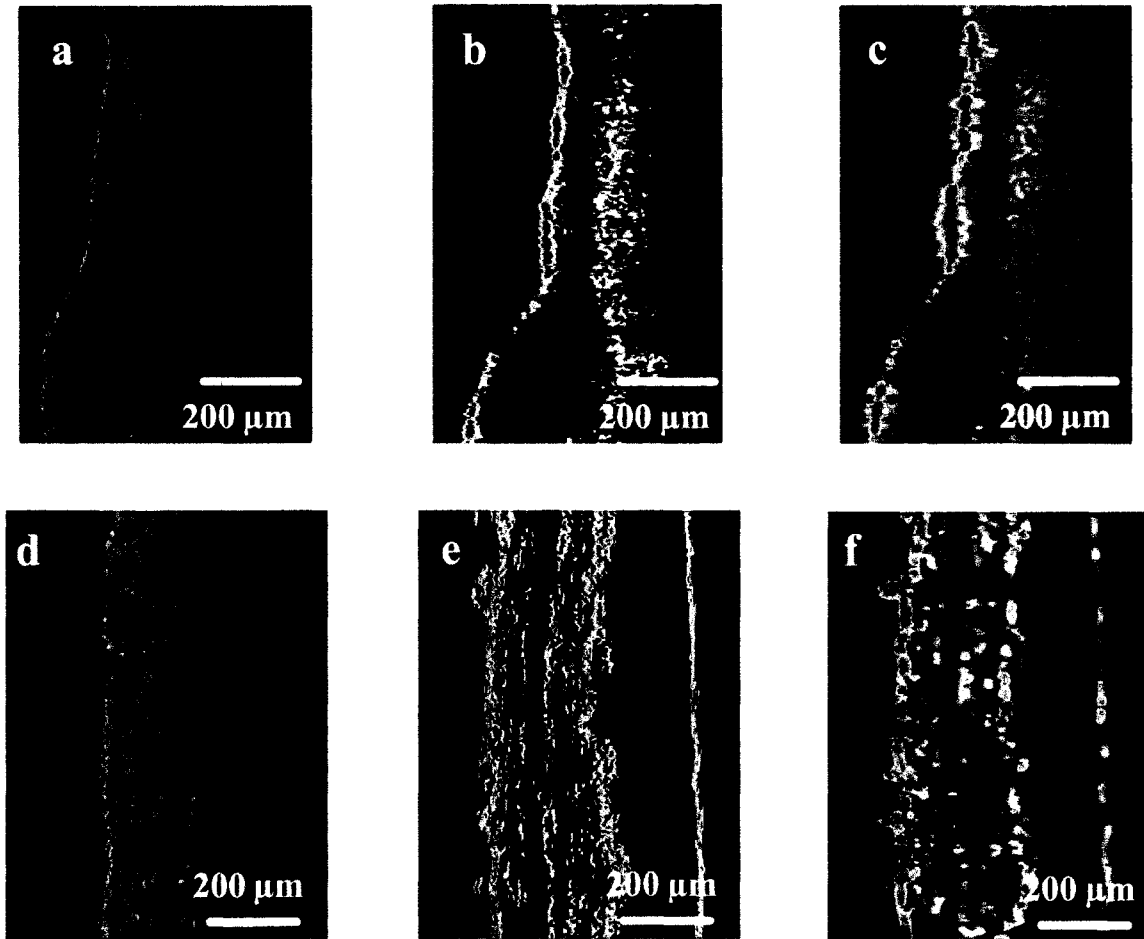


Fig. 2.24 OCT images of a chicken heart ventricle wall (top row) and mouse ear lobe (bottom row). From left to right, 810 nm Ti:Sapphire laser, 1330 nm broadband source, and 1570 nm SLD.

v). Measurements of attenuation and backscattering

In order to make the comparison concerning the OCT image made by three different sources more conclusive, some additional measurement of attenuation and backscattering were necessary. We have explained in chapter 1 that based on Eq. (1-11), the attenuation and backscattering coefficients can be obtained graphically.

To apply that graphical method, we need to extract the relevant parameters from the data acquisition of each A-scan. First, P_{in}^{meas} and P_{out}^{meas} can be read directly from the received

interference signal. R_{GS} and T_{GS} are obtained by comparing the OCT-measured optical thickness of a small chamber when it holds the tissue sample and when it is empty. The structure of the chamber is shown in Fig. 1.5, and the refractive index of glass n_G is assumed to be equal to 1.51. The refractive index of the tissue samples studied in this work n_S for each source was measured with the abovementioned method, and typical values between 1.39 and 1.42 have been obtained.

The parameters A_{in} and $A(z')$ in the formula are related to the fact that the probe beam is focused inside the sample. For that reason, the interference signal is weaker for in-depth cells that are far from focus, giving rise to a reduced OCT signal. This effect has been corrected by introducing the aperture-correction function $A(z')$, which is the ratio of the reduced OCT amplitude measured at a distance z' from the focus and the maximum OCT amplitude measured at the focus point, and A_{in} , which is that ratio at the position where the glass and tissue interface is located. Measurements were made for each source and are shown in Fig. 2.25.

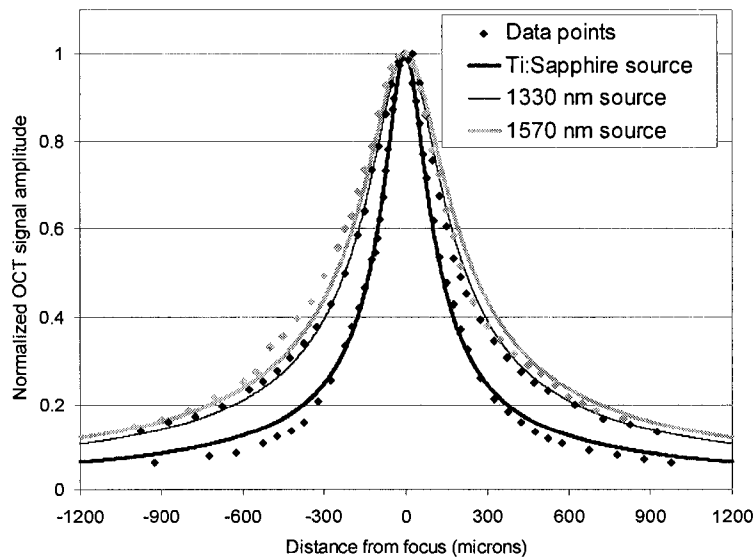


Fig. 2.25 Measured aperture function for the sources used in the experiment. Points are measured data while solid curves are fits with a Gaussian function.

Measurements of attenuation and backscattering were carried out on several in vitro tissue samples: chicken aorta intimal surface, myocardium surface, liver, and human epidermis in the finger end region. Each in-depth scan was repeated 5 times and averaged in order to substantially reduce electronic noise [30]. An example of an OCT scan performed on a chicken aorta wall with the Ti:Sapphire laser is shown in Fig. 2.26. We can see that the scan is easily fitted by a straight line for relatively shallow depths in the sample. As we go deeper into the sample, the curve slope tends to decay until $B(z')$ becomes a constant. The slope and offset of the straight line gives α_t and α_b , respectively.

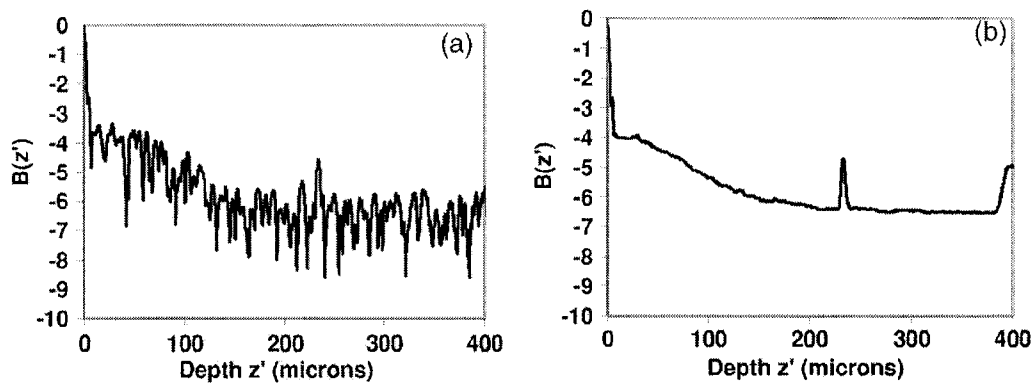


Fig. 2.26 Comparison of OCT profiles for a single in-depth scan (a) and for a spatially and temporally averaged in-depth scan (b). The peak in the middle of the scan is an artifact.

The attenuation and backscattering coefficients are given in table 2.1. Mean values are obtained from fitting the spatially and temporally averaged in-depth scans for each sample. Standard deviations are calculated based on statistics of the coefficients measured for each transverse point. For more visibility, we present the results on histograms in Fig. 2.27. It turns out that attenuation decreases for higher wavelengths. This is particularly true for skin, in which attenuation decreases continuously from 8 mm^{-1} at 810 nm down to 4 mm^{-1} at 1570 nm. For other samples, attenuation decreases abruptly between 810 nm and 1330 nm, but this trend is less pronounced between 1330 nm and 1570 nm.

Table 2.1. Optical coefficients of several samples measured by OCT with 810, 1330 and 1570 nm sources

Sample	Source	α_b (mm ⁻¹)	Standard deviation (mm ⁻¹)	α_t (mm ⁻¹)	Standard deviation (mm ⁻¹)
	810 nm	0.033	0.0073	9.13	0.99
Chicken aorta	1330 nm	0.0061	0.0021	6.13	1.59
	1570 nm	0.0063	0.0033	6	2.23
	810 nm	0.0039	0.0019	4.16	2.43
Chicken myocardium	1330 nm	0.0012	0.00074	2.10	2.09
	1570 nm	0.00097	0.00067	1.39	0.56
	810 nm	0.0135	0.0052	11.17	2.27
Chicken liver	1330 nm	0.0071	0.0037	2.1	0.13
	1570 nm	0.0015	0.00023	2.07	0.32
	810 nm	0.008	0.0036	8.12	2.27
Human skin	1330 nm	0.0025	0.0014	6.2	1.96
	1570 nm	0.0011	0.00071	3.9	2.68

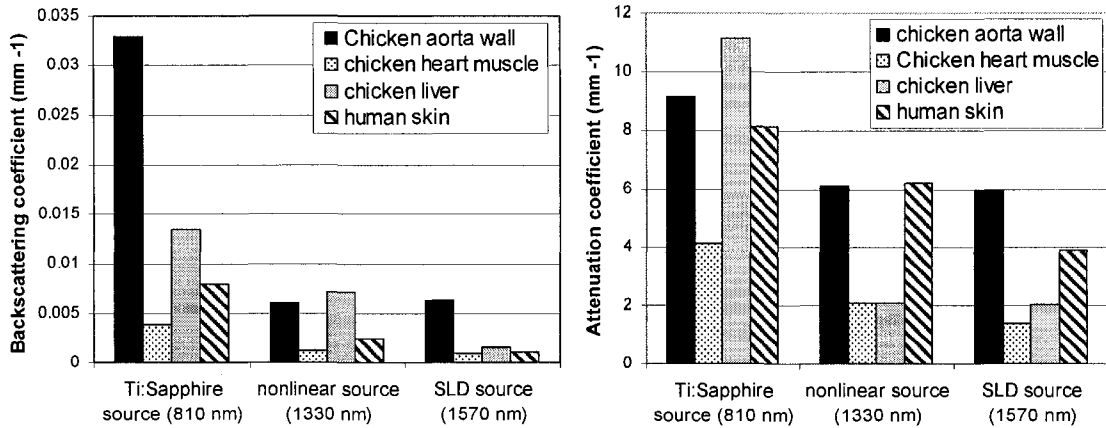


Fig. 2.27. Comparison of attenuation and backscattering coefficients of several samples measured by OCT with 810, 1330 and 1570 nm sources.

More surprising are the low backscattering values found for some samples. While the myocardium and the liver were known to be poor backscatterers, in the case of skin we measured backscattering coefficients one or two orders of magnitude lower than those found in a previous study [31]. The fact that we made in vitro measurements might be important in our case. For aorta samples, no precise measurements were found in the literature, but it has been shown that the anisotropy coefficient of arteries is usually close to 1 [32][14]. In other words, as most of the light is scattered forward, one should expect a weak backscattering coefficient for this sample. The general trend for backscattering confirms the decrease of scattering as a function of wavelength [33]. Nevertheless the decrease is not pronounced between 1330 and 1570 nm, especially for the myocardium and the aorta.

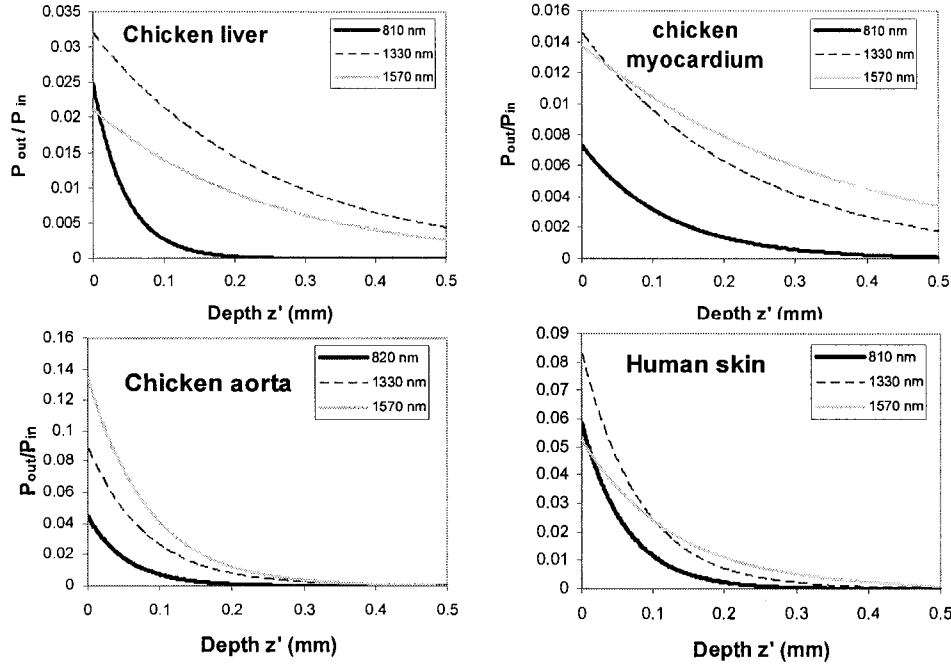


Fig. 2.28. Comparison of ratio of backscattered power over incident power as a function of depth for several samples at 810, 1330 and 1570 nm sources.

In order to get a better grasp of our source comparison, we reported the measured values of α_t and α_b in a simplified form of equation (1-11):

$$\frac{P_{out}(z')}{P_{in}} = \frac{l_c}{2} \cdot \alpha_b \cdot \exp(-2\alpha_t z') \cdot \frac{T_{GS}^2}{R_{GS}} \quad (2-4)$$

We neglected here the aperture effect as it mainly depends on the microscope objectives and thus can be modified independently from the source. For each sample, we compared in Fig. 2. 28 the behaviour for each source of the ratio P_{out}/P_{in} calculated from (2-4). The results show that the 1570 nm SLD source gives the best results for the myocardium and the aorta. For the liver and shallow depths in human skin, the 1330 nm broadband source gives the highest P_{out}/P_{in} ratio. The Ti:sapphire laser source is found to be best suited for OCT applications requiring high axial resolution, but suffers from poor penetration depth because

of its emission wavelength.

CHAPTER 3

An assessment of the Wigner distribution method in Doppler OCT

3.1 Introduction

Doppler OCT has raised much interest since it was first introduced in 1995 [1]. By analyzing the frequency content of the detected fringe intensity coming from the interference between the reference and target arms, Doppler OCT can yield precious information on the velocity of moving structures inside a sample. Therefore, the velocity distribution is simply calculated from the received frequency shift. Furthermore, since interference fringes can be observed only when the optical path lengths between the light backscattered from the sample and that from the reference arm are matched within the coherence length of the broad bandwidth light source, the A-scan can resolve the velocity profile along the scan. At each position of a scan, the detected velocity is the average of all the velocity components at that point within a small volume determined by the coherence length and focusing spot size. Since the dimension of this volume is quite small, roughly 10 μm in diameter, the number of scatterers is limited in the case of steady flow conditions. This property of the interferogram enable Doppler OCT to detect flow beneath the surface of a scattering sample [12]. Izatt et al [4] reported Doppler OCT images of bidirectional flow in biological tissues where the velocity was color coded to indicate the magnitude and the direction of flow. These early Doppler OCT experiments employed the short-time Fourier transform (STFT) to obtain the power spectrum from the temporal fringe intensity. The Doppler shift was then calculated by applying the centroid method to the spectrum.

A numbers of alternative implementations have been found to retrieve the frequency shift from the interferogram data. Each method has its own characteristics. For instance, the phase-resolved Doppler OCT technique deduces the structural and velocity images from the amplitude and phase information contained in the real and imaginary parts of the complex

signal [26, 34, 35]. The autocorrelation method appears to have certain advantages in terms of speed for real-time hardware implementations [17, 36] at the cost of less precise results. Our primary objective was to look for a high precision data processing method for Doppler OCT of a given interferogram obtained either via the time-domain or frequency domain approaches.

We are the first to propose the Wigner distribution method for Doppler OCT and by comparison with some other data processing methods, we will show that this method can provide more accurate instantaneous frequency and group delay values of the signal at a given time compared to STFT or the Hilbert transform methods. In our experiment, the fluid sample was a laminar flow in a rectilinear cylindrical tube using an intralipid solution.

3.2 Description of the commonly used methods in Doppler OCT

STFT

The simplest and the most commonly used time-frequency analysis approach is the short-time Fourier transform (STFT). The basic idea of the short-time Fourier transform is to divide the signal into small time segments (also called STFT windows), and apply a Fourier transform to each time segment in order to extract the frequencies that are present in that time interval. The window is then shifted to the next time segment in order to generate another local spectrum. The totality of such spectra provides the power distribution in the signal with respect to time and frequency simultaneously:

$$\text{STFT}(f, \tau) = \int y(t)w(t+\tau)e^{-j2\pi ft} dt \quad (3-1)$$

where $w(t+\tau)$ is a short time analysis window, f is the frequency, and $y(t)$ is the signal. In STFT, the spectral centroid method is frequently used for each window to obtain the first moment of the power spectrum f_c within each time segment.

$$f_c(\tau_i) = \frac{\sum_m f_m \text{STFT}(f_m, \tau_i)}{\sum_m \text{STFT}(f_m, \tau_i)}. \quad (3-2)$$

This centroid method employed for obtaining the Doppler frequency shift has been reported in many Doppler OCT papers [26, 37, 38]. The final flow velocity image is produced by displaying these first moments at each pixel.

However, the STFT method has several limitations. In particular, this method cannot attain high time and frequency resolution simultaneously. For instance, short time segments carry high time resolution, i.e. small time windows which contain a smaller number of sample points, but which give inaccurate frequency values. This is just another manifestation of the Heisenberg uncertainty relation applied classically.

The Hilbert method

The phase information of certain real-valued signals $s(t)$ can be derived from their analytic signals which can be built with the help of the Hilbert transform. This phase information is essential to extract the Doppler frequency shift of the signal and thus to determine the velocity of the flowing sample. The Hilbert transform of $s(t)$ has the effect of shifting the negative frequency components of $s(t)$ by 90° ($\pi / 2$ radians) and the positive frequency components by -90° . For example, the Hilbert transform of $\cos(t)$ is $\sin(t)$ and the full analytic signal of $\cos(t)$ is $\cos(t) + i \cdot \sin(t)$. By definition, the analytic signal $z(t)$ of $s(t)$ can be written as:

$$z(t) = s(t) + j \cdot \hat{s}(t) \quad (3-3)$$

where $\hat{s}(t)$ is the Hilbert transform of $s(t)$:

$$\hat{s}(t) = \frac{1}{\pi} \int_{-\infty}^{+\infty} \frac{s(t')}{t-t'} dt' \quad (3-4)$$

In detail, if we represent the Fourier transform of $s(t)$ as $S(\omega)$, we have:

$$S(\omega) = \frac{1}{\sqrt{2\pi}} \int_{-\infty}^{+\infty} s(t) e^{-j\omega t} dt \quad (3-5)$$

$S(\omega)$ has positive and negative frequencies. To obtain the complex signal, $z(t)$, whose spectrum is composed of the positive frequencies only, we take the inverse Fourier transform of $S(\omega)$ over the positive frequencies only:

$$\begin{aligned} z(t) &= \frac{2}{\sqrt{2\pi}} \int_0^{\infty} S(\omega) e^{j\omega t} d\omega \\ &= \frac{1}{\pi} \int_0^{\infty} \int_{-\infty}^{+\infty} s(t') e^{-j\omega t'} e^{j\omega t} dt' d\omega \\ &= \frac{1}{\pi} \int_0^{\infty} \int_{-\infty}^{+\infty} s(t') e^{j\omega(t-t')} dt' d\omega \end{aligned} \quad (3-6)$$

By applying $\int_0^{\infty} e^{j\omega x} d\omega = \pi \cdot \delta(x) + \frac{j}{x}$

We have:

$$\begin{aligned} z(t) &= \frac{1}{\pi} \int_{-\infty}^{\infty} s(t') \left[\pi \delta(t-t') + \frac{j}{t-t'} \right] dt' \\ &= s(t) + \frac{j}{\pi} \int_{-\infty}^{\infty} \frac{s(t')}{t-t'} dt' \\ &= s(t) + j \cdot \hat{s}(t) \end{aligned} \quad (3-7)$$

So, with the Hilbert transform, one can obtain the complex form of any real signal. This way, the phase information at each sample point becomes available. Once the phase of the signal is available, the instantaneous frequency of the signal can be obtained since the instantaneous frequency of the signal is the derivative of the phase.

Autocorrelation

If we consider an interferogram $s(t)$, its Fourier transform $S(\omega)$ yields the spectrum of

the signal. The energy density spectrum is defined as the intensity per unit frequency at frequency ω , which equals to $|S(\omega)|^2$. The Fourier transform of the energy density spectrum is defined as:

$$\begin{aligned}
 R(\tau) &= \int_{-\infty}^{+\infty} |S(\omega)|^2 e^{j\omega\tau} d\omega \\
 &= \iint S(\omega) e^{j\omega(t+\tau)} s^*(t) d\omega dt \\
 &= \int_{-\infty}^{+\infty} s^*(t) e^{j\omega\tau} s(t) dt \\
 &= \int_{-\infty}^{+\infty} s^*(t) s(t+\tau) dt
 \end{aligned} \tag{3-8}$$

where * represents the complex conjugate and for a real function, $s(t)^* = s(t)$. The function $R(\tau)$ which correlates the signal at two different times is the autocorrelation function at lag τ . The autocorrelation is the cross-correlation of a signal $s(t)$ with itself. It is used frequently in signal processing for analyzing functions or time series for determining the presence of a periodic signal buried in noise, or for identifying a frequency modulation encoded with a carrier frequency. Consider the interferogram written as an envelope and carrier:

$$\tilde{s}(t) = s(t) \cos(\omega t) \tag{3-9}$$

where ω is the instantaneous angular frequency of the carrier and t is time. By definition, the autocorrelation of the interferogram is the integral of the product of the interferogram with its delayed version:

$$\begin{aligned}
\tilde{R}(\tau) &= \int_{-\infty}^{\infty} \tilde{s}(t) \tilde{s}(t + \tau) dt \\
&= \int_{-\infty}^{\infty} s(t) \cos(\omega t) s(t + \tau) \cos(\omega t + \omega \tau) dt \\
&= \frac{1}{2} \int_{-\infty}^{\infty} s(t) s(t + \tau) [\cos(2\omega t + \omega \tau) + \cos(\omega \tau)] dt \quad (3-10) \\
&= \frac{1}{2} \int_{-\infty}^{\infty} s(t) s(t + \tau) \cos(\omega \tau) dt \\
&= \frac{1}{2} R(\tau) \cos(\omega \tau)
\end{aligned}$$

Hence, the phase modulation encoded in the carrier of the interferogram is identified with the carrier of the autocorrelation of the interferogram. Once the delay τ is selected, it stays constant. Furthermore, we can also make $R(\tau)$ constant by a normalization of the amplitude of the interferogram. Therefore, the autocorrelation reduces to a cosinusoidal function with the instantaneous frequency ω as the signal varies:

$$\tilde{R}(\tau) \propto \cos(\omega \tau) \quad (3-11)$$

Finally, the Doppler frequency shift f can be recovered by the following formula:

$$f = \frac{\arccos(\tilde{R}(\tau))}{2\pi\tau} \quad (3-12)$$

3.3 Description of the proposed Wigner distribution method

The recorded experimental interferogram appears as an optical power modulation with time or a variable chirp. Hence, the total signal can be seen as an energy distribution over two variables: time and frequency. The Wigner distribution provides such a description. The Wigner distribution of a signal $y(t)$ is defined as:

$$W(t, \omega) = \frac{1}{2\pi} \int y^* \left(t - \frac{1}{2}\tau\right) y \left(t + \frac{1}{2}\tau\right) e^{-j\omega\tau} d\tau. \quad (3-13)$$

Unlike the STFT which extracts the frequency information as a function of time by dividing the signal into many small time segments and Fourier analyzes each one of them, the Wigner distribution at a particular time t is determined by folding the left part of the signal over the right part and Fourier transforming the product. It is known that one of the advantages of the Wigner distribution over STFT is that one does not have to bother with the choice of a window [39]. In particular, the Wigner distribution is always real-valued. It preserves time and frequency shifts and it satisfies the following marginal distribution properties:

$$\int W(t, \omega) dt = |Y(\omega)|^2 \quad (3-14)$$

$$\int W(t, \omega) d\omega = |y(t)|^2, \quad (3-15)$$

where $Y(\omega)$ is the frequency energy distribution of the signal. This means that if we integrate the time-frequency energy density along one variable, we obtain the energy density corresponding to the other variable. We also need to keep in mind that the Wigner distribution suffers from some artifact causing the frequency spectra to broaden near the start and the end of the time interval. Also it is well known that the Wigner-Ville distribution produces artifacts, cross terms, when the frequency changes abruptly. To improve the signal-to-noise ratio of the Wigner distribution, a function $h(\tau)$ peaked around $\tau = 0$, has been introduced to define a pseudo Wigner distribution. This way, we make the Wigner distribution local for the purpose of emphasizing the signal around time t . The definition of the pseudo Wigner (PW) distribution is:

$$PW(t, \omega) = \frac{1}{2\pi} \int h(\tau) y^* \left(t - \frac{1}{2}\tau\right) y \left(t + \frac{1}{2}\tau\right) e^{-j\omega\tau} d\tau \quad (3-16)$$

The function $h(\tau)$ acts as a windowing operator and performs a frequency smoothing of the time-frequency analysis. As a consequence, the PW distribution improves the

signal-to-noise ratio of the Wigner distribution by attenuating the cross terms for multicomponent signals. This is because we have made the Wigner distribution local. On the other hand, the recover frequency width will be broadened due to this operation. From now on, we mean the pseudo Wigner method when we refer to the Wigner method.

3.4 Experimental setup

To put this approach to the test, we performed flow measurements with a Doppler OCT system which has been described in section 2.7 of chapter 2. In brief, this experimental setup is based on a fiber-optic Michelson interferometer which uses a superluminescent diode (SLD) as the low-coherence light source. This source is characterized by a central wavelength of $\lambda_0 = 1545$ nm and a bandwidth of $\Delta\lambda = 32$ nm. Light is focused onto the sample with a near-infrared, low-numerical aperture (0.25 N.A., 10X magnification) microscope objective in order to get a long depth of field. The sample and reference mirror scans are provided by motorized stages moving at a typical speed of 1.5 mm/s. In the sample arm, as shown in Fig. 3.1, a 1.4 mm inner-diameter glass capillary tube with a 1% intralipid in water solution flowing inside was fixed by the sample holder on an adjustable stage. The flow rate was adjusted by a controller and a pump. The angle between the probing beam and the flow direction was set to be 80° . The carrier frequency of the fringe signal was 1.94 kHz since the scan speed of the reference mirror was 1.5 mm/s. OCT images of the tube section were captured to extract the velocity profile. The mean flow velocity was set at 16 mm/s. As the Reynolds number is much less than the critical number, the flow was always laminar and therefore, the velocity profile in the circular tube was parabolic [27]:

$$V(r) = V_c \left[1 - \left(\frac{r}{d/2} \right)^2 \right]. \quad (3-17)$$

where $V(r)$ is the velocity at radial position r , V_c is the central peak velocity, and d is the

inner diameter of the tube.

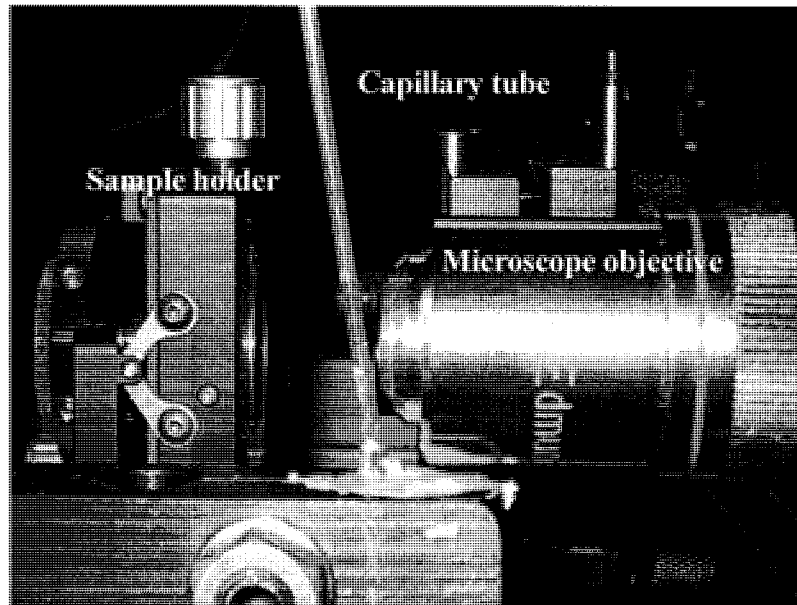


Fig. 3.1. Sample arm of the experimental setup for the Doppler frequency-shift measurements.

3.5 Results and discussion

The background of Fig. 3.2 shows the structural OCT image of a section of the capillary glass tube with intralipid flow described in the Doppler experimental setup in the previous section. The comparison of the data processing methods was based on a full A-scan Doppler OCT interferometric signal indicated by the white line on Fig. 3.2. Fig. 3.3 (a) shows the original signal at a sampling rate of 100 kHz. We first checked that the signal was symmetrical with reference to the zero amplitude axis. This important condition is ensured by the balanced detectors used for measuring the output signal from the OCT system. By dividing the interferogram by its local envelope, we obtained the normalized signal shown in Fig. 3.3 (b). We have verified that the normalization procedure has a negligible effect on the position of the zero crossing points which determine the frequency distribution.

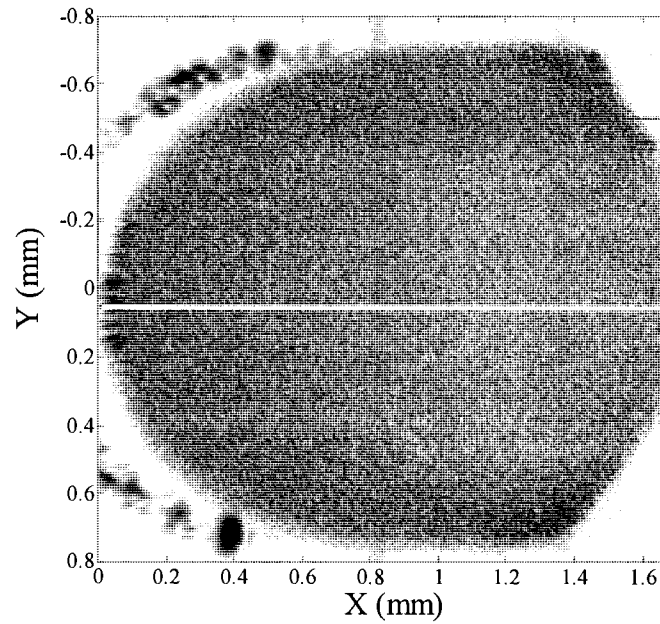


Fig. 3.2 OCT cross-sectional image of the tube. The white line indicates the A-scan that is studied afterwards in this thesis.

Based on the normalized signal of this A-scan, we compared the Wigner distribution method to the short-time Fourier transform method, the Hilbert-based phase-resolved method and the autocorrelation method. We will show that the pseudo Wigner-distribution signal processing method is overall more precise than other often-used methods in Doppler OCT for the analysis of cross-sectional velocity distributions.

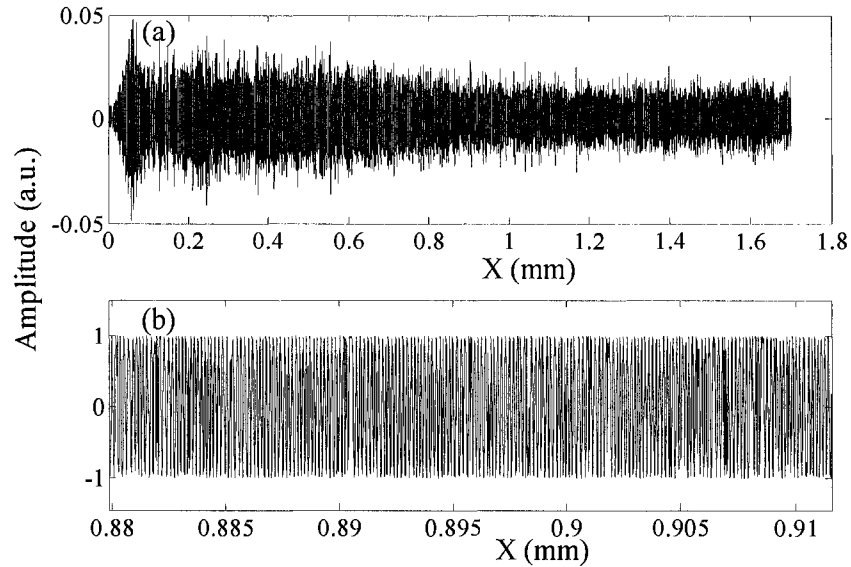


Fig. 3.3 (a) The original interferogram signal along the center of the tube and (b) the normalized data.

i). Comparison with STFT [40]

Many limitations of time-frequency analysis arise from the compromise between the spatial resolution and the velocity sensitivity. In a typical approach, the accuracy of the flow velocity calculated with STFT depends on the window size of the Fourier transform for each pixel.

The full A-scan Doppler OCT interferogram indicated by the white line on Fig. 3.3 has been submitted to both STFT and Wigner distribution methods. By zooming in onto the signal, we can see some details of the signal processing. Fig. 3.4 shows a small time span, from Fig. 3.2 (b), which includes 94 points of the data sampled at a rate of 100 kHz leading to a 10 μ s time interval between two points. A Hanning window function is used for apodization and the size of the window is chosen so as to contain 17 points which leads to a 0.17 ms time interval. Such an interval guarantees that each window contains at least one frequency cycle.

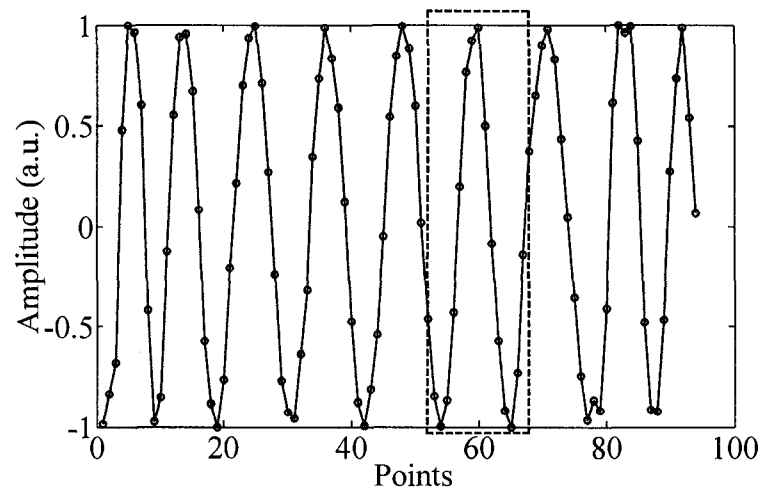


Fig. 3.4 Small segment of the detected signal at a 100 kHz sampling rate. The boxed region represents the STFT window size.

First, we submitted this 94 points signal to the STFT. A color-coded 3D time-frequency plot, as shown in Fig. 3.5, is produced as a first step. The frequency axis is limited by the Nyquist frequency which is half the sampling rate of 100 kHz. The illustrated local spectrum contains all the frequency components of the signal at each sampling point. In STFT, one usually performs the Fourier transform for each window. Although one could display the time-frequency distribution for each window, we show in Fig. 3.5 a «sliding-window» plot using the above Hanning window characteristics. Thus, a spectrum is generated at each sampling point. A Matlab function `specgram` [41] was employed to calculate the frequency content of the signal at different points in time. This function is based on the STFT algorithm. Here, we present the code for this procedure.

```
s=signal(59773:59866); % sampling the signal from the original
A=s./abs(hilbert(s)); % normalize this signal
% calculating the spectrogram of the signal
% using the 17 points length hanning window
[BFT,FFT,TFT]=specgram(A,1023,94,hanning(17),16);
```

```

%display the time-frequency 3D plot
imagesc(TFT,FFT,abs(BFT)) ;
colormap(jet);
xlabel('Time (ms)');
ylabel('Frequency (kHz)');

```

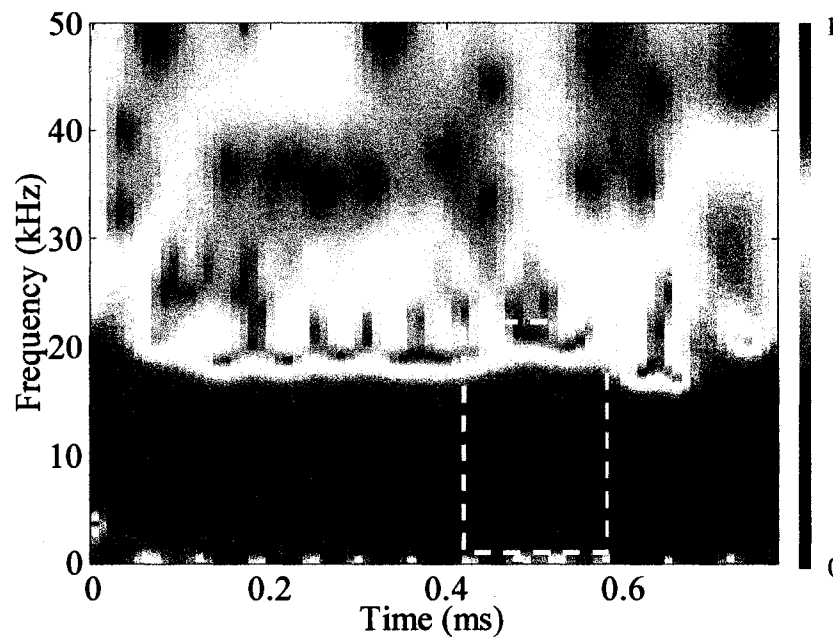


Fig. 3.5 STFT time-frequency distribution of the sample signal (color coded relative intensity).

In comparison, the Wigner distribution is capable of tracing locally this instantaneous frequency variation at each sampling point with a better resolution. The boxed region in Fig. 3.6 clearly shows the frequency variation with time. An advantage of the Wigner distribution over STFT is that the calculated bandwidth of the spectrum is more precise.

In Matlab, a time-frequency toolbox is available for the calculation of the Wigner distribution of time domain signals [41]. The code used for this procedure is presented below.

```

% using the 17 points length hanning window

```

```

[TFR,T,F]=tfrpwv(hilbert(A'),1:94,512,tfb_window(17,'hanning'),1);
F=100*F; % display frequency in kHz
T=0.01*T; % display time in ms
% display the time-frequency 3D plot
imagesc(T,F,TFR) ;
colormap(jet);
colorbar;
xlabel('Time (ms)');
ylabel('Frequency (kHz)');

```

Fig. 3.7 displays two frequency spectra calculated with the Wigner method at two specified time values (points No. 52 and No. 59 from the signal in Fig. 3.4) and compares them with the frequency distributions calculated by STFT over a window delimited by points 52 and 68.

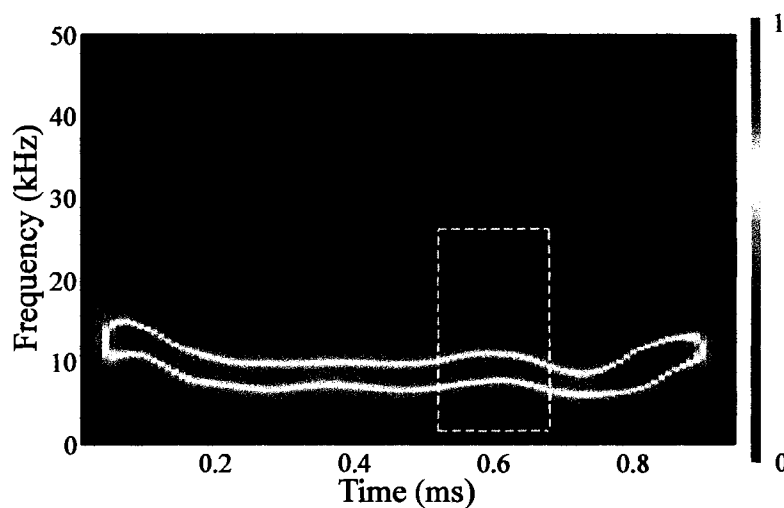


Fig. 3.6 Time-frequency distribution of the sample signal obtained with the Wigner distribution (color coded relative intensity).

The spectral bandwidths of the frequency plots using the Wigner distribution approach are significantly narrower than those calculated with STFT. Since one period contains

10 kHz. From the Wigner time-frequency distribution, the calculated frequencies at point 52 and 59 are 8767.1 and 9799.5 Hz respectively if we use the centroid method, while their maximum frequencies are 8708 and 9491.2 Hz, respectively. It seems to make sense that the maximum frequency is close to the frequency calculated by the centroid method for this particular Wigner distribution spectrum. However, while the maximum frequency from the STFT spectrum (9491.2 Hz) lies within the estimated frequency range, the frequency calculated from the centroid method is overestimated (11683 Hz).

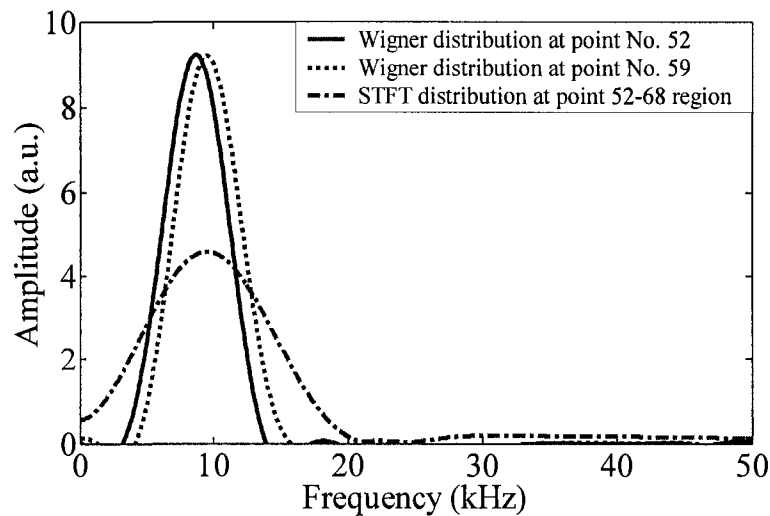


Fig. 3.7 Comparison of the frequency spectra calculated with two time-frequency methods.

Part of the broad bandwidth spectrum corresponds to negative frequency components. This part is not accounted for in the centroid calculation. Moreover, side lobes appear for higher frequency components. This arises as a consequence of the well known spectral leakage in STFT caused by a relatively short window function. While a more extended analysis could provide additional information, one should also account for spurious artifacts caused by distortions in the shape of the signal due to the low sampling rate and to speed fluctuations in the feedback-controlled motorized stage that drives the in-depth scan. Thus, unwanted frequency components appear in the recorded signal. This indicates that the calculated maximum frequency is more likely to give a better estimate of the real frequency

than the frequency calculated using centroid method. In Fig. 3.8 (b), the 55 spectra calculated with the Wigner method at each sampling point shown in Fig. 3.8 (a) have been plotted. This figure shows that the main problem with the Wigner method might lie as well with these side lobes appearing in the calculated spectra. These side lobes result in a systematic overestimation of the frequency calculated with the centroid method. Moreover, if we retain only the peak frequencies, the side lobes do not even contribute to the final results, leading to a better estimate of the frequencies in the signal. These spectra clearly show that the maximum frequency peaks all lie within a small range and give a reasonable approximation of the actual frequency. Therefore, as just shown, the maximum frequency method is much more adequate than the centroid method and will be used exclusively.

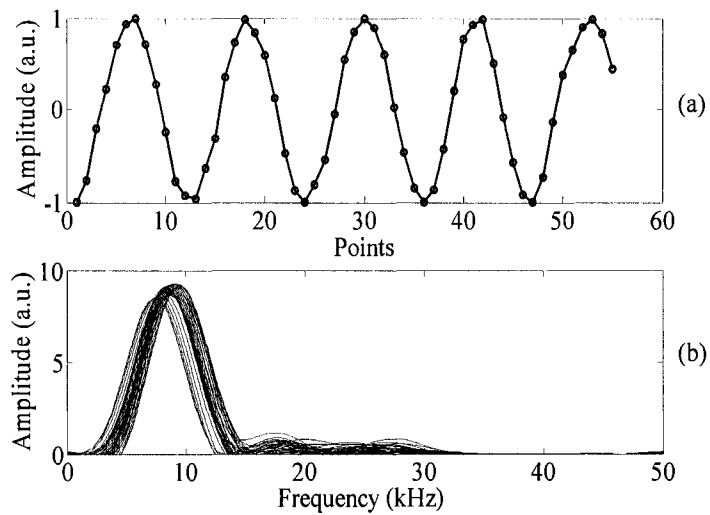


Fig. 3.8 Spectra calculated at each sampling point of the signal using the Wigner

ii). Other methods

For a more extended performance comparison [40], various methods were used for processing the data of the A-scan represented by the white line on Fig. 3.3. Our first consideration refers to the time-domain and spectral-domain OCT methods. In the latter case, the primary signal is the spectrum of the interferogram [19, 42]. An inverse Fourier

transform is used in spectral-domain OCT to obtain the interferogram which is the starting point for our digital signal processing comparison. It is well known that the spectral-domain OCT usually gives a better SNR over time-domain OCT and should be advantageous for weak signals. In our case, this difference is mitigated by the fact that we use normalized interferograms for the phase determination.

Our comparison will be done on four phase detection methods: the Wigner distribution method, the phase-resolved method, the autocorrelation method, and STFT. Their principles have been reviewed in the previous section. As can be surmised from the literature [34, 35], in most cases, the phase-resolved method consists in obtaining the phase from the corresponding analytic signal via the Hilbert transform. We will therefore refer to this class of phase-resolved methods as the Hilbert transform method. The autocorrelation method is borrowed from ultrasound Doppler techniques which has been used as another phase detection technique [17, 36]. This method appears to have certain advantages in terms of speed for real-time hardware implementations. Nevertheless, if the velocity range is too large, this method introduces ring features that must be dealt with. Also the delay inherent to this method must be chosen appropriately.

As mentioned previously, we have chosen to compare the various methods on a similar platform singling out the signal processing aspects to the exclusion of other features in order to discover how they compare relatively to the theoretical result, at least in the present capillary tube experiment. Again, in a spirit of increased commonality, we have used the Matlab Time-Frequency Toolbox [41] in all cases, keeping in mind that the comparison bears not so much on the speed of execution of this or that algorithm but on the precision that is eventually achieved.

iii). Methodology and results

In Fig. 3.9, we illustrate a block diagram of the algorithm used in this comparison of different data processing methods. Our analysis starts with the normalized interferogram data. The objective is to obtain the time-frequency two-dimensional (2-D) scatter plots which we fit to a parabola after noise filtering which is the velocity profile in a tube with laminar flow.

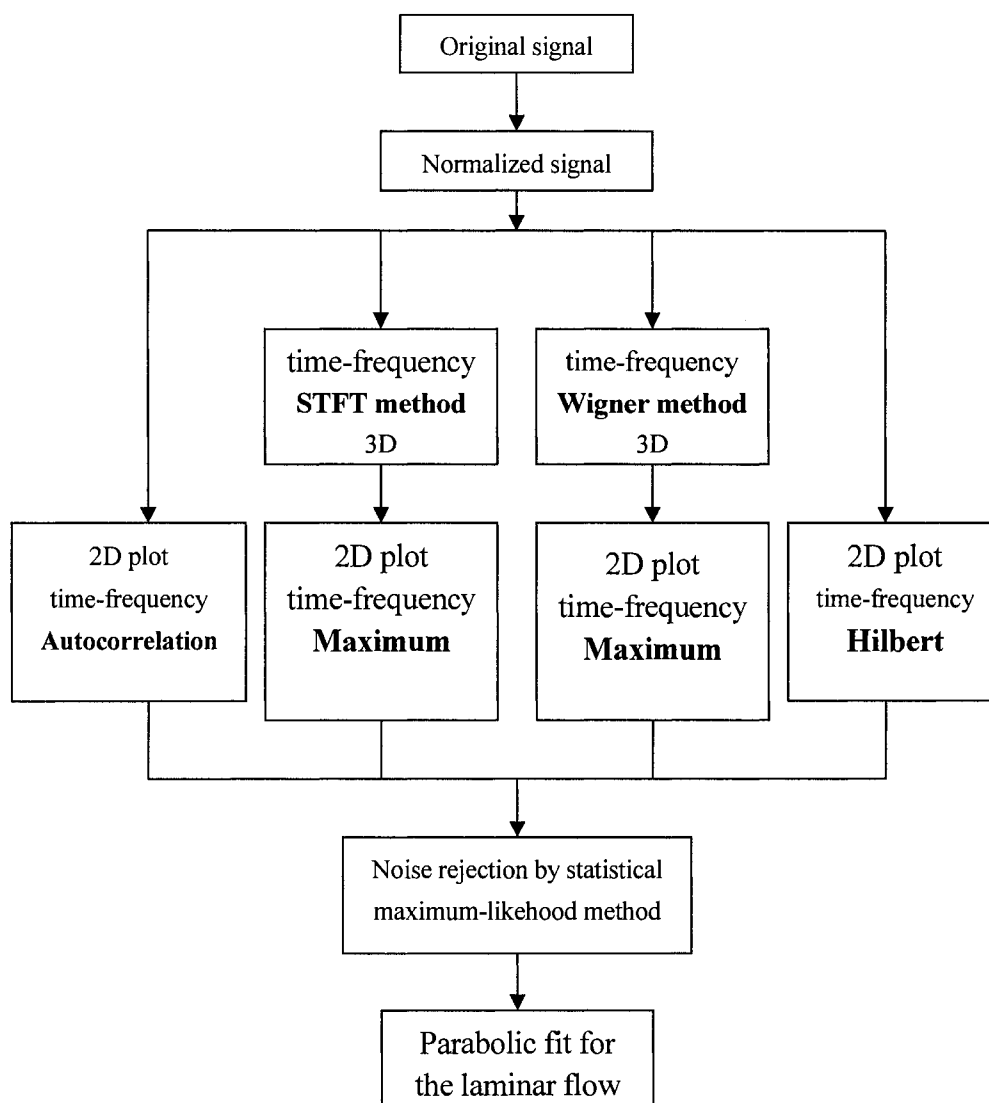


Fig. 3.9 Block diagram of the algorithm used in the comparison.

In the case of STFT, we produce the 3D time-frequency plot as a first step. We obtain then a 2D time-frequency plot by choosing the maximum frequency of the frequency distribution at each temporal sample point, as illustrated in Fig. 3.10 (black dots). As explained in the previous section, the peak frequencies of the spectrum at each sampling point give the best estimate of the local frequency of the signal. Since the received Doppler frequency information is quite noisy, further filtering is necessary. We use a statistical maximum-likelihood method to process the data. The essence of the procedure is to generate a histogram of the frequencies found within a given (short) time span. The data outside a FWHM (full width at half maximum) of the histogram for that time span are considered to be noise and are discarded since we assume that at least for a laminar flow across the tube, the frequency variation should be smooth and only dependent on the speed [43]. Hence, the complete A-scan data are divided into several time segments, each of which related to a time duration of 5 ms. Within one time segment, the histogram was built in 500 Hz steps ranging from 0 to 50 kHz. The white trace in Fig. 3.10 corresponds to the data remaining after the filtering procedure. We present the computer code for the data processing for this step in Appendix A.

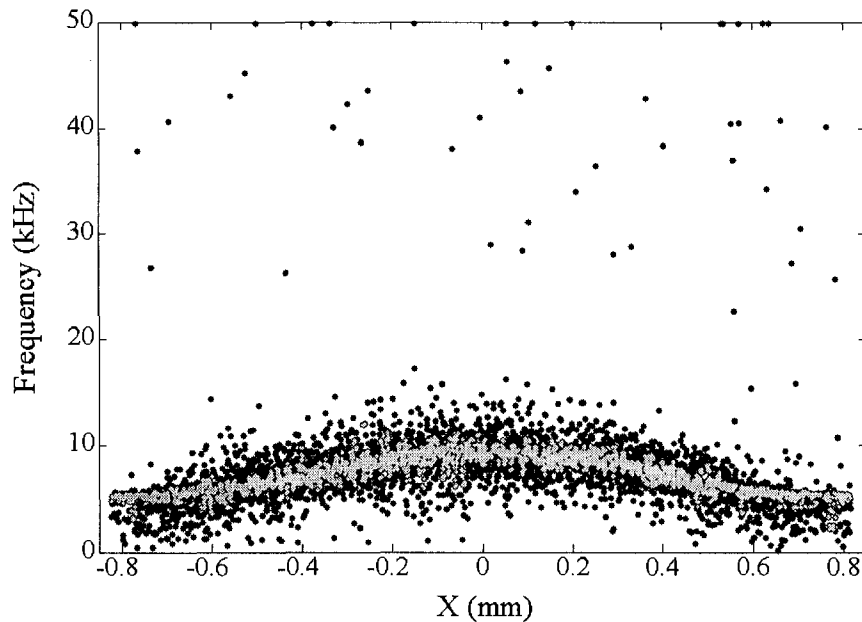


Fig. 3.10 Two-dimensional frequency distribution of the signal using the STFT method. The black dots indicate the maximum frequency values of the spectra at each measured point while the white trace corresponds to the filtered frequency distribution.

In the case of the Wigner method, as in STFT, we produce the 3D time-frequency plot as a first step and then, we obtain a 2D time-frequency plot by choosing the maximum frequency of the frequency distribution at each temporal sample point, as illustrated in Fig. 3.11 (black dots). The same noise rejection procedure as the one described previously for the STFT method is applied to the signal. The white trace in Fig. 3.11 shows the sampling points remaining after the procedure. We present the computer code for the data processing for this step in Appendix B.

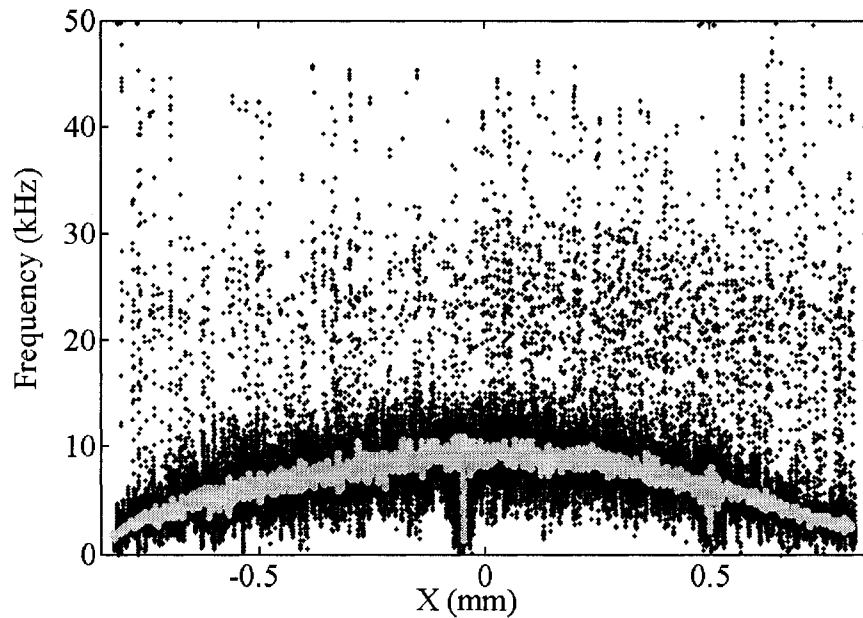


Fig. 3.11. Two-dimensional frequency distribution of the signal using the Wigner method. The black dots indicate the maximum frequency values of the spectra at each measured point while the white trace corresponds to the filtered frequency distribution.

In the case of the Hilbert phase-resolved method, the phase and frequency are obtained from the quadrature components such that we can produce the 2D time-frequency distribution directly at each temporal sample point, as illustrated in Fig. 3.12 (black dots). The same noise rejection procedure as the one described previously for the STFT and Wigner methods is applied next to the signal. The white trace in Fig. 3.12 shows the sampling points remaining after the procedure. We present the computer code for the data processing for this step in Appendix C.

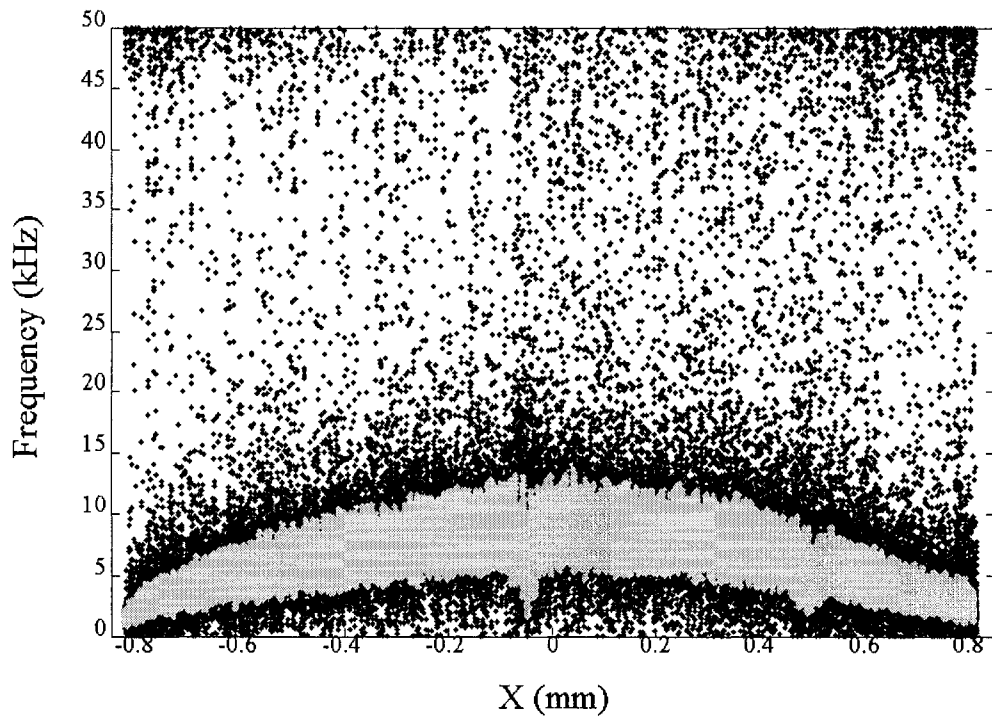


Fig. 3.12. Two-dimensional frequency distribution of the signal using the Hilbert method. The black dots indicate the raw frequencies at each measured point. The white trace corresponds to the filtered frequency distribution.

For the autocorrelation method, the flow diagram of [36] is reproduced with a Matlab simulation. What is believed to be the best delay was chosen in that particular case. The 2-D time-frequency scatter plots are produced, (black dots in Fig. 3.13), and then processed by the same noise filtering procedure, (white trace in the same figure). We present the computer code for the data processing of the autocorrelation method in Appendix D.

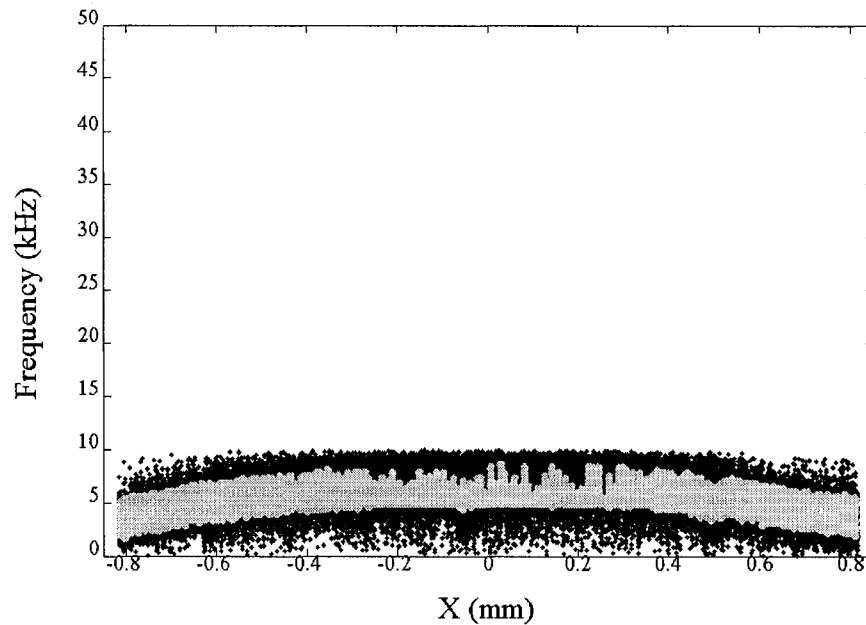


Fig. 3.13. Two-dimensional frequency distribution of the signal by the autocorrelation method. The black dots indicate the raw frequencies and the white trace shows the resulting frequency distribution after noise rejection.

The processed data, (white traces in the previous figures), are finally fitted to the two parameter parabola given in Eq. 3-17. The velocity at the wall of the capillary tube is left floating. That means our fits were done varying both the maximum velocity V_c and the diameter of the tube d which is therefore determined experimentally. The results are plotted in Fig. 3.14. The uncertainties shown on the plots come from the error on the determination of the position of the interface between the fluid and the tube wall. The curve pertaining to the autocorrelation method was obtained for a delay corresponding to 0.05 msec for data sampled at a rate of 100 kHz which gave the best result for that method.

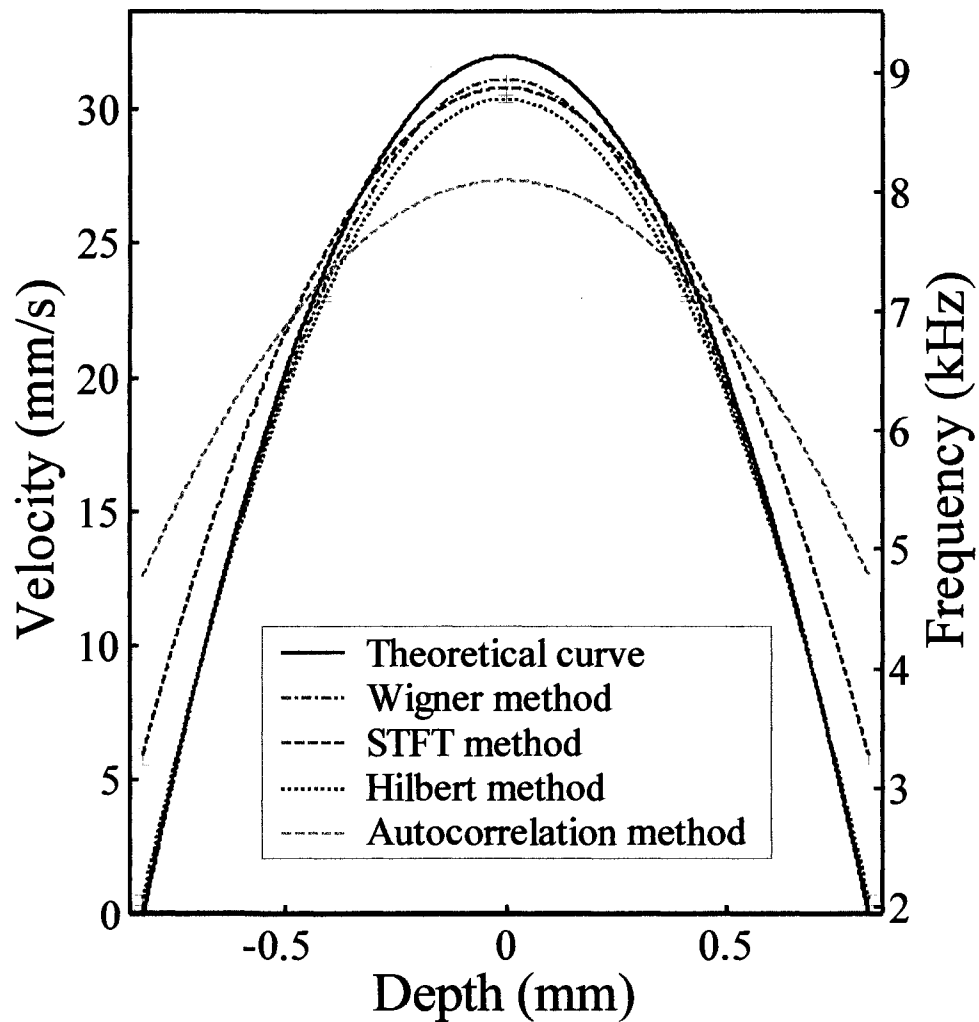


Fig. 3.14 Computed flow profiles using a quadratic fit.

The maximum values of the curves give the central peak velocity V_c . This parameter was calculated for each method and was then reported in Table 3.1. In Fig. 3.14, a theoretical flow profile is also shown. This curve was obtained by repeating several measurements of the mean flow inside the tube with the help of a flowmeter. Assuming a laminar flow model, a theoretical value of V_c was then deduced by multiplying the mean velocity by a factor 2. The theoretical flow profile is then plotted by inserting V_c into Eq. 3-17. Following our investigation, it appears that the Wigner distribution method offers the best precision overall at this stage. Near the maximum, the Wigner and STFT methods are close but for low

velocities, the STFT method overestimates the theoretical result substantially. The phase-resolved Hilbert method gives good results for low velocities but appears to be slightly inferior at higher velocities. Finally, the autocorrelation method is definitely not so good even though we phase-unwrapped a secondary ring in our analysis.

Table 3.1. Main parameters of the plots in Fig. 3.14

	V_c (mm/s)	+/- (mm/s)
Theoretical result	32	
Wigner distribution with maximum method	31.16	0.17
STFT with maximum method	30.84	0.36
Hilbert method	30.41	0.24
Autocorrelation method	27.40	

iv). Discussion.

The main conclusion is therefore that the Wigner method should be preferred. In spite of a great deal of research, the Wigner distribution method remains somewhat unfamiliar. We can list a few important features taken from the abundant literature, for instance [39, 44]. The Wigner-Ville transform has several advantageous properties for the time-frequency analysis of nonstationary signals. It has a bilinear form and is compatible with linear filtering and modulation. One can get the instantaneous frequency, the spectral density, the instantaneous power and group delay by computing moments. It provides a real-valued representation. The Wigner function gives the clearest picture of the instantaneous frequency and group delay.

The pseudo Wigner distribution is a smoothed version of it. Nevertheless while the conditional averages are exactly the instantaneous frequency and group delay, the pseudo Wigner distribution loses this characteristic. This distribution is known to suffer from artifacts in form of cross-terms especially when the frequencies change abruptly. For instance, the observed artifacts of a broadening of the spectra at both ends of Fig. 3.6 result from the onset and ending of the computation which can be assimilated to an abrupt frequency change. Furthermore, it is often perceived that the discrete Wigner distribution as a time-frequency spectral estimator is computationally intensive. In fact, the Wigner distribution can be done with an FFT network half the size of the one needed to perform a standard STFT [45][19]. In [46], it is stated that the pseudo Wigner distribution can be computed with a complexity of $\frac{1}{2}M(\log_2 M + 4)$ where M is the length of the window. This is of the same order of magnitude as STFT. Finally in another paper [47], it was shown that the Wigner transform is 37.5% faster than the Fourier transform while having the similar accuracy and noise sensitivity for signals with high SNR. The Hilbert transform requires $2n\log(n) + n$ complexity operations where n is the number of samples per A-line as stated in [48]. For fast real-time applications, the Hilbert method with hardware in-phase and quadrature demodulation and Kasai autocorrelation over several A-scans [48] appears to offer the best tradeoff at the present time with a slight disadvantage on precision.

In spite of its merits, the Wigner transform method is still some what computationally intensive. For that reason, we sought a better method which is the topic of the next chapter.

CHAPTER 4

A zero-crossing detection method applied to Doppler OCT

4.1 Introduction

In the previous chapter, we have introduced a novel data processing method, the Wigner distribution method, for DOCT which can provide a precise frequency estimation based on the time domain OCT (TDOCT). In this chapter, we propose yet another novel and simple software zero-crossing detection method for the data processing in time-domain Doppler OCT [49]. This algorithm is based on the detection of the points where the recorded amplitudes of the signal reach their zero values, and calculates the frequencies from the intervals between the zero-crossing points. The main advantage of the algorithm is that it provides the Doppler frequency estimate with both accuracy and ease.

In general, a signal under study may be subjected to distortion and amplitude and frequency fluctuations induced by noise. Hence, for applications where precise Doppler-speed metrology is essential, the emphasis is on sensitivity to noise, accuracy, and a wide dynamic range in velocity. This is true for a number of applications such as microfluidics and ex-vivo experiments where the sweep rate is less important than accuracy on the velocity. The performance of the proposed zero-crossing method has been compared to other techniques in this context. As a benchmark, we will pay special attention to the pseudo-Wigner method since this method was found to be the most accurate so far [40]. Nevertheless other methods (such as the Hilbert transform method) will be considered as well because of their widespread use. For our investigation, we take experimental data and perform the signal processing comparison numerically off-line putting aside hardware considerations or particular implementations in an attempt to provide as much as possible a balanced comparison. As an example, the approach is tested by providing the Doppler-OCT velocity distribution of a laminar flow in a rectilinear cylindrical tube using the scattering

data obtained from an intralipid solution.

Zero-crossing (ZC) methods and algorithms have been applied in various fields such as signal and image processing [50], optics [51], biomedical engineering [52] and fluid mechanics [53]. Indeed, zero-crossing detectors were often used for Doppler flow velocity measurements in both laser Doppler velocimetry [54] and ultrasound Doppler velocimetry [55]. In the case of ultrasound Doppler velocimetry, the hardware detectors provide a sharp pulse that matches very closely the zero-crossing voltage of the primary signal. The frequency response is then obtained by counting the number of pulses over a certain period of time (typically several tens of ms). Initially, the wide dynamic range and relative simplicity of hardware implementation made these detectors very attractive for applications such as blood flow measurements [56]. This technique can be shown to be adequate for simple periodic signals. Nonetheless, in these applications, the received signal is the superposition of composite Doppler signals induced by the presence of many scatterers with different velocities present in an extended volume of the sample. Under the assumption that there is no phase relation between the different scatterers, it has been shown that the output frequency from the zero-crossing detector is the root mean square frequency of the signal [57]. Thus, in the case of wide and complex frequency spectra (for instance in the regions of turbulent flow), the zero-crossing detector only gives a rough approximation of the mean frequency [58, 59]. Furthermore the various noise sources cannot be separated out and may strongly corrupt the results. For these reasons, software methods based on the computation of the complete power spectrum gradually replaced the ZC detectors and other more precise approaches such as the Fast Fourier Transform [60] were preferred.

In the case of laser Doppler velocimetry, software and hardware implementations of zero-crossing counting were also developed. Like the ultrasound Doppler velocimetry counterpart, the signal results from a superposition of many Doppler signals originating from

scatterers of different velocities found in an extended sample volume. In this case, the zero-crossing method is based on measuring the time elapsed between each successive zero-crossing point. Researchers have applied a method which is based on the statistical properties of the zero crossing intervals to obtain the complete Doppler frequency spectrum [61]. It appears that this method works only for low SNRs and low depths of field [62].

Nevertheless, the fact that the zero-crossing method is deemed suitable for DOCT applications relies on the fact that this technique provides an excellent performance when processing simple periodic signals. In the case of laminar flows, the local OCT interference signal is almost a single periodic waveform since the local Doppler frequency spectrum is so narrow because the OCT signal within a small time interval relates to the flow of the scatterers that are located within a minute volume. We believe that the relative simplicity of the spectral content of such signals is crucial to the use of the zero-crossing approach in Doppler OCT. The situation for non-laminar flow remains to be investigated. Here, we show that, as far as precision is concerned, the zero-crossing (ZC) method outperforms the Wigner method in general, and hence all other existing signal processing methods in time-domain Doppler OCT. The main reason is that, because in Doppler OCT we obtain the spatially (or temporally) resolved frequency shifts from strongly localized scatterers (to first order), much of the drawbacks observed in laser velocimetry applications of the zero-crossing method are strongly mitigated.

In this chapter, we will pay special attention to accuracy and ease of implementation in the Doppler velocity determination. The main goal is therefore to show that the zero-crossing algorithm applied to the data processing of the Doppler OCT signal provides the best estimate so far of the Doppler frequency with an acceptable spatial resolution in the «textbook» case of the laminar flow in a rectilinear tube which we used as a phantom. In our view, one of the main reason the zero-crossing method gives better results is that it is

essentially local giving the instantaneous frequency accurately at a given time whereas the other methods are non-local since they involve integrals or mathematical transforms (Fourier, Wigner, and Hilbert) which need to probe the data over an extended range even if windowing is used. It is here that the time-domain implementation of OCT shows its real advantage.

4.2. Principles

As mentioned previously, the zero-crossing method works well for singly periodic waveform. Fortunately, the Doppler OCT signal in our case fits this condition because the local OCT interferogram is almost singly periodic. In this case, the 2D time-frequency plot can be obtained directly by calculating the half-period $\Delta t = (t_z)_{N+1} - (t_z)_N$ between two consecutive zero-crossing points $(t_z)_N$ and $(t_z)_{N+1}$ as shown in Fig. 4.1. We assume that within two such points, the instantaneous frequency of the signal F can be taken to be constant and equal to the inverse of twice the half-period Δt :

$$F = \frac{1}{2 \cdot \Delta t} \quad (4-1)$$

The zero-crossing points t_z are calculated by finding all the pairs of adjacent signal values S_1 and S_2 that have opposite signs. If the sampling instants are t_1 and t_2 , then the zero-crossing time t_z is determined by a simple linear triangulation formula as illustrated in Fig. 4.1:

$$t_z = t_1 + \tau \left/ \left(1 + \frac{S_1}{S_2} \right) \right. \quad (4-2)$$

where τ is the sampling rate.

In contrast to the Wigner method, the time resolution of which is determined by the sampling rate only, this zero-crossing method has two factors that may reduce its

time-frequency resolution, as inferred from Fig. 4.1. The first one is the uncertainty δF that arises from the sampling of the signal. Because of the phase and frequency variations inherent to the OCT signal, the actual zero-crossing point may be located anywhere between the points S_1 and S_2 , even though there is a strong probability that it lies near the point determined by Eq. (4-2). The error on the half-period is:

$$\delta(\Delta t) = 2\tau \quad (4-3)$$

The relative error on the frequency is then:

$$\delta F/F = \delta(\Delta t)/\Delta t = 4\tau F \quad (4-4)$$

The other factor that reduces the time-frequency resolution is the spatial resolution δx in the axial direction of the A-scan. As the frequency can only be calculated at zero-crossing points of the signal along the axial direction, δx is determined by the distance between two consecutive zero-crossing points:

$$\delta x = \Delta t \cdot nV_{\text{scan}} \quad (4-5)$$

where V_{scan} is the speed of the axial scan, and n is the index of refraction of the sample. In order to avoid confusion with the spatial resolution of the structural OCT image, δx is called the effective sampling parameter of the frequency. From Eq. (4-1), we then obtain:

$$\delta x = nV_{\text{scan}}/2F \quad (4-6)$$

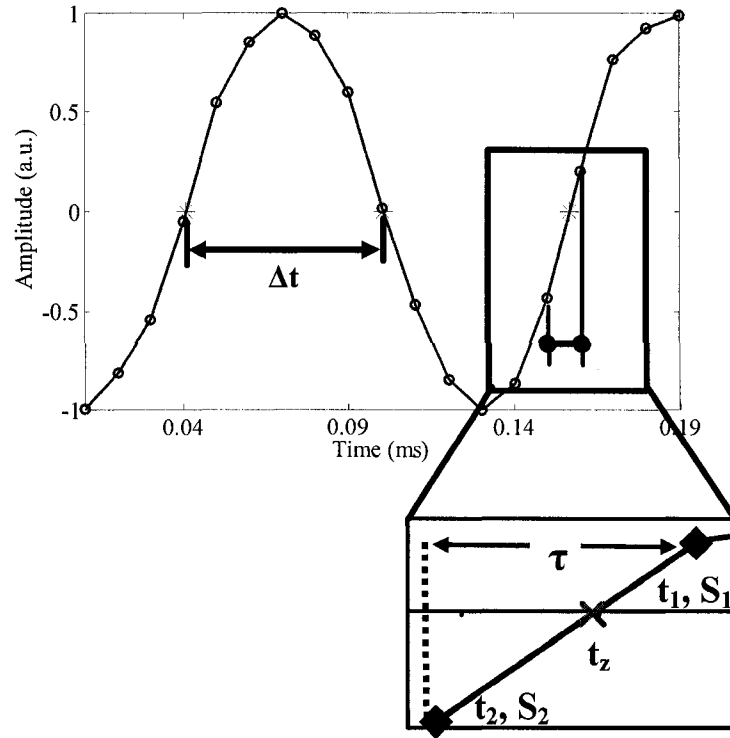


Fig. 4.1 A sample signal used to calculate the zero-crossing points (red cross) and the defined time durations.

Thus, for a fixed sampling rate (i.e. for fixed τ) and fixed axial scan speed, Eqs. (4-3) and (4-5) reveal a tradeoff between effective sampling and relative error on frequency that depends only on the flow velocity. In other words, when the frequency of the signal under measurement is very low (i.e. for a long wavelength optical source and low flow velocities), the large separation between two consecutive zero-crossing points leads to a less precise localization on the spatial velocity map. On the other hand, there will be more sampling points per half-period leading to a better velocity precision expressed by $\delta F/F$. In the case of high frequency signals (i.e. for a short wavelength optical source and high flow velocities), the velocity map will display a higher effective sampling of the velocity while the velocity precision will be less due to a lower number of sampling points per half-period.

To illustrate this point, the effective sampling parameter and the frequency precision

were calculated in the case of an ad-hoc A-scan signal containing different Doppler frequency components from 2 to 10 kHz obtained at a fixed sampling rate of 100 kHz and for an axial scan speed of $V_{\text{scan}} = 1.5$ mm/s. The results are shown in Fig. 4.2. We see that a combination of limited frequency precision and limited effective sampling is obtained for intermediate frequencies (around 5 kHz). In that case, a typical effective sampling parameter of $0.2 \mu\text{m}$ is combined with a frequency precision of 20 %. At first sight, a further increase of the measured Doppler frequency would decrease its relative precision (higher $\delta F/F$). Nevertheless, when this precision becomes too poor, (i.e. the number of data points per half-period is too low) the measurement of the half-period is too coarse. In that case, the frequency measurement is done by counting several zero-crossing points over a time range that is large enough to collect a sufficient number of data points. As a consequence, the frequency precision becomes better at the expense of a poorer effective sampling. Anyway, in our experiment, we are far from this case because the data sampling rate is one order of magnitude higher than the maximal average measured frequency.

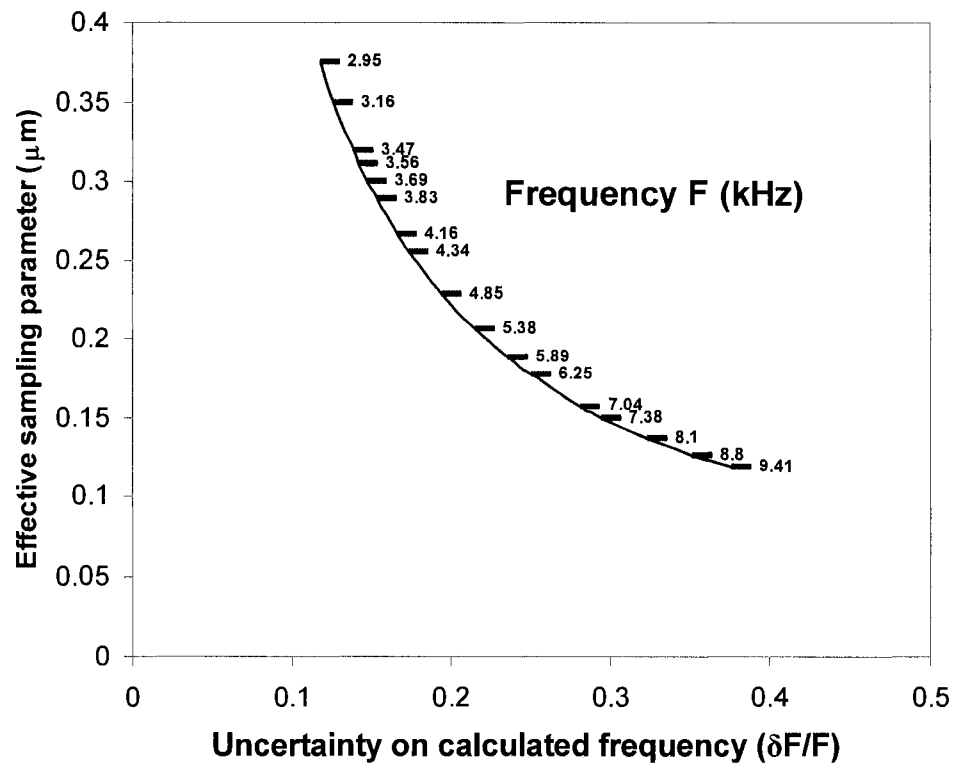


Fig. 4.2 Effective sampling parameter of map velocity and precision of calculated frequency as a function of Doppler frequency F.

In a nutshell, the zero-crossing method processes data by dividing the signal into variable length time windows, each of which is bordered by consecutive zero-crossing points. The duration of each time window is determined and taken to be one half the local period. The frequency of this time window is then calculated as the inverse of the period. After that, the window is shifted to the next time segment in order to generate another local frequency. Apart from accuracy considerations discussed previously, this method leads to a computational time saving based on a measurement of the execution time to process the data for an A-scan. We obtained 48.9 seconds for the pseudo-Wigner method and 1.876 second for the zero-crossing method which is a gain factor of 26 in speed (Matlab run using a PC equipped with an Intel Pentium IV, 2.6 GHz processor, 1 GB of RAM). There are two reasons for this. First, no integral or convolution needs to be calculated and the arithmetic

operations involved within each time step remain simple. Also, the calculations are performed only on a subset of all the data points, namely at the positions where the signal amplitudes are equal to zero, but this feature leads to a lower-density spatial grid for the velocity map, as explained previously.

4.3. Experimental setup

The proposed zero-crossing method has been tested with the experimental conditions described in the previous chapter. The source used is a superluminescent diode characterized by a central wavelength of $\lambda_0 = 1545$ nm and a bandwidth of $\Delta\lambda = 32$ nm. In that experiment, the sample is a 1.4 mm inner-diameter glass capillary tube with a 1% intralipid in water solution flowing inside. The angle between the probing beam and the flow direction was 80° . The carrier frequency of the fringe signal was 1.94 kHz since the scan speed of the reference mirror was 1.5 mm/s. OCT images of the tube section were captured to obtain the velocity profile. The mean flow velocity was set at 16 mm/s. As the Reynolds number is much less than the critical number, the flow was always laminar and therefore, the velocity profile in the circular tube was parabolic:

$$V(r) = V_c \left[1 - \left(\frac{r}{d/2} \right)^2 \right] \quad (4-7)$$

Here $V(r)$ is the velocity at radial position r , V_c is the central peak velocity, and d is the inner diameter of the tube.

4.4. Results and discussion

4.4.1 Comparison with the Wigner method

Let us select a single A-scan taken along the center of the tube (the white line shown in Fig. 3.3) to illustrate the procedure. Figure 4.3(a) shows the original interferogram signal at a

sampling rate of 100 kHz. We first checked that the signal was symmetrical with reference to the zero amplitude axis. This important condition is ensured by the balanced detectors used for measuring the output signal from the OCT system. By dividing the interferogram by its local envelope, we obtained the normalized signal shown in Fig. 4.3(b). We have verified that the normalization procedure has a negligible effect on the position of the zero crossing points which determine the frequency distribution.

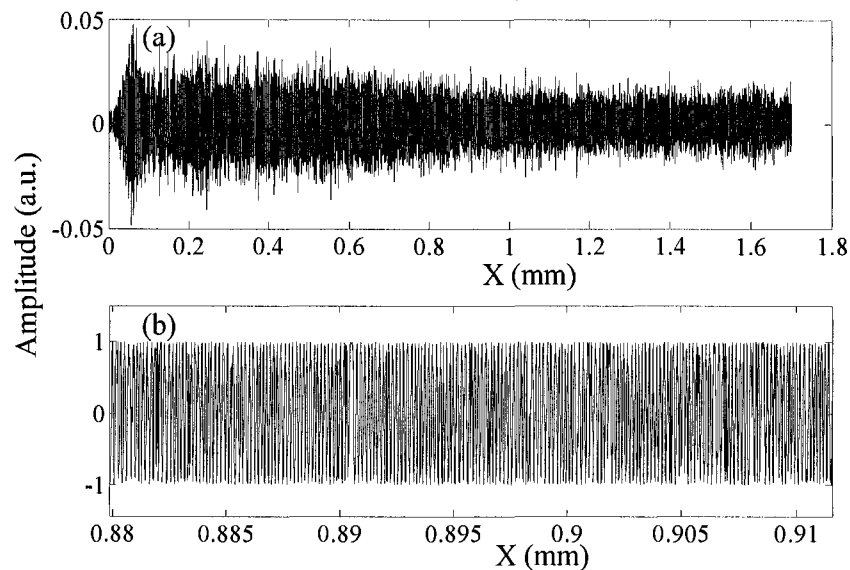


Fig. 4.3. (a). The original interferogram along the center of the tube and (b) the normalized data.

First, we submit this signal to the Wigner method and a color-coded 3D time-frequency plot, as shown in Fig. 4.4, is produced as a first step. The frequency axis is limited by the Nyquist frequency which is half the sampling rate of 100 kHz. A local, broad-bandwidth spectrum containing all the frequency components of the signal at each sampling point is obtained. In Chapter 3, we have concluded that the peak frequencies of the spectrum at each sampling point give the best estimate of the local frequency of the signal at that moment. Therefore, a 2D time-frequency plot can be produced by choosing the maximum frequency of the frequency distribution at each temporal sample point. Then, we perform the statistical maximum-likelihood method to process the data until the noise signal has been washed out,

as shown in Fig. 3.11.

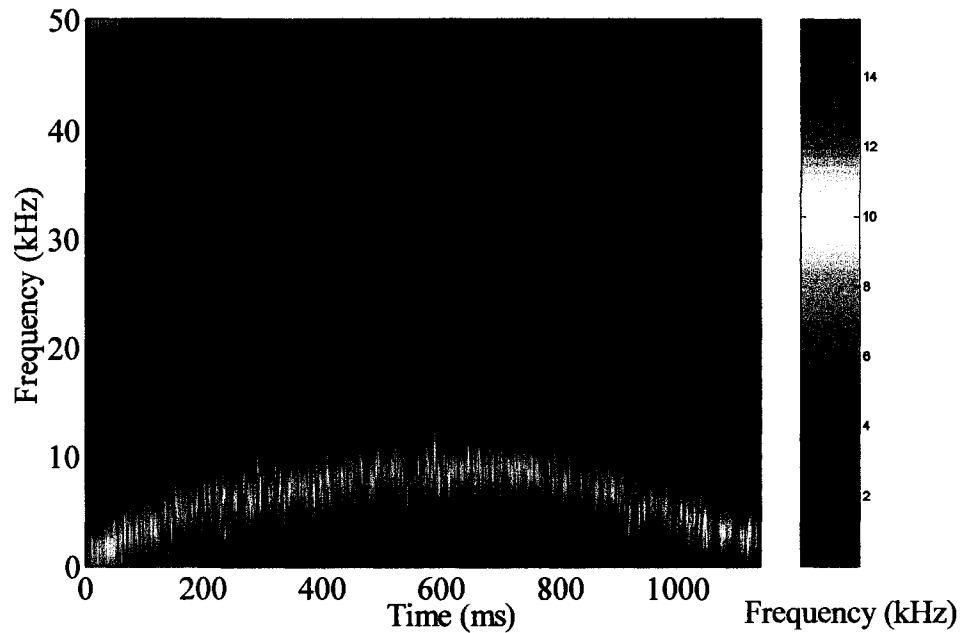


Fig. 4.4. Color-coded 3D time-frequency distribution of the signal along the center of the tube using the Wigner method.

The next step implements the zero-crossing method. Fig. 4.5 provides an example of zero-crossing points (indicated by stars) calculated over a small part of the normalized signal shown in Fig. 4.3. We zoom-in on 94 points of data sampled at a rate of 100 kHz leading to a $10 \mu\text{s}$ time interval between two points. We now assess the performance of the zero-crossing method by comparing its results with those provided by the Wigner method. In Fig. 4.6, we display the calculated instantaneous frequency of the signal shown in Fig. 4.5 using both the Wigner and the zero-crossing methods. The blue points indicate the instantaneous peak frequencies of the local spectra calculated using the Wigner method. The stars in Fig. 4.6 correspond to the local frequencies obtained by the zero-crossing method. Each resulting local frequency is positioned in the middle of the time interval between two adjacent zero-crossing points.

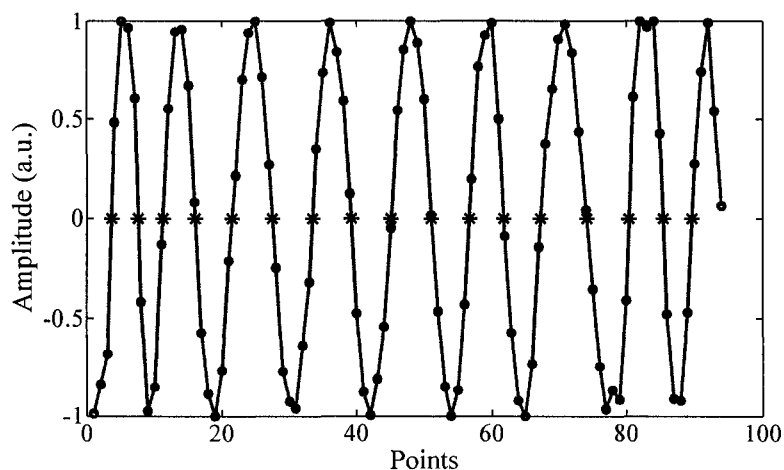


Fig. 4.5. Small segment of the detected signal at a 100 kHz sampling rate. The stars indicate the zero-crossing points.

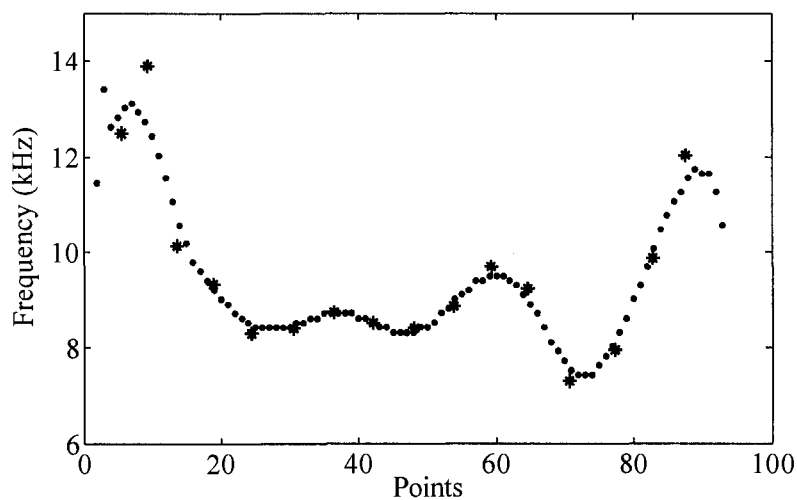


Fig. 4.6 Comparison of Wigner and zero-crossing time-frequency distributions of the sample signal of Fig. 4.5. The points correspond to the Wigner method using the maximum values of the local spectra. The stars come from the zero-crossing method.

As we can see in Fig. 4.6, the results given by the Wigner and the zero-crossing methods match rather well except at the ends of the plot because the Wigner distribution is known to

suffer from artifacts brought by cross-terms especially when the frequencies change abruptly. Since we show truncated data on this plot, the observed discrepancy at both ends of the plot results from the onset and ending of the computation which can be assimilated to an abrupt frequency change. The Wigner method has the distinct advantage of a higher effective sampling locally. In contrast, the zero-crossing method produces only 16 data points and does not need a Fourier transform at each data point. As said before, the processing time is extremely short. Both methods are capable of tracing locally the instantaneous frequency variation with an acceptable spatial resolution when the full data set is considered. The zero-crossing method is sparser but follows the instantaneous frequency of a signal arguably as well as the Wigner method and is potentially better for abrupt velocity changes. Note that the Wigner method also requires the intermediate processing steps of getting the local frequency distribution and finding the local maximum of that distribution.

Now, we apply the zero-crossing method to the full normalized A-scan data set. The 2D frequency distribution of the signal can be obtained directly by this method as shown in Fig. 4.7 (black dots). The same noise rejection procedure as the one described previously for the Wigner method is applied next to the signal. The white trace in Fig. 4.7 shows the sampling points remaining after the procedure.

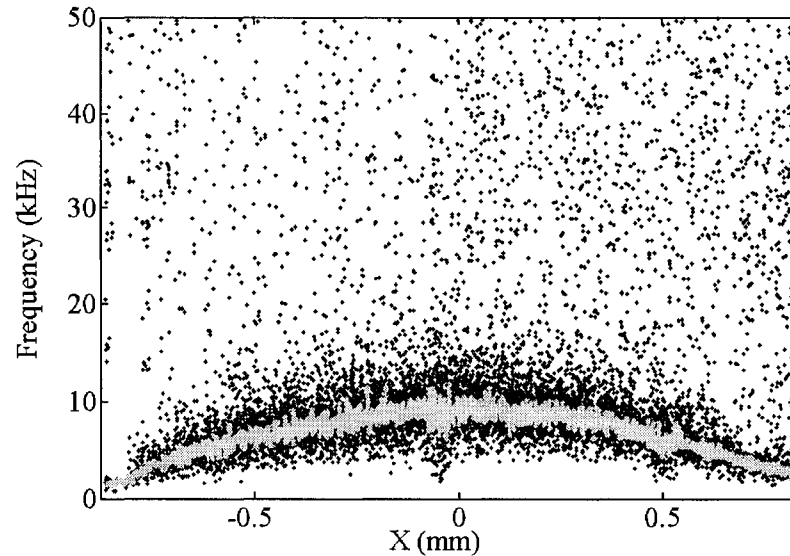


Fig. 4.7 Two-dimensional frequency distribution of the signal by the zero-crossing method. The black dots indicate the obtained frequencies and the white trace shows the resulting frequency distribution after noise rejection.

We present the computer code for the data processing with Wigner method in Appendix E.

4.4.2 Other methods

For a more extended performance comparison, another widespread method was also used for processing the same data of the A-scan. As mentioned in the previous chapter, the Wigner method was found to be the most precise up until then, and the next best method appeared to be the phase-resolved Hilbert distribution method. We have therefore chosen to compare these two processing methods with the zero-crossing method using a common platform based only on the signal processing aspects to the exclusion of other features in order to discover how well they compared with the theoretical result, at least in the present capillary tube experiment.

4.4.3 Methodology and results

Our analysis starts with the normalized interferogram data presented in Fig. 4.3 (b). The time-frequency two-dimensional (2-D) scatter plots are obtained for the Wigner and zero-crossing methods and are then noise-filtered using the procedure described previously. In the case of the Hilbert phase-resolved method, the phase and frequency are obtained from the quadrature components. The resulting data points are finally fitted to a parabola based on Eq. (4-7) using the two parameters V_c and d , which means that the velocity at the wall of the capillary tube is left floating. The results are plotted in Fig. 4.8. The flow velocity information is finally deduced from the frequency shift via Eq. (1-8). The uncertainty shown on the plots comes from the error on the determination of the position of the interface between the fluid and the tube wall.

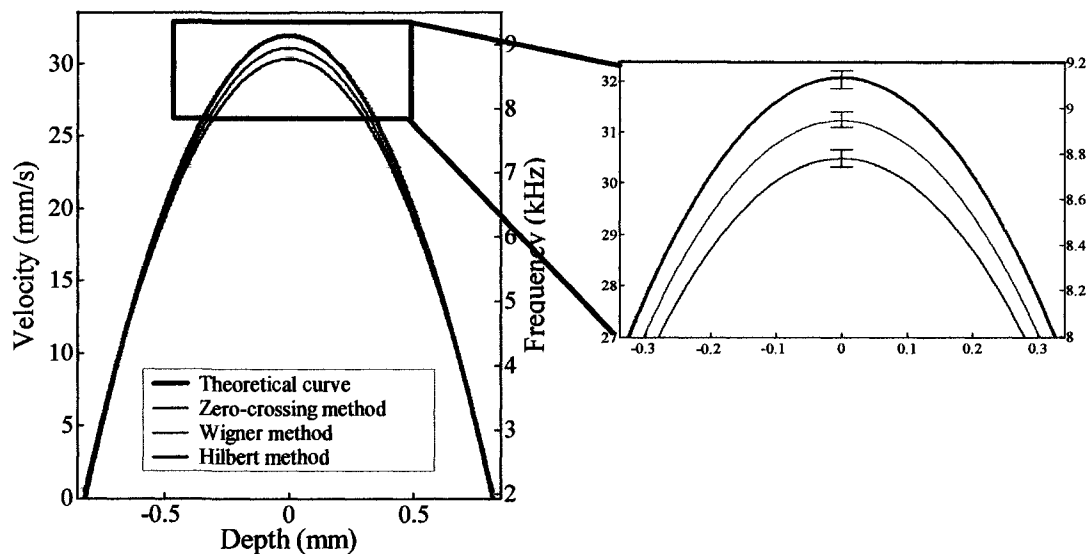


Fig. 4.8. Computed flow profiles using a quadratic fit.

The maximum values of the curves give the central peak velocity V_c . In Fig. 4.8, a theoretical flow profile is also shown. This curve was obtained by repeating several measurements of the mean flow inside the tube with the help of a flowmeter. Assuming a

laminar flow model, a theoretical value of V_c was then deduced by multiplying the mean velocity by a factor 2. The theoretical flow profile is then plotted by inserting V_c into Eq. (4-7).

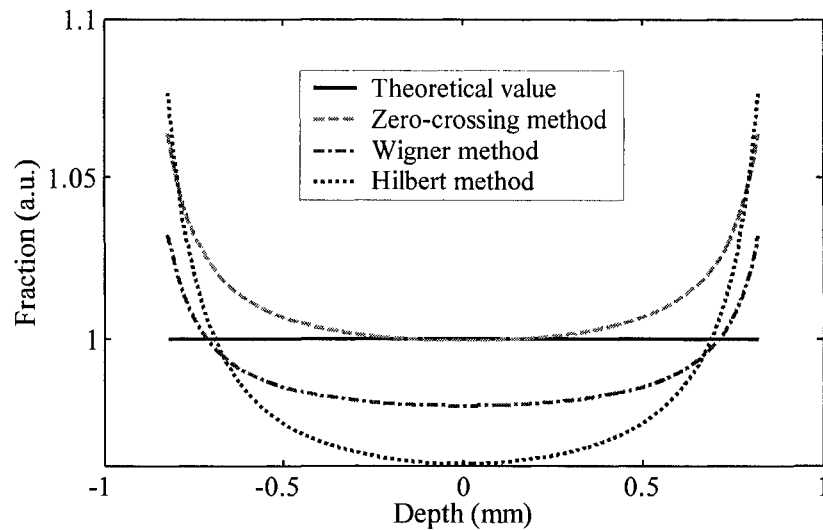


Fig. 4.9 Comparison of the deviations of the three methods from the theoretical results.

From our investigation, these three methods give results in the same range and match the theoretical curve more or less accurately. At the zoomed scale on Fig. 4.8, the zero-crossing method appears to fit the theoretical curve almost perfectly. A more detailed comparison is necessary and has been illustrated in Fig. 4.9. The deviations of these methods from the theoretical result are shown. It appears that the zero-crossing method is the one that offers the best precision overall except in a very limited region close to the tube wall. The Wigner method appears to be the next best one. It is less precise in the higher velocity region though, but it is slightly better for low velocities. Finally, the phase-resolved Hilbert method appears to be less accurate.

The comparison of the data processing methods was then extended to a full 2D-OCT profile. The gray-scale background of Fig. 4.10 shows the OCT image of a section of the capillary glass tube with intralipid flow described in the experimental setup.

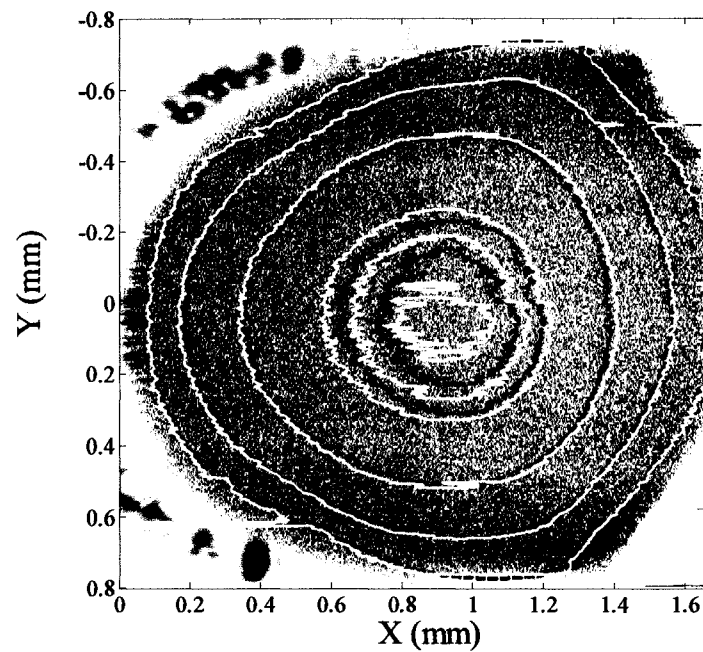


Fig. 4.10 OCT image of the tube profile. The superimposed contour plots correspond to the frequencies calculated using experimental values and the Pseudo-Wigner method (black solid curves). The white curves indicate the calculated frequencies using the zero-crossing method. The white curve near the center of the tube is the contour at 9 kHz given only by zero-cross method.

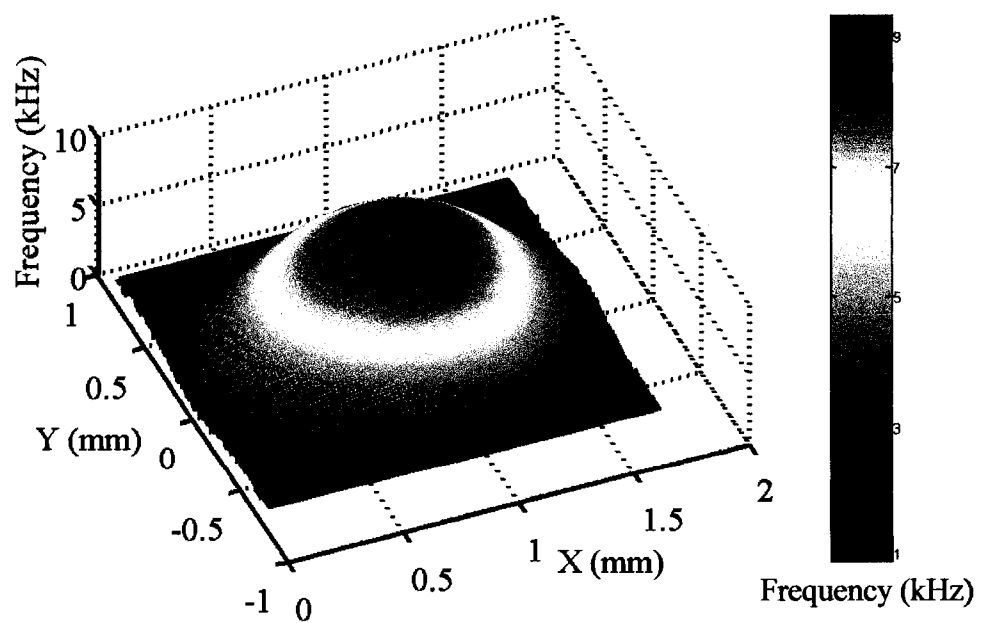


Fig. 4.11 3D velocity distribution of the cross section of the tube calculated from experimental values using the zero-crossing method.

By performing the described data processing procedure on each A-scan from the cross sectional image, we can build a velocity distribution within this image. In Fig. 4.10, the contour frequency-shift plots are superimposed to the structural image in order to give a better appreciation of the correlation between the actual sample and the fluid velocity distribution at any position inside the tube. The black solid curves indicate the frequency values of 2, 4, 6, 8, and 8.5 kHz calculated by the Wigner method. The white curves correspond to the frequency values of 2, 4, 6, 8, 8.5, and 9 kHz obtained with the zero-crossing method. This figure shows that, in the region near the glass wall where the velocity is relatively slow, the Wigner method produces results similar to the zero-crossing method. On the other hand, in the region near the center, where the velocity is relatively higher, the zero-crossing method provides more precise results. This confirms the observations deduced from Fig. 4.9. Hence, the zero-crossing method is the one that gives the most precise velocity distribution estimation within the tube. For a better visibility, a 3D velocity distribution plot of the cross section of the tube obtained with the zero-crossing method is given in Fig. 4.11.

4.4.4 Susceptibility to noise

In Fig. 4.8, we showed that the zero crossing method gives results more precise than those with the pseudo-Wigner method at least in the higher Doppler-velocity regime. The question arises if this is also the case for lower signal-to-noise ratios. In Fig. 4.12(a), we display a portion of the normalized interferogram for an intralipid solution at rest in which there are lower SNR regions (in the vicinity of point number 36400) resulting from speckle effects or lower backscattering. The raw signal appears in black and the normalized signal, in blue. The “instantaneous” frequency is extracted using the different methods. Figure 4.12(b) shows the results prior to any filtering. The theoretical value for the frequency is indicated with a dashed line and corresponds to the mirror sweep. One immediately notices that the

Hilbert method has an overall wider spread in frequencies (FM noise) than the Wigner and the zero-crossing methods. Actually, the zero-crossing method tracks the theoretical value very closely except at the points where there are rapid fluctuations in the vicinity of the zero-crossing points. In Fig. 4.13, we show the resulting statistics for the solution at rest (in red) and the solution in motion (in blue) corresponding to 3000 points in the center of the capillary, where the frequency is assumed to be nearly constant. Note that as the Doppler shift increases, the distribution widens, which is expected [43]. The distribution for the zero-crossing method is close to that of the pseudo-Wigner method and even narrower, except for a spill-over of frequencies at high values. For the fluid at rest, it is clear that the Hilbert method has a wider distribution. We then use the histograms of Fig. 4.13 to implement our maximum likelihood method whereby we reject all frequencies outside the FWHM (full width at half maximum) value of the distribution. This amounts to using an adaptive bandpass filter which follows the velocity distribution curve. By this filtering procedure, the spill-over effect of the zero-crossing method is strongly reduced. The rejection procedure is also helped by the fact that we normalize the signal, going from the black to the blue trace in Fig. 4.12(a). Indeed, upon rescaling, noisy transitions acquire higher slopes which translate into high frequencies which are filtered out more easily. In addition, the noise signal between the zero-crossing points never shows up in our procedure which means that in calculating the noise power to obtain the appropriate SNR value, one should integrate the noise power only over a sparse subset which puts in question the relevance of previous spectral-domain versus time-domain comparisons of SNR in our case.

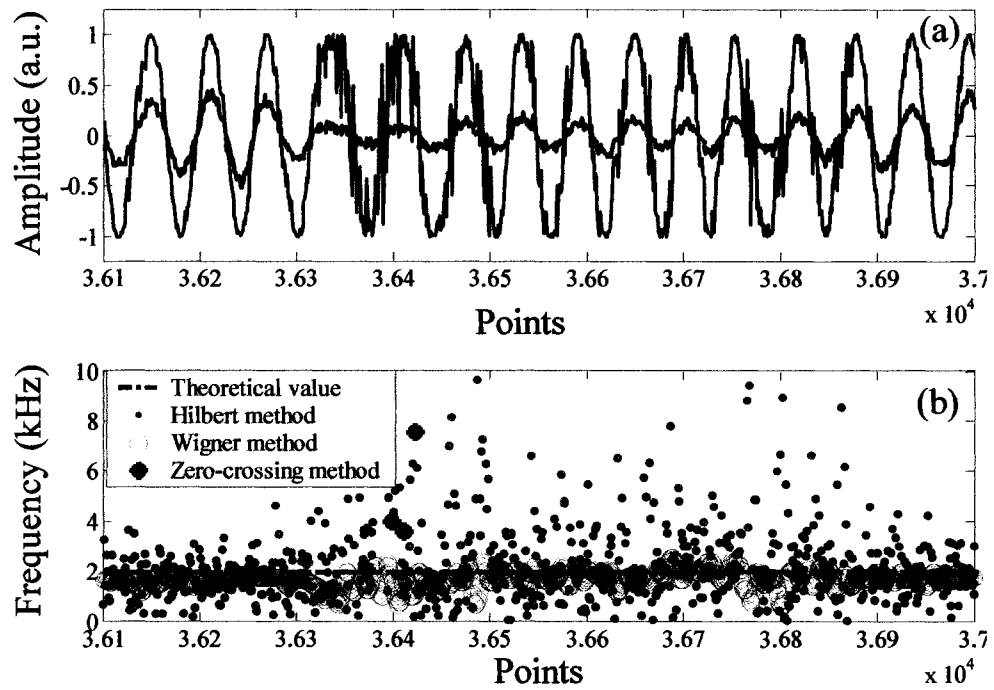


Fig. 4.12 (a). OCT raw signal sample (black curve) and normalized signal sample (blue curve) used for frequency calculation. (b). Local frequencies calculated with different methods.

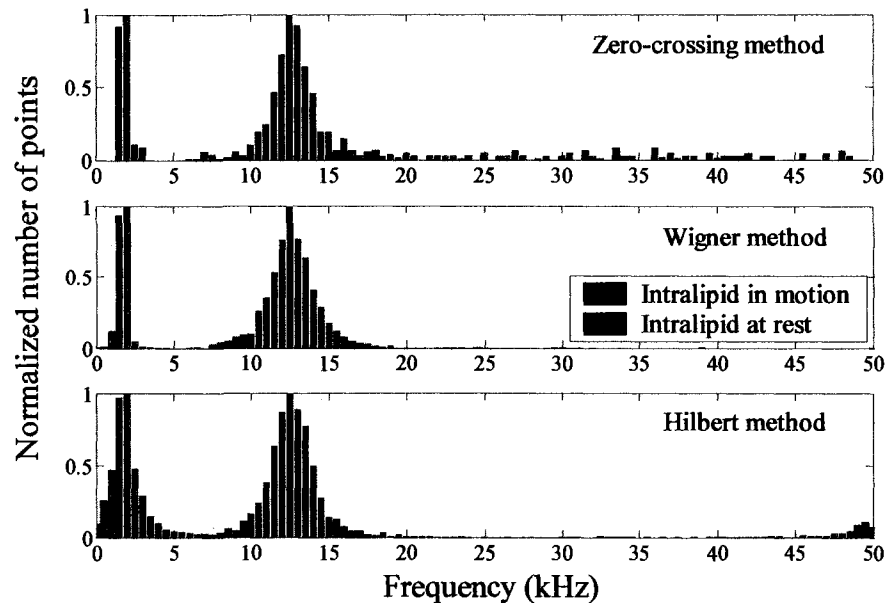


Fig. 4.13 Normalized frequency distributions obtained with the three methods with fluid at rest (red) and with fluid in motion (blue).

In order to get some feeling for the SNR sensitivity, we did several experiments changing the source power using a neutral density filter. In Fig. 4.14, we present the results for the 3000 points corresponding to the center of the tube, where the frequency is assumed to be nearly constant. The figure shows the FM SNR $f_{\max}/\Delta f$ (where f_{\max} and Δf are the maximum frequency and the FWHM width of the frequency distributions of Fig. 4.13, respectively) as a function of incident optical power for the fluid at rest (plot (a)) and with the fluid in motion (plot (b)). It is clear that the zero crossing method almost always gives the best FM SNR, especially for high input optical power (i.e. high AM SNR). For lower optical power (i.e. low AM SNR), the zero crossing advantage compared to Wigner is not significant anymore. The FM SNR of the Hilbert method is almost always the worst one. This result shows that for acceptable AM SNRs, the zero crossing method tends to be less sensitive to noise than the Wigner and Hilbert methods. This observation holds whether there is flow inside the tube or not. The fluctuations in Fig. 4.14 are the results of individual

scans which may arguably convey more information than the averages.

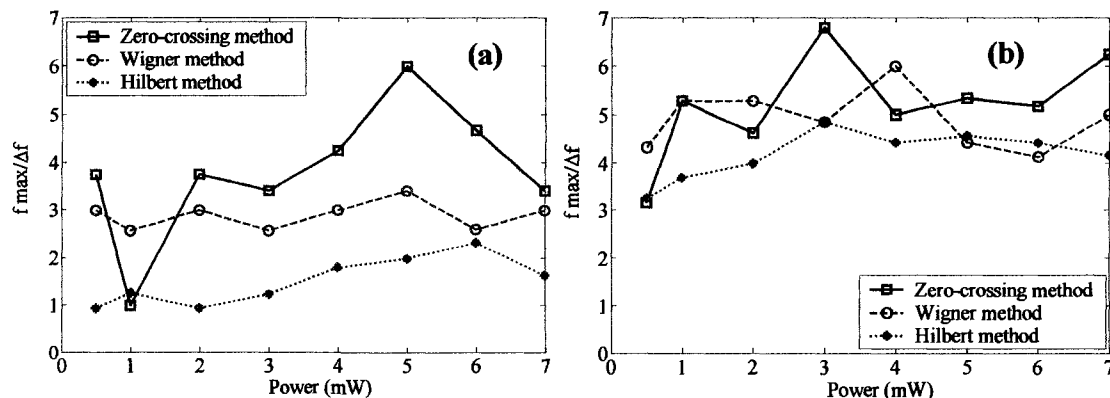


Fig. 4.14. FM SNR $f_{\max}/\Delta f$ at the center of the capillary tube calculated by the three methods (a) without and (b) with flow motion inside the tube.

A similar comparison was done for data points close to the capillary wall and the results are shown in Fig. 4.15. Again the FM SNR turns out to favor the zero-crossing method most of the time in this low velocity regime for the experimental conditions we used, being followed closely by the pseudo-Wigner method, but the difference is not overwhelming. The Hilbert method looks inferior.

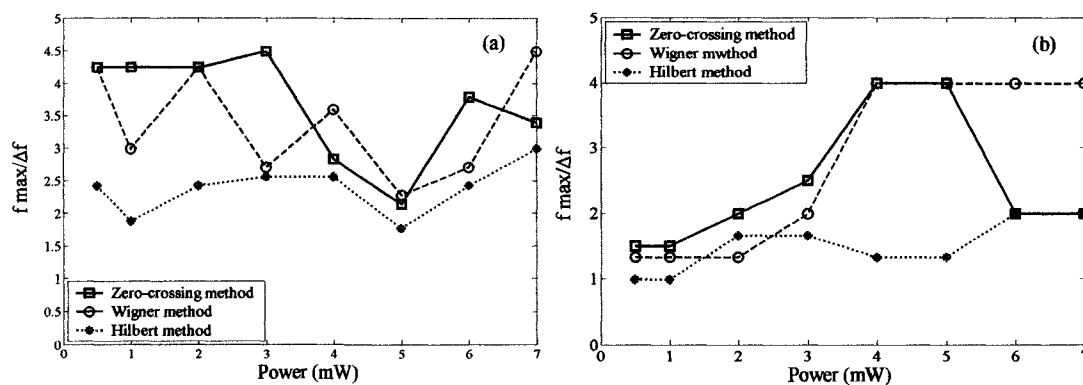


Fig. 4.15 FM SNR $f_{\max}/\Delta f$ at the edge of the capillary tube calculated by the three methods (a) without and (b) with flow motion inside the tube.

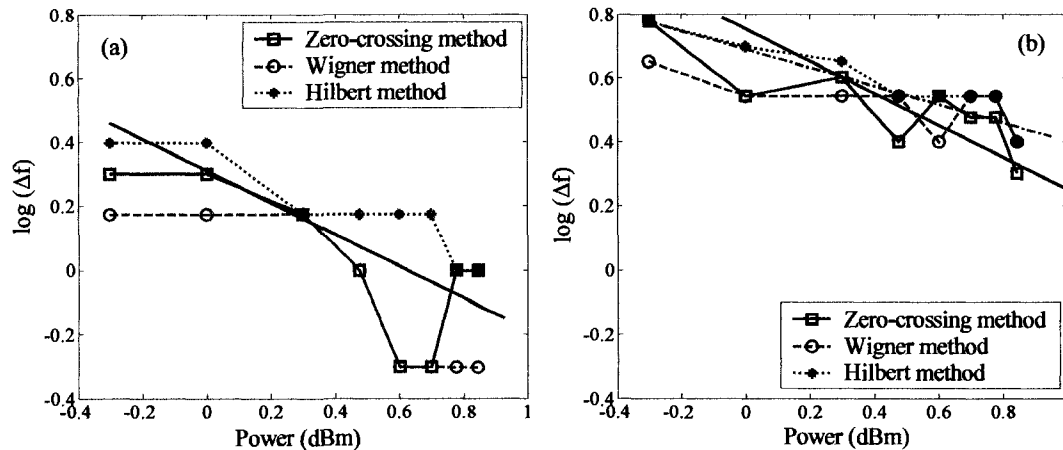


Fig. 4.16 The frequency spread Δf at the edge of the capillary tube (a) and in the middle of the tube (b) as a function of the source power. Black line has a slope of -0.5 . Dark brown dotted line represents the linear fit of the zero-crossing method results and has a slope of -0.29 .

Fig. 4.16 shows the frequency spread at the edge of the tube and at its middle. This is to be compared with the usual $1/\sqrt{SNR}$ dependency which is indicated by the black line. The dark brown dotted line is a linear fit of the results given by zero-crossing method. Instead of a -0.5 slope, we found a slope of -0.29 . These figures are indicative of the fact that our method does not seem to follow precisely the straightforward phase noise analysis often found in the literature.

4.5 Conclusion

We have shown that the zero-crossing method can produce the most accurate Doppler-velocity estimation based on a comparison of some of the currently used data processing methods in Doppler OCT. This can be attributed in part to the fact that the OCT signal is an almost a single periodic waveform in the time domain. In addition, we have also shown that the computational time used by zero-crossing method has been reduced by an order of magnitude compared to other aforementioned methods. Furthermore, the

zero-crossing is found to be globally less sensitive to noise than the Wigner and Hilbert methods. We will employ this method for processing the data of our experimental results from now on.

CHAPTER 5

Application of the time-domain Doppler OCT system

5.1 Introduction

More than 71 million Americans suffer from cardiovascular disease [63]. Among them, atherosclerosis is the main disease and becomes the most common cause of death and disability in western countries. Occlusive and aneurysm are the two of the principal manifestations of this kind of disease. The former comes from the intimal hyperplasia development leading to stenosis which can increase pressure losses and decrease the downstream blood flow. The latter is a dilatation of the aortic wall which has the risk of rupture. Previous work has shown that, wall shear stress (WSS) has been the most important indicator of both intimal hyperplasia development and aneurysm rupture [64]. WSS acts on the artery in two ways. The first one is the direct damage of the wall of the artery; the second is the attack of the endothelial cells which are located on the surface of the wall [65]. In fact, WSS is proportional to the velocity gradient of the area within $250 \sim 300 \mu\text{m}$ from the boundary of the fluid and the wall [66]. The vessel segments of the location where the WSS is either low or oscillating values are considered to be the highest risk for development of atherosclerosis [67]. Therefore, it is now widely accepted that there is a strong link between the WSS and the “disturbed” area of the fluid flow pattern of certain sample. This indicates that the distribution of atherosclerosis development is not uniform in the cardiovascular system, but some of the specific region has much higher risk to produce atherosclerosis. For instance, atherosclerosis is most likely to be found near the centre of a bifurcation especially in the area of vertex and apex. Flow separation occurs in the apex and the appearance of vortex induces a big variation in WSS around vertex. These two reasons are the major factors of introducing vascular intimal hyperplasia. Recently, catheter-based therapies such as angioplasty and stents are the main treatment strategies in dealing with atherosclerosis.

Among them, stent has shown a greatly increases of long-term success [68]. The idea of stent implantation into the human cardiovascular for curing atheroma is to create a slightly oversized opening and reducing the effects of wall thickening to the site of the lesion. Compared to angioplasty which is performed by surgery, the stent is delivered by means of the angioplasty balloon to the lesion, expands by the inflating of the balloon and then remains in position after the balloon is deflated and removed from the artery. The risk of restenosis has been miniature for angioplasty due to the extensive investigations of using stents. However, drastic impact of stent on fluid dynamics may induce again a “disturbed” area leading to restenosis. As a consequence, knowledge of WSS distribution is the key information for both estimating the risk for development of atherosclerosis and optimizing the implantation of stent. Quantitative measurements of the WSS in models of the human arterial system became essential. As mentioned above, WSS can be derived based on the velocity gradient of the flow fluid and therefore, knowledge of the pattern of blood velocities within a particular vessel or lesion becomes a fundamental issue which allows evaluation of WSS values of the sample. Efforts have been performed on this purpose with various methods such as, in vivo, phase contrast magnetic resonance imaging (PC MRI) [69-71], pulsed Doppler ultrasound [72, 73], in vitro, particle image velocimetry (PIV) [74, 75], and laser Doppler anemometry [76]. But all techniques suffer from poor spatial resolution, lack of velocity detection near the wall boundary, and some with poor velocity resolution. None of the existing methods so far can provide reliable blood flow velocity measurement, resulting in incomplete WSS estimation [66].

Doppler Optical Coherence Tomography enables subsurface cross-sectional velocity distribution determination of even non-transparent biological samples [34, 42]. Sub-10 μm spatial resolution can easily be obtained with this method since it depends only on the coherence length of the broadband light source used. More importantly, Doppler OCT can provide precise velocity gradient information near the wall boundary area. These advantages

put Doppler OCT in a leading position to become the preferred technique for measuring fluid flow distribution thus achieving clinical relevance for the estimation of WSS.

In this chapter, we will (1) examine the feasibility of Doppler OCT method to provide 2D high resolution velocity distributions of a laminar flow within a bifurcation phantom, (2) obtain the 2D velocity vector field which is needed for calculating WSS, and (3) correlate the experimental results with computational fluid dynamics (CFD) simulations for validation.

5.2. Principle

5.2.1 Wall shear stress

A viscous fluid moving along a solid boundary will incur a frictional force that is exerted between the adjacent layers of the flow and between the fluid and the wall of the conduit. This frictional force is induced by the viscous properties of the fluid and refers to the viscosity of the fluid. The viscosity is an indicator of how easy or difficult a fluid to move against fluid layers surrounding it. Since we know that the flow speed at the boundary is null, and that at some height from the boundary toward the center the flow speed reaches a certain value which defines a thin layer of the fluid named the boundary layer. Surface forces are formed through the direct contact between the boundary and the boundary layer. The component of the surface force which is normal to the contact area is called normal stress while the one which is tangential to the contact surface is called shear stress. WSS is defined as the tangential force per unit area that is imparted by the flowing fluid onto the boundary of the conduit. Here we define the velocity gradient in the near-wall region as the wall shear rate (WSR), and the WSS value τ_w can be expressed as proportional to WSR:

$$\tau_w = \mu \cdot \frac{\partial u}{\partial y} = \mu \cdot \dot{\gamma}_w \quad (5-1)$$

where μ is the dynamic viscosity of the fluid, u is the velocity of the fluid along the boundary,

$\dot{\gamma}_w$ is the wall shear rate, and y is the height of the boundary. Shear rate is measured in reciprocal second (s^{-1}), WSS is measured in pressure unit Pa, and the dynamic viscosity is measured in poise or in Pa·s. This relationship can be exploited to measure the wall shear stress once the velocity distribution is received. If a sensor could directly measure the gradient of the velocity profile at the wall, then multiplying by the dynamic viscosity would yield the shear stress. When the dynamic viscosity of the fluid is constant according to different WSR, we define the fluid as a Newtonian fluid such as water. In contrast, when the dynamic viscosity of the fluid depends on WSR, we term the fluid as non-Newtonian fluid. For instance, whole blood is a kind of non-Newtonian fluid since the measured dynamic viscosity depends on the WSR [77]. However, in most applications, the whole blood is considered as an approximate Newtonian fluid under specific conditions because the behavior of a non-Newtonian fluid is too complex. In practice, a laminar flow of a Newtonian fluid within a rigid wall cylindrical tube is usually referred to as a Hagen-Poiseuille flow. The cross-sectional velocity distribution is parabolic velocity profile. In this case, the WSS can be derived from the parabolic parameters of the Hagen-Poiseuille flow as [66]:

$$\tau_w = \frac{2\mu \cdot u_{\max}}{R} \quad (5-2)$$

where u_{\max} indicates the highest velocity at the center of the tube, and R is the inner radius of the cylindrical tube.

5.2.2 Vector velocity field

One drawback of Doppler OCT velocity detection is that the received velocity distribution is only the projection of the actual velocity along the optical axis of the sample arm. For the calculation of the normal velocity gradient in the near-wall region, one needs to have the full vector field of the velocity distribution at that position. Very few methods have been published on the experimental generation of the vector velocity field [27, 78, 79]. In our

view, the spectrum broadening method [79] suffers from FM noise and hence it can induce a spreading of the spectrum. The dual-angle method [27] is applicable only for small size sample. They are not, therefore, acceptable in our case. In this thesis, we propose our own method to obtain the 2D velocity vector field within the sample. Fig. 5.2 illustrates the principle of this method.

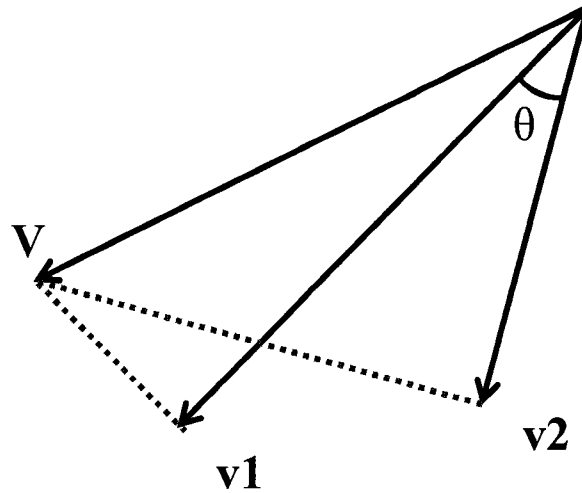


Fig. 5.2 Graphic method for obtaining the velocity vector by means of two measured velocity components with a known angle

For simplicity, we measure the first velocity component v_1 with Doppler OCT. Then, we turn the probe with a small angle θ and measure the velocity component v_2 . V is the calculated velocity vector at this specific position. The formula needed to produce the velocity vector can be derived from Fig. 5.3. The x axis projection and the y axis projection of the main velocity V are V_x and V_y , respectively. V_x is measured when the probe objective is perpendicular to the tube (0° Doppler angle). We assume the velocity makes an angle α from the x axis. Hence, V_x and V_y are equal to $V\cos(\alpha)$ and $V\sin(\alpha)$ respectively.

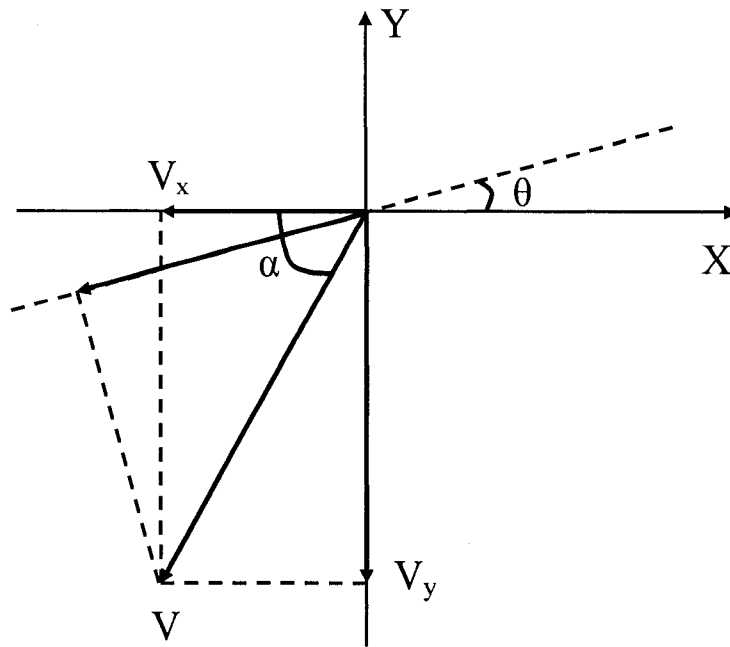


Fig. 5.3 The velocity and its projections.

So, we derive the following equations:

$$V \cos \alpha = \frac{\lambda_0 (\Delta f_D)_0}{2n} \quad (5-3)$$

$$V \cos(\alpha - \theta) = \frac{\lambda_0 (\Delta f_D)_\theta}{2n} \quad (5-4)$$

where n is the index of refraction of the fluid, $(\Delta f_D)_0$ and $(\Delta f_D)_\theta$ are the measured Doppler frequency shifts at 0 and θ Doppler angle respectively, and λ_0 is the central wavelength of the source.

We rewrite (5-4) as:

$$V \cos \alpha \cos \theta + V \sin \alpha \sin \theta = \lambda_0 \frac{(\Delta f_D)_\theta}{2n} \quad (5-5)$$

Therefore, the projection of the velocity on the y axis is:

$$V \sin \alpha = \frac{1}{\sin \theta} \left[\frac{\lambda_0 (\Delta f_D)_0}{2n} \cos \theta - \frac{\lambda_0 (\Delta f_D)_\theta}{2n} \right] \quad (5-6)$$

5.3. Experimental setup

5.3.1 Doppler OCT setup

To test our technique, we have used the experimental setup for Doppler velocity measurements presented in section 2.7 of this thesis. The source had a central wavelength of $\lambda_0 = 1545$ nm and a bandwidth of $\Delta\lambda = 32$ nm. We used a low-numerical aperture (0.25 N.A., 10X magnification) microscope objective in order to get a long depth of field. The scan speed was 1.5 mm/s.

In the sample arm, we designed and built a sample holder which rotates the sample tube horizontally in order to perform the measurements under different Doppler angles. A flow controller and a pump were employed to precisely adjust the flow rate. Depending on the sample size, two kinds of fluid were selected, one is intralipid in water solution for microfluidics, the other one is vegetable oil with titanium scatters for large samples.

5.3.2 Experimental details

In Fig. 5.4, we plot the bifurcation phantom used for the measurement of the velocity map. It is made of plastics with an inner diameter of 2.30 mm. The length of the main tube is 12.6 mm, while the length of the upper branch is 13.19 mm and that of the lower branch is 13.1 mm. The angles of the upper and lower branches from the horizontal line are 31° and 30° respectively. In order to make sure that the inlet flow to the bifurcation was stationary, we used a 75 mm length rigid copper tube as a guide with an inner diameter of 3.56 mm. We used soya oil (with titanium oxide particles as scatterers) as a fluid. The fluid was flowing from the main tube to the branches. A sample holder was employed which can be adjusted along 5 axes. The bifurcation sample was fixed on the sample holder horizontally such that the two braches were at the same level. The sample probe objective was also adjusted in the same plane, formed by the three central axes of the three tubes. We defined this plane as the central plane of the bifurcation and the 2D velocity distributions were measured in this central plane. The bifurcation phantom can be rotated horizontally by means of a precise rotation stage with a resolution of 0.01 degree. The experimental setup of the sample arm is shown in Fig. 5.5.

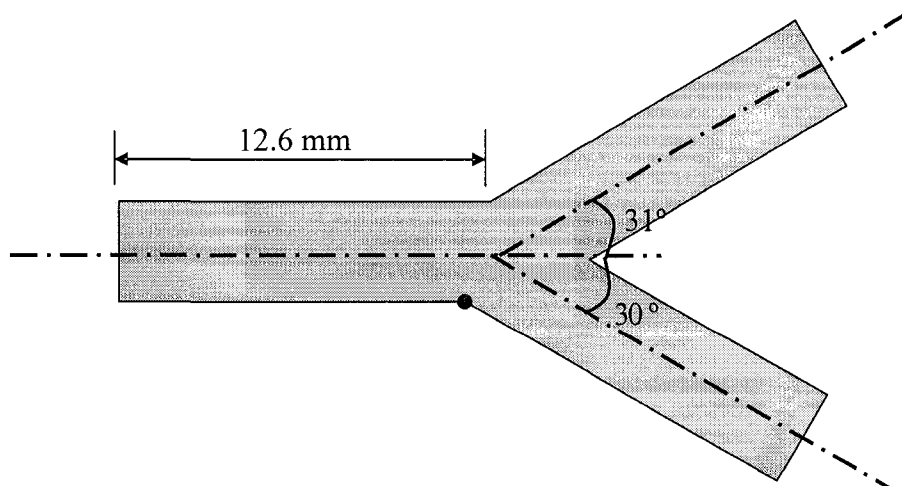


Fig. 5.4. Configuration of the bifurcation sample.

The viscosity of the soya oil was measured as 0.04970 Pa·s with an acknowledgement to Ms. M. Hamdine in the Mechanical Engineering Department at Ecole Polytechnique, and is plotted in Fig. 5.6. We mixed the oil with some titanium white particles of roughly 1 μm in diameter as homogeneous as possible. The flow rate could be adjusted precisely with a flow meter. The focusing field of the sample objective was adjusted at the center position of the tube to enhance the backscattered light.

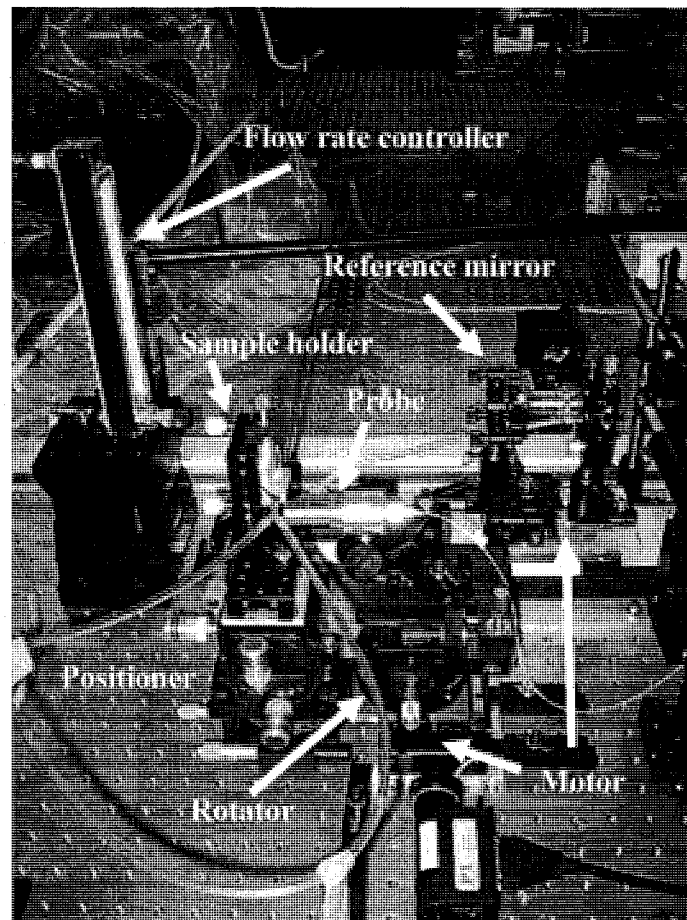


Fig. 5.5. Experimental setup for measurement of the Doppler frequency-shift for the bifurcation sample.

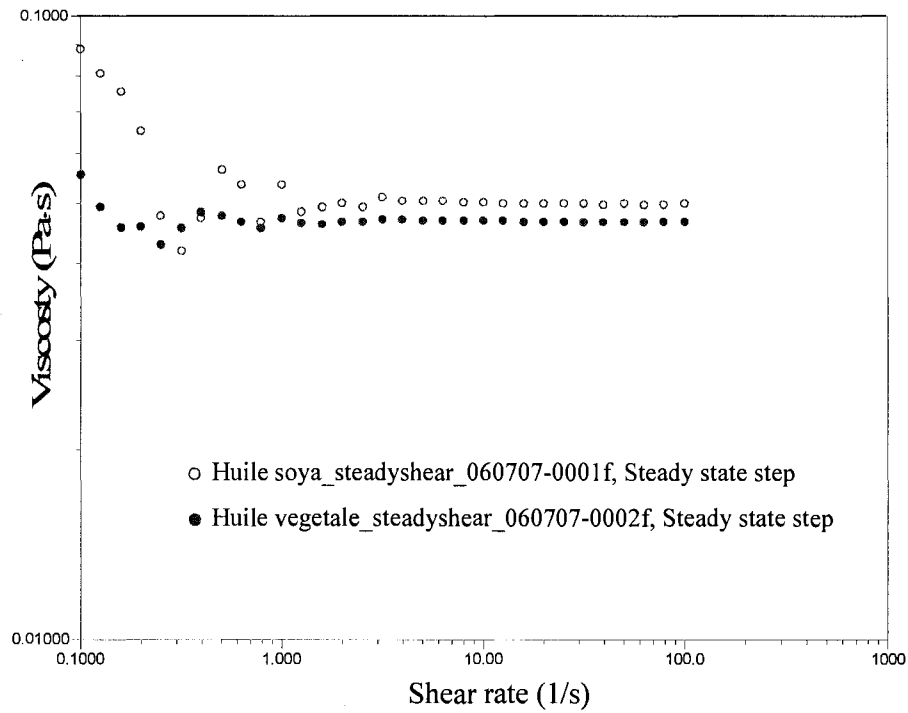


Fig. 5.6. Measured viscosities of the vegetable oil and the soya oil.

5.4. Results and discussion

5.4.1 Simulation results by Fluent

In this section a short description of Fluent, used for the simulations, is given. Let us describe briefly the process for creating and then meshing the bifurcation phantom. After, the procedures of the flow simulations using Fluent will be addressed.

Fig. 5.7 illustrates the main panel of Gambit which is used for coding the experimental models. The first row contain: create, mesh, boundary type, and tools. The second row refers to the geometry types that are used for each operation in the first row. Because our phantom is a combination of three cylindrical tubes, our first sequence was Geometry \rightarrow Volume \rightarrow Create Volume (Cylinder) and opened the interface window of Create Real Cylinder as Fig. 5.8 shows. The parameters of the entrance tube were as follows, a length 12.6 mm and radius

1.15 mm, chose axis location as Positive Z and then click Apply. The tube is then displayed on the screen. The other two branch tubes can be handled using the same method but rotating by 31° from Z axis for the upper one and -30° for the other one. The next step is to combine these three tubes into one object as shown in Fig. 5.9.

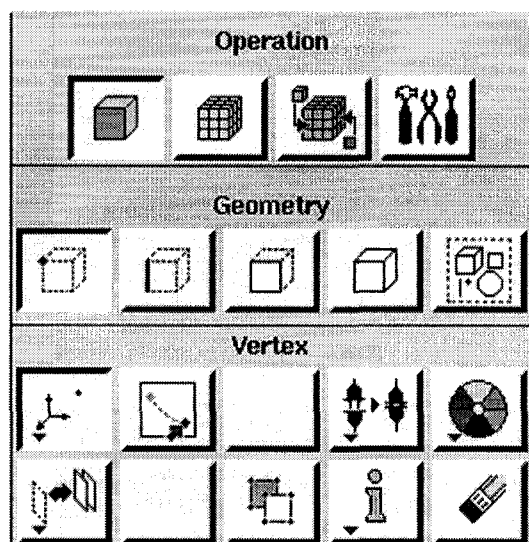


Fig. 5.7 Main panel of Gambit

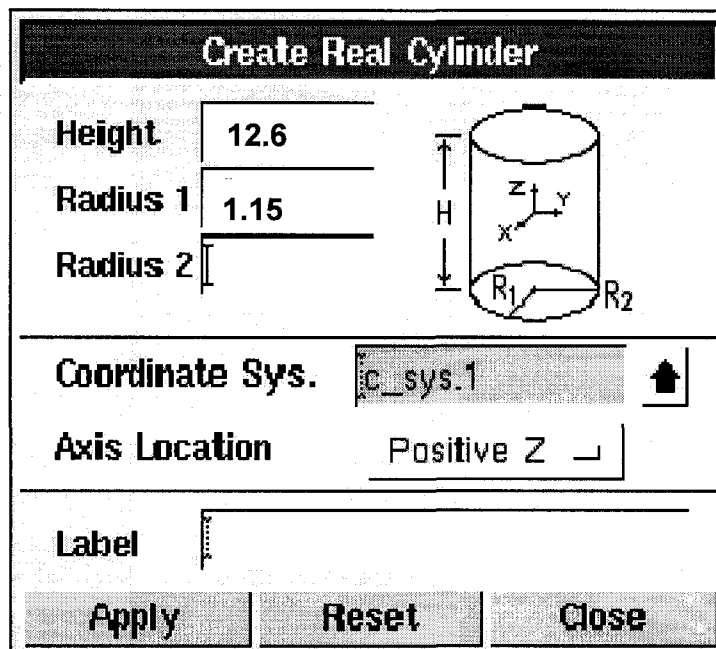


Fig. 5.8. Interface window of Gambit to create cylindrical objects.

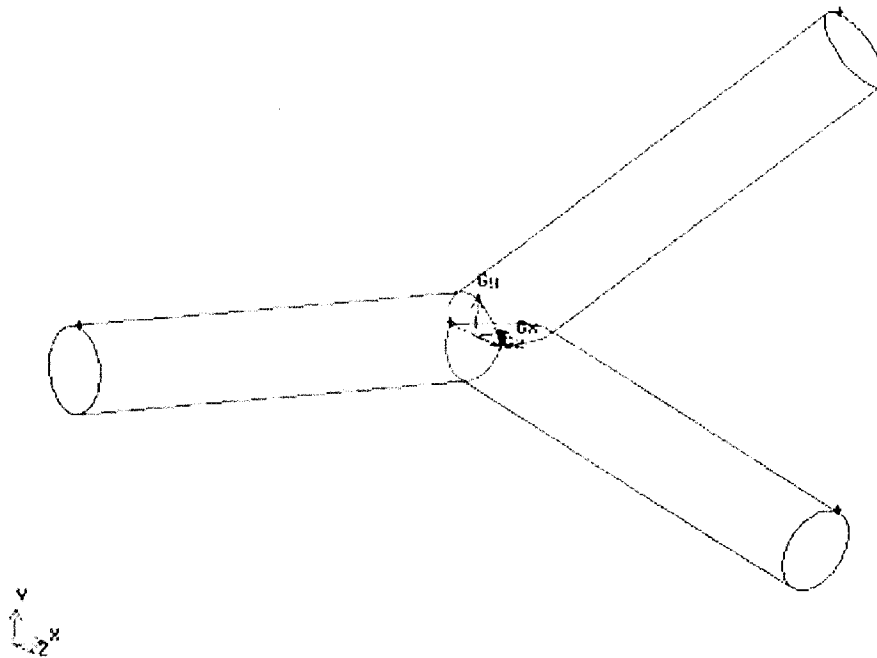


Fig. 5.9. The finished bifurcation phantom before meshing.

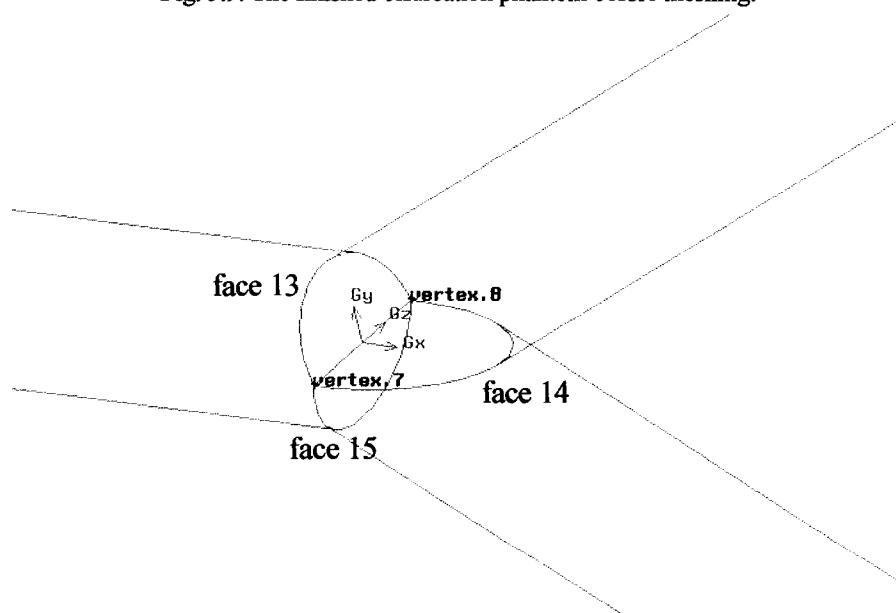


Fig. 5.10. Defining the two points where the three tubes were jointed together.

The next step will be meshing this object. First, we defined two points as vertex 7 and vertex 8 (where the three tubes were jointed and created a straight edge) as indicated on Fig. 5.10. Then, we defined three faces, 13, 14, and 15, and used them to split the whole volume

into three small volumes by means of the split volume window as shown in Fig. 5.11.

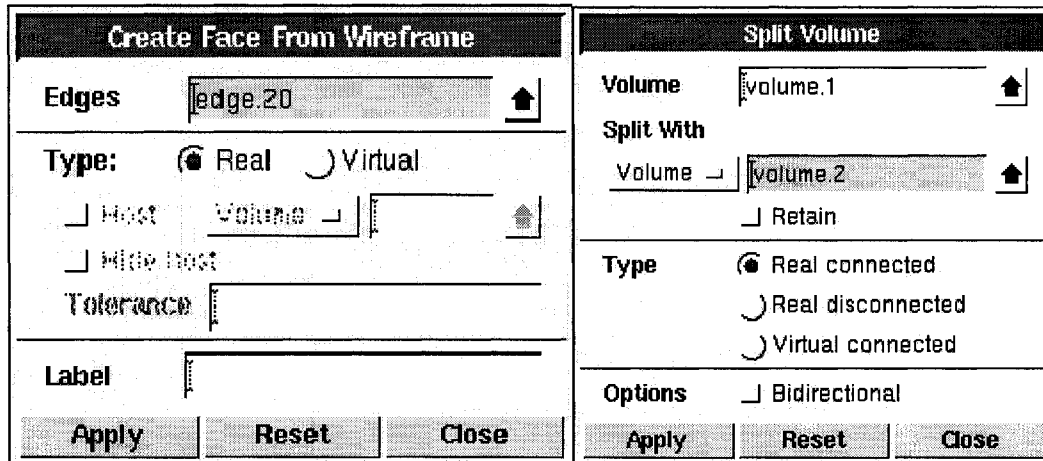
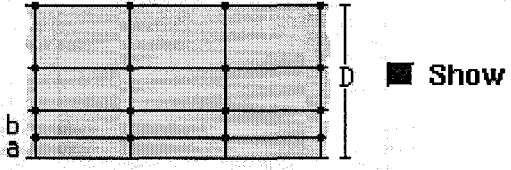


Fig. 5.11. The windows for creating face and splitting the volume.

Since our calculations of the WSS require detailed information of the velocity distribution close to the boundary, we had to define a denser mesh in that area. The boundary layer function is used for this purpose, and six thin layers were defined in our case. Fig. 5.12 shows this interface window. Fig. 5.13 shows the finished boundary layers on each end face of the tubes. Fig. 5.14 displays the window used for meshing one tube at each time. We then applied this function to the other tubes. The final mesh model is shown in Fig. 5.15 (surface plots). A detailed meshing figure which shows the boundary layers and the meshing elements on the end face is given in Fig. 5.16.

Create Boundary Layer



Definition:

First row (a)

Growth factor (b/a)

Rows

Depth (D)

Internal continuity

Transition pattern:

1:1
 4:2
 3:1
 5:1

Transition Rows

Attachment:

Edges

Label

Apply
Reset
Close

Fig. 5.12. The window for creating boundary layers.

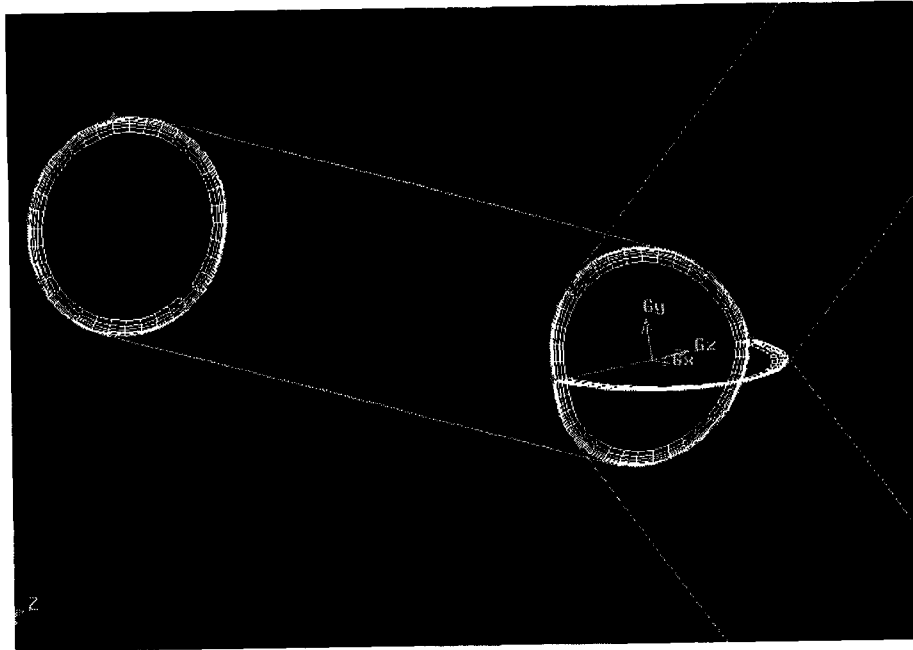


Fig. 5.13. The finished boundary layer meshing of the tubes.

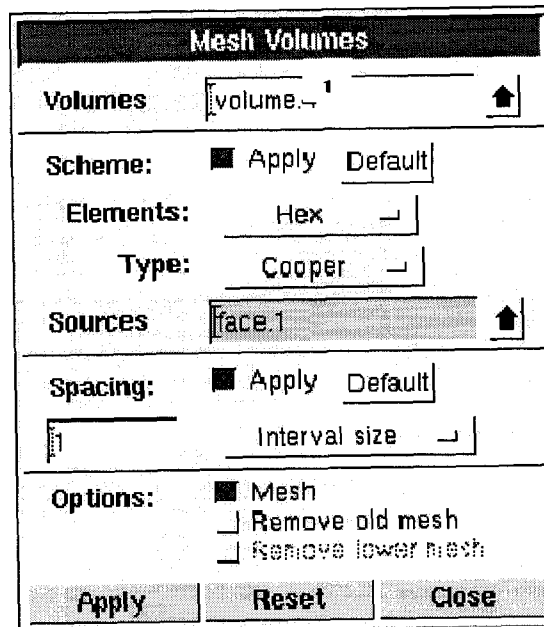


Fig. 5.14. The window for meshing a real volume.

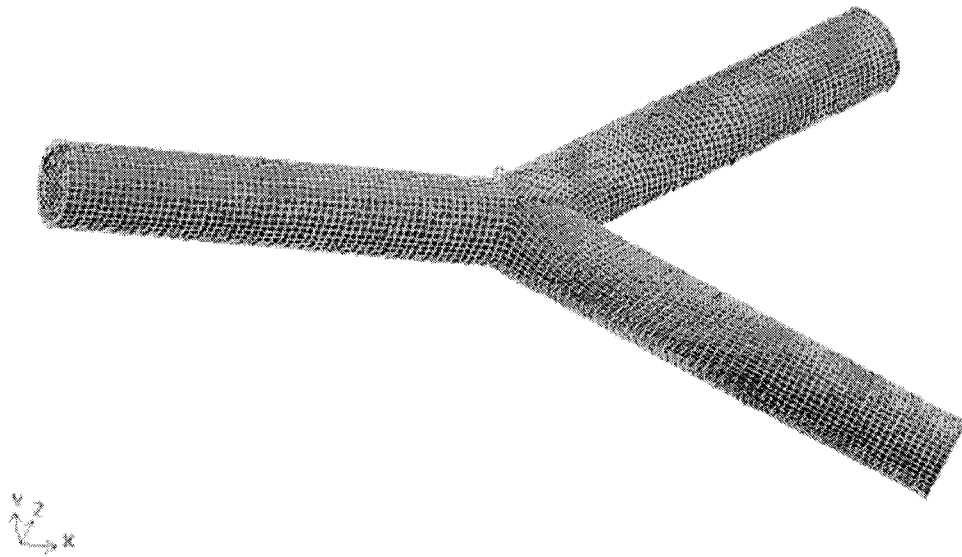


Fig. 5.15. The meshed bifurcation model (surface plot).

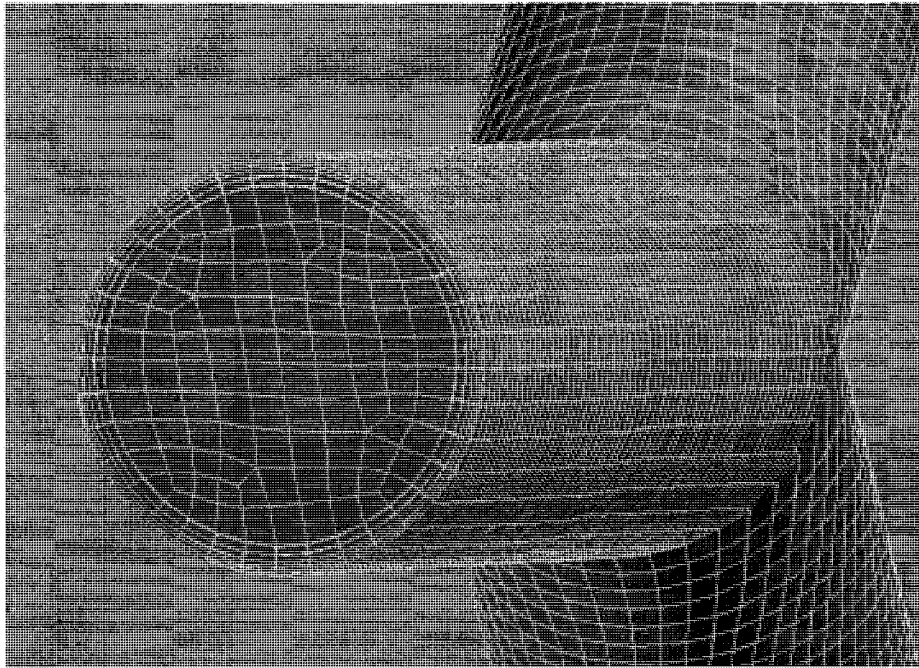


Fig. 5.16. The boundary layers on one end face of the bifurcation model.

The simulation results are shown in the following three figures. Fig. 5.17 shows the vector velocity distribution in the phantom. It shows that in most regions, the flow is along the wall and the velocity projection in the normal direction of the wall is null. Fig. 5.18 shows the contour of the velocity distribution within the sample.



Fig. 5.17. Vector velocity within the phantom.

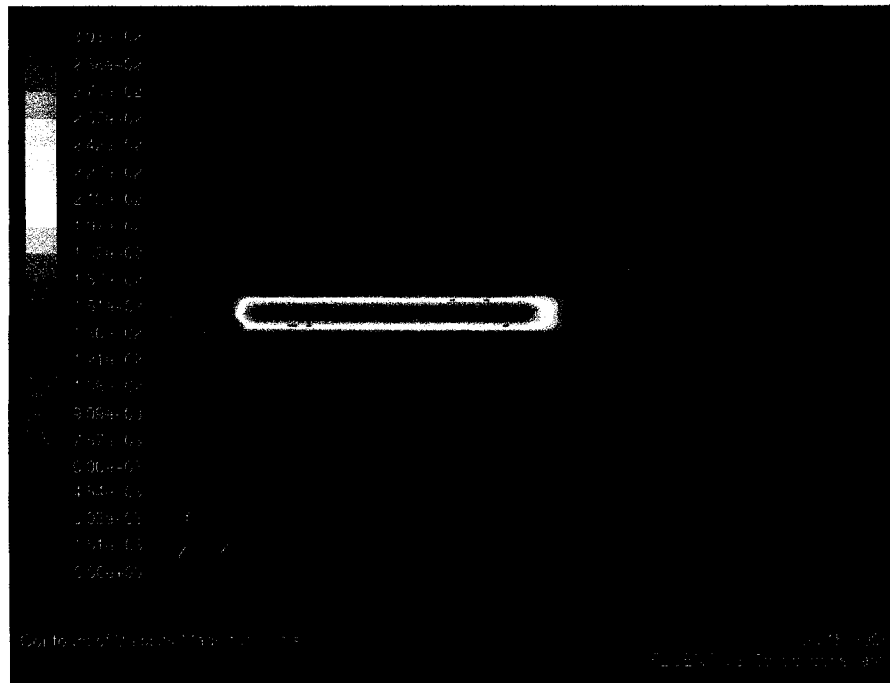


Fig. 5.18. Velocity distribution within the phantom.

5.4.2 Experimental results

The first measurement on the bifurcation phantom was performed on the main tube at the beginning of the inlet with a Doppler angle of 81° that is the probe objective was adjusted with an angle of 9° from the normal direction of the tube. The A-scan length was 3.6 mm at a sampling rate of 100 kHz. Fig. 5.19 depicts the received interferogram of this A-scan. For completeness, we give a detailed account on how to apply the zero-crossing method on this interferogram in order to obtain the Doppler frequency shift and to extract the velocity distribution.

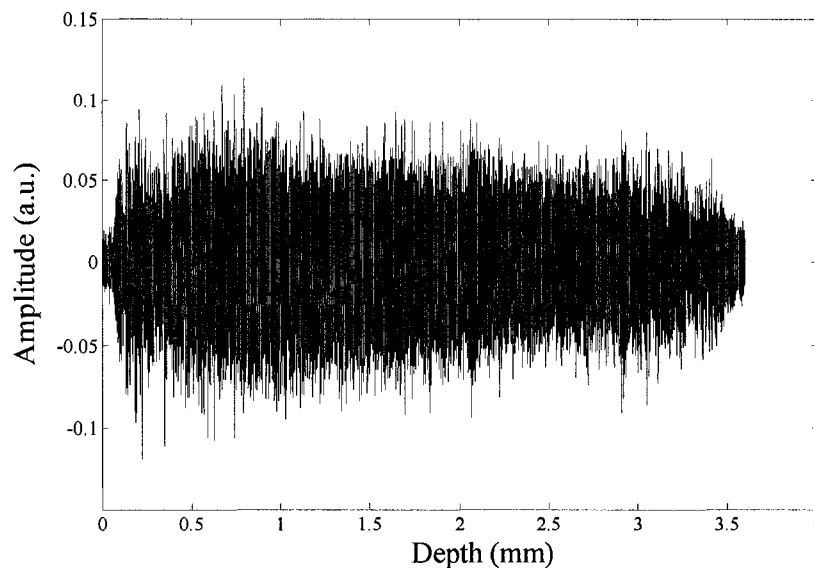


Fig. 5.19 The interferogram of the inlet tube.

The first step is to find out the zero-crossing points within this signal. The following code was used for this procedure:

```
I=[];
for i=1:3997
if (abs(sample(i)+sample(i+1))~=(abs(sample(i))+abs(sample(i+1))));
I=[I i]; %positions just before zero cross
end
```

```

end
V=1+abs(sample(1))./(abs(sample(1))+abs(sample(I+1))); % zero cross position
v=diff(V);
P=1./(2*v)*100; % frequencies at each point
X=V(1:(end-1))+0.5.*v; %central positions
X=X.*(3.6/239997); %depth values
m=find(P<=25);
newX=X(m);
newP=P(m);
plot(newX,newP,'k.');
```

The result of this procedure is plotted in Fig. 5.20 as black points which indicate the raw Doppler frequency shifts. The next step is to apply the band pass filter to trim out the noise and keep only the maximum likelihood frequency values. The code used at this step is given now and the filtered signal is plotted in Fig. 5.20 as yellow points.

```

beltP=buffer(newP,35);
beltX=buffer(newX,35);
n=ceil(length(newX)/35);
new_P=[];
new_X=[];
for i=1:n
y=beltP(:,i);
x=beltX(:,i);
x60=0:0.5:50;
[valu,xnew]=hist(y,x60);
npoints=200;
xinterp=0.50/(npoints-1):50;
yinterp=interp1(xnew,valu,xinterp,'pchip');
J=find(yinterp==max(yinterp));
J=J(1);
maximum=yinterp(J);
```

```

halfmax=0.5*maximum;
kk=find(yinterp>=halfmax);
lower=min(kk);
higher=max(kk);
ymin=xinterp(lower);
ymax=xinterp(higher);
nsigmax=1;
nsigmin=1;
coords=find(y<=nsigmax.*ymax & y>=nsigmin.*ymin);
y=y(coords);
x=x(coords);
new_P=[new_P; y];
new_X=[new_X; x];
end

```

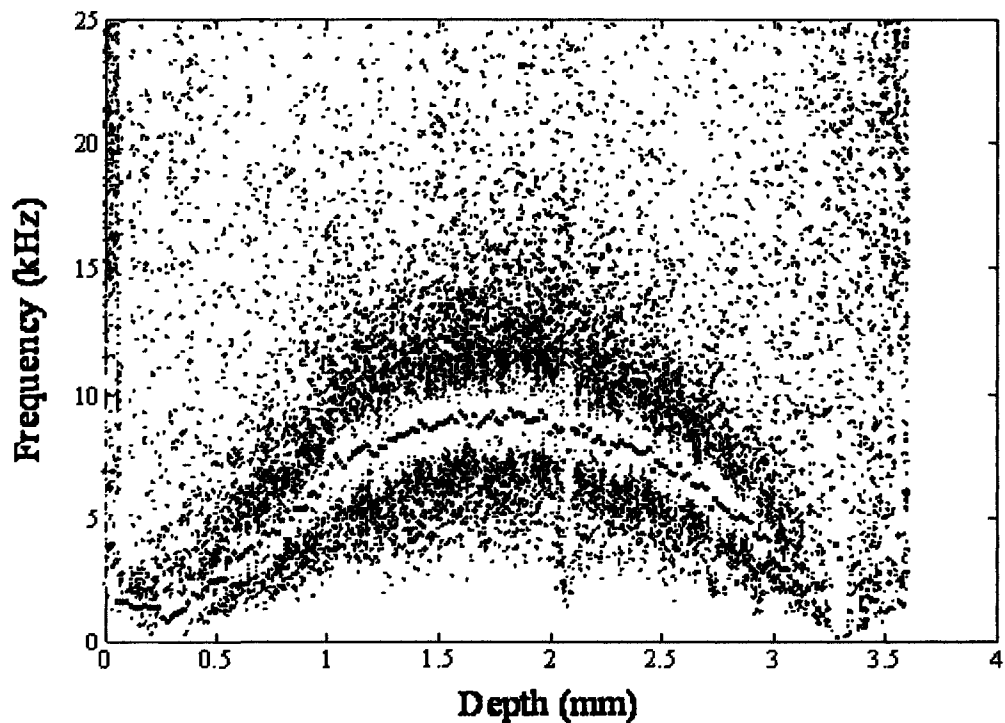


Fig. 5.20 The Doppler frequency shifts of the interferogram calculated with the zero-crossing method. Black points: raw frequency signal. Yellow points: Maximum likelihood values. Red points: Frequencies at each pixel.

In order to determine more precise frequency values, we divide the whole A-scan into 181 pixels, the size of each pixel being 20 μm in air. In each pixel, we define the frequency at this point as the average of all the frequency values within this pixel. Finally, the red points in Fig. 5.20 indicate the velocity profile of this A-scan. Theoretically, this velocity profile should have a parabolic shape since a 75 mm rigid straight tube was employed as an entrance guide to ensure a laminar flow at the inlet of the bifurcation. Indeed, the red points show that the profile is symmetrical. Therefore, the experimental results support the hypothesis that the flow at the inlet of the bifurcation is laminar. The code used for finding the frequencies at each pixel is:

```

pixel_X=[0:0.02:3.6];
pixel_Fre=[];
pixel_P=[];
for u=1:181 % 3.6 mm for the length of the scan
    v=find(new_X>=0.02*(u-1) & new_X<0.02*u);
    if length(v)==0
        pixel_P(u)=nan; %in case of divided by zero
    else
        pixel_P(u)=mean(new_P(v));
    end
end
pixel_Fre=[pixel_Fre;pixel_P];
plot(pixel_X,pixel_Fre,'r');

```

The frequency at the boundary of the tube where the velocities vanish is 1.724 kHz which is the carrier frequency. As we move further from the wall, the frequencies decrease to 0.5 kHz and then increase to a maximum values at 9.24 kHz. The calculated maximum frequency is 11.684 kHz. Based on Eq. (1-8), we calculate the maximum flow velocity as 31.14 mm/s at the center of the inlet position of the bifurcation tube. The average flow speed on that cross section is half the value of the maximum which is 15.57 mm/s. We have used

this value as the initial inlet velocity to perform the simulations with Fluent.

After the confirmation that the inlet flow of the bifurcation is laminar, the measurement of the velocity distribution in the lower branch tube was performed. First, measurements were done with incident light beam perpendicular to the tube and other measurements were performed by rotating the probe objective by an angle of 9° from the normal direction. The starting points of both measurements were at the same position on the surface of the bifurcation phantom (red mark in Fig. 5.4). The interferogram signals were processed with the zero-crossing method as explained in detail previously. Fig. 5.21 shows an example of the results on one A-scan. In that figure, the blue points indicate the raw Doppler frequencies, the black points indicate the signal filtered by the maximum likelihood method, and the yellow points are the final frequencies at each pixel. The frequencies below 1.724 kHz indicate a flow in the opposite direction. 67 A-scans have been performed covering 6.6 mm which gives a distance between two consecutive A-scan of 0.1 mm. Fig. 5.22 shows the 2D Doppler frequency shifts in this experiment when the Doppler angle is equal to 9° .

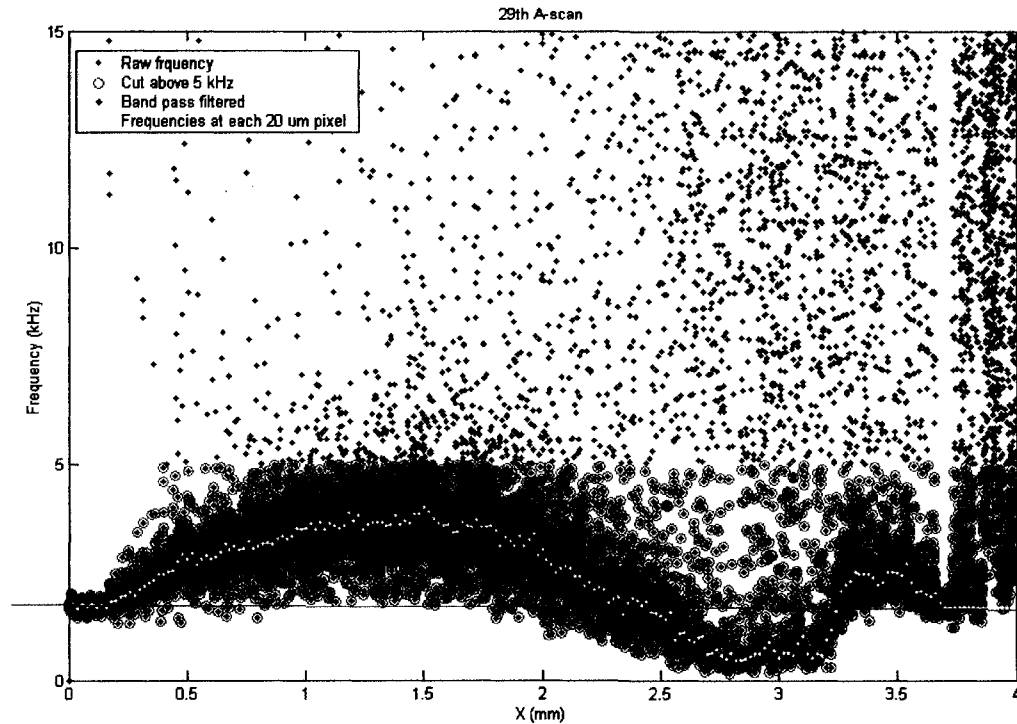


Fig. 5.21 The Doppler frequency shifts of one scan based on the zero-crossing method. The green line indicates the frequency of the non moving objects.

In Fig. 5.22, we can see that in part of this branch tube, the flow is stationary and most of the flow direction is the same as that of the main flow. Only a small region in middle right hand side of the figure shows a disturbance. The small blue area indicates that the velocities in that region are in the opposite direction with respect to the main flow.

In Fig. 5.22, we cannot assign true values to the velocities in red because the range of velocities in that area is very broad, (see Fig. 5.23). This broadening of the range comes from the fact that in this area, where three tubes are joined together, the flow has a greater chance of being unsteady. Thus, the amplitudes and directions of the flow in this area are more dispersed than in other areas. The velocities detected by our Doppler OCT system are limited by the data sampling rate of 100 kHz. This parameter sets the dynamic range of the system to

about 20 kHz. Therefore, the velocity values are not reliable because the measured velocities exceed the dynamic range of the system although one might think that this velocity dispersion comes from turbulence or other disturbances of the laminar flow.

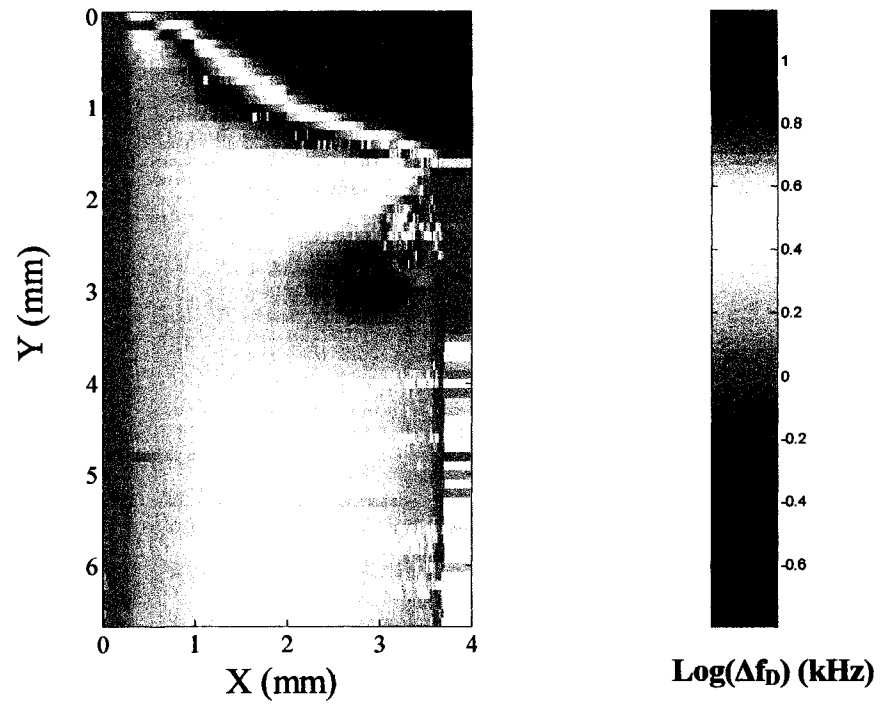


Fig. 5.22 2D Doppler frequency shifts in the right branch tube at 9° Doppler angle (relative frequency; carrier frequency at 1.724 kHz appears as 0 kHz)

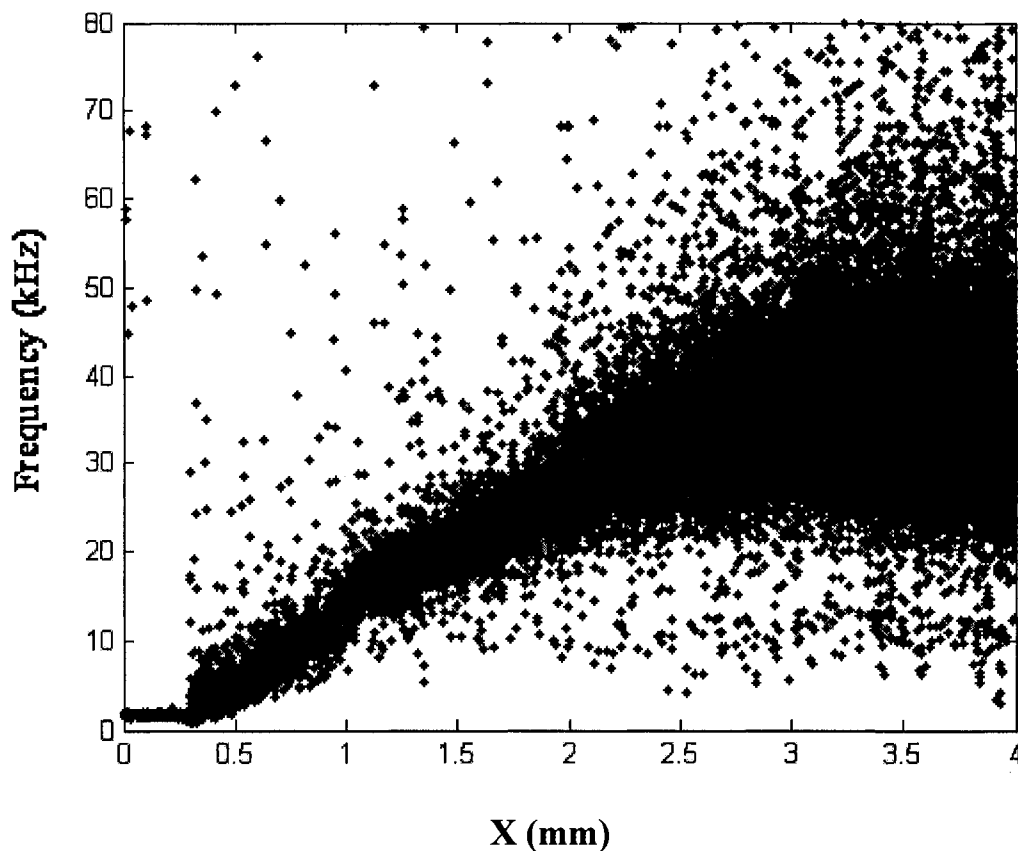


Fig. 5.23 The Doppler frequency shifts of one A-scan in the red area of Fig. 5.22 based on the zero-crossing method. The black line indicates that the frequency increases linearly in the beginning.

Fig. 5.24 shows the 2D Doppler frequency shifts of this experiment when the incident light beam is perpendicular to the tube (0° Doppler angle). The red area, which corresponds to « anomalous » velocity components, appears also where the three tubes are joined together. Excluding that region, the velocity distribution appears quite homogeneous, except for the small dark blue area in the central region. This means that the system detected a flow in opposite direction in this area but the speeds are very low. In general, Doppler OCT detect the velocity projection on the optical axis of the probe beam. As we expect that most of the liquid flows along the direction of the wall of the tube, only weak velocity components will be detected if we adjust the light beam to be perpendicular to the tube. Once the velocity

projection at a certain location is significant, we realize that there, the velocity vector has a certain components away from the direction parallel to the wall of the tube. These areas are important since they indicate vortices and disturbances in the flow.

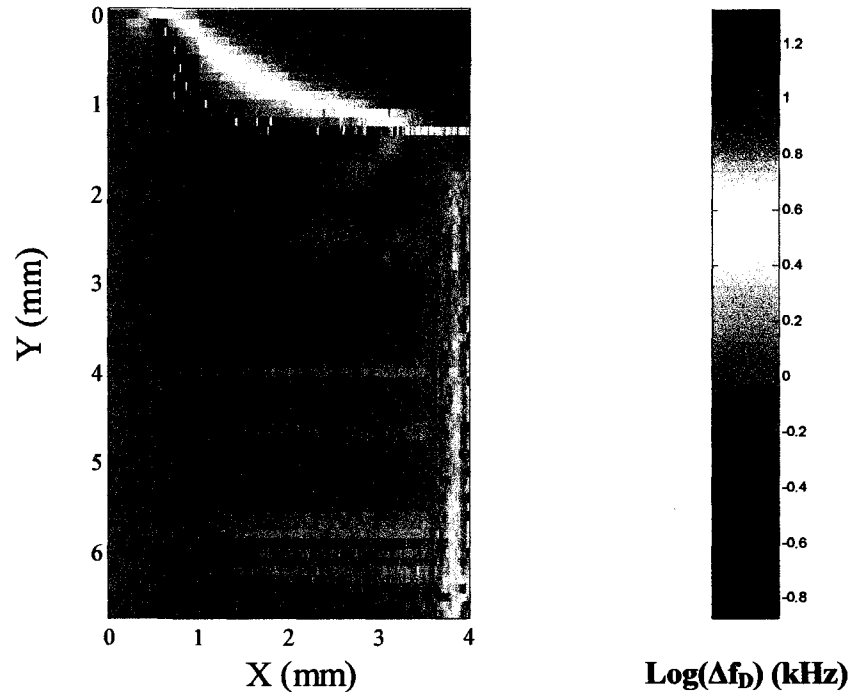


Fig. 5.24 2D Doppler frequency shifts in the right branch tube at 0° Doppler angle (relative frequency; carrier frequency at 1.724 kHz appears as 0 kHz).

After the velocity distributions for the 0° and 9° angles have been detected, we can derive the vector distribution using the method described in section 5.2.4. From Fig. 5.2, v_1 and v_2 are the velocity projections at 9° and 0° Doppler angles, respectively. The angle θ is the angle between these two projections which is calculated to be 5.655° based on the index of refraction of the plastic wall which is 1.5873. In contrast to the measurement at 0° Doppler angle whose optical path is the diameter of the tube multiplied by the index of refraction of the fluid, the measurement at 9° Doppler angle has a longer optical path for each A-scan. Therefore, we need to rotate the 2D velocity distribution obtained for the 9°

Doppler angle in order to match the spatial dimensions of the 0° Doppler angle measurement, as shown in Fig. 5.25.

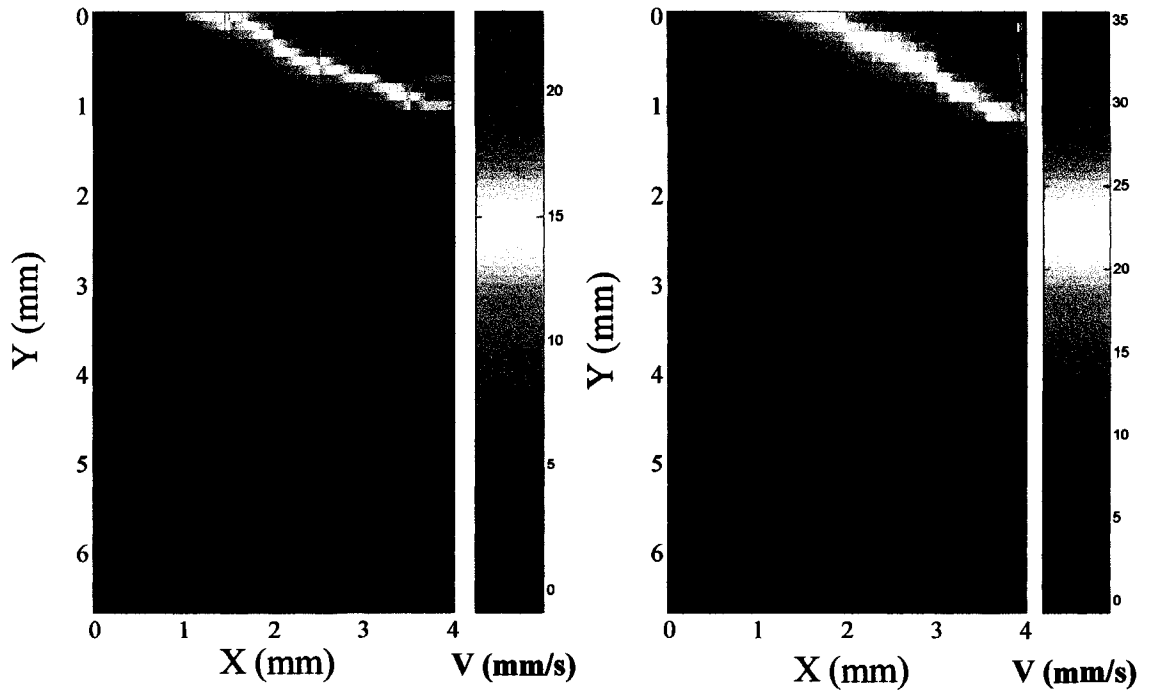


Fig. 5.25 The rotated 2D Doppler frequency shift distribution for the 9° Doppler angle (left) which spatial dimensions match the Doppler frequency shift distribution for the 0° Doppler angle (right).

Fig. 5.26 displays the final vector velocity distribution within the lower branch tube, in the case when the two angles are 0° and $\theta = 9^\circ$, based on formula (5-10).

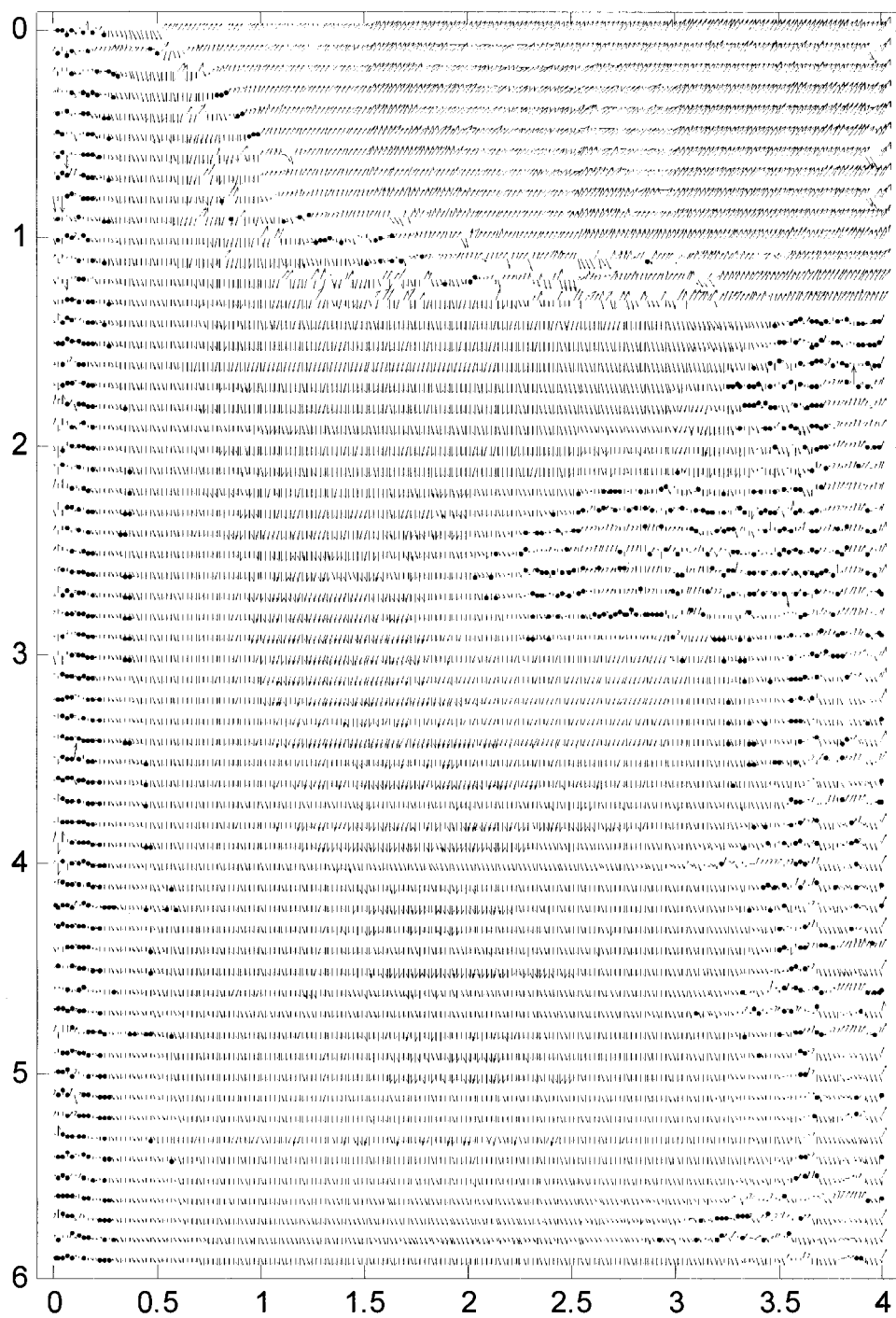


Fig. 5.26 The vector velocity distribution within the lower branch tube.

From the values of the velocity projections in the y direction (parallel to the wall of the tube), we can calculate the WSS. We begin with the velocities of the last A-scan where the velocity profile is similar to a parabolic distribution. We use Eq. 5.1 to calculate the WSS for the velocities from the boundary of the wall to 0.5 mm into the fluid where the velocity gradient is expected to cause WSS.

In Fig. 5.27 (a), the WSS have been plotted for every 20 μm (solid line). Fig. 5.27 (b) illustrates the velocity distribution of the A-scan within the region of the calculation. Fig. 5.27 (a) shows clearly that, Doppler OCT is capable of obtaining a detailed WSS distribution even at the border of the flow. This is the first WSS distribution, to the best of our knowledge, ever obtained with such a resolution from an experimental measurement. This WSS distribution contains very useful information that can improve the diagnosis of some cardiovascular diseases. The dashed line gives the WSS averaged over this region. Other velocity measurement techniques suffer from a lack of spatial resolution: they have to calculate the WSS with the velocity that can be detected as close to the border as possible, normally around 1 mm from the border. The dotted line indicates such a WSS calculated with the velocity at 1 mm from the wall. The last line (dash-dot line) illustrates the WSS calculated with Eq. 5.2. This formula is based on the assumption that the flow profile is parabolic, which is often used to estimate the WSS. Fig. 5.27 (a) can be considered as a quantitative comparison of the real WSS with estimations obtained with other current techniques such as laser velocimetry.

Next, we compare three methods for obtaining the WSS along the length of the tube. The 0 position corresponds to the red dot in Fig. 5.4 which is known as the vertex of the bifurcation. The dashed line in Fig. 5.28 shows the measured average WSS. We still use the dotted line to identify the WSS calculated with the velocity at 1 mm from the wall, and the

dash-dot line to illustrate the WSS calculated using Eq. 5.2. The measured average WSS displays a peak indicating that a strong WSS occurs near the vertex of the bifurcation. This result agrees with well known phenomena. The values found by the other two methods do not fit expected behaviour. In the region where the flow is believed to be parabolic, the three methods give a similar WSS which means that the currently used methods for obtaining the WSS are applicable only when the flow is laminar.

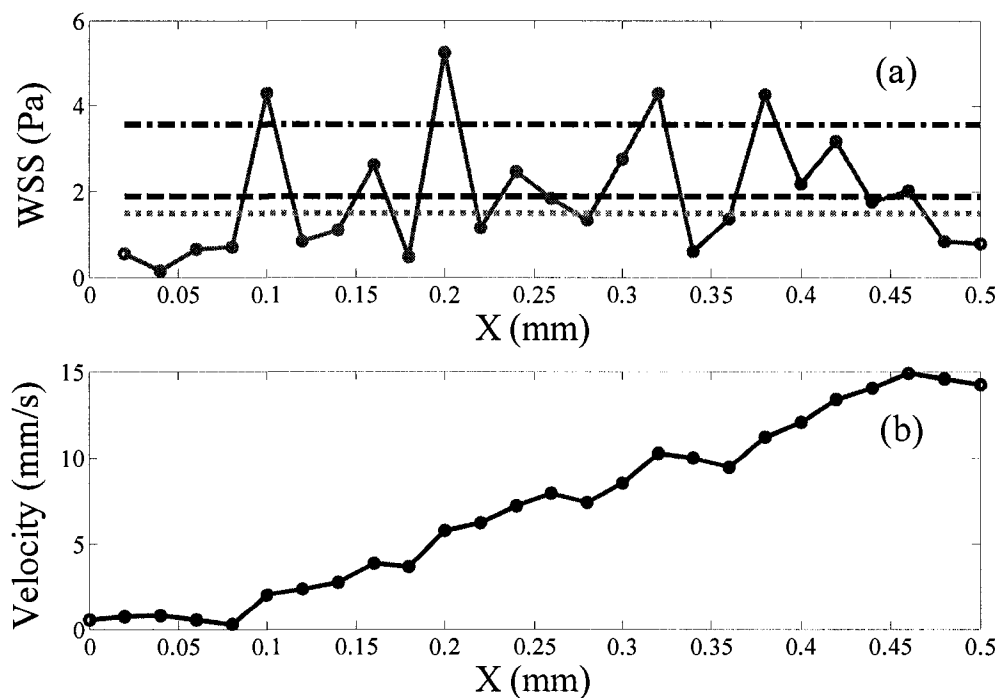


Fig. 5.27 The WSS values (a) obtained with the measured y-axis velocity values (b). The WSS calculated based on Eq. 5.1 (solid curve), average of the WSS (dashed line), calculated WSS based on the measured velocity at 1 mm from the border (dotted line), and based on Eq. 5.2 (dash-dot line).

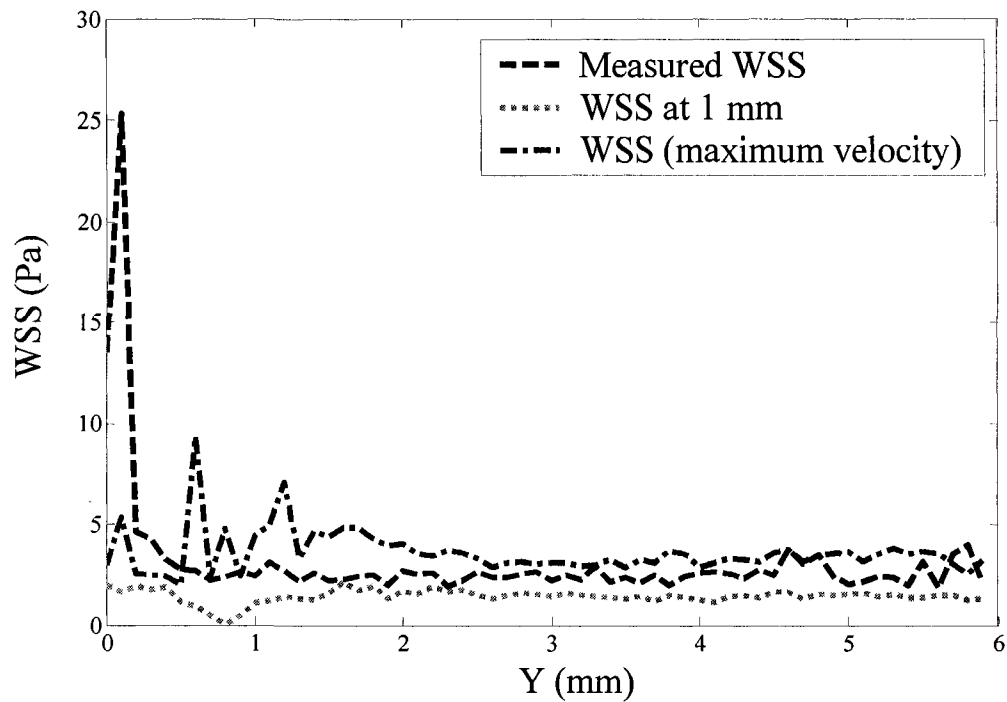


Fig. 5.28 The WSS calculated along the tube. The measured average WSS (dashed curve), calculated WSS based on the measured velocity at 1 mm from the border (dotted curve), and based on Eq. 5.2 (dash-dot curve).

5.4.3 Discussion

We also performed reproducibility checks for an Doppler OCT system:

- As illustrated in Fig. 5.29a, under steady laminar flow, the velocities change very little. We obtained this result by fixing the reference arm in a certain position, and recording the interferogram which corresponds to a signal within a small volume of the focus region of the microscope objective. The measurements were repeated 10 times with the same result .

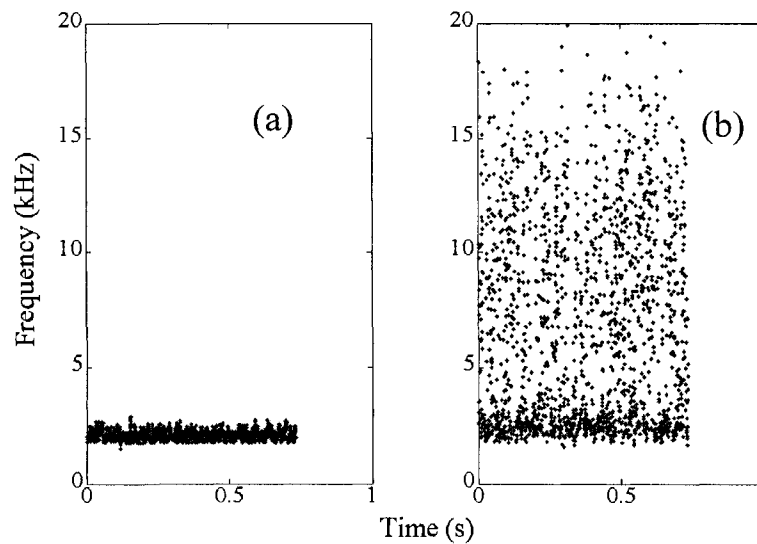


Fig. 5.29 The velocity change with time at a specified position within the phantom. (a) Stationary velocity. (b) Unstable velocity.

- With the liquid at rest, we obtained the Doppler frequency shift corresponding to the carrier frequency with a bandwidth of 0.5267 kHz. This bandwidth changed to 0.6442 kHz when the fluid flows. This means that the flow speed has a fluctuation of 115 Hz which could come from amplitude or direction variations.
- We also verified that the flow speed in the two branches is almost equal with a 2 % difference.
- Fig. 5.30 shows nine measurements of the velocities of single A-scan at the two different positions of the bifurcation phantom. The results indicate that the measurements are repeatable and the flow is steady.

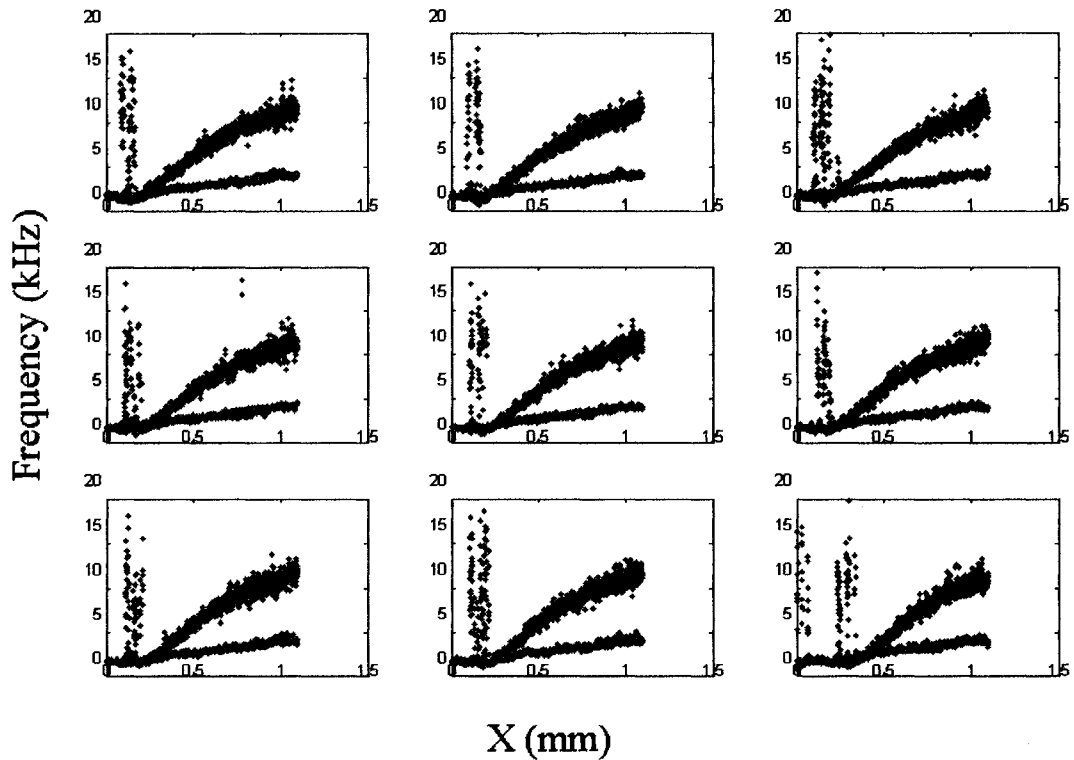


Fig. 5.30 The velocity curves at two positions within the phantom for nine measurements. Blue: velocity at the vertex (red mark in Fig. 5.4). Red: other region. At the origin, the large frequency fluctuations correspond to low SNR.

5.5 Conclusion

In conclusion, a quantitative analysis of WSS along the inside interface of a bifurcation phantom has been done based on the measurement of the velocity gradient close to the border by means of Doppler OCT. The experimental results have shown a significant improvement on the values of WSS obtained with currently used methods. This improvement is achieved because the Doppler OCT is capable of measuring velocity distribution with both high accuracy and high spatial resolution. These results support the view that Doppler OCT can become a powerful tool for the diagnosis of cardiovascular diseases by providing accurate WSS distributions.

5.6 Flow in the phantom of a stenosis using Doppler OCT [80]

The direct visualization of tissue structure and blood flow dynamics provides important information for biomedical research and clinical diagnostics. Also, simulations analytical models of fluid flow inside artery-shaped phantoms can be confirmed and quite useful for clinicians.

There are two often used phantoms in hemodynamics. The first one is the bifurcation phantom which has been discussed previously. The other one is the stenosis which is normally used to study the flow characteristics of blood when the vessel has some restriction. A typical stenosis is formed when fatty and inflammatory tissue builds up on the inside surface of an artery (plaque) which accumulates platelets, fibrin and other blood products to form a clot (thrombus). This leads to blockage of flow through the artery, which is known as an arterial stenosis as shown in Fig. 5.31.

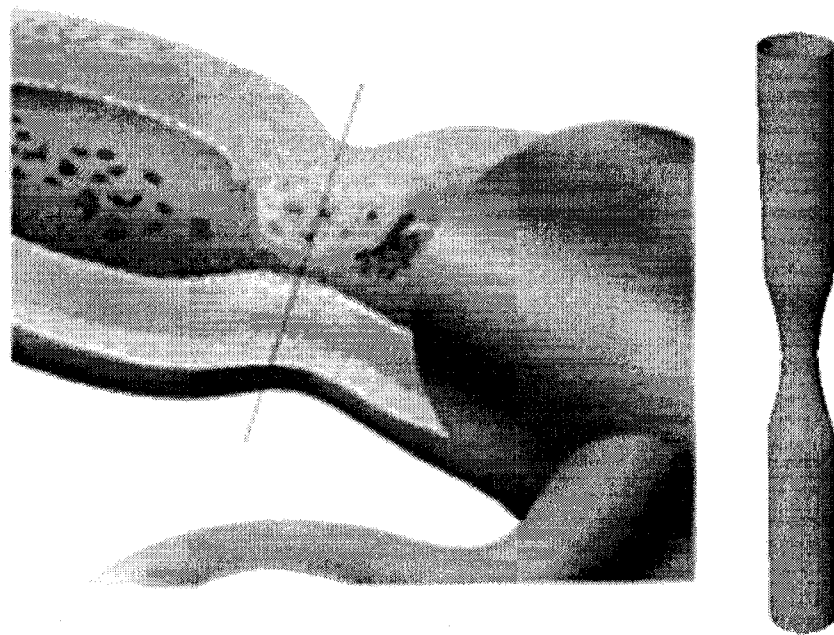


Fig. 5.31 A typical arterial stenosis [81].

An arterial stenosis may result in an abnormally high flow velocity that can induce very severe health problems, even leading to death. Therefore, the blood flow characteristics in the vicinity of a stenosis become very important for the study of the relationship between the restriction and the build up rate of fatty deposits. We propose to apply the Doppler OCT technique to blood flow monitoring inside the phantom of a stenosis in the hope of gaining some information on the mechanism of plaque formation and growth. Currently, the often used fluid for Doppler OCT measurements is a water solution of Intralipid. However, the strong absorption in the near infrared region has limited the penetration depth of light to only a few millimetres. In addition, most of the reported 2D velocity distributions of cross section are plots of the velocity projections on the A-scan axis. There are relatively few published methods for measuring the real vector velocity within the cross section of the fluid sample [27]. Our goal is to propose and demonstrate the capability of Doppler OCT for monitoring the laminar fluid-flow velocity distribution within a stenosis both with ultra-high penetration depth (~12 mm) and with the real velocity vectors. The experimental measurement of the vector velocity maps for liquid flow in stenosis phantom is highly relevant to cardiologists in order to better understand the effect of blood flow on the rupture potential of atherosclerotic plaques.

5.6.1 Experimental sample and setup

Fig. 5.32 shows the stenosis phantom used for the experiments. It has been tooled precisely from a polymethyl methacrylate (PMMA, commonly called Plexiglas) piece. The length of whole stenosis is 14 mm. The maximum diameter is 6 mm (outside the stenosis). The minimal diameter, which is located at the waist of the stenosis, is about 3.5 mm. It has then been fitted on both sides into a plexiglas tubes whose inner diameter was previously tooled in order to match exactly the diameter of the ends of the stenosis. Since the whole thickness of the stenosis is much larger than the penetration depth if one uses an intralipid

solution as the fluid sample, we used vegetable oil as the flowing liquid since it has a low absorption at the operating wavelength. We added titanium white paint (with particles about $1\ \mu\text{m}$ in size) as the scattering component. The flow rate inside the tube was taken to be constant and was adjusted by a flowmeter and a pump. Our Doppler OCT experimental setup has been presented in Chapter 2 and the analysis of the velocity distributions has also been discussed in detail previously in this thesis. In brief, this Doppler OCT experimental setup is based on a fiber-optic Michelson interferometer that uses a superluminescent diode (SLD) as the low-coherence light source. This source is characterized by a central wavelength of $\lambda_0 = 1545\ \text{nm}$ and a bandwidth of $\Delta\lambda = 32\ \text{nm}$. The scans are done at a typical speed of $1.5\ \text{mm/s}$ which amounts to a carrier frequency f_c of $1.94\ \text{kHz}$. Analog-to-digital conversion is achieved with a digital multimeter.

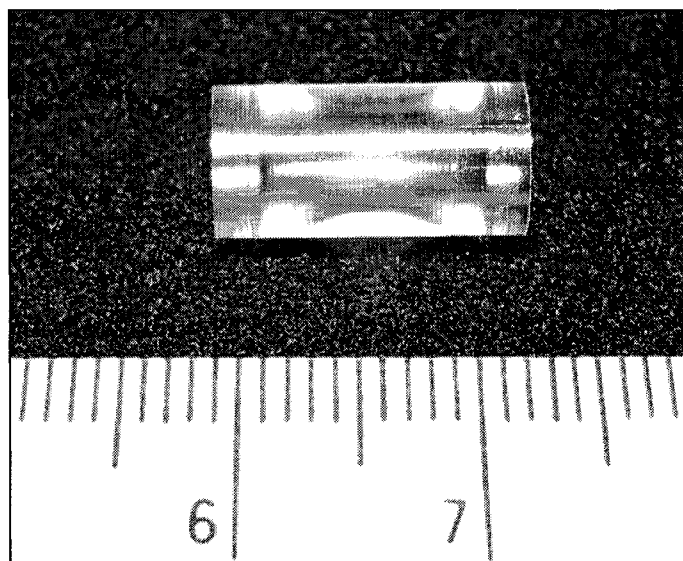


Fig. 5.32 The picture of the Plexiglas stenosis phantom used for the experiments.

First, we performed the cross-sectional OCT image of the phantom to make sure the sample is in the imaging field of the OCT setup. For emphasizing the backscattering signal

from the back interface of the stenosis, the focusing spot of the light beam was adjusted at a position deep into the fluid. Fig. 5.33 shows the OCT structural image of the sample. The fluid itself is homogeneous. The dark region indicates that the backscattering signal is stronger in the central area compared to that from the edges. The asymmetry comes from the fact that the image was acquired with an 8° angle between the normal direction of the tube and the sample beam.

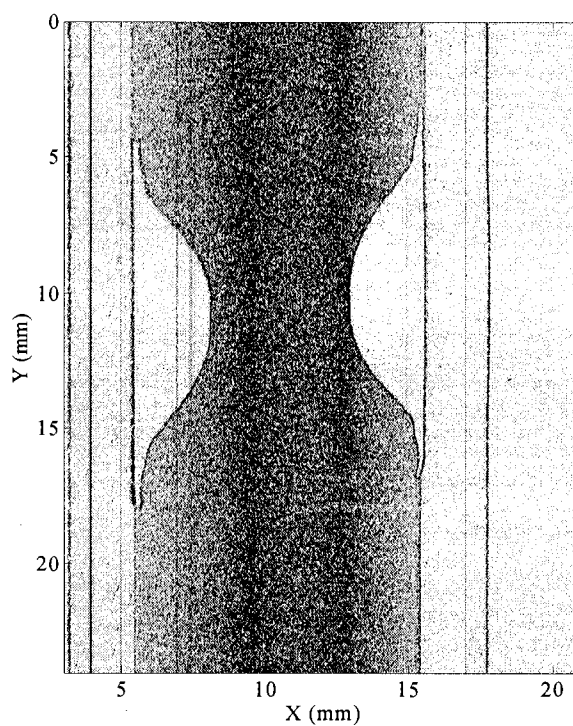


Fig. 5.33 The cross-sectional OCT image of the stenosis sample with scattering particles.

5.6.2 Experimental results and discussion

Then, we ran Doppler OCT experiments by increasing the sampling rate to 100 kHz for each A-scan (with the Doppler angle set at 8° from the normal direction). Once the data acquisition was finished, the data were saved into a Matlab file. We used our offline software for the phase detection using the zero-crossing algorithm. Details of this method can be

found in chapter 4 of this dissertation. The acquired raw frequency data was quite noisy since it contains many sources of noise coming from dispersion, high order scattering, a limited number of sampling points, and fluctuations of the scan speed of the reference mirror. Fig. 5.34 depicts the color coded raw frequency distribution within the stenosis sample. The raw frequency signal was then processed with the maximum likelihood method to the unwanted noise leading to the final Doppler frequency shift distribution of the stenosis shown in Fig. 5.35. For a better visibility, a 3D velocity distribution plot of the cross section of the stenosis obtained with the zero-crossing method is given in Fig. 5.36.

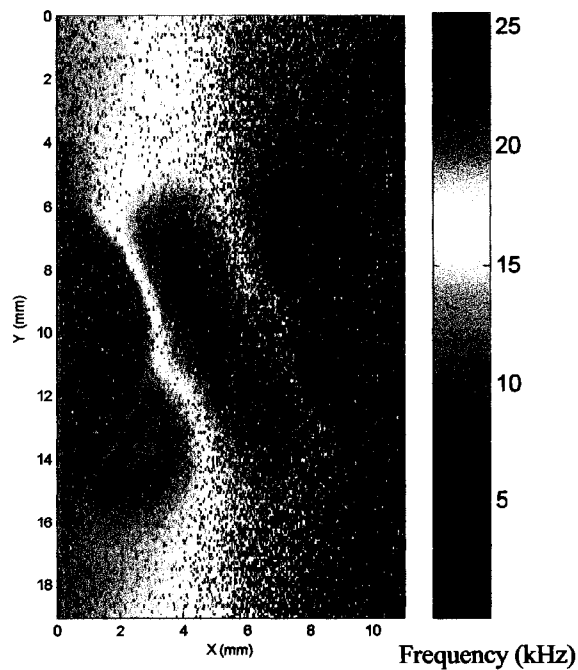


Fig. 5.34 The raw data of the cross-sectional velocity distribution of the stenosis.

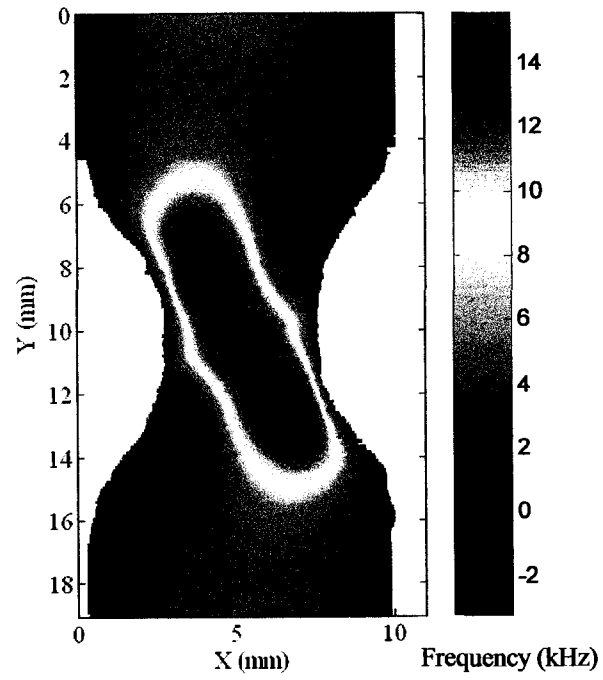


Fig. 5.35 The color coded 2D velocity distribution of the stenosis phantom.

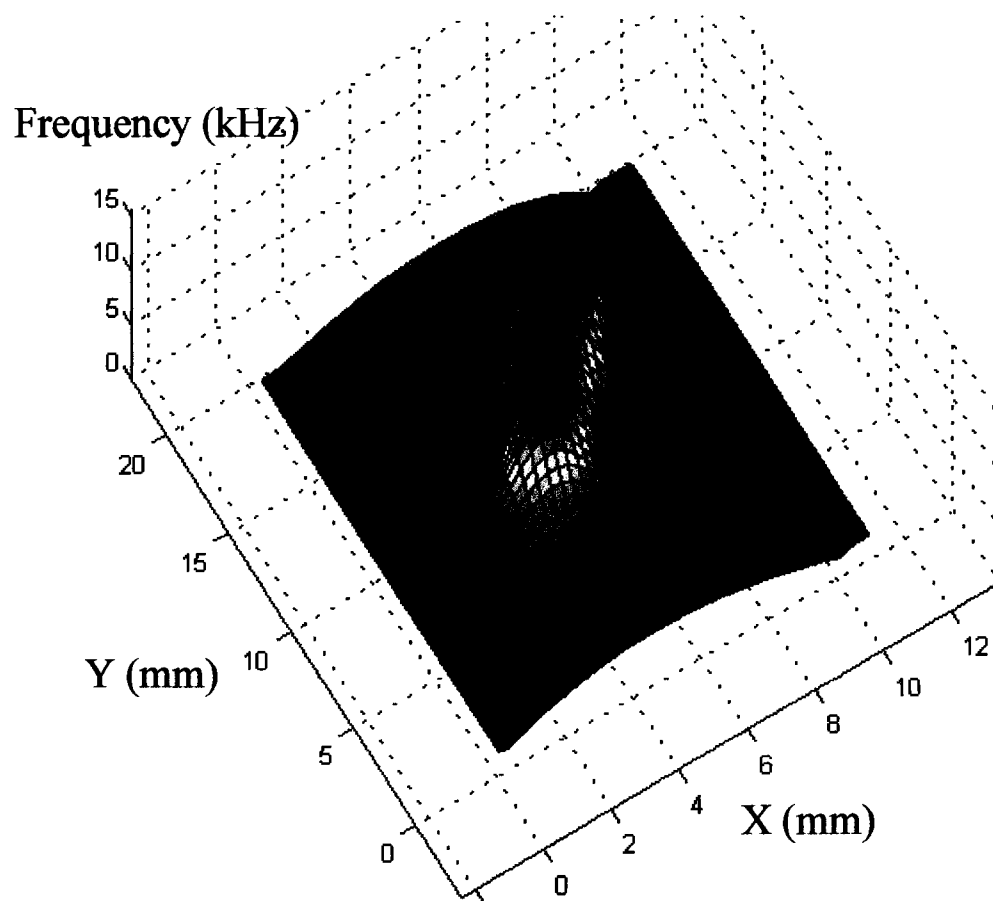


Fig. 5.36 3D representation of the 2D velocity distribution of the stenosis phantom. Color scale is the same as the one in Fig. 5.35.

5.6.3 Vector velocity map

We have stated earlier that the measured scalar velocity distribution is the velocity projection on the optical axis of the sample beam. This velocity projection is less meaningful than the real vector velocity since the latter contains more complete information, especially when the configuration of the sample is complicated. In order to obtain the vector velocity distribution inside the stenosis phantom, we performed another Doppler OCT experiment by using the method described in section 5.2.4. A vector measurement of the flow velocity in the image plane requires Doppler imaging at two different Doppler angles. For convenience, we chose the first angle as normal incidence with respect to the external surface of the tube,

as shown in Fig. 5.37. The second angle was chosen at 10° from the normal incidence. The vector velocity \vec{V} can be calculated from the measured velocity projections v_{0° and v_{10° using formula 5-10.

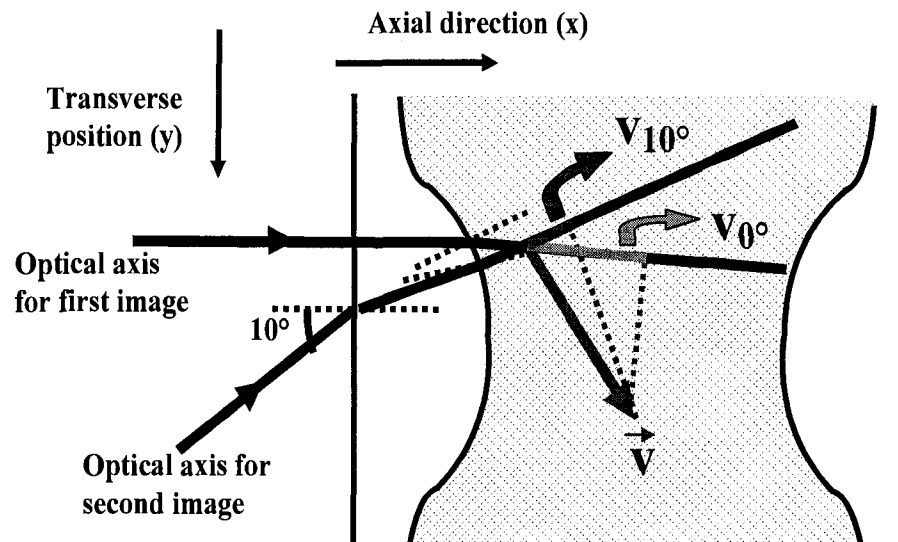


Fig. 5.37 Schematic representation of light propagation inside the stenosis.

In order to get a laminar flow at the input of the stenosis, we used a 1.5 m long rigid straight tube as a transition guide. To confirm that the input velocity profile of the stenosis was parabolic, we first performed a Doppler OCT measurement of the velocity profile at a position located approximately 4 mm upstream from the beginning of the stenosis. The measurements were done at normal incidence and 10° from the normal incidence. The results indicated that the speed component parallel to the x axis was negligible compared to the speed component measured at 10° incidence. We concluded that the flow was almost unidirectional in the y direction at this position. Fig. 5.38 depicts the speed profile at this position which is parabolic, thus indicating a typical laminar flow.

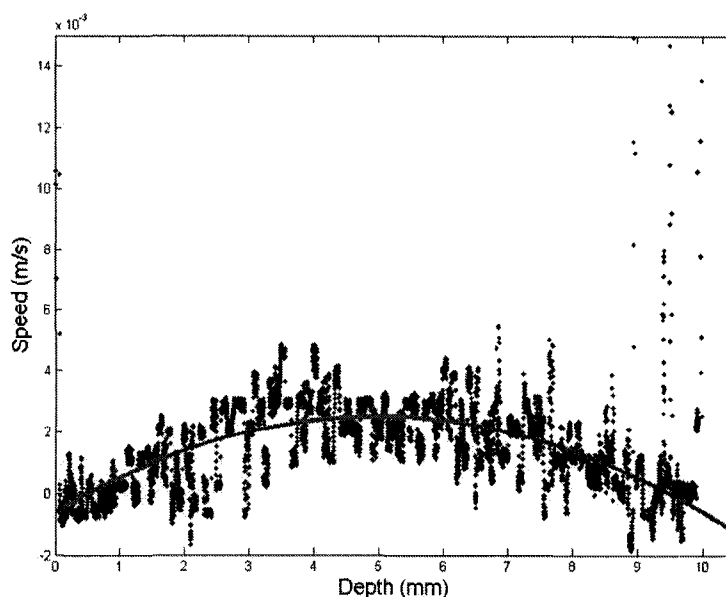


Fig. 5.38 Flow profile inside the tube 4 mm before the beginning of the stenosis. The red curve is a parabolic fit.

As we have discussed in section 5.4.2, we had to apply a geometrical transformation to the 2D velocity distribution obtained at 10° from the normal incidence in order to match the optical paths when we overlap it with the map obtained at normal incidence. This way, Doppler images at 0° and 10° are congruent and a 2D vectorial flow map can be obtained on a common grid.

We have applied this method to find the 2D vector velocity maps inside the stenosis as shown in Fig. 5.39. We provide experimental results at two different flow rates ($70 \mu\text{l/s}$ and $30 \mu\text{l/s}$). The distance between two lateral A-scans was set at $100 \mu\text{m}$ which determines the lateral resolution of the Doppler frequency distribution images realized at 0 and 10° (a and d). We need also to define a coordinate grid for plotting the velocity vectors at each position within the stenosis. In (c) and (f) the grid is depicted and has a mesh of $900 \mu\text{m}$ in the transverse direction and $280 \mu\text{m}$ in the axial direction. The 2D vector velocity maps (d and f) provide a clearer version of the flow information than the scalar 2D velocity distribution

images (a, b, d, and e). In general, the 2D vector velocity maps show a clear laminar regime over the whole diameter of the stenosis. It is attributed to the fact that the flow rates are very low and comes from a very low Reynolds number which indicates that the flow is stable. In addition, compared to the velocity distribution of the bifurcation phantom, the stenosis does not show an anomalous area where the velocities are out of the measurement range of the Doppler OCT system. This is also due to the fact that the stenosis phantom changes its shape smoothly without any abrupt geometry change. Near the waist of the phantom, we can see clearly that the velocity increases which illustrates the venturi effect. This is one of the main factors causing plaque rupture[82, 83] since it induces an increasing shear stress near the wall. Furthermore, near the regions where the diameter changes rapidly, we can see vortices appearing near the walls. In these regions, the speed seems to follow a circular pattern the centre of which the velocity becomes null. These regions are equally important in the development of atherosclerotic plaque since it may be propitious to fat particles deposition on the artery walls [84].

In conclusion, an experimental 2D vector velocity map of flow within a stimulated phantom has been obtained for the first time with our Doppler OCT system. This system uses time-domain OCT signals on which we apply an accurate phase detection algorithm. The general flow is characterized as laminar with a speed increasing in the waist region. Vortices have shown up as expected from simulation models. These maps provide very important velocity information which is valuable for clinical applications such as cardiovascular hemodynamics.

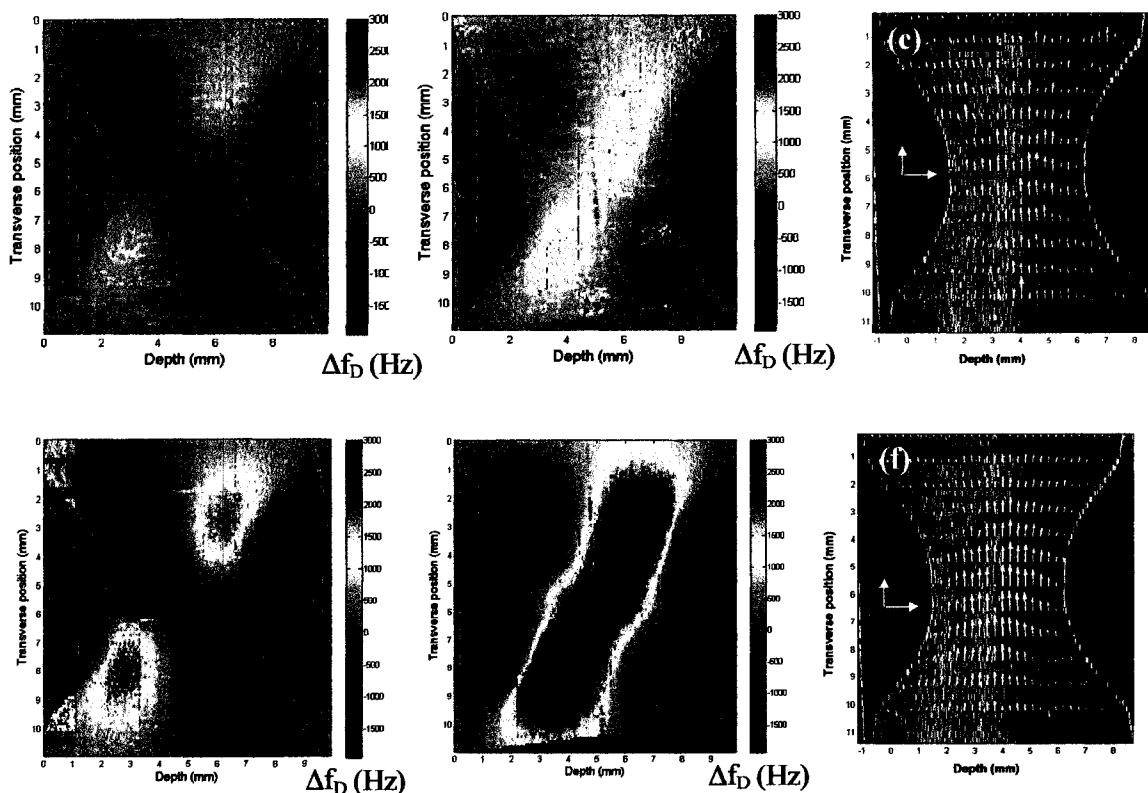


Fig. 5.39. Flow profiles and 2D vectorial flow maps inside a stenosis phantom at mean flow rates of $70 \mu\text{l/s}$ (a, b, c) and $30 \mu\text{l/s}$ (d, e, f). From left to right, Doppler frequency map at 0° incidence angle, Doppler frequency map at 10° incidence angle, and 2D flow map superposed on structural OCT image.

5.7 Applications in microfluidics and in a rectangular channel

Microfluidic devices have attracted a great deal of attention during the past several years because of their applications in analysis, medical diagnostics, and synthetic chemistry. These devices offer several advantages over macroscale laboratory operations, e.g., small fluid volume consumption, faster analysis and response times, and integration of multiple lab processes. For instance, instead of the current laboratory practice which requires much larger amounts of samples and reactants and which entails slower reaction times, microfluidic methods require a thousand times less chemicals and bring about much faster reaction rates due to short diffusion distances and smaller heat capacities.

A better understanding of the physics of the motion behaviour inside a microchannel environment is essential for a precise control of that motion. Since the fluids move in microchannels as thin as a hair, their behaviour can differ from macroscopic behaviour because of many factors such as surface tension, energy loss, and so on. These differences may induce a flow behaviour that differs from usual theoretical predictions. Therefore, an experimental method for obtaining the velocity distribution within microfluidic circuits becomes essential. Existing tools such as Doppler ultrasound suffer from low spatial resolution. Laser Doppler velocimetry provides the flow speed with poor accuracy. Doppler OCT is currently the only method capable of yielding flow velocity profiles in microfluidic circuits with sufficient resolution.

The description of our Doppler OCT system has been given previously in this dissertation. For the microfluidics sample, we used an internally developed broadband light source with a low coherence length ($\sim 10 \mu\text{m}$) in order to match the small scale of the sample [85]. This source is characterized by a central wavelength of $\lambda_0 = 1525 \text{ nm}$ and a bandwidth of $\Delta\lambda = 145 \text{ nm}$. A test was performed on a micro channel ($\sim 110 \mu\text{m}$) to make sure that our system works well for a small size sample. The fluid used was 1% intralipid water solution whose flow rate was controlled by a flow meter and a pump. Fig. 5.40 depicts the OCT structural image of the channel. Since the small size channel can be covered by the focusing field of the sample beam, the cross-sectional OCT image appears homogeneous everywhere within the sample.

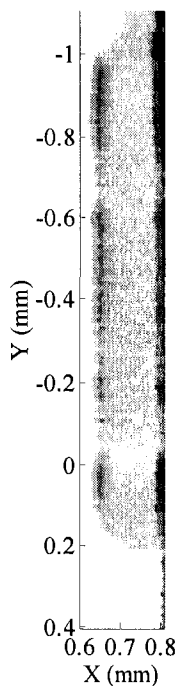


Fig. 5.40 Cross-sectional image of the microchannel.

Afterwards, we performed the Doppler OCT imaging in order to obtain the velocity profiles of the fluid sample. We also used the zero-crossing algorithm for the phase detection. The final 2D velocity distribution and a 3D plot are given in Fig. 5.41. It shows that the flow was laminar with a parabolic profile although the dimensions were very small. By overlapping the structural image with the velocity distribution map, we obtain a color coded distribution map of the velocity at each position of the fluid sample, as shown in Fig. 5.42.

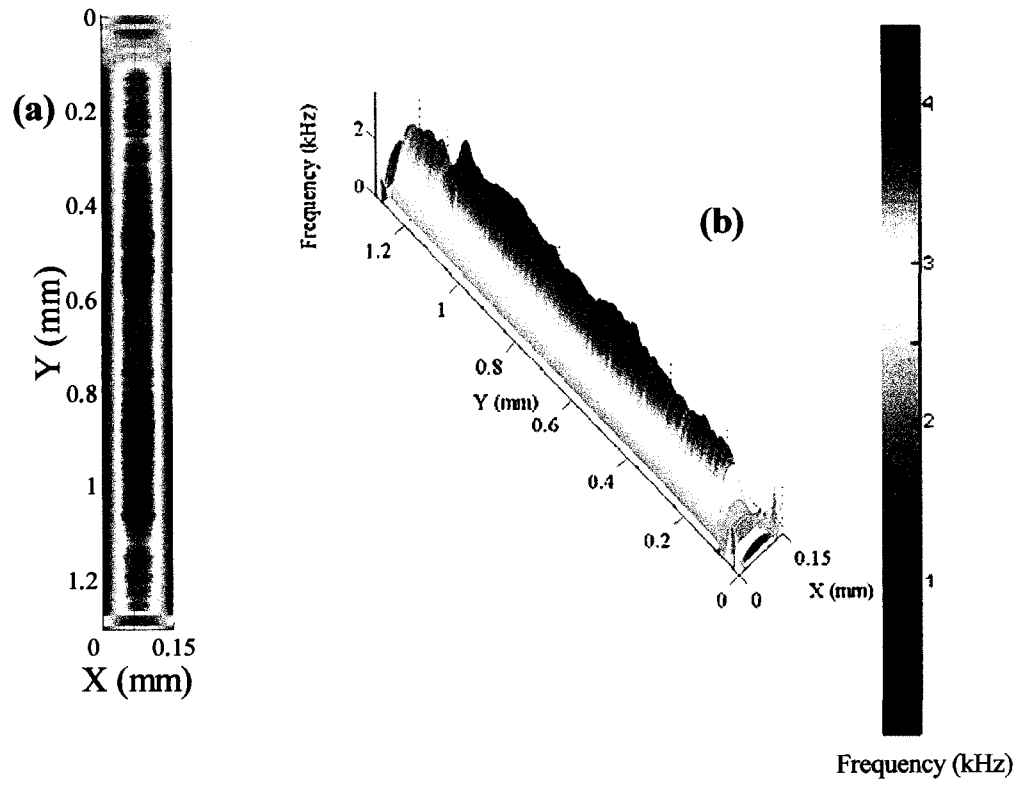


Fig. 5.41 2D and 3D Velocity distribution within the microchannel.

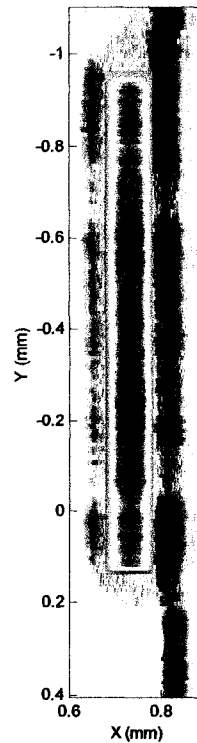


Fig. 5.42 Overlap of the structural image with the velocity distribution map. The color scale is the same as in Fig. 5.41. Carrier frequency is 1.94kHz.

We have used our Doppler OCT setup on a microfluidic circuit provided by Prof. O. Guenat and his group (see Fig. 5.43). This sample was fabricated by a microfabrication process used for obtaining a mask with photolithography and wet etching. The material was polydimethylsiloxane (PDMS). The inlet and outlet ports were fitted with thin glass tubes and connected to the sample with silicon glue to prevent leaking. The sealing of the circuit on a thin glass plate ($\sim 200 \mu\text{m}$ thickness) was achieved with RIE. This microfluidic circuit is used to study the interaction between some injected cells and the buffer fluid when they mix. It is a common application for microfluidic circuits since a complete and thorough mixing is necessary for many biochemical reactions. Fig. 5.44 depicts the detailed structure of the micro channels. Our goal in this experiment was to verify if the sample had some structural anomalies and to obtain the velocity maps of the eight microchannels in order to see if they

matched what was designed.

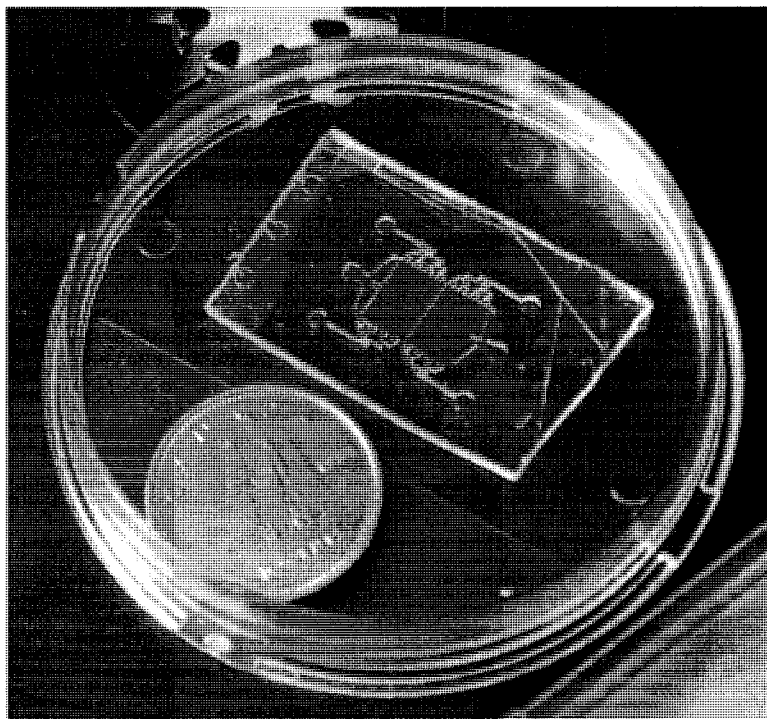


Fig. 5.43 Example of microfluidic circuit developed at Ecole Polytechnique (O. Guenat).

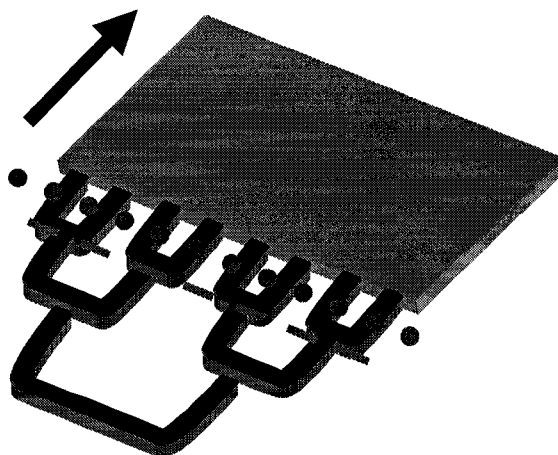


Fig. 5.44 Structure of the microchannels in the microfluidic sample (O. Guenat).

In Fig. 5.45, we illustrate the experimental results for the measurement of the flow

behaviour within the multi-channel sample. It can be seen that some of the microchannels had defects in their structural features even though the absolute geometric accuracies and precision are very high. These defects can cause severe problems for this kind of devices since they may affect the flow characteristics strongly. One expects that the flow is laminar with a parabolic velocity profile in each single microchannel. However, the measured velocity distributions indicate that most of the microchannels are not parabolic. In addition, the flow speeds in the microchannels are different from one another. The direct visualization of the fluid flow velocity in microfluidic samples carries very important information on motion inside the microchannels which is quite useful for both the inspection of the structural features and for the control of motion. The ability of resolving the velocity profile on a microscale using Doppler OCT depends on the coherence length of the light source, which is about $10\ \mu\text{m}$ in our case.

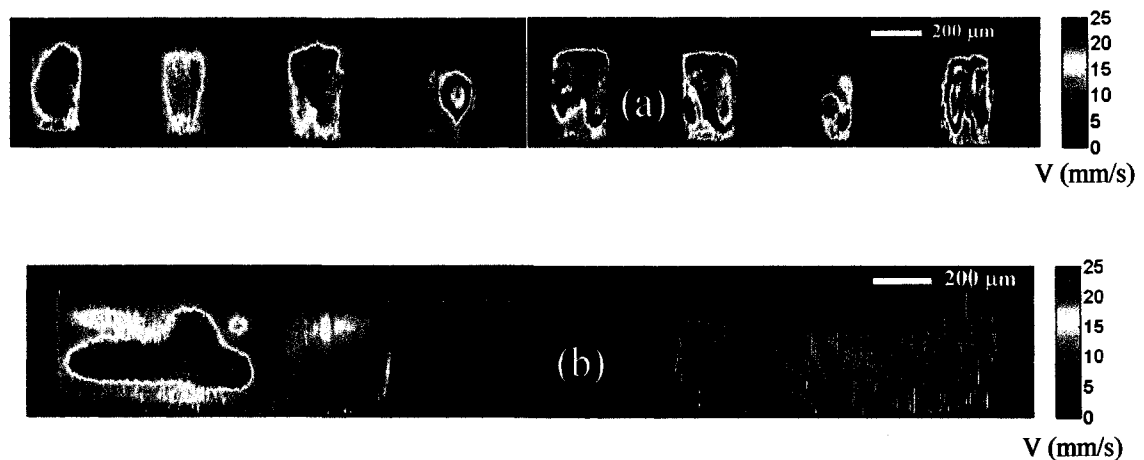


Fig. 5.45 2D visualizations of fluid dynamics of the microchannel sample. (a) microchannel indicated as dotted line in Fig. 5.44 (b) microchannel indicated as dashed line in Fig. 5.44. Scale corresponds to optical path (index dependent; for intralipid solution: $n = 1.33$).

We also tried to use our Doppler OCT system on a larger size (\sim tens of cm) fluidic circuit. It was possible with a fluid that had a low attenuation at the working wavelength.

That circuit was a Y junction with rectangular shape channels and was provided by Prof. Kadem from Concordia U. The flow was set to be very slow using a pump to ensure a laminar behaviour. Fig. 5.46 shows the velocity distributions at four selected positions of the circuit. The results indicate the Doppler OCT was successfully applied in larger size fluid channels and was capable of producing velocity distribution information with high accuracy in a non-invasive way. These measured flow fields can now be compared with the experimental results obtained by other methods such as particle imaging velocimetry (PIV) and magnetic resonance imaging (MRI).

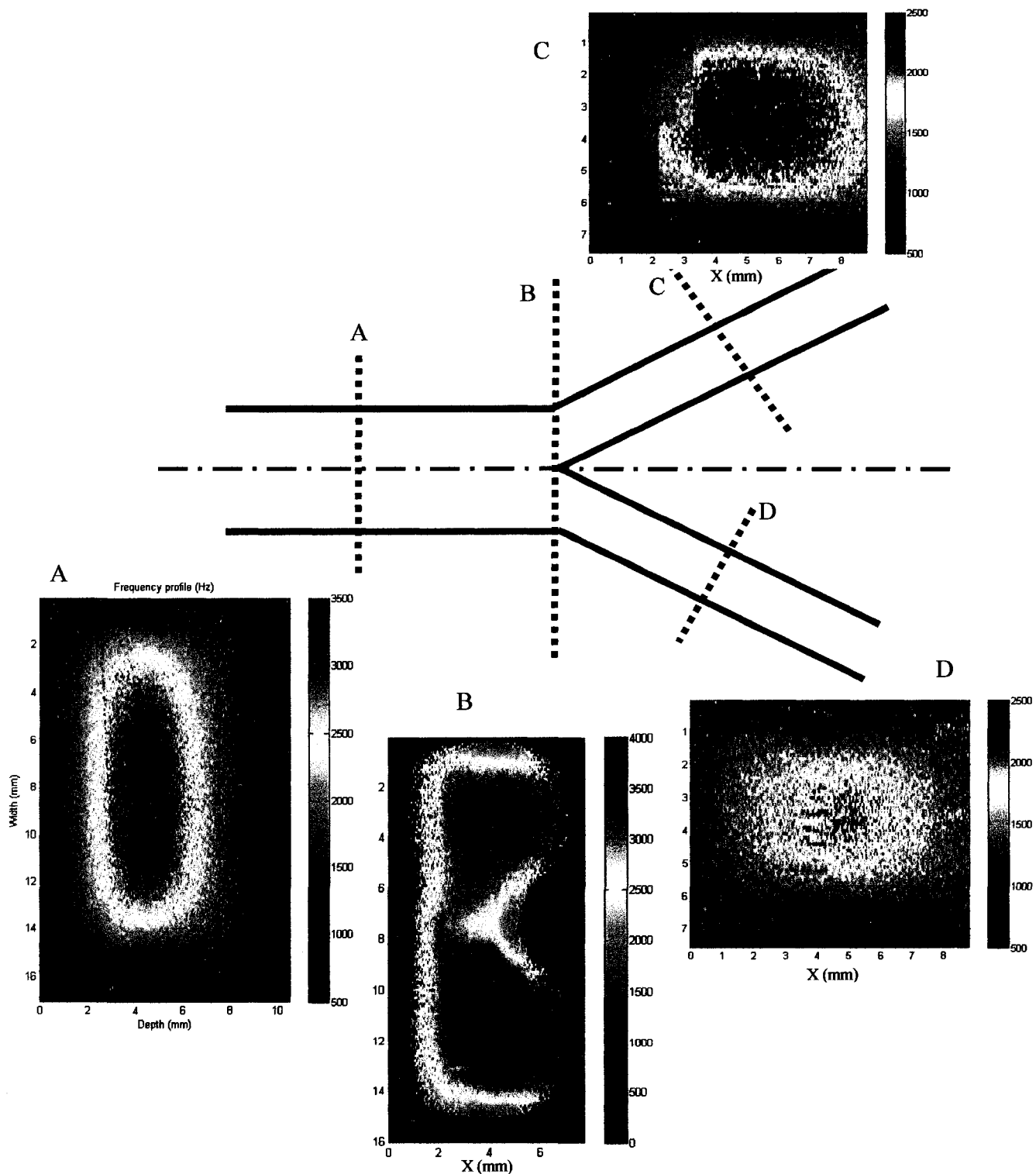


Fig. 5.46 2D local velocity distributions for a stationary flow at different cross-sections in a Y junction circuit. All the color bars are expressed in Hz.

CHAPTER 6

Conclusion

6.1 Summary

This dissertation described the development of a non-invasive optical imaging implementation of OCT for detecting both the structural and flow information of various samples. Several applications of this system have been demonstrated and discussed in detail pointing at significant progress, especially in the fields of microfluidics and cardiovascular hemodynamics. This research project focused on the accuracy that Doppler OCT can achieve for velocity detection without restriction on some other important parameters such as the dynamic range of the measurement. Also, the performance of the system is such that the wall shear stress (WSS) can be directly detected using the measured velocity gradient within the fluid near the boundary. This work focused also on searching for the most accurate algorithm for data processing in order to detect and quantify the velocity profiles within a sample of microscopic scale. By choosing a proper fluid, we have increased the working depth of the Doppler OCT system into the centimetre scale from a few millimetres which is usual for a standard Doppler OCT system. This thesis has been devoted to the above topics and has demonstrated the potential of Doppler OCT as a powerful tool for the vector velocity mapping of the flow in the investigated phantoms. This research led to nine (9) publications listed earlier. The progress made in this dissertation is summarized below.

In Chapter 2 the design and fabrication of free-space and fiber based OCT implementations has been illustrated. A Ti:sapphire mode-locked femtosecond pulsed laser was employed as the broadband source providing an axial resolution as high as $3.5 \mu\text{m}$ in the resulting structural OCT images. By performing the envelop detection of the interferogram in hardware, the time for the data acquisition has been reduced by. Deconvolution has also

been developed in software in order to eliminate the sidelobe effects leading to a better contrast of the OCT image without a significant degradation of the resolution.

The completed OCT systems have been used in the study of the relationship between the optical properties of a sample and the quality of the image in terms of contrast and penetration depth. We accomplished these comparative studies using three different sources with central wavelength at 810 nm, 1.3 μm and 1.5 μm , for several in vitro biological tissues, employing a graphical method. We have concluded that the 1.3 μm sources provide a good compromise among these three sources.

As described in Chapter 3, a data processing approach was proposed to evaluate the possibility of adapting a pseudo Wigner distribution phase detector as a velocity estimator in time-domain Doppler OCT. Its performance was demonstrated by a comparison with other currently used algorithms in terms of accuracy. Using the well understood case of a laminar flow in a rectilinear capillary tube, we were able to conclude that the pseudo Wigner-distribution signal processing method is overall more precise.

We also put forward the assumption that in Doppler OCT the time-domain approach is preferable to the Fourier domain approach and have defended this point of view by compiling the results of a survey of recently available publications. We have shown the advantages of choosing the time domain for Doppler OCT as it can cover a wider velocity span (from 1 $\mu\text{m/s}$ up to 10 to 20 m/s), giving a dynamic range of 70 dB and more. We have described, in Chapter 4, another novel, simple and less time-consuming processing method based on the zero-crossing point detection in OCT for obtaining the Doppler frequency shifts. The principle on which the zero-crossing method relies for its successful performance is that the local OCT interference signal is almost a single periodic waveform. We also found that the zero-crossing method is less dependent on slowly-varying velocity profiles and has a

lower signal-to-noise ratio. Furthermore, the relative simplicity of the arithmetic operations also reduces the computational time substantially.

Finally, we have demonstrated applications of our Doppler OCT system in microfluidics and cardiovascular hemodynamics by obtaining accurate 2D velocity distribution. We have also calculated the 2D velocity vector plots of some flow phantoms which is an important step towards a better understanding of the fluid dynamics involved in cardiovascular research. These flow characteristics are believed to play an important role in atherosclerosis formation and growth. We also simulated the experimental phantoms theoretically by means of software Fluent under steady flow conditions. The proposed approach for obtaining the vector velocity map of the flow can be extremely useful as an initial step for blood flow characterization in stenosis and bifurcation phantoms.

6.2 Unsolved issues

- The data acquisition time of our Doppler OCT apparatus is limited by two main factors. First, the maximum speed of the reference mirror is only 1.5 mm/s. The second one is that the maximum sampling rate of the digital multimeter for A/D converter, is only 100 kHz.
- The zero-crossing phase detection method is software-based offline which limits the data processing rate.
- Because of a long data acquisition time, the fluid flow characteristics within the phantoms can change and turbulent conditions cannot be investigated with our current Doppler OCT apparatus.
- For more accurate WSS calculation and more detailed vortex information, 3D vector velocity distributions are needed.

- The currently used probe station could be more compact which would permit velocity detection of large size or complicated samples.

Most if not all of these limitations can be solved if sufficient funding can be provided as now explained.

6.3 Future prospects

In the real clinical applications or motion investigations in flow phantoms, a real-time, highly accurate velocimetry with a large measurement dynamic range is always preferable. Therefore, our Doppler OCT system could be widely accepted if the following two parameters are addressed. The first one is to increase the scanning rate of the reference mirror from around 1 Hz to 2 kHz by employing a fast rotating reflector shaped by a circular involute curve for instance. Fast delay lines are available at a cost. The second one is to replace the digital multimeter by a PCI card thus increasing the sampling rate of the system from the current 100 kHz to 200 MHz. This way, a frame rate of more than 10 OCT images per second can be expected.

Another issue that needs to be addressed is to perform the zero-crossing detection by a frequency-to-voltage converter or another online hardware method. This way, real-time frequencies of the interference fringe intensities can be obtained automatically and be recorded by the computer directly.

A key parameter in OCT is the image resolution which mainly depends on the coherence length of the broadband source. Our fiber-based OCT setup has an ultra broad bandwidth source which can work in both the 1.3 μm and 1.5 μm wavelength regime. Using a combination of semiconductor amplifier with the optical amplifier [85], we have achieved more than 145 nm bandwidth at a central wavelength of 1525 nm. The next stage would be to

add a broadband source in the 1.3 μm range. The idea is to produce an ultra broad source that covers the spectral range from 1.3 μm to 1.5 μm . This way, sub-3 μm spatial resolution OCT image can be expected. Other broadband sources can also be developed.

The construction of a flexible probe or catheter could be realized incorporating a small lens on a fiber end and on optical fiber assemblies. This catheter-like probe station could be used to perform Doppler OCT acquisitions on complicated samples.

The purpose of this research work was to open the way to a larger acceptance of Doppler OCT but many improvements can obviously be envisaged. It is a matter of time, money and ingenuity.

REFERENCES

- [1] D. Huang, E. A. Swanson, C. P. Lin, J. S. Schuman, W. G. Stinson, W. Chang, M. R. Hee, T. Flotte, K. Gregory, C. A. Puliafito, and J. G. Fujimoto, "Optical Coherence Tomography," *Science*, vol. 254, pp. 1178-1181, 1991.
- [2] G. J. Tearney, M. E. Brezinski, S. A. Boppart, C. Pitris, B. E. Bouma, J. F. Southern, and J. G. Fujimoto, "High resolution imaging of pathologic gastrointestinal tissues using optical coherence tomography.," *Gastroenterology*, vol. 112, pp. A667-A667, 1997.
- [3] J. G. Fujimoto, C. Pitris, S. A. Boppart, and M. E. Brezinski, "Optical coherence tomography: An emerging technology for biomedical imaging and optical biopsy," *Neoplasia*, vol. 2, pp. 9-25, 2000.
- [4] J. A. Izatt, M. D. Kulkarni, S. Yazdanfar, J. K. Barton, and A. J. Welch, "In vivo bidirectional color Doppler flow imaging of picoliter blood volumes using optical coherence tomography," *Optics Letters*, vol. 22, pp. 1439-1441, 1997.
- [5] A. Das, M. V. Sivak Jr, A. Chak, R. C. K. Wong, V. Westphal, A. M. Rollins, J. Willis, G. Isenberg, and J. A. Izatt, "High-resolution endoscopic imaging of the GI tract: A comparative study of optical coherence tomography versus high-frequency catheter probe EUS," *Gastrointestinal Endoscopy*, vol. 54, pp. 219-224, 2001.
- [6] W. Drexler, U. Morgner, F. X. Kartner, C. Pitris, S. A. Boppart, X. D. Li, E. P. Ippen, and J. G. Fujimoto, "In vivo ultrahigh-resolution optical coherence tomography," *Optics Letters*, vol. 24, pp. 1221-1223, 1999.
- [7] L. C. R. Maciejko, M. Lestrade, Z. Xu, and R. Kashyap, "Optical sources for OCT," *Photons*, vol. 3, pp. 28-30, spring 2005.
- [8] J. L. Hougaard, L. Kessel, B. Sander, K. Kyvik, O. Kirsten, and M. Larsen, "Variation in retinal nerve fibre layer thickness: a twin-study," *Acta Ophthalmologica Scandinavica*, vol. 81, pp. 93-94, 2003.
- [9] R. G. Cucu, A. G. Podoleanu, J. Pedro, J. A. Rogers, R. B. Rosen, M. Van Velthoven, P. Garcia, and V. Shidlovski, "Dual SLO/T-scan based en face ultrahigh resolution OCT for ophthalmic imaging," San Jose, CA, United States, 2006.
- [10] R. D. Ferguson, D. X. Hammer, L. A. Paunescu, S. Beaton, and J. S. Schuman, "Tracking optical coherence tomography," *Optics Letters*, vol. 29, pp. 2139-2141, 2004.
- [11] R. Gurses-Ozden, C. Teng, R. Vessani, S. Zafar, J. M. Liebmann, and R. Ritch, "Macular and retinal nerve fiber layer thickness measurement reproducibility using optical coherence tomography (OCT-3)," *Journal of Glaucoma*, vol. 13, pp. 238-244,

2004.

- [12] Z. P. Chen, T. E. Milner, D. Dave, and J. S. Nelson, "Optical Doppler tomographic imaging of fluid flow velocity in highly scattering media," *Optics Letters*, vol. 22, pp. 64-66, 1997.
- [13] X. J. Wang, T. E. Milner, and J. S. Nelson, "Characterization of fluid flow velocity by optical Doppler tomography," *Optics Letters*, vol. 20, pp. 1337-9, 1995.
- [14] Z. Chen, T. E. Milner, S. Srinivas, X. Wang, A. Malekafzali, M. J. C. van Gemert, and J. S. Nelson, "Noninvasive imaging of in vivo blood flow velocity using optical Doppler tomography," *Optics Letters*, vol. 22, pp. 1119, 1997.
- [15] S. A. Boppart, G. J. Tearney, B. E. Bouma, J. F. Southern, M. E. Brezinski, and J. G. Fujimoto, "Noninvasive assessment of the developing Xenopus cardiovascular system using optical coherence tomography," *Proceedings of the National Academy of Sciences of the United States of America*, vol. 94, pp. 4256-4261, 1997.
- [16] S. Yazdanfar, M. D. Kulkarni, and J. A. Izatt, "High resolution imaging of in vivo cardiac dynamics using color Doppler optical coherence tomography," *Optics Express*, vol. 1, pp. 424-431, 1997.
- [17] D. Morofke, M. C. Kolios, I. A. Vitkin, and V. X. D. Yang, "Wide dynamic range detection of bidirectional flow in Doppler optical coherence tomography using a two-dimensional Kasai estimator," *Optics Letters*, vol. 32, pp. 253-255, 2007.
- [18] R. A. Leitgeb, L. Schmetterer, C. K. Hitzenberger, A. F. Fercher, F. Berisha, M. Wojtkowski, and T. Bajraszewski, "Real-time measurement of in vitro flow by Fourier-domain color Doppler optical coherence tomography," *Optics Letters*, vol. 29, pp. 171-3, 2004.
- [19] B. J. Vakoc, S. H. Yun, J. F. De Boer, G. J. Tearney, and B. E. Bouma, "Phase-resolved optical frequency domain imaging," *Optics Express*, vol. 13, pp. 5483-5493, 2005.
- [20] R. A. Leitgeb, L. Schmetterer, W. Drexler, A. F. Fercher, R. J. Zawadzki, and T. Bajraszewski, "Real-time assessment of retinal blood flow with ultrafast acquisition by color Doppler Fourier domain optical coherence tomography," *Optics Express*, vol. 11, pp. 3116-3121, 2003.
- [21] J. M. Schmitt, A. Knüttel, and R. F. Bonner, "Measurement of Optical-Properties of Biological Tissues by Low-Coherence Reflectometry," *Applied Optics*, vol. 32, pp. 6032-6042, 1993.
- [22] K. Naganuma, and K. Mogi, "50-fs pulse generation directly from a colliding-pulse mode-locked Ti:Sapphire laser using an antiresonant ring mirror," *Optics Letters*, vol. 16, pp. 738-740, 1991.

- [23] D. E. Spence, P. N. Kean, and W. Sibbett, "60-fsec pulse generation from a self-mode-locked Ti:Sapphire Laser," *Optics Letters*, vol. 16, pp. 42-44, 1991.
- [24] C. Huang, H. C. Kapteyn, J. W. Mcintosh, and M. M. Murnane, "Generation of transform-limited 32-fs pulses from a self-mode-locked Ti:Sapphire Laser," *Optics Letters*, vol. 17, pp. 139-141, 1992.
- [25] Z. Xu, "Implementations of optical coherence tomography," *Ecole Polytechnique*, vol. Master's thesis, 2003.
- [26] Z. P. Chen, Y. H. Zhao, S. M. Srinivas, J. S. Nelson, N. Prakash, and R. D. Frostig, "Optical Doppler tomography," *Ieee Journal of Selected Topics in Quantum Electronics*, vol. 5, pp. 1134-1142, 1999.
- [27] L. Wu, "Simultaneous measurement of flow velocity and Doppler angle by the use of Doppler optical coherence tomography," *Optics and Lasers in Engineering*, vol. 42, pp. 303-313, 2004.
- [28] M. Bashkansky, M. D. Duncan, and J. Reintjes, "Signal processing for improving field cross-correlation function in optical coherence tomography," *Applied Optics*, vol. 37, pp. 8137-8138, 1998.
- [29] Y. T. Pan, R. Birngruber, J. Rosperich and R. Engelhardt, "Measurement of optical-interaction coefficients of intralipid in visible and NIR range," *Proc. SPIE*, vol. 2134, pp. 354-363, 1994.
- [30] A. I. Kholodnykh, I. Y. Petrova, K. V. Larin, M. Motamedi, and R. O. Esenaliev, "Precision of measurement of tissue optical properties with optical coherence tomography," *Applied Optics*, vol. 42, pp. 3027-3037, 2003.
- [31] J. M. Schmitt, A. Knüttel, M. Yadlowsky and M. A. Eckhaus, "Optical-coherence tomography of a dense tissue: statistics of attenuation and backscattering," *Phys. Med. Biol.*, vol. 39, pp. 1705-1720, 1994.
- [32] D. Levitz, L. Thrane, M. H. Frosz, P. E. Andersen, C. B. Andersen, J. Valanciunaite, J. Swartling, S. Andersson-Engels, and P. R. Hansen, "Determination of optical scattering properties of highly-scattering media in optical coherence tomography images," *Optics Express*, vol. 12, pp. 249-259, 2004.
- [33] Y. Pan and D. L. Farkas, "Noninvasive imaging of living human skin with dual-wavelength optical coherence tomography in two and three dimensions," *J. Biomed. Opt.*, vol. 3, pp. 446-455, 1998.
- [34] Y. H. Zhao, Z. P. Chen, C. Saxer, S. H. Xiang, J. F. de Boer, and J. S. Nelson, "Phase-resolved optical coherence tomography and optical Doppler tomography for imaging blood flow in human skin with fast scanning speed and high velocity sensitivity," *Optics Letters*, vol. 25, pp. 114-116, 2000.

- [35] L. Wang, W. Xu, M. Bachman, G. P. Li, and Z. P. Chen, "Phase-resolved optical Doppler tomography for imaging flow dynamics in microfluidic channels," *Applied Physics Letters*, vol. 85, pp. 1855-1857, 2004.
- [36] A. M. Rollins, S. Yazdanfar, R. Ung-arunyawee, and J. A. Izatt, "Real time color Doppler optical coherence tomography using an autocorrelation technique," *Proceedings of SPIE - The International Society for Optical Engineering*, vol. 3598, pp. 168-176, 1999.
- [37] B. E. Bouma, and G. J. Tearney, *Handbook of Optical Coherence Tomography*. Switzerland: Marcel Dekker Inc., 2002.
- [38] Z. Chen, T. E. Milner, S. Srinivas, X. Wang, A. Malekafzali, M. J. C. van Gemert, and J. S. Nelson, "Noninvasive imaging of in vivo blood flow velocity using optical Doppler tomography," *Optics Letters*, vol. 22, pp. 1119-1121, 1997.
- [39] L. Cohen, *Time-frequency analysis*. Englewood Cliffs, N.J: Prentice Hall PTR, 1995.
- [40] Z. Q. Xu, L. Carrion, and R. Maciejko, "An assessment of the Wigner distribution method in Doppler OCT," *Optics Express*, vol. 15, pp. 14738-14749, 2007.
- [41] F. Auger, Flandrin, P., Gonçalvès, P., and Lemoine, O., "Time-Frequency Toolbox tutorial," *CNRS (France), Rice U. (U.S.A.)*, vol. <http://tftb.nongnu.org/> and <http://gdr-isis.org/tftb/tutorial/tutorial.html>., 2005.
- [42] B. White, M. Pierce, N. Nassif, B. Cense, B. Park, G. Tearney, B. Bouma, T. Chen, and J. de Boer, "In vivo dynamic human retinal blood flow imaging using ultra-high-speed spectral domain optical Doppler tomography," *Opt. Express*, vol. 11, pp. 3490-3497, 2003.
- [43] I. Imai, and K. Tanaka, , "Direct velocity sensing of flow distribution based on low-coherence interferometry," *J. Opt. Soc. Am. A.*, vol. 16, pp. 2007-2012, 1999.
- [44] T. P. Zielinski, "On a software implementation of the Wigner-Ville transform," *Comp. Phys. Comm.*, vol. 50, pp. 269-272, 1988.
- [45] N. Bergmann, "New formulation of discrete Wigner-Ville distribution," *Electron. Lett.*, vol. 27, pp. 111-112, 1991.
- [46] T. Claasen, and W. Mecklenbräuker, "The Wigner distribution - a tool for time-frequency signal analysis Part II: Discrete time signals.," *Philips J. Res.*, vol. 35, pp. 276-300 1980.
- [47] T. P. Zielinski, "Wigner transform instantaneous phase estimator," *Eusipco-96, Trieste, PDE.*, vol. 10, 1996.
- [48] V. X. D. Yang, M. L. Gordon, A. Mok, Y. Zhao, Z. Chen, R. Cobbold, B. Wilson, and I. Alex Vitkin, "Improved phase-resolved optical Doppler tomography using the Kasai velocity estimator and histogram segmentation," *Opt. Comm.*, vol. 208, pp. 209-214,

2002.

- [49] Z. Q. Xu, L. Carrion, and R. Maciejko, "A zero-crossing detection method applied to Doppler OCT," *Optics Express*, vol. 16, pp. 4394-4412, 2008.
- [50] R. W. A. Scarr, "Zero crossings as a means of obtaining spectral information in speech analysis," *IEEE Trans. Audio Electroacoustics AU-16*, pp. 247-255, 1968.
- [51] J. Ohtsubo, "Exact solution of the zero crossing rate of a differentiated speckle pattern," *Opt. Commun.* , vol. 42, pp. 13-18, 1982.
- [52] T. Masuda, H. Miyano, and T. Sadoyama, , "The measurement of muscle fiber conduction velocity using a gradient threshold zero-crossing method," *IEEE Trans. Biomed. Eng. BME-29*, pp. 673-678, 1982.
- [53] K. R. Sreenivasan, A. Prabhu, and R. Narasimha, "Zero-crossings in turbulent signals," *J. Fluid Mech.*, vol. 137, pp. 251-270, 1983.
- [54] R. J. Adrian, "Statistics of laser Doppler velocimeter signals: frequency measurements," *J. Phys. E: Sci. Instrum.* , vol. 5, pp. 91-95, 1972.
- [55] D. L. Franklin, W. Schlegel, and R. F. Rushmer, "Blood flow measured by Doppler frequency shift of backscattered ultrasound," *Science* vol. 134, pp. 564-565, 1961.
- [56] A. M. Zeiher, H. Drexler, H. Wollschlager, and H. Just, "Endothelial dysfunction of the coronary microvasculature is associated with coronary blood flow regulation in patients with early atherosclerosis," *Circulation*, vol. 84, pp. 1984-1992, 1991.
- [57] S. O. Rice, "Selected Papers on Noise and Stochastic Processes," *Part III*, N. Wax, ed., (Dover, N.Y.), 1954.
- [58] C. Di Mario, J. Roelandt, P. De Jaegere, D. T. Linker, J. Oomen, and P. W. Serruys, , "Limitations of the zero crossing detector in the analysis of intracoronary Doppler: A comparison with fast Fourier transform analysis of basal, hyperemic, and transstenotic blood flow velocity measurements in patients with coronary artery disease," *Cath. Cardiovasc. Diagn.* , vol. 28, pp. 56-64, 1993.
- [59] M. J. Lunt, "Accuracy and limitations of the ultrasonic Doppler blood velocimeter and zero crossing detector," *Ultrasound Med. Biol.*, vol. 2, pp. 1-10, 1975.
- [60] G. L. Cote and M. D. Fox, "Comparison of zero-crossing counter to FFT spectrum of ultrasound Doppler," *IEEE Trans. Biomed. Eng. BME-29*, vol. 35, pp. 498-502, 1988.
- [61] B. Kedem, "Spectral analysis and discrimination by zero-crossings," *Proc. IEEE*, vol. 74, pp. 1477-1493, 1986.
- [62] I. Popov, "Accuracy of zero crossing counting in laser Doppler velocimetry," *Proc. SPIE* vol. 4827, pp. 394-402, 2002.
- [63] H. N. Thom, T. Rosemond, W. Howard, and V. Rumafeld J, "Heart disease and stroke statistics: 2006 update. A report from the American Heart Association Statistics

- Committee and Stroke Statistics Subcommittee," *Circulation Research*, vol. 113, pp. e85-151, 2006.
- [64] J. H. Leung, A. R. Wright, N. Cheshire, J. Crane, S. A. Thom, A. D. Hughes, and Y. Xu, "Fluid structure interaction of patient specific abdominal aortic aneurisms: A comparison with solid stress models," *BioMedical Engineering Online*, vol. 5, pp. 33, 2006.
- [65] K. Rhee, and J. Tarbell, "A study of the wall shear rate distribution near the end-to-end anastomosis of a rigid graft and a compliant artery," *Journal of Biomechanics*, vol. 27, pp. 329-338, 1994.
- [66] D. Katritsis, L. Kaiktsis, A. Chaniotis, J. Pantos, E. P. Efstathopoulos, and V. Marmarelis, "Wall shear stress: Theoretical considerations and methods of measurement," *Progress in Cardiovascular Diseases*, vol. 49, pp. 307-329, 2007.
- [67] A. M. Shaaban, and A. J. Duerinckx, "Wall shear stress and early atherosclerosis: A review," *AJR Am J Roentgenol*, vol. 174, pp. 1657-1665, 2000.
- [68] S. Fabregues, K. Baijens, R. Rieu, and P. Bergeron, "Hemodynamics of endovascular prostheses," *Journal of Biomechanics*, vol. 31, pp. 45-54, 1998.
- [69] S. Oyre, E. M. Pedersen, and S. Ringgaard, "In vivo wall shear stress measured by magnetic resonance velocity mapping in the normal human abdominal aorta," *Eur J Vasc Endovasc Surg*, vol. 13, pp. 263-271, 1997.
- [70] R. S. Reneman, T. Arts, and A. P. Hoeks, "Wall shear stress-An important determinant of endothelial cell function and structure-In the arterial system in vivo. iscrepancies with theory," *J Vasc Res*, vol. 43, pp. 251-269, 2006.
- [71] R. Stokholm, S. Oyre, and S. Ringgaard, "Determination of wall shear rate in the human carotid artery by magnetic resonance techniques," *Eur J Vasc Endovasc Surg* vol. 20, pp. 427-433, 2000.
- [72] A. Gnasso, C. Irace, and C. Carallo, "In vivo association between low wall shear stress and plaque in subjects with asymmetrical carotid atherosclerosis," *Stroke*, vol. 28, pp. 993-998, 1997.
- [73] C. Irace, C. Cortese, and E. Fiaschi, "Wall shear stress is associated with intima-media thickness and carotid atherosclerosis in subjects at low coronary heart disease risk," *Stroke*, vol. 35, pp. 464-468, 2004.
- [74] J. Bale-Glickman, K. Selby, and D. Saloner, "Experimental flow studies in exact-replica phantoms of atherosclerotic carotid bifurcations under steady input conditions," *J Biomech Eng*, vol. 125, pp. 38-48, 2003.
- [75] P. Hochareon, K. B. Manning, and A. A. Fontaine, "Wall shear-rate estimation within the 50cc Penn State artificial heart using particle image velocimetry," *J Biomech Eng*,

vol. 126, pp. 430-437, 2004.

- [76] B. K. Bharadvaj, R. F. Mabon, and D. P. Giddens, "Steady flow in a model of the human carotid bifurcation. Part II- Laser-Doppler anemometer measurements," *J Biomech*, vol. 15, pp. 363-378, 1982.
- [77] A. L. Zydney, J. D. Oliver, and C. K. Colton, "A constitutive equation for the viscosity of stored red-cell suspensions- effect of hematocrit, shear rate, and suspending phase," *J Rheol* vol. 35, pp. 1639-1680, 1991.
- [78] C. J. Pedersen, D. Huang, M. A. Shure, and A. M. Rollins, "Measurement of absolute flow velocity vector using dual-angle, delay-encoded Doppler optical coherence tomography," *Optics Letters*, vol. 32, pp. 506-508, 2007.
- [79] S. G. Proskurin, Y. He, and R. K. Wang, "Determination of flow velocity vector based on Doppler shift and spectrum broadening with optical coherence tomography," *Optics Letters*, vol. 28, pp. 1227-1229, 2003.
- [80] L. Carrion, Z. Xu, and R. Maciejko, "Applications of Doppler Optical Coherence Tomography based on zero-crossing detection to flow monitoring inside a simulated stenosis " presented at Photonics North, Montreal, 2008.
- [81] J. Fingberg, "Cardiovascular Simulation Software," in *C&C Research Laboratories*, G.-E. M. S. Services, Ed. Sankt Augustin (Germany).
<http://www.it.neclab.eu/gemss/index.html>.
- [82] K. Fujii, G. S. Mintz, S. G. Carlier, J. Jr. Ribamar Costa, M. Kimura, K. Sano, K. Tanaka, R. A. Costa, and J. Lui, "Intravascular ultrasound profile analysis of ruptured coronary plaques," *Am. J. Card.*, vol. 98, pp. 429-435, 2006.
- [83] C. Cheng, D. Tempel, R. Van Haperen, A. Van Der Baan, F. Grosveld, M. Daemen, R. Krams, and R. De Crom, "Atherosclerotic lesion size and vulnerability are determined by patterns of fluid shear stress," *Circulation*, vol. 113, pp. 2744-2763, 2006.
- [84] M. B. Robertson, U. Köhler, P. R. Hoskins, and I. Marshall, "Flow in elliptical vessels calculated for a physiological waveform," *J. Vasc. Res.*, vol. 38, pp. 73-82, 2001.
- [85] D. Beitel, L. Carrion, L. R. Chen, and R. Maciejko "Development of Broadband Sources Based on Semiconductor Optical Amplifiers and Erbium-Doped Fiber Amplifiers for Optical Coherence Tomography," *IEEE Journal of Selecte Topics in Quantum Electronics*, vol. 14, pp. 1-6, 2008.

APPENDIX A

Data processing with the STFT method

The following Matlab code was used for the STFT method.

```

testF_max1=[]; % Vector of the final peak frequencies
for i=1:6666
    l=abs(BFT(:,i));
    Summ=l'*testF;
    [M,k]=max(l);
    f_max=testF(k);
    testF_max1=[testF_max1; f_max];
end
FFT_max=testF_max1; %%% peak frequencies
plot(x,FFT_max,'k. '); %%% Indicate the peak frequencies in black dots
xlabel('X (mm)');
ylabel('Frequency (kHz)');
hold on;
% Statistical maximum-likelihood method
Y=buffer(FFT_max,30); %Divide the data by time segments
X=buffer(T_fft_02,30);
newY=[];
newX=[];
for i=1:222
    y=Y(:,i);
    x=X(:,i);
    x60=0:0.5:50; %500 Hz steps ranging from 0 to 50 kHz
    [valu,xnew]=hist(y,x60); % The histogram processing
    npoints=200;

```

```
j=find(yinterp==max(yinterp));
j=j(1);
maximum=yinterp(j);
halfmax=0.5*maximum; % Set the FWHM limitations
kk=find(yinterp>=halfmax);
lower=min(kk);
higher=max(kk);
ymin=xinterp(lower);
ymax=xinterp(higher);
nsigmax=1;
nsigmin=1;
coords=find(y<=nsigmax.*ymax & y>=nsigmin.*ymin);
y=y(coords);
x=x(coords);
newY=[newY; y];
newX=[newX; x];
end
plot(newX,newY,'y.');
```

% Indicate the noise rejected signal in yellow dots

APPENDIX B

Data processing with the Wigner method

The following Matlab code was used for the Wigner method.

```

testF_max1=[]; % Vector of the final peak frequencies
for i=2:113332
    l=testTFR1(:,i);
    j=find(l<=0);
    l(j)=0;
    Summ=l'*testF;
    [M,k]=max(l);
    f_max=testF(k);
    testF_max1=[testF_max1; f_max];
end
testF_max1=[testF_max1(1); testF_max1; testF_max1(end)];
FW_max=testF_max1; % peak frequencies
plot(x,FW_max,'k. '); % Indicate the peak frequencies in black dots
xlabel('X (mm)');
ylabel('Frequency (kHz)');
hold on;
% Statistical maximum-likelihood method
Y=buffer(FW_max_data2,500); %Divide the data by time segments
X=buffer(T_02,500);
newY=[];
newX=[];
for i=1:219
    y=Y(:,i);
    x=X(:,i);

```

```
yinterp=interp1(xnew,valu,xinterp,'pchip');
j=find(yinterp==max(yinterp));
j=j(1);
maximum=yinterp(j);
halfmax=0.5*maximum;
kk=find(yinterp>=halfmax);
lower=min(kk);
higher=max(kk);
ymin=xinterp(lower);
ymax=xinterp(higher);
nsigmax=1;
nsigmin=1;
coords=find(y<=nsigmax.*ymax & y>=nsigmin.*ymin);
y=y(coords);
x=x(coords);
newY=[newY; y];
newX=[newX; x];
end
hold on;
plot(newX,newY,'y. '); % Indicate the noise rejected signal in yellow dots
```

APPENDIX C

Data processing with the Hilbert method

The following Matlab code was used for the Hilbert method.

```
[H,HT]=instfreq(hilbert(A'));
H=[H(1); H; H(end)];
plot(T,H,'k. '); % Indicate the frequencies in black dots
xlabel('X (mm)');
ylabel('Frequency (kHz)');
hold on;
% Statistical maximum-likelihood method
Y=buffer(H,500); %%%%Divide the data by time segments
X=buffer(T,500);
newY=[];
newX=[];
for i=1:219
y=Y(:,i);
x=X(:,i);
x60=0:0.5:50; %500 Hz steps ranging from 0 to 50 kHz
[valu,xnew]=hist(y,x60); %%%% The histogram processing
npoints=200;
xinterp=0:50/(npoints-1):50;
yinterp=interp1(xnew,valu,xinterp,'pchip');
j=find(yinterp==max(yinterp));
j=j(1);
maximum=yinterp(j);
halfmax=0.5*maximum;
kk=find(yinterp>=halfmax);
```

```
nsigmax=1;
nsigmin=1;
coords=find(y<=nsigmax.*ymax & y>=nsigmin.*ymin);
y=y(coords);
x=x(coords);
newY=[newY; y];
newX=[newX; x];
end
plot(newX,newY,'y. '); % Indicate the noise rejected signal in yellow dots
```

APPENDIX D

Data processing with the autocorrelation method

The following Matlab code was used for the autocorrelation method.

```

q=6; % Setup of the delay
A_delay=[A3(q:end) A3(1:(q-1))];
mult=A3.*A_delay;
M=acos(mult);
FA=M./(0.02*pi*(q-1));
plot(x,FA,'k. '); % Indicate the frequencies in black dots
xlabel('X (mm)');
ylabel('Frequency (kHz)');
hold on;
% Statistical maximum-likelihood method
Y=buffer(FA,500);
X=buffer(x,500);
newY=[];
newX=[];
for i=1:218
y=Y(:,i);
x=X(:,i);
x60=0:0.5:50;
[valu,xnew]=hist(y,x60);
npoints=200;
xinterp=0:50/(npoints-1):50;
yinterp=interp1(xnew,valu,xinterp,'pchip');
j=find(yinterp==max(yinterp));
j=j(1);

```

```
higher=max(kk);
ymin=xinterp(lower);
ymax=xinterp(higher);
nsigmax=1;
nsigmin=1;
coords=find(y<=nsigmax.*ymax & y>=nsigmin.*ymin);
y=y(coords);
x=x(coords);
newY=[newY; y];
newX=[newX; x];
end
plot(newX,newY,'y. '); % Indicate the noise rejected signal in yellow dots
```

APPENDIX E

Data processing with the zero-crossing method

The following Matlab code was used for the zero-crossing method.

```

matrisP=[];
matrisX=[];
sample=signal(156,:);
    I=[];
for i=1:113332
if (abs(sample(i)+sample(i+1))~=(abs(sample(i))+abs(sample(i+1))));
I=[I i]; %positions just before zero cross
end
end
V=I+abs(sample(I))./(abs(sample(I))+abs(sample(I+1))); % zero cross position
v=diff(V);
P=1./(2*v)*100; % frequencies at each point
X=V(1:(end-1))+0.5.*v; % central positions
X=X.*(1.7/113332); % depth values
m=find(P<=15);
newX=X(m);
newP=P(m);
% Band pass filter
beltP=buffer(newP,65);
beltX=buffer(newX,65);
n=ceil(length(newX)/65);
new_P=[];
new_X=[];
for i=1:n
y=beltP(:,i);
x=beltX(:,i);
x60=0:0.5:50;
[valu,xnew]=hist(y,x60);

```

```
npoints=200;
xinterp=0:50/(npoints-1):50;
yinterp=interp1(xnew,valu,xinterp,'pchip');
J=find(yinterp==max(yinterp));
J=J(1);
maximum=yinterp(J);
halfmax=0.5*maximum;
kk=find(yinterp>=halfmax);
lower=min(kk);
higher=max(kk);
ymin=xinterp(lower);
ymax=xinterp(higher);
nsigmax=1;
nsigmin=1;
coords=find(y<=nsigmax.*ymax & y>=nsigmin.*ymin);
y=y(coords);
x=x(coords);
new_P=[new_P; y];
new_X=[new_X; x];
end
```